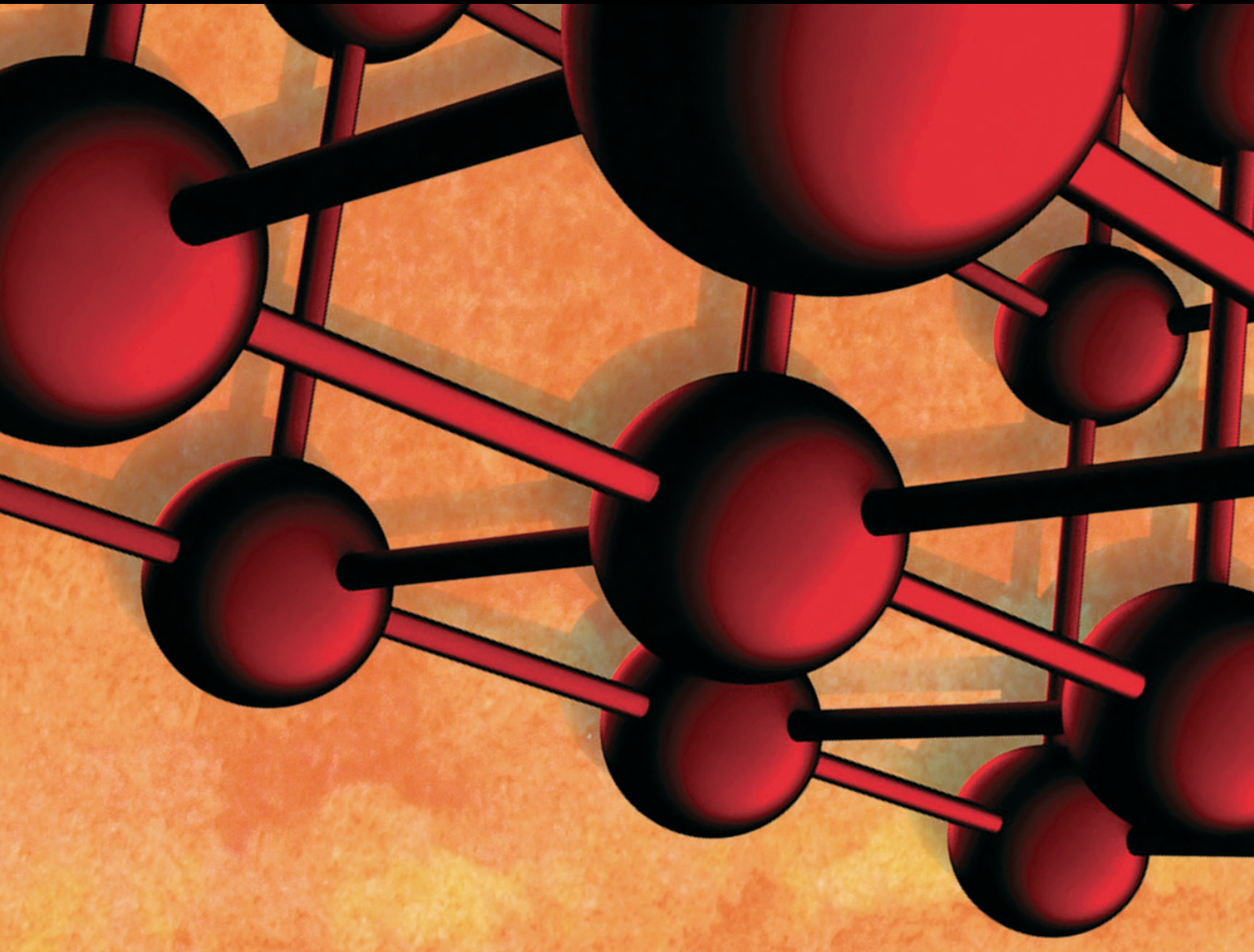


Advances in Materials Science and Engineering

Fiber-Reinforced Cement Composites: Mechanical Properties and Structural Implications

Lead Guest Editor: Doo-Yeol Yoo

Guest Editors: Nemkumar Banthia, Kazunori Fujikake, Young H. Kim,
and Rishi Gupta





Fiber-Reinforced Cement Composites: Mechanical Properties and Structural Implications

Advances in Materials Science and Engineering

Fiber-Reinforced Cement Composites: Mechanical Properties and Structural Implications

Lead Guest Editor: Doo-Yeol Yoo

Guest Editors: Nemkumar Banthia, Kazunori Fujikake,
Young H. Kim, and Rishi Gupta



Copyright © 2018 Hindawi. All rights reserved.

This is a special issue published in “Advances in Materials Science and Engineering.” All articles are open access articles distributed under the Creative Commons Attribution License, which permits unrestricted use, distribution, and reproduction in any medium, provided the original work is properly cited.

Editorial Board

- Antonio Abate, Germany
Michael Aizenshtein, Israel
Jarir Aktaa, Germany
Amelia Almeida, Portugal
K. G. Anthymidis, Greece
Santiago Aparicio, Spain
Alicia E. Ares, Argentina
Farhad Aslani, Australia
Renal Backov, France
Markus Bambach, Germany
Amit Bandyopadhyay, USA
Massimiliano Barletta, Italy
Mikhael Bechelany, France
Avi Bendavid, Australia
Brahim Benmokrane, Canada
Jamal Berakdar, Germany
Jean-Michel Bergheau, France
G. Bernard-Granger, France
Giovanni Berselli, Italy
Patrice Berthod, France
Michele Bianchi, Italy
Hugo C. Biscaia, Portugal
Antonio Boccaccio, Italy
Federica Bondioli, Italy
Susmita Bose, USA
Heinz-Günter Brokmeier, Germany
Steve Bull, UK
Gianlorenzo Bussetti, Italy
Jose M. Cabrera, Spain
Antonio Caggiano, Germany
Veronica Calado, Brazil
Marco Cannas, Italy
Paolo Andrea Carraro, Italy
Michelina Catauro, Italy
Jose Cesar de Sa, Portugal
Peter Chang, Canada
Daolun Chen, Canada
Gianluca Cicala, Italy
Francesco Colangelo, Italy
Marco Consales, Italy
José A. Correia, Portugal
María Criado, UK
Gabriel Cuello, France
Lucas da Silva, Portugal
- Narendra B. Dahotre, USA
João P. Davim, Portugal
Angela De Bonis, Italy
Abílio De Jesus, Portugal
Luca De Stefano, Italy
Francesco Delogu, Italy
Luigi Di Benedetto, Italy
Aldo Di Carlo, Italy
Maria Laura Di Lorenzo, Italy
Marisa Di Sabatino, Norway
Luigi Di Sarno, Italy
Ana María Díez-Pascual, Spain
Guru P. Dinda, USA
Nadka Tzankova Dintcheva, Italy
Mingdong Dong, Denmark
Frederic Dumur, France
Stanislaw Dymek, Poland
Kaveh Edalati, Japan
Philip Eisenlohr, USA
Claude Estournès, France
Luís Evangelista, Norway
Michele Fedel, Italy
F. J. Fernández Fernández, Spain
Isabel J. Ferrer, Spain
Paolo Ferro, Italy
Dora Foti, Italy
Massimo Fresta, Italy
Pasquale Gallo, Japan
Germà Garcia-Belmonte, Spain
Santiago Garcia-Granda, Spain
Carlos Garcia-Mateo, Spain
Georgios I. Giannopoulos, Greece
Ivan Giorgio, Italy
Antonio Gloria, Italy
Vincenzo Guarino, Italy
Daniel Guay, Canada
Gianluca Gubbiotti, Italy
Jenő Gubicza, Hungary
Xuchun Gui, China
Benoit Guiffard, France
Ivan Gutierrez-Urrutia, Japan
Hiroki Habazaki, Japan
Simo-Pekka Hannula, Finland
David Holec, Austria
- Satoshi Horikoshi, Japan
David Houivet, France
Rui Huang, USA
Yi Huang, UK
Michele Iafisco, Italy
Saliha Ilican, Turkey
Md Mainul Islam, Australia
Ilia Ivanov, USA
Alfredo Juan, Argentina
kenji Kaneko, Japan
Katsuyuki Kida, Japan
Akihiko Kimura, Japan
Soshu Kirihara, Japan
Paweł Kłosowski, Poland
Jan Koci, Czech Republic
Fantao Kong, China
Ling B. Kong, Singapore
Pramod Koshy, Australia
Hongchao Kou, China
Alexander Kromka, Czech Republic
Andrea Lamberti, Italy
Luciano Lamberti, Italy
Fulvio Lavecchia, Italy
Marino Lavorgna, Italy
Laurent Lebrun, France
Joon-Hyung Lee, Republic of Korea
Pavel Lejcek, Czech Republic
Cristina Leonelli, Italy
Ying Li, USA
Yuanshi Li, Canada
Guang-xing Liang, China
Barbara Liguori, Italy
Jun Liu, China
Meilin Liu, Georgia
Shaomin Liu, Australia
Yunqi Liu, China
Zhiping Luo, USA
Fernando Lusquinos, Spain
Peter Majewski, Australia
Georgios Maliaris, Greece
Muhamamd A. Malik, UK
Dimitrios E. Manolakos, Greece
Enzo Martinelli, Italy
Alessandro Martucci, Italy

Yoshitake Masuda, Japan
Bobby Kannan Mathan, Australia
Roshan Mayadunne, Australia
Shazim A. Memon, Kazakhstan
Philippe Miele, France
A. E. Miroshnichenko, Australia
Hossein Moayedi, Iran
Jose M. Monzo, Spain
Michele Muccini, Italy
Alfonso Muñoz, Spain
Rufino M. Navarro, Spain
Miguel Navarro-Cia, UK
Ali Nazari, Australia
Luigi Nicolais, Italy
Peter Niemz, Switzerland
Hiroshi Noguchi, Japan
Chérif Nouar, France
Olanrewaju Ojo, Canada
Dariusz Oleszak, Poland
Laurent Orgéas, France
Togay Ozbakkaloglu, Australia
Nezih Pala, USA
Marián Palcut, Slovakia
Davide Palumbo, Italy
Gianfranco Palumbo, Italy
Anna Maria Paradowska, Australia
Zbyšek Pavlík, Czech Republic
Matthew Peel, UK
Gianluca Percoco, Italy
Claudio Pettinari, Italy
Giorgio Pia, Italy
Daniela Pilone, Italy
Teresa M. Piqué, Argentina
Candido Fabrizio Pirri, Italy
Alain Portavoce, France

Simon C. Potter, Canada
Ulrich Prael, Germany
Viviana F. Rahhal, Argentina
Carlos R. Rambo, Brazil
Shahed Rasekh, Portugal
Manijeh Razeghi, USA
Paulo Reis, Portugal
Yuri Ribakov, Israel
Aniello Riccio, Italy
Anna Richelli, Italy
Antonio Riveiro, Spain
Marco Rossi, Italy
Sylvie Rossignol, France
Pascal Roussel, France
Fernando Rubio-Marcos, Spain
Francesco Ruffino, Italy
Mark H. Rummeli, China
Pietro Russo, Italy
Antti Salminen, Finland
F.H. Samuel, Canada
MariaGabriella Santonicola, Italy
Hélder A. Santos, Finland
Carlo Santulli, Italy
Fabrizio Sarasini, Italy
Michael J. Schütze, Germany
Raffaele Sepe, Italy
Kenichi Shimizu, USA
Fridon Shubitidze, USA
Mercedes Solla, Spain
Donato Sorgente, Italy
Charles C. Sorrell, Australia
Andres Sotelo, Spain
Costas M. Soukoulis, USA
Damien Soulat, France
Adolfo Spgehini, Italy

Antonino Squillace, Italy
Manfred Stamm, Germany
Koichi Sugimoto, Japan
Baozhong Sun, China
Sam-Shajing Sun, USA
Youhong Tang, Australia
Kohji Tashiro, Japan
Miguel Angel Torres, Spain
Laszlo Toth, France
Achim Trampert, Germany
Luca Valentini, Italy
Ashkan Vaziri, USA
Lijing Wang, Australia
Rui Wang, China
Zhongchang Wang, Portugal
Lu Wei, China
Jörg M. K. Wiezorek, USA
Guoqiang Xie, China
Dongmin Yang, UK
Zhonghua Yao, China
Hemmige S. Yathirajan, India
Yee-wen Yen, Taiwan
Wenbin Yi, China
Ling Yin, Australia
Hiroshi Yoshihara, Japan
Belal F. Yousif, Australia
Lenka Zajičková, Czech Republic
Michele Zappalorto, Italy
Jinghuai Zhang, China
Li Zhang, China
Mikhail Zheludkevich, Germany
Wei Zhou, China
You Zhou, Japan
Hongtao Zhu, Australia

Contents

Fiber-Reinforced Cement Composites: Mechanical Properties and Structural Implications

Doo-Yeol Yoo , Nemkumar Banthia , Kazunori Fujikake, Young Hoon Kim, and Rishi Gupta 
Editorial (2 pages), Article ID 8395461, Volume 2018 (2018)

Evaluation of Selected Physicomechanical Properties of SFRC according to Different Standards

Tereza Komárková , Jaromír Láník, and Ondřej Anton
Research Article (9 pages), Article ID 7098065, Volume 2018 (2018)

Utilization of Local Ingredients for the Production of High-Early-Strength Engineered Cementitious Composites

Hanwen Deng  and Shunzhi Qian
Research Article (15 pages), Article ID 8159869, Volume 2018 (2018)

Flexural Behavior of RC Slabs Strengthened in Flexure with Basalt Fabric-Reinforced Cementitious Matrix

Sugyu Lee, Kinam Hong , Yeongmo Yeon, and Kyusan Jung
Research Article (12 pages), Article ID 2982784, Volume 2018 (2018)

Feasibility of Reduced Lap-Spliced Length in Polyethylene Fiber-Reinforced Strain-Hardening Cementitious Composite

Wonchang Choi , Seok-Joon Jang, and Hyun-Do Yun 
Research Article (10 pages), Article ID 1967936, Volume 2018 (2018)

Air-Cured Fiber-Cement Composite Mixtures with Different Types of Cellulose Fibers

Ali Murat Soydan , Abdul Kadir Sari, Burcu Duymaz, Recep Akdeniz, and Bahadır Tunaboylu
Research Article (9 pages), Article ID 3841514, Volume 2018 (2018)

Mechanical Properties and Durability of Latex-Modified Fiber-Reinforced Concrete: A Tunnel Liner Application

Joo-Ha Lee, Hwang-Hee Kim, Sung-Ki Park, Ri-On Oh, Hae-Do Kim, and Chan-Gi Park 
Research Article (14 pages), Article ID 2134873, Volume 2018 (2018)

Effects of Reinforcing Fiber and Microsilica on the Mechanical and Chloride Ion Penetration Properties of Latex-Modified Fiber-Reinforced Rapid-Set Cement Concrete for Pavement Repair

Woong Kim, Jong-Chan Jeon, Byung-Hwan An, Joo-Ha Lee, Hae-Do Kim, and Chan-Gi Park 
Research Article (8 pages), Article ID 6839350, Volume 2018 (2018)

Mechanical Attributes of Uniaxial Compression for Calcium Carbonate Whisker Reinforced Oil Well Cement Pastes

Yuanyi Yang, Shun Fu, and Xingkui Li
Research Article (13 pages), Article ID 2939057, Volume 2017 (2018)

Mechanical Properties of Fiber-Reinforced Concrete Using Composite Binders

Roman Fediuk, Aleksey Smoliakov, and Aleksandr Muraviov
Research Article (13 pages), Article ID 2316347, Volume 2017 (2018)



Kinetic Hydration Heat Modeling for High-Performance Concrete Containing Limestone Powder

Xiao-Yong Wang

Research Article (11 pages), Article ID 4090265, Volume 2017 (2018)

Flexural Strengthening of RC Slabs Using a Hybrid FRP-UHPC System Including Shear Connector

Jiho Moon, Mahmoud M. Reda Taha, and Jung J. Kim

Research Article (7 pages), Article ID 4387545, Volume 2017 (2018)

Editorial

Fiber-Reinforced Cement Composites: Mechanical Properties and Structural Implications

Doo-Yeol Yoo ¹, **Nemkumar Banthia** ², **Kazunori Fujikake**³, **Young Hoon Kim**⁴,
and Rishi Gupta ⁵

¹Department of Architectural Engineering, Hanyang University, 222 Wangsimni-ro, Seongdong-gu, Seoul 04763, Republic of Korea

²Department of Civil Engineering, The University of British Columbia, 6250 Applied Science Lane, Vancouver, BC, Canada V6T 1Z4

³Department of Civil and Environmental Engineering, National Defense Academy, Yokosuka 239 8686, Japan

⁴Department of Civil and Environmental Engineering, University of Louisville, Louisville, KY 40292, USA

⁵Department of Civil Engineering, University of Victoria, 3800 Finnerty Road, Victoria, BC, Canada V8W 2Y2

Correspondence should be addressed to Doo-Yeol Yoo; dyyoo@hanyang.ac.kr

Received 13 March 2018; Accepted 13 March 2018; Published 24 June 2018

Copyright © 2018 Doo-Yeol Yoo et al. This is an open access article distributed under the Creative Commons Attribution License, which permits unrestricted use, distribution, and reproduction in any medium, provided the original work is properly cited.

To overcome inherent brittleness of concrete, extensive research on the development of high-ductility fiber-reinforced cement composites (FRCCs) has been conducted so far. Several types of FRCCs incorporating metallic, polymeric, carbon, glass, nylon, and waste tire fibers were successfully developed and effectively applied for infrastructure (i.e., buildings, tunnels, and bridges) because of their benefits of limiting crack propagation and widening through fiber bridging. Furthermore, (ultra-) high-performance fiber-reinforced cement composites showing strain- or deflection-hardening behavior with formation of multiple microcracks were invented in recent years, and various relevant studies are actively underway.

This special issue aims to give a comprehensive overview on FRCCs, including aspects related to mechanical behaviors, strengthening performance, and structural implications under various loading conditions (i.e., quasistatic, impact, blast, and fire). The selection of papers in this special issue was also very rigorous.

A several number of experimental and numerical papers reported new research findings regarding the mechanical properties of FRCCs. R. Fediuk et al. have studied to create a high-density impermeable FRCC and proposed the optimum binder proportions of 55 wt.% of ordinary Portland cement, 40 wt.% of fly ash, and 5 wt.% of limestone crushed wastes. Based on this optimization process, the FRCC with a high compressive strength of about

100 MPa and diffusion coefficient of about $1.36 \cdot 10^{-4} \text{ cm}^2/\text{s}$ was successfully developed. Y. Yang et al. have examined the effect of CaCO_3 whisker on the mechanical properties of cement paste. In their study, the optimum dosage of the CaCO_3 whisker was suggested to be 10%, which most significantly enhanced the tensile strength of cement paste. In addition, various mechanical properties, such as the peak strength, elastic modulus, and energy absorption capacity of the cement composites with CaCO_3 whisker, were reinforced with an increase in the amount of CaCO_3 whisker. J.-H. Lee et al. have assessed various mechanical properties and durability of latex-modified FRCCs with polyolefin-based macrosynthetic fibers and hybrid macrosynthetic-polypropylene fibers for tunnel lining application. They have concluded that the hybrid FRCCs exhibit the better mechanical performance and durability in terms of the higher compressive strength, flexural strength, impact resistance, abrasion resistance, and resistance to chloride ion penetration as compared to the macrosynthetic FRCCs. In order to develop a low-cost FRCC using various cellulose fibers, A. M. Soydan et al. have performed several mechanical tests. Based on the experimental results, they noted that the mechanical properties, that is, modulus of rupture and elastic modulus of FRCCs with bleached eucalyptus and araucaria cellulose fibers, are superior to those with cropped virgin cellulose fibers, especially after long air-cure

cycles, due to the higher density and packing of the formers. H. Deng and S. Qian have investigated the feasibility of using local ingredients for making high-early-strength engineered cementitious composites (ECCs) for rapid repair of existing transportation infrastructures. They reported that, by using the 0.8% local polyethylene fibers, the high-early-strength ECC with a tensile strength of 2.5 MPa and tensile strain capacity of 3% within 6 hours was successfully developed. This material can also lead to the ultimate compressive and tensile strengths of 49 and 5 MPa, respectively, and the ultimate tensile strain capacity of 3.5% after 60 days. The cost of all ingredients was greatly saved up to 70% by using the domestic products. K. Tereza et al. have evaluated various physicommechanical properties of steel fiber-reinforced concrete (SFRC) and noted that the flexural and residual strengths were improved by increasing the amount of steel fibers, and also, X. Y. Wang have suggested kinetic hydration heat models of high-performance concrete containing limestone powder.

Several researchers have investigated strengthening and repairing systems of existing structures using FRCCs. S. Lee et al. evaluated the flexural performance of reinforced concrete (RC) slabs strengthened with basalt fabric FRCCs. Based on their test results, the load carrying capacity of ordinary RC slab was improved as much as 11.2 to 98.2% by strengthening it with basalt fabric FRCCs, but the energy ratio and ductility were reduced with increasing the amount of fabric and tensile steel reinforcement, changing the ductile failure mode to the brittle failure mode. W. Kim et al. have examined the effects of reinforcing fibers and microsilica contents on the properties of latex-modified FRCCs for pavement repair. They recommended to use the microsilica at a substitution ratio of 3% or less and the macrosynthetic fibers as the reinforcement for the performance of latex-modified FRCCs for emergency repair of concrete pavement and to satisfy all the target strength requirements. J. Moon et al. have studied to evaluate a feasibility of hybrid fiber-reinforced polymer (FRP) and ultra-high-performance concrete (UHPC) system for flexural strengthening of RC slabs. This proposed strengthening system could improve the ultimate load carrying capacity of the RC slab by 70%, the stiffness by 60%, and the toughness by 128%, and also, the effectiveness of shear connectors on ductile behavior of the strengthened RC slab was confirmed. Lastly, W. Choi et al. have studied to decrease the lap-spliced length of reinforcement using a polyethylene FRCC showing strain-hardening response. They have verified that, by using the polyethylene FRCC, the development length of lap splice was effectively reduced as much as 60% of the splice length recommended by ACI 318-11 code, and the addition of expansive admixture to the FRCC mixture enhanced the initial performance and mitigated the cracking behavior in the lap splice region.

We hope that readers of this special issue are able to obtain useful experimental and numerical results and discover some recent research trends with regard to the FRCCs. We also wish that the readers' academic curiosities are satisfied and research questions are solved based on the valuable research results in this special issue from experimental and numerical findings. This publication considers a wide range of

disciplines, which include civil, architectural, and construction materials engineering, and may appeal to the engineers and scientists.

*Doo-Yeol Yoo
Nemkumar Banthia
Kazunori Fujikake
Young Hoon Kim
Rishi Gupta*

Research Article

Evaluation of Selected Physicomechanical Properties of SFRC according to Different Standards

Tereza Komárková , Jaromír Láník, and Ondřej Anton

Faculty of Civil Engineering, Brno University of Technology, Veveří 95, Brno, Czech Republic

Correspondence should be addressed to Tereza Komárková; tereza.komarkova@vutbr.cz

Received 2 September 2017; Revised 31 January 2018; Accepted 4 March 2018; Published 14 May 2018

Academic Editor: Rishi Gupta

Copyright © 2018 Tereza Komárková et al. This is an open access article distributed under the Creative Commons Attribution License, which permits unrestricted use, distribution, and reproduction in any medium, provided the original work is properly cited.

Steel fiber reinforced concretes are currently very popular, especially in the construction of industrial floors of warehouses and other halls with relatively large floor areas. However, it is important to mention that despite the rapid development of steel fiber reinforced concretes, the standards and regulations for their designing and testing have not been unified yet. This paper presents findings about the physicomechanical parameters of the steel fiber reinforced concretes manufactured by adding steel fibers into the truck mixer on the building site. The experimentally obtained results from the performed tests of tensile strength in bending according to various procedures are compared, and the suitability of the methods used is assessed according to these procedures.

1. Introduction

In the current building practice, steel fiber reinforced concrete is still mostly considered a new material. However, the idea of adding hard fibers to lower the undesirable natural fragility of the common building material is relatively old. The beginning of the 1960s marked a new period of a rising interest in reinforcing fragile building materials with fibers. First steel fiber reinforced concretes and glass fiber cement appeared. The various fiber technologies underwent rapid development, with ever-improving technical parameters, such as tensile strength and elasticity modulus (carbon fibers, aramid fibers, etc.) [1]. Various fibers were being experimentally added to concrete. The first three types to be employed in the building practice were steel wires, glass fibers, and polypropylene fibers. Their purpose was to improve the basic physicomechanical property of the composite, that is, to increase the tensile strength in bending at which the first crack caused by the dispersed fiber reinforcement appears, compared to the bending strength of common concrete. The dispersed fibers, however, can substantially increase the final strength, that is, the maximum load that the test specimen can sustain. However, this is preceded by a significant deformation, which in most

practical applications exceeds the acceptable values, accompanied by an appearance of a number of very narrow cracks. The problems with strength lead to the promotion of steel fiber reinforced concretes focusing on their uniquely high toughness [2]. Steel fiber reinforced concretes usually display high-transformation work related to the ability to keep the useful load capacity even in large deformations. The toughness and the related properties are based on the fracture process of the composite, during which fibers are drawn and broken simultaneously with the increase in the number and width of cracks in the structure of the manufactured composite. Toughness, that is, the ability of steel fiber reinforced concrete to transfer load even after a relatively high deformation (compared to common concrete), is a useful property which is increasingly demanded but rarely appropriately specified. The even dispersion of fibers leads to the effect of spatial action of fibers in the structure of a composite and to stiffening of its whole structure [3]. As such, the fibers cannot be regarded as a reinforcement in the traditional sense of the word but rather as a stiffening element of the relatively fragile structure of plain concrete [4, 5]. The initial optimistic predictions of the wide usage of steel fiber reinforced concretes assumed full-fledged interaction between the fibers and the structure of the original

hardened common concrete. The interaction depends on cohesion between the fibers and the cement paste of the composite. There are many technologies for steel fiber manufacturing, which causes that they have various physical mechanical properties. Dimensions are also very important, such as length, thickness, or shape. These parameters are very important for required cohesion of fibers and cement matrix, which improves mechanical properties of steel-reinforced concrete. A vast majority of fibers with a practical use in steel fiber reinforced concretes show very low natural cohesion with the hardened concrete [4]. The efficiency of dispersed fibers does not depend on the cohesion only [5]. In practice, all steel fiber reinforced concretes face the inevitable problems of the correct amount and concentration of fibers and their even dispersion and orientation [5, 6]. Fiber-reinforced concrete with steel fibers gradually became commonplace in applications where it was required for the structural element to keep its loading capacity even after a considerable deformation, not to exhibit wide cracks, and, in the case of damage, not to fall apart for as long as possible. Its higher strength against impact load and other dynamic impacts proved to be also quite useful in such cases. This is reflected by a common use of steel fiber reinforced concretes for large industrial floors with heavy duty traffic or high load.

The insufficient homogeneity can be partially due to the manufacturing process of the fresh mixture or its processing. During the manufacturing process, the steel fibers, which determine the characteristics of the resulting steel fiber reinforced concrete as its principal component, must be dosed in the order required by the type of aggregate used. The diversity of fiber types results in the need to respect the recommended main principles determined on the basis of the long-term experience obtained from testing the manufacture of steel fiber reinforced concretes. All types of steel fibers must be added as the last ingredient of the mixture. Considering the variety of the existing machinery used for the manufacture of common concrete, which should also be used for the manufacture of common steel fiber reinforced concrete, it is always necessary to determine in advance that the machinery and given procedure of dosing fibers in the manufacture of fresh steel fiber reinforced concrete lead to achieving the necessary homogeneity of the mixture. A reliable path to manufacturing homogenous steel fiber reinforced concrete leads through the use of the machinery used in concrete plants, that is, compulsory mixers. The standard manufacture of concrete, done so far mostly in truck mixers, is not an optimal solution. Although the main principle for the use of steel fibers—to add steel fibers as the last component—is fulfilled, achieving homogeneity is difficult and at a cost of prolonging the time of mixing because the performance of truck mixers is considerably lower than that of compulsory mixers. In practice, where only the minimum amount of steel fibers per unit volume of fresh concrete is applied (as in the case of SFRC floors of the industrial halls), achieving the homogeneity of steel fiber reinforced concrete remains a pipe dream. The same can be

said about its characteristics when applied, considering the influence of fibers on the hardening of the structure of cement composite. The relatively extensive usage of steel fiber reinforced concrete in floors leads to the emergence of new steel fiber manufacturers, new types of fibers, and thus a wide range of fibers which allows for choosing a suitable type of fiber for the required application.

Achieving broader knowledge of the properties of steel fiber reinforced concrete similar to that of other materials is only possible through a set of tests and experience obtained from real applications over a sufficiently long period of time. Only by connecting the material testing and the practice, we can achieve the defined objective. At the moment, it is possible to contribute to accelerating the aforementioned process by achieving a higher number of applications with a practical use of steel fiber reinforced concrete in a short time. One of the possibilities is a gradual unification of the testing procedures, which will lead to a unified assessment of the main characteristics of steel fiber reinforced concrete and to outputs allowing for a common procedure during preparations and implementation. For certain structures, the properties of steel fiber reinforced concretes can not only bring economic benefits but also be crucial for the implementation of the structures themselves. This applies even in the cases where steel fiber reinforced concrete is to be used in structures with traditional reinforcing-steel reinforcements or in prestressed structures. The method of testing the properties of steel fiber reinforced concretes, which slowly became a common part of structure designs, is currently not unified in terms of size of the test specimens, test arrangement, and their assessment. Fiber reinforced concrete with steel fibers must be included into building materials. The prerequisite for its use in concrete applications is having a good knowledge of the properties of the resulting composite obtained from mechanical tests with an appropriate assessment [7–14].

In this article, there are compared designed mixtures of steel fiber reinforced concrete, and they are tested according to standards common in Middle Europe. As it was mentioned before, resulting physicomaterial properties of the composite are affected by many factors. Authors focused on the test evaluation options according to described legislative standards with purpose of confirming of uniting methodology of determination bending strength, which is crucial for the steel fiber reinforced concrete classification.

2. Experiment

The experiment target was, according to the findings, to compare commonly used mixtures of the concrete of specified strength classes with concrete, where various amount of steel fibers were added, according to the flexural strength after cracks formations. The next target of the experiment was to compare the results evaluated according to various recommendations and standards for designing the steel fiber reinforced concrete constructions. Tests results were evaluated by three chosen recommendations for

TABLE 1: Design of construction concrete with individual amounts of steel fibers [7].

Concrete	Amount of fibers (kg per m ³)
C 16/20	—
	20
	25
C 20/25	30
	—
	20
C 25/30	25
	30
	—
C 30/37	20
	25
	30

construction designing and steel fiber reinforced concrete testing:

- (1) Technické podmínky 1: Vláknobeton—Část 1 Zkoušení vláknobetonu: Vyhodnocení destruktivních zkoušek a stanovení charakteristického pracovního diagramu vláknobetonu pro navrhování vláknobetonových konstrukcí. hereinafter referred as TP FC 1-1 [15].
- (2) According to the Directive Österreichische Vereinigung für Beton- und Bautechnik, hereinafter referred as ÖVBB [16].
- (3) Performance classes of steel fiber reinforced concrete [17].

The concrete mixture was prepared in a laboratory. From each batch prepared, three test prisms with the dimensions of 150 × 150 × 700 mm were made for the tests of tensile strength in bending and for the determination of the residual strength after the appearance of cracks. 4 mixtures of fresh concrete with 4 variations of steel fibers amount, totally 48 test specimens, were made considering the required minimum amount of specimens for statistic evaluation and scale of experiment (Table 1).

Every fresh mixture was tested in consistency by the method of the slump test and flow test, and the air content was also tested. The specimens were cured and kept according to ČSN EN 12390-2 Testing hardened concrete—Part 2: Making and curing specimens for strength tests [18].

The steel fibers, from the German manufacturer Krampe-Harex s.r.o., marked as DE50/0,1 N, were used in every mixture. The parameters of these fibers taken from the technical list are described in Table 2. Due to the requirement for pumpability of fresh concrete, there was chosen a procedure of dosing fibers in steps by 20 kg–25 kg–30 kg per m³ of fresh concrete.

For experimental testing, reference mixtures were used, which contained not only cement and aggregate but also fine slag (JMS), plasticizer, and power fly ash (Tables 3 and 4).

TABLE 2: Properties of the steel fibers.

Fibers	Length (mm)	Diameter (mm)	Material	Tensile strength
DE 50/1,0 N	50 ± 10%	1.0 ± 10%	C7D	1100 ± 15%

During the experiment, the manufactured test prisms with the dimensions of 150 × 150 × 700 mm were subjected to bending tests with the testing span of supports set to 600 mm. The bending tests were carried out on a testing device which allowed for loading by a continuous controlled deformation up to the point of damage. The bending tests of prisms were always performed in four-point bending setup according to regulation TP FC 1-1 [15]. The four-point test setup was chosen on purpose so that the specimen is broken by bending in the critical cross section dependent on the distribution of steel fibers in the test specimen (Figure 1). The results of the test of steel fiber reinforced concrete prisms in four-point bending without a notch are mostly on the safe side. That was also the main reason why this type of arrangement of the test had been chosen. The bending tests were carried out on a mechanical testing press with a set range of 0–40 kN. The values of the strength parameters were read by a calibrated strain gauge. The rate of the controlled deformation was set to 0.04 mm/min¹, and the strain rate was constant during the test. The deflection of the test prism was read above the support with the use of a rigid steel measuring frame located on the upper surface of the test specimen, and the values were doubled afterwards. The reading was performed by a calibrated inductance trajectory sensor HBM with a measuring range of up to 100 mm and a sensitivity of 0.001 mm. The output values were recorded with the data storage rate of 5 Hz. The duration of the executed bending tests of standard steel fiber reinforced concrete prisms ranged from 45 to 60 minutes. In the case of reference concretes without steel fibers, the tests took from half to one third of the time. The values of deflection were considered as half of the value at the point of reading, and the values of monitored parameters (loadings and deflections) were rounded to 4 decimal places.

On the basis of the data obtained from the bending tests executed on the series of SFRC specimens, tensile strengths were calculated according to the individual regulations. The results are shown in Table 5 and Figures 2–11.

The values of the tensile strength in bending of the reference concrete mixtures tested according to the individual regulations do not show significant differences. When the individual values are compared, it is not possible to determine unambiguously which assessment approach is the most suitable because no marked differences were recorded during the evaluation, nor is it possible to observe any dependence between the individual approaches to the calculation of the tensile strength in bending.

By adding 20 kg of steel fibers into the reference concrete mixtures of the individual strength classes, no significant increase in the tensile strength in bending was achieved. The increase of the tensile strength depended only on the class of the concrete.

TABLE 3: Composition of the referential concrete mixture in kg per m³ [19].

Concrete	Cement CEM I 42,5 R	JMS	Fly ash	Aggregates 0–4	Aggregates 8–16	Aggregates 11–22	Amount of additive	Water
C 16/20	220	50	30	901	536	425	2.3	176
C 20/25	240	50	30	880	536	425	2.5	177
C 25/30	260	50	30	860	536	425	2.6	178
C 30/37	280	50	30	855	546	435	2.1	170

TABLE 4: Composition of the steel fiber reinforced concrete mixtures in kg per m³.

Concrete	Amount of fibers	Cement CEM I 42,5 R	JMS	Fly ash	Aggregates 0–4	Aggregates 8–16	Aggregates 11–22	Amount of additive	Water
C 16/20	20	220	50	30	890	530	425	2.30	180
	25						420		181
	30						415		182
C 20/25	20	240	50	30	870	530	425	2.47	181
	25						420		182
	30						415		183
C 25/30	20	260	50	30	850	530	425	2.64	182
	25						420		183
	30						415		184
C 30/37	20	280	50	30	845	540	435	2.23	174
	25						430		175
	30						425		176



FIGURE 1: Process of the bending test of the SFRC prisms.

By adding 25 kg of steel fibers into the reference concrete mixtures of the individual strength classes, no significant change in the values of the tensile strength in bending was achieved. The values increase only in relation to the strength class of the concrete.

Admixture of 30 kg of steel fibers into the reference concrete mixtures caused a decrease in the tensile strength in bending in the strength class C 25/30. This fact could have been caused, for example, by exhaustion of the cement paste. Adding steel fibers caused an increase of the specific surface area which had to be bound to the cement paste, probably causing the exhaustion of the cement paste and the decrease of values.

Then the laboratory tests for residual bending strengths after crack formation were executed. The summary results of average values in MPa are stated in Table 6.

Calculation of the residual strength for reference concretes without dispersed steel reinforcement is rather misleading. The calculation results are strongly influenced by friction of aggregate in the emerging macrocrack. During the

test prism loading controlled by deformation at low rates (0.2 mm/min¹), the friction of aggregate grains in the emerging microcrack is relatively high and “artificially” influences the values of residual strengths at larger deflections. In case the prism was loaded with a controlled force (hydraulic testing press), the values of residual forces would not be high, and the prism damage would suddenly occur at lower deflections. The phenomenon of grain friction in the macrocrack would be almost negligible, as is the case with common tests of tensile strength in bending executed according to the procedure described in ČSN EN 12390-5 [20].

A dose of 20 kg of steel fibers per cubic meter of fresh concrete mixture is regarded as a minimum in most steel fiber reinforced concrete formulas in terms of the resulting composite keeping its ability to transfer load after the appearance of a microcrack. It is apparent from the results of the experiments executed that the dose of 20 kg of steel fibers is a borderline amount for ensuring sufficient residual strengths after the appearance of a crack in all the monitored strength classes. The individual assessment procedures showed different results depending on the method of recommended calculation. The lowest results were obtained when calculated according to the procedure described in the regulation TP FC 1-1 [15], where the minimum recommended residual strength after the emergence of a macrocrack is 0.4 N/mm². The best results were achieved when calculated according to the recommendation of the Performance classes of SFRC [17]. These differences were caused by different approaches of individual formulas to the calculation of residual strength.

By increasing the dose of steel fibers to 25 kg/m³, a higher residual strength was achieved in all monitored strength classes. However, when evaluated according to TP FC 1-1, the resulting values of residual strength were on the boundary of applicability, especially for strength class C

TABLE 5: Assessment of the tensile strength in bending according to the Austrian standard (ÖVB) [20], Performance classes of SFRC [6], and TP FC 1-1 [10] in MPa.

Concrete mixtures	ÖVBB	Performance classes of SFRC	TP FC 1-1	
Referential	C 16/20	3.8	4.5	4.1
	C 20/25	4.9	5.0	5.1
	C 25/30	4.2	4.7	4.4
	C 30/37	5.0	4.8	5.0
20 kg	C 16/20	3.8	4.2	4.0
	C 20/25	3.7	4.2	3.9
	C 25/30	4.6	5.1	4.8
	C 30/37	4.9	4.8	5.0
25 kg	C 16/20	3.9	4.5	4.2
	C 20/25	3.9	3.9	4.0
	C 25/30	4.3	4.2	4.5
	C 30/37	5.1	5.5	5.4
30 kg	C 16/20	3.8	3.7	4.0
	C 20/25	4.9	5.2	5.1
	C 25/30	3.8	3.9	3.8
	C 30/37	5.7	5.6	5.8

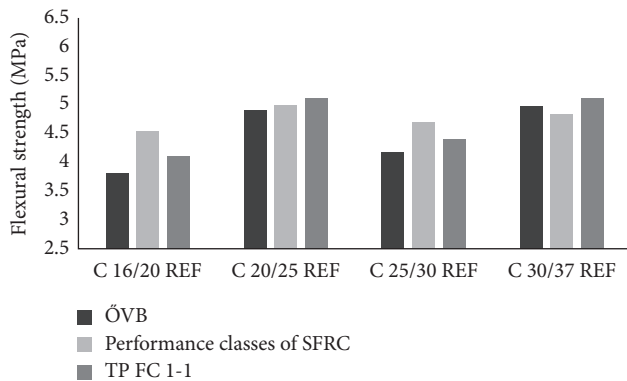


FIGURE 2: Bending strength of reference concrete mixtures.

20/25. In the case of strength class C 16/20, a relatively significant increase in residual strength was observed when calculated according to the Performance classes of SFRC, where the performance calculation procedure involves a comparison between the resulting SFRC composite and the reference mixture.

Adding a dose of 30 kg of steel fibers into the individual reference mixtures caused an increase in the residual tensile strength in bending of the resulting steel fiber reinforced concrete. The most significant increase was observed in strength classes C 16/20 and C 20/25. The assessment of residual strengths according to the individual procedures showed that the highest benefit of the dose of steel fibers for the residual strength was found within strength class C 20/25. The calculation results according to the procedure in TP FC 1-1 are again on the boundary of applicability in terms of the required residual strength after the emergence of a macrocrack. However, in strength class C 20/25, a significant increase in this strength was observed even when calculated according to the procedure in TP. The best results

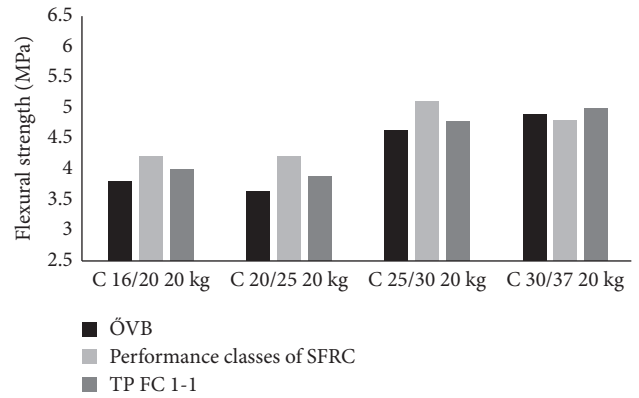


FIGURE 3: Bending strength of SFRC—amount of fibers: 20 kg/m³.

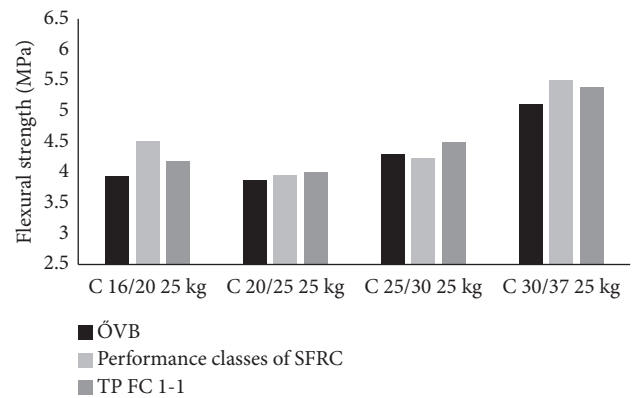


FIGURE 4: Bending strength of SFRC—amount of fibers: 25 kg/m³.

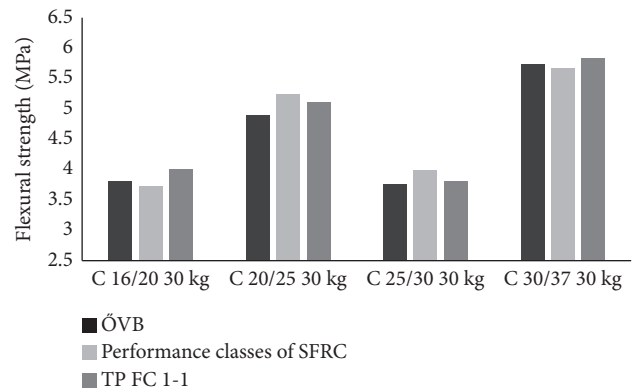


FIGURE 5: Bending strength of SFRC—amount of fibers: 30 kg/m³.

of the residual tensile strength in bending were, again, achieved when the procedure described in the Performance classes of SFRC was used.

Table 7 shows the results of the individual calculations according to the selected procedures and recommendations for designing and assessment of manufactured SFRC composites on the basis of tests of tensile strength in bending performed on the manufactured standard test specimens after 28 days of maturing in a controlled environment.

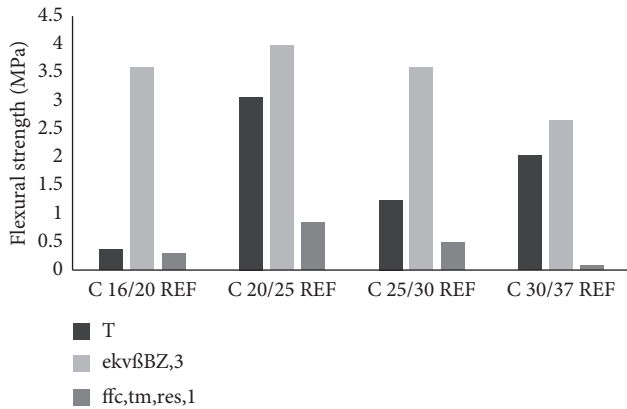


FIGURE 6: Residual tensile strength in bending at the moment of achieving a deflection of 3.5 mm, reference mixture of common concrete.

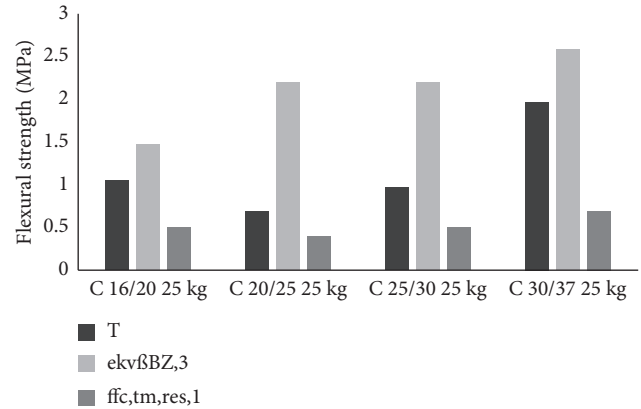


FIGURE 8: Residual tensile strength in bending at the moment of achieving a deflection of 3.5 mm, steel fiber reinforced concrete with a dose weight of 25 kg/m³.

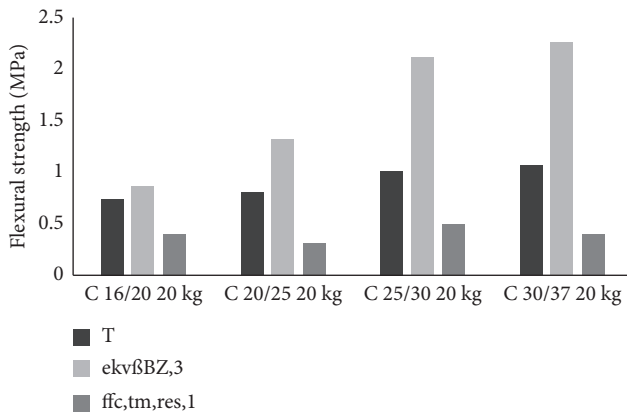


FIGURE 7: Residual tensile strengths in bending at the moment of achieving a deflection of 3.5 mm, steel fiber reinforced concrete with a mass dose of 20 kg/m³.

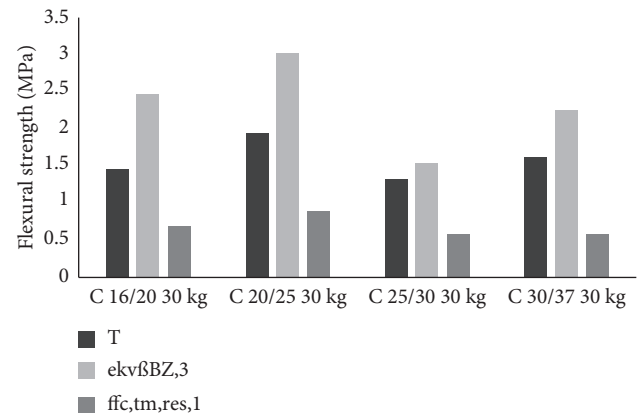


FIGURE 9: Residual tensile strengths in bending at the moment of achieving a deflection of 3.5 mm, steel fiber reinforced concrete with a dose weight of 30 kg/m³.

3. Evaluation of the Performed Bending Tests according to a Simplified Calculation of Specific Fracture Energy

Calculation of specific fracture energy for the individual tested sets of manufactured steel fiber reinforced concretes was driven by an effort to assess the influence of the amount of fibers on the energy necessary for the bending damage of the tested specimen to occur and the degree of influence of the given amount of fibers in the reference cement matrix on the bending damage. The results of calculations are summarized in the following table and included an evaluation of a standard deviation and a coefficient of variation for the individual sets. The values are only approximate because the specific fracture energy is calculated by a highly simplified procedure, and the ambient and other factors are disregarded in this case. The calculations are designed to compare the individual sets of test specimens with each other and cannot be used in more complex applications, such as MKP models (finite element method). If they were to be used for a modelling of the given matter by means of MKP methods, it would be necessary to use more complex procedures for determining the specific fracture energy and to approach experts on the given field (Table 8).

On the basis of the graphic representation of the results of simplified calculations of specific fracture energy, it is possible to conclude that the increasing content of steel fibers in concrete leads to an increase of fracture work, or fracture energy, compared to the reference mixture of common concrete. In some cases, it was possible to observe an opposite phenomenon where fibers decreased the value of the specific fracture energy compared to the reference concrete mixture. This phenomenon could have been caused, for example, by incorrect distribution of fibers in the reference concrete or by the loosening of the concrete due to admixture of steel fibers into a fresh mixture, potentially increasing the content of air pores in the hardened concrete. A higher content of air pores in the hardened concrete, acting as perfectly compressible nonhomogeneities in the structure of the composite, can influence the ability of the concrete composite to transmit.

Calculations of the standard deviation and the coefficient of variation when determining the specific fracture energy showed that increasing the amount of steel fibers in concrete causes an increase in the dispersion of measured values (tensile strength in bending). When higher doses of

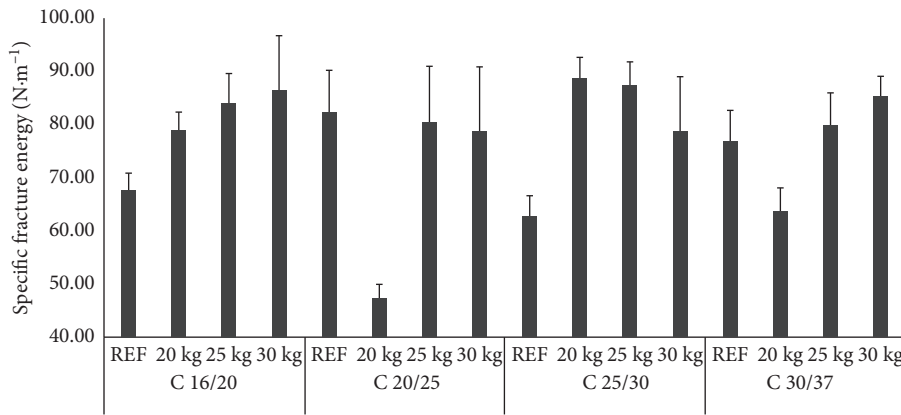


FIGURE 10: Results of calculations of specific fracture energy.

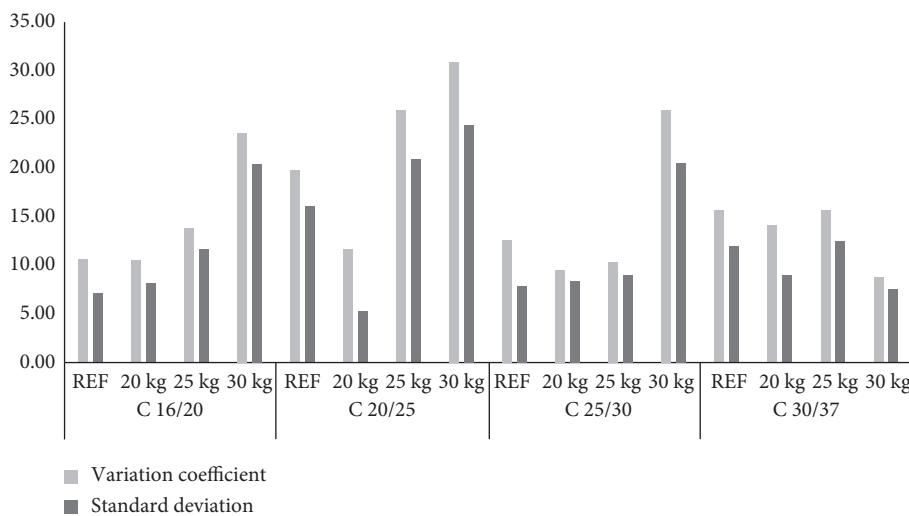


FIGURE 11: Representation of the coefficient of variation and standard deviation in the calculations of specific fracture energy from the working diagrams of the performed tests.

dispersed steel reinforcement (30 kg/m^3) are used, the distribution of fibers in the critical cross section is more random than in the case of lower doses. The dispersion of steel fibers when using higher doses is so significant that it considerably influences the dispersion of values in the bending tests where the critical cross section of the damage is not determined in advance, such as in the case of tests performed according to ČSN EN 14651 + A1 [21], where a three-point bending with a central notch is considered. When performing the bending tests of SFRC according to ČSN EN 14651 + A1 [21], the dispersion of values is lower even with higher doses of steel fibers. However, the question is which the method of damage testing is closer to reality and to the real influence of steel fibers in the manufactured cross section of, for example, floor panels in relation to the dosing of fibers to the truck mixer on the construction site.

4. Conclusion

During the bending tests of the manufactured steel fiber reinforced concretes, it was observed that the values of

bending strength increase with the increasing amount of fibers. However, the increase of values was not as significant as expected. In relation to the increase in bending strengths, an increase in the residual strengths was observed. Based on the results of the performed tests, it is possible to say that the steel fiber reinforced concrete made from the basic mixture of the C 16/20 strength class with a 30 kg dose of steel fibers showed very similar properties in the residual tensile strength in bending as the SFRC one made from the basic mixture C 30/37 with a 30 kg dose of steel fibers. The assessment of the executed bending tests of steel fiber reinforced concrete according to the three selected procedures (TP FC 1-1, Performance classes of SFRC, and Austrian standard for SFRC) showed that it is very important to choose a correct procedure according to which the tests of SFRC will be executed. The methods for determination of the tensile strength and residual tensile strength are rather different in the individual procedures and the calculation results vary significantly. The best results for residual strengths were always obtained using the procedure given by the “Performance classes of SFRC,” while the residual strength

TABLE 6: Assessment of the residual tensile strength in bending at a deflection of 3.5 mm according to the Austrian Standard [16], Performance classes of SFRC [17], and TP FC 1-1 [15] in MPa.

Concrete mixture		ÖVBB	Performance classes of SFRC		TP FC 1-1
		T	ekv $\beta_{BZ,3}$		$f_{fc,tm,res,1}$
REF	C 16/20	0.38	3.59		0.30
	C 20/25	3.09	3.96		0.90
	C 25/30	1.27	3.61		0.50
	C 30/37	2.06	2.68		0.10
20 kg	C 16/20	0.74	0.86		0.40
	C 20/25	0.80	1.31		0.30
	C 25/30	1.01	2.10		0.50
	C 30/37	1.07	2.26		0.40
25 kg	C 16/20	1.06	1.48		0.50
	C 20/25	0.69	2.21		0.40
	C 25/30	0.97	2.21		0.50
	C 30/37	1.98	2.60		0.70
30 kg	C 16/20	1.48	2.48		0.70
	C 20/25	1.95	3.03		0.90
	C 25/30	1.33	1.54		0.60
	C 30/37	1.63	2.26		0.60

TABLE 7: Summary table with the results of assessment of the performed bending tests in MPa.

Identification		ÖVB			Performance classes of SFRC			TP FC 1-1	
		BZ	G	T	β_{BZ}	ekv $\beta_{BZ,2}$	ekv $\beta_{BZ,3}$	$f_{fc,tm,fl}$	$f_{fc,tm,res,1}$
C 16/20	20 kg	3.82	1.73	0.74	4.22	1.73	0.86	4.00	0.40
	25 kg	3.94	1.98	1.06	4.52s	1.76	1.48	4.20	0.50
	30 kg	3.81	2.47	1.48	3.74	2.05	2.48	4.00	0.70
	REF	3.82	1.12	0.38	4.53	3.27	3.59	4.10	0.30
C 20/25	20 kg	3.66	1.47	0.80	4.22	1.74	1.31	3.90	0.30
	25 kg	3.90	2.55	0.69	3.95	2.21	2.21	4.00	0.40
	30 kg	4.88	2.84	1.95	5.23	2.36	3.03	5.10	0.90
	REF	4.91	4.81	3.09	5.00	3.65	3.96	5.10	0.90
C 25/30	20 kg	4.63	2.22	1.01	5.13	2.41	2.10	4.80	0.50
	25 kg	4.31	2.05	0.97	4.24	2.36	2.21	4.50	0.50
	30 kg	3.75	2.41	1.33	3.98	1.64	1.54	3.80	0.60
	REF	4.18	3.77	1.27	4.70	3.32	3.61	4.40	0.50
C 30/37	20 kg	4.90	2.94	1.07	4.81	2.25	2.26	5.00	0.40
	25 kg	5.12	3.05	1.98	5.51	2.54	2.60	5.40	0.70
	30 kg	5.71	3.15	1.63	5.64	2.48	2.26	5.80	0.60
	REF	4.99	4.72	2.06	4.84	3.34	2.68	5.10	0.10

TABLE 8: Results of calculations of specific fracture energy from the working diagrams in N/m.

Identification		Specimen A	Specimen B	Specimen C	Average value	Standard deviation	Coefficient of variation
C 16/20	REF	74.79	57.46	69.66	67.30	7.27	10.80
	20 kg	86.95	80.82	67.15	78.31	8.28	10.57
	25 kg	100.19	79.1 2	72.79	84.03	11.71	13.94
	30 kg	64.69	113.95	81.11	86.582	20.48	23.65
C 20/25	REF	83.00	61.93	101.94	82.29	16.34	19.86
	20 kg	55.23	42.96	43.96	47.38	5.56	11.74
	25 kg	108.99	58.81	74.25	80.68	20.98	26.01
	30 kg	66.65	56.75	113.04	78.81	24.54	31.13
C 25/30	REF	59.90	73.84	54.92	62.89	8.01	12.73
	20 kg	79.79	100.24	85.84	88.62	8.58	9.68
	25 kg	78.03	99.94	84.55	87.51	9.19	10.50
	30 kg	73.11	106.36	56.96	78.81	20.57	26.10
C 30/37	REF	80.04	60.69	89.89	76.87	12.13	15.78
	20 kg	53.54	62.11	75.59	63.75	9.08	14.24
	25 kg	88.52	62.12	89.04	79.89	12.57	15.73
	30 kg	79.60	96.21	80.41	85.41	7.65	8.95

calculations according to the recommendations of the Austrian standard for SFRC also lead to relatively good results. The results of calculations of residual strengths of SFRC according to the Czech Technical Regulation TP FC 1-1 were relatively low, often on the boundary of usability of the manufactured composite in the given application. These differences were caused by different approaches to the determination of residual strengths based on the bending tests. The foreign procedures perform calculations either on the basis of performance, where the benefit of steel fibers is assessed by comparing a reference mixture of common concrete and the same mixture with the steel fibers added, or by means of an “energetic” approach in which the area below the curve of the working diagram of the SFRC bending test up to the conventional deformation is evaluated. It is thus very important to know which approach to the assessment of residual strength of SFRC to choose so that the resulting composite has the required properties. If someone specifies, or guarantees, the properties or steel fiber reinforced concrete, it is necessary to know according to which regulation and procedure these properties, especially residual strength, were calculated. From the results achieved with the manufactured steel fiber reinforced concretes in the experimental part, it is apparent that the individual procedures and recommendations for SFRC should not be combined because the results deemed satisfactory according to one procedure but can be nonsatisfactory when calculated according to another. Based on the results, the authors recommend the procedure according to the TP FC 1-1.

Conflicts of Interest

The authors declare that they have no conflicts of interest.

Acknowledgments

This paper has been worked out under the Project no. LO1408 “AdMaS UP-Advanced Materials, Structures and Technologies,” supported by Ministry of Education, Youth and Sports under the “National Sustainability Programme I.”

References

- [1] T. F. Flory, J. Hearle, H. Mckenna, and M. Parsey, “About 75 years of synthetic fiber rope history,” in *Proceedings of the OCEANS MTS/IEEE Conference*, Washington, DC, USA, October 2015.
- [2] T. Simões, H. Costa, D. Dias-da-Costa, and E. Júlio, “Influence of fibres on the mechanical behaviour of fibre reinforced concrete matrixes,” *Construction and Building Materials*, vol. 137, no. 1, pp. 548–556, 2017.
- [3] G. Appa Rao and A. Sreenivasa Rao, “Toughness indices of steel fiber reinforced concrete under mode II loading,” *Materials and Structures*, vol. 42, no. 9, pp. 1173–1184, 2009.
- [4] V. Veselý, J. Vodička, J. Vašková, and J. Krátký, “Tests of structural fibre concrete,” in *Beton: Technologie, Konstrukce, Sanace*, pp. 43–47, Czech Concrete Society, Praha, Czech Republic, 2010.
- [5] R. Gettu, D. R. Gardner, H. Saldívar, and B. E. Barragán, “Study of the distribution and orientation of fibers in SFRC specimens,” *Materials and Structures*, vol. 38, no. 1, pp. 31–37, 2005.
- [6] P. J. M. Bartoš, “Fibre reinforced concrete,” in *Beton: Technologie, Konstrukce, Sanace*, pp. 69–77, Czech Concrete Society, Praha, Czech Republic, 2012.
- [7] J. Vodička, V. Veselý, K. Kolář, and J. Krátký, “Fibre concrete in practice,” in *Beton: Technologie, Konstrukce, Sanace*, pp. 53–55, Czech Concrete Society, Praha, Czech Republic, 2010.
- [8] A. Blanco, P. Pujadas, A. de la Fuente, S. H. P. Cavalaro, and A. Aguado, “Assessment of the fibre orientation factor in SFRC slabs,” *Composites Part B: Engineering*, vol. 68, no. 1, pp. 343–354, 2015.
- [9] P. Stähli, R. Custer, and J. G. M van Mier, “On flow properties, fibre distribution, fibre orientation and flexural behaviour of FRC,” *Materials and Structures*, vol. 41, no. 1, pp. 189–196, 2008.
- [10] P. Pytlík, *Technologie Betonu*, VUTIUM, Brno, Czech Republic, 2000.
- [11] J. Vodička, V. Veselý, and J. Krátký, “Specifics of fibre concrete technology,” in *Beton: Technologie, Konstrukce, Sanace*, pp. 38–42, Czech Concrete Society, Praha, Czech Republic, 2010.
- [12] J. Krátký, J. Vodička, and J. Vašková, “Design of fibre concrete structural elements,” in *Beton: Technologie, Konstrukce, Sanace*, pp. 87–89, Czech Concrete Society, Praha, Czech Republic, 2010.
- [13] J. Vašková, “Experimental verifying of fibre concrete elements behaviour,” in *Beton: Technologie, Konstrukce, Sanace*, pp. 74–78, Czech Concrete Society, Praha, Czech Republic, 2010.
- [14] J. Štoller and E. Zezulová, “The application of fibre reinforced concrete for protective shelter from auxiliary material,” *Key Engineering Materials*, vol. 755, pp. 374–381, 2017.
- [15] TP FC 1-1, *Technické podmínky 1: Vláknobeton – Část 1 Zkoušení vláknobetonu: Vyhodnocení Destrutivních Zkoušek a Stanovení Charakteristického Pracovního Diagramu Vláknobetonu pro Navrhování Vláknobetonových Konstrukcí*, Českomoravský Beton, a.s., Praha, Czech Republic, 2007.
- [16] ÖVBB-Richtlinie Faserbeton, *Österreichische Vereinigung für Beton und Bautechnik: Faserbeton*, Austrian Structural Engineering Association, Vienna, Austria, 2008.
- [17] H. Falkner, M. Teutsch, and H. Klinkert, *Massivbau und Brandschutz: Leistungsklassen von Stahlfaserbeton*, IBMB, Braunschweig, Germany, 1999.
- [18] ČSN EN 12390-2, *Testing Hardened Concrete: Part 2: Making and Curing Specimens for Strength Tests*, Czech Office for Standards, Metrology and Testing, Praha, Czech Republic, 2009.
- [19] T. Komárková, J. Láník, and P. Dvořák, “Influence of dispersed reinforcement on the physico-mechanical properties of the SFRC,” *Key Engineering Materials*, vol. 755, pp. 75–81, 2017.
- [20] ČSN EN 12390-5, *Testing Hardened Concrete—Part 5: Flexural Strength of Test Specimens*, Czech Office for Standards, Metrology and Testing, Praha, Czech Republic, 2009.
- [21] ČSN EN 14651 + A1, *Test Method for Metallic Fibered Concrete: Measuring the Flexural Tensile Strength (Limit of Proportionality (LOP), Residual)*, Czech Office for Standards, Metrology and Testing, Praha, Czech Republic, 2008.

Research Article

Utilization of Local Ingredients for the Production of High-Early-Strength Engineered Cementitious Composites

Hanwen Deng¹ and Shunzhi Qian²

¹School of Transportation, Southeast University, Sipailou 2, Nanjing 210096, China

²School of Civil and Environmental Engineering, Nanyang Technological University, Singapore 639798

Correspondence should be addressed to Hanwen Deng; dhw0075@163.com

Received 18 August 2017; Accepted 25 February 2018; Published 5 April 2018

Academic Editor: Rishi Gupta

Copyright © 2018 Hanwen Deng and Shunzhi Qian. This is an open access article distributed under the Creative Commons Attribution License, which permits unrestricted use, distribution, and reproduction in any medium, provided the original work is properly cited.

The rapid repair and retrofitting of existing transportation infrastructure requires dimensional stability and ductile repair material that can obtain sufficiently high strength in a few hours to accommodate the large loading and deformation at an early age. Engineering cementitious composites (ECCs) is a class representative of the new generation of high-performance fiber-reinforced cement-based composites (HPFRCC) with medium fiber content. The unique properties of tremendous ductility and tight multiple crack behavior indicate that ECC can be used as an effective retrofit material. The wide application of this material in China will require the use of all local ingredients. In this study, based on Chinese domestic ingredients, including matrix materials and all fibers, high-early-strength ECC (HES-ECC) was designed under the guidance of strain-hardening criterion of ECC. The matrix properties and fiber/matrix interfacial micromechanics properties were obtained from three-point-bending test and single-fiber pullout test. The mechanical properties of HES-ECC were achieved by direct tensile test. The experimental results show that HES-ECC was successfully developed by using all Chinese materials. When using the domestic PVA fiber at 2%, the strength requirement can be achieved but only a low ductility. When using the domestic PE fiber at 0.8%, the strength and deformation requirement both can be obtained. The HES-ECC developed in this study exhibited compressive strength of more than 25 MPa within 6 hours, and an ultimate tensile strength of 5-6 MPa and tensile strain capacity of 3-4% after 60 days. Moreover, the cost of using domestic fiber can be largely reduced compared with using imported fiber, up to 70%; it is beneficial to the promotion of these high-early-strength ECCs in the Chinese market.

1. Introduction

With the rapid development of China's economy and the increasing number of transportation infrastructure, the concrete structure for repair and retrofit requires the shortest traffic interruption time. Meanwhile, the demand for high-strength or fast-hardening concrete is also increased. For example, the Road Transport Department often requires repair work to be completed within 6-8 hours in the evening to facilitate the road to be able to reopen in the early morning of the next day [1]. In the past three decades, academics and industrial scholars have done a lot of experimental research and successfully developed the repair materials which can attain enough high compressive strength and bending strength at a very early age. These concrete materials obtain

early high strength by using either special fast-setting cement [2-6] or combined use of ordinary cement with accelerating agent [7-9], resulting in various strength increasing rates.

Unfortunately, the traditional concrete repairs are often lacking durability. According to conservative estimates, nearly a half of traditional concrete repair is failure [10-12]. About three-quarters of the failures are attributing to the lack of durability, and one-quarter of failure is due to structural failure. Early damage often occurs in the use of repair location because many of special cementitious materials have an unpredictable performance in different construction conditions. For instance, in many high-early-strength concrete mixtures, the freeze-thaw resistance will be decreased [4]. In addition, early cracking, accompanying autogenous

shrinkage and rapid hydration caused by heat release under high temperature, will exacerbate the deterioration.

Engineered cementitious composite (ECC, a type of fiber-reinforced cement-based composites (FRC)) is considered to be an ideal repair and retrofit material because it has a very high ductility and a tight crack width. Ductility is increasingly recognized as the most important performance in durability repair. As a repair material, ECC can exhibit excellent deformation compatibility with concrete substrate structure. The high fracture toughness and multiple cracking behaviors can make ECC effectively improve the unstable crack propagation caused by the surrounding concrete or old/new concrete interface. Therefore, it reduces the common early damage types in repair structures such as spalling and interlaminar fracture [13–15]. Unlike conventional fiber-reinforced composites, the crack width of ECC at the strain-hardening stage is an inherent characteristic itself and less than $100\ \mu\text{m}$. When the crack width is less than $100\ \mu\text{m}$, the flow rate in cracked concrete is almost 0 [16]. The permeability of water through a crack in ECC will be the lowest [17], so it can prevent the corrosion of steel in reinforced concrete. In preloaded reinforced concrete beams test under dry and wet cycles, Hiraishi et al. [17] found that the corrosion of steel was significantly eliminated while substituting ECC for concrete. Moreover, even if corrosion occurs, the strain-hardening and multiple cracking behavior of ECC will also accommodate the expansion effect caused by corrosion and prevent the occurrence of spalling. Therefore, repair and retrofit ECC can effectively extend the durability of infrastructure [15, 18].

Typical ECC materials consist of cement, quartz sand, fly ash (FA) or silica fume (SF), water, super plasticizer, and chaotic short fibers. Less than or equal to 2% of the volume fraction of fibers is very favorable in terms of mixed construction and economic feasibility of the infrastructure [15, 19]. For the large-scale application of ECCs, the use of local ingredients has become the first choice from the perspective of economic factors and the sustainability of infrastructure. The feasibility of using ECCs for the local ingredient and imported materials has been developed by a large number of researchers [20–22]. The use of domestic fiber and local ingredients in ECC has been designed and developed by Zhang and Qian [20], Ma et al. [21], and Pan et al. [22]. Zhang and Qian [20] analyzed the feasibility of ECC localization by bending test. Ma et al. [21] successfully developed a strain capacity more than 6% of domestic ECC by optimal design from fly ash and rubber particles. Pan et al. [22] studied the mechanical properties of ECC containing domestic fiber and imported fiber, respectively.

In this study, author focus on high-early-strength ECC (HES-ECC) with all local ingredients, including cement, quartz sand, silica fume, polyvinyl alcohol (PVA), fiber and polyethylene (PE) fiber. In order to get high early strength, the sulfoaluminate cement was used in this investigation. In the ECC design theory, the strain-hardening criterion of the material is determined by the fracture toughness of the matrix, the bridging capacity of fiber, and the size distribution of initial defects. Therefore, in order to obtain the domestic HES-ECC, authors measure the micromechanics

parameters by single-fiber pullout test and three-point bending test, respectively. Furthermore, the mechanical properties of HES-ECC will also be tested by compression test and direct tensile test, including compressive strength, elastic modulus, ultimate tensile strength, and ultimate tensile strain.

2. Strain-Hardening Criterion

ECC was developed by Li of the University of Michigan in 1990s, based on the design concept of ISMD (integrated structure and material design), which is a kind of strain-hardening behavior characteristics of cement-based composite with a steady crack width of $60\ \mu\text{m}$, meanwhile, high ductility with strain range from 1% to 4%. ECC effectively linked microcut, mesoscopic material properties, and macromechanical properties. Therefore, the whole design basis of ECC is based on the multiscale link from micro to macro. Li and coworkers [23–25] proposed the ECC design theory, which was further improved by Lin et al. [26], Kanda and Li [27], and Yang et al. [28]. In this theory, the occurrence of steady-state flat crack propagation must meet two criteria: strength criterion and energy criterion.

2.1. Strength Criterion. In order to make ECC possess the ability of multiple cracking and high ductility, ECC should meet the strength criterion in the design process. The strength criterion stipulates that the first cracking strength σ_{fc} must be less than the bridging stress σ_0 . That is,

$$\sigma_{fc} \leq \sigma_0. \quad (1)$$

Based on the strength criterion, the material composition design of ECC can be modulated by adjusting the bridge stress of fiber, fracture toughness, and defect size of the matrix so as to better gain the ability of multiple cracking and high ductility performance.

2.2. Energy Criterion. The steady-state cracking of crack means that the crack width δ_{ss} and the external force σ_{ss} are required to remain stable during the propagation of the crack. It was first proposed by Marshall and Cox [29] in the study of continuous fiber-reinforced ceramic materials. Based on the principle of fracture mechanics, they suggested that the steady-state cracking strength σ_{ss} is calculated by using J -integral. The general solution of steady-state cracking of crack is shown in (2). Although this equation is designed only based on continuous fiber-reinforced ceramic materials, it is still applicable to other fiber-reinforced materials, including ECC:

$$\sigma_{ss} \delta_{ss} - \int_0^{\delta_{ss}} \sigma(\delta) d\delta = J_{tip}, \quad (2)$$

where $\sigma(\delta)$ is expressed as the relationship between the fiber bridge stress σ and the crack width δ , as shown in Figure 1. J_{tip} represents the crack tip toughness. In case of lower fiber content, J_{tip} is determined by the matrix fracture toughness K_m and matrix Young's modulus E_m , as shown in the following equation:

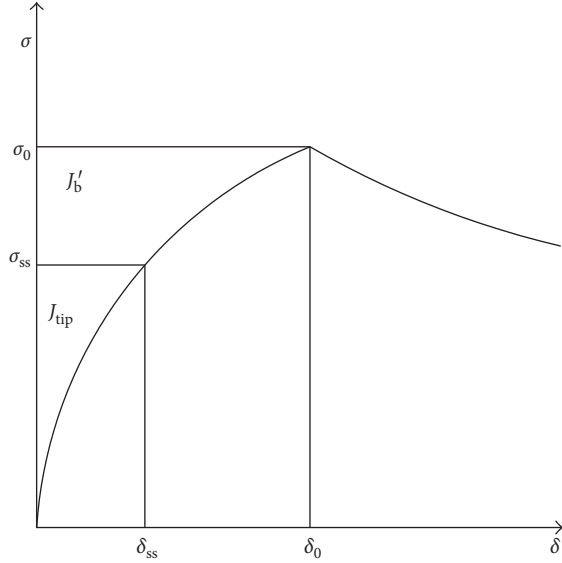


FIGURE 1: Typical $\sigma(\delta)$ curve for tensile strain-hardening composites.

$$J_{\text{tip}} = \frac{K_m^2}{E_m}. \quad (3)$$

Equation (2) represents the energy conservation theorem in the whole steady-state crack propagation process. $\sigma_{ss}\delta_{ss}$ is the external force acting on the crack. The crack tip width changes from 0 to δ_{ss} , where the fiber bridging capability has consumed some of the energy, which is the left part of the formula. While the complementary energy is used to cause the matrix to crack at the crack tip, thereby arouse the crack to continue to develop. The fiber bridging stress will reach to a peak value σ_0 due to the effect of fiber, matrix, and fiber/matrix interface properties so the complementary energy also has a maximum value J'_b , as shown in Figure 1. In order to ensure that the crack can be steady-state cracking, the maximum complementary energy J'_b must be greater than or equal to the crack tip toughness J_{tip} , which is the energy criterion:

$$J_{\text{tip}} \leq \sigma_0 \delta_0 - \int_0^{\delta_0} \sigma(\delta) d\delta = J'_b. \quad (4)$$

According to formula (4), in order to meet energy criterion, the crack tip toughness J_{tip} is limited by adjusting the mix proportion of the matrix, or the maximum complementary energy J'_b is enhanced by designing the fiber/matrix interface parameters.

Based on the above description, in order to design the ECC materials with strain-hardening and multiple cracking behaviors, (1) and (4) should be satisfied at the same time. In addition, considering the fiber in the composites would be fractured, Wu [30] suggested $J'_b/J_{\text{tip}} > 3$ and $\sigma_0/\sigma_{fc} > 1.45$ to achieve the saturated strain-hardening capacity of ECC for PVA fiber. Meanwhile, for the PE fiber, Kanda [31] indicated that the σ_0/σ_{fc} index observed from crack pattern needs to be modified, and it should be greater than 1.2 instead of 1.45.

3. Experiment Program

3.1. Materials and Mixture Proportions. The raw materials used in this study were all produced by local manufacturers. The sulfoaluminate cement (SAC) [32] and silica fume [33] meet Chinese standards. The chemical compositions of SAC and SF are displayed in Table 1. The particles size of SAC and SF is 60 to 80 μm and 0.15 to 0.20 μm , respectively. SF does not make chemical reaction when water is added, and it, as a high activity supplementary cementitious material, will stimulate the formation of secondary hydration products. Therefore, it will enlarge the hydrated calcium silicate (C-S-H) and contribute to obtain a high compressive strength [32]. The aggregates used in this study are silica sand and silica flour, which have diameters range of 106 to 212 μm and 25 to 48 μm , respectively. Using such a small aggregate ensures uniform distribution of the fibers. Moreover, according to Ranade et al. [34], it also effectively reduces the fracture toughness of the matrix caused by crack initiation during steady-state flat crack propagation and contributes to obtain good ductility of composites. A domestic polyethylene (PE) fiber and a domestic PVA fiber (BHL, produced by Bao Hua Lin Co. Ltd. in China) were used in this study, both produced in China. As control, the imported PVA fiber (REC-15) was also investigated in this paper, produced in Japan. The physical and mechanical properties of all fibers are listed in Table 2.

According to the previously mentioned strain-hardening criterion, the strain-hardening and multiple cracking behaviors of ECC are determined by fiber, matrix, and fiber/matrix interfacial parameters. In this paper, different types of fibers will be used to research, which would result in different fiber/matrix interfacial parameters. Four ECC mixtures are listed in Table 3. ECC2, ECC3, and ECC4 have the same mix composition as the control mixture ECC1, but the imported fiber (REC-15) is directly replaced by domestic fiber. Due to rapid hardening of cement and small diameter of PE fiber, a lower PE fiber content of 0.5% and 0.8% was selected to facilitate mixing and efficient and uniform fiber distribution. The fiber content in ECC1 and ECC2 were kept at 2% by mixture volume.

All ECC materials were mixed by using a metal mixer with 10 L capacity. Firstly, all solid materials mixing with low speed for 1 min, so that the mixtures were fully stirred evenly. Then, water and super plasticizer were added, continued to stir at a low speed for 1 min, following at a high speed for another 1 min. When the matrix slurry was homogeneous, the fibers were slowly added and sustained stirred at low speed for another 3 min until the fibers were dispersed uniformly, without agglomeration, and ECC slurry was in good fluidity. The fresh ECC was cast into molds and demolded after 2 hours, then the HES-ECC specimens were cured in a standard curing condition with $95 \pm 5\%$ RH and $20 \pm 2^\circ\text{C}$ until testing ages.

3.2. Single-Fiber Pullout Test. To design HES-ECC, it is necessary to experimentally determine the relevant microscopic parameters. Based on the multiscale design of ECC,

TABLE 1: Chemical composition of sulfoaluminate cement and silica fume (by weight percentage).

Materials	CaO	SiO ₂	Al ₂ O ₃	Fe ₂ O ₃	MgO	TiO ₂	MnO	P ₂ O ₃	Cr ₂ O ₃	ZrO ₂	SO ₃	K ₂ O
SAC	45.25	10.96	28.93	3.71	1.45	0.62	0.01	0.05	0.03	0.03	8.88	0.12
SF	1.15	89.02	1.23	2.63	—	—	—	—	—	—	—	1.32

TABLE 2: Physical and mechanical properties of all fibers.

Fiber types	Diameter, d_f (μm)	Length, L_f (mm)	Elongation (%)	Density (g/cm^3)	Elastic modulus (GPa)	Tenacity (MPa)	Price (yuan/kg)	Manufacturer
REC-15	39	12	7	1.3	42.8	1620	225	Kuraray Co. Ltd. in Japan
BHL	39	12	7	1.3	22	1250	80	Bao Hua Lin Co. Ltd. in China
PE	24	9	4	0.97	116	2740	150	Yizheng Co. Ltd. in China

TABLE 3: Mix design of domestic ECCs (weight ratios).

Mix ID	Cement	Silica fume	Silica flour	Silica sand	Water	Super plasticizer	Fiber (by volume)
ECC1	1	0.18	0.18	0.74	0.39	0.02	2% (REC-15 PVA)
ECC2	1	0.18	0.18	0.74	0.39	0.02	2% (BHL PVA)
ECC3	1	0.18	0.18	0.74	0.39	0.02	0.5% (PE)
ECC4	1	0.18	0.18	0.74	0.39	0.02	0.8% (PE)

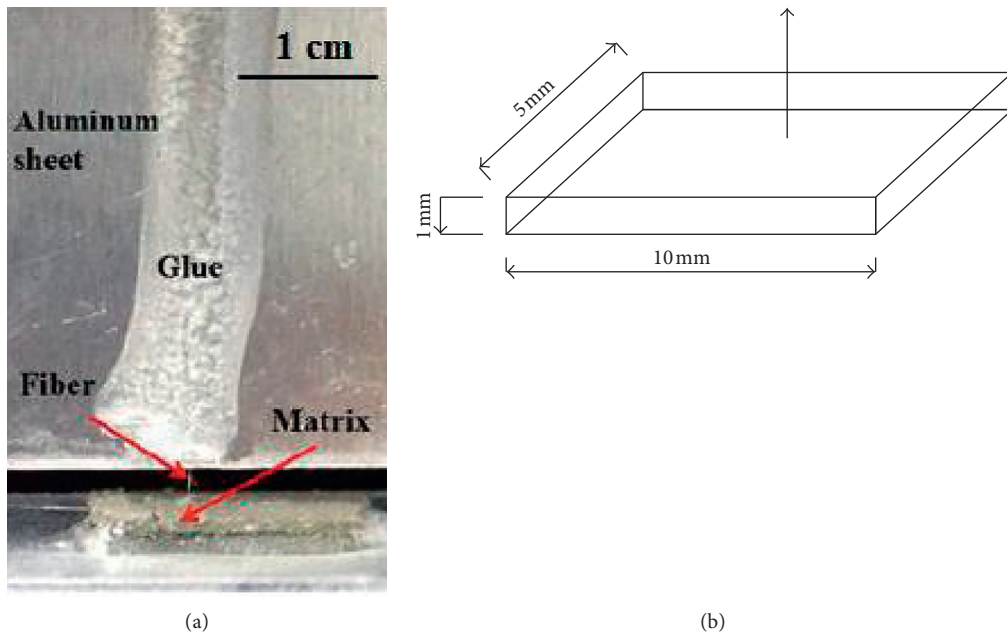


FIGURE 2: Single fiber pullout test setup: (a) the tested specimens; (b) the dimension of specimens (all dimensions in mm).

Katz and Li [35] suggested that the microscopic design parameters of fiber/matrix interface was measured by single fiber pullout test, including chemical bond G_d , frictional bond τ_0 and slip-hardening coefficient β . Firstly, a long continuous fiber was neatly arranged in the mold. And then pour ECC matrix slurry until it reached the specified age. The dimension of the specimen is approximately $10 \times 5 \times 1 \text{ mm}^3$. In order to ensure that the fiber can completely draw out from matrix during pullout process, the depth of fiber is controlled at 1 mm. The test setup is shown

in Figure 2, and the displacement control was used in this test with a rate of 0.4 mm/min.

3.3. Three-Point Bending Test. In order to obtain the crack tip toughness J_{tip} and the matrix fracture toughness K_m , this study refers to the three-point bending test in ASTM E399 developed by the American Society for Materials and Testing [36]. The solution of the matrix fracture toughness K_m is shown in (5) and (6). The matrix of ECC is equivalent to

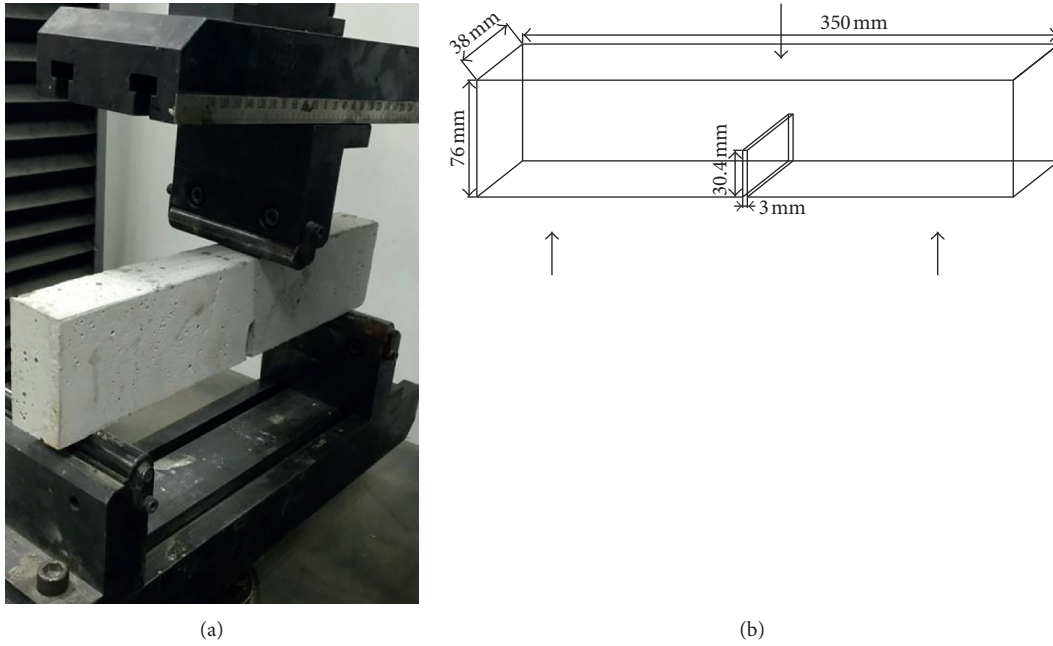


FIGURE 3: The setup of three-point bending test: (a) the tested specimens; (b) the dimension of specimens (all dimensions in mm).

cement mortar and belongs to a brittle material with linear elasticity. Therefore, this method is also suitable for measuring the fracture toughness K_m of the ECC matrix. The test setup and the specimen size are shown in Figure 3.

The dimension of tested specimen is $350 \times 76 \times 38 \text{ mm}^3$, and the bottom of the specimen has a notch. The ratio of the notch depth to height is 0.4. The test rate is controlled by displacement with 0.06 mm/min.

$$K_Q = \frac{P_Q S}{\sqrt{B B_N} W^{3/2}} f\left(\frac{a}{W}\right), \quad (5)$$

$$f\left(\frac{a}{W}\right) = 3\sqrt{\frac{a}{W}} \frac{1.99 - (a/W)(1 - (a/W)) [2.15 - 3.93(a/W) + 2.7(a/W)^2]}{2(1 + 2(a/W))(1 - (a/W))^{3/2}}, \quad (6)$$

where K_Q is the matrix fracture toughness ($K_Q = K_m$, $\text{MPa}\cdot\text{m}^{1/2}$), P_Q is the peak load (N), S is the span of support point in the specimen (mm), B is the thickness of the specimen ($B = B_N$, mm), W is the width of specimens (mm), a is the notch depth (mm), and $f(a/W)$ is the correction coefficient and the function of (a/W) .

3.4. Uniaxial Tensile Test. The uniaxial tensile test is based on the method recommended by the Japan Society of Civil Engineers (JSCE) for testing the properties of fiber-reinforced cement-based composites (HPFRCC) [37]. The test setup and dimension of ECC specimen are shown in Figure 4. Two external linear variable displacement transducers (LVDTs), fixed on both sides of the specimen, are used to measure the deformation of the specimen during test process. The loading rate of this setup is 0.5 mm/min.

The mechanical properties of high-early-strength ECC under compressive and tensile strength are studied in this paper. All specimens will be tested at 6 hours, 24 hours, 7

days, 28 days, and 60 days, respectively. The compressive specimen size is $75 \times 75 \times 75 \text{ mm}$. Due to the variable of different ECC materials, four specimens are prepared for each experiment.

4. Results and Discussions

4.1. Composites Compressive Strength. Figure 5 shows the results of the compressive test for HES-ECC specimens. Each of the data in Figure 5 is calculated from four compressive specimens. As shown in Figure 5, the compressive strength of the controlled ECC1 specimen was 25.4 MPa at 6 hours. In case of ECC2, ECC3, and ECC4, these values were 23.7, 25.3, and 26.0 MPa, respectively. The compressive strength of all specimens at 6 hours can reach more than 50% that of 28 days. The compressive strength of specimens at 24 hours can gain 70% that of 28 days. These results of all compressive strength showed an increasing trend up to 60 days, including all mixtures type. The growth rate at early

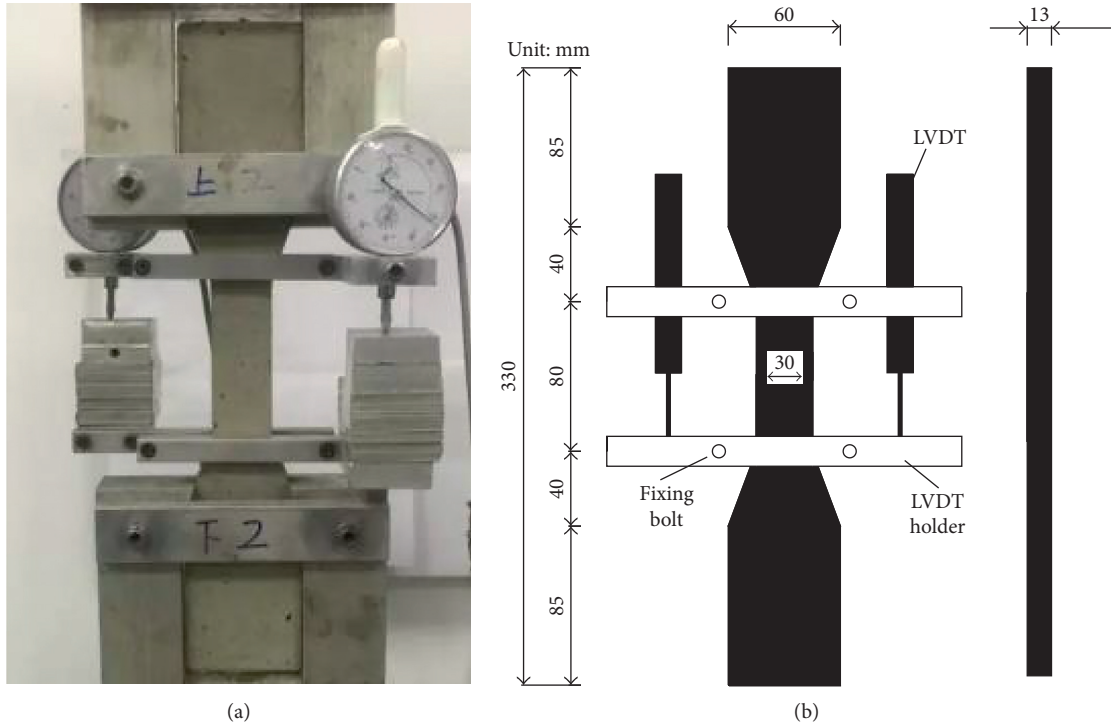


FIGURE 4: The uniaxial tensile test: (a) test setup and (b) specimen dimensions.

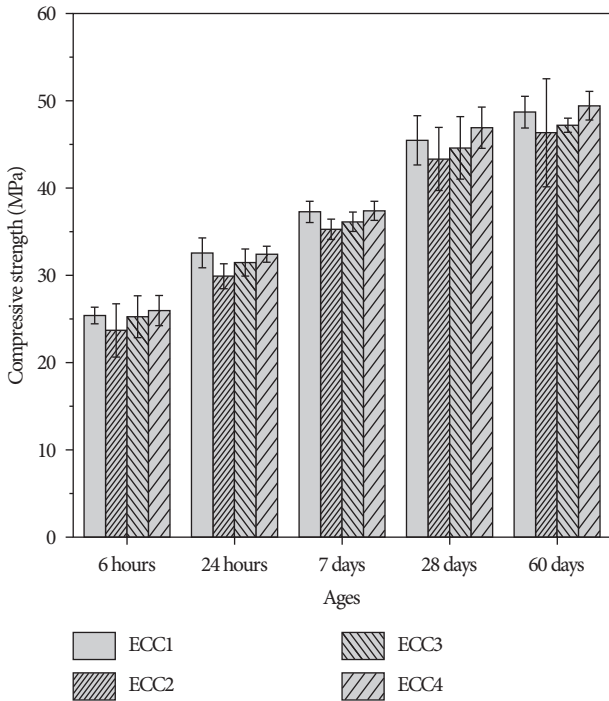


FIGURE 5: Compressive strength development of HES-ECC mixtures.

ages was faster than that of the latter ages. Compared with the controlled mixtures ECC1, the compressive strength of ECC3 and ECC4 did not change much. It indicated that the introduction of domestic PE fibers at small volume fraction has demonstrated similar effect on compressive strength at

all ages. The experimental results showed that the minimum compressive strength of 20 MPa required for the fast repair of pavement materials was satisfied by all mixture types in this study.

4.2. *Control Composites Tensile Properties.* As shown in Figure 6, all the curves show a significantly strain-hardening behavior. As a control mixture, the maximum ultimate tensile strain is more than 3%. The first cracking strength and ultimate tensile strength of ECC1 increase with the increase of age. It is explained that as the age increases, the unhydrated cement particles in ECC1 continue to hydrate and produce more hydration products, resulting in a denser matrix and a greater matrix fracture toughness K_m ; the chemical bond G_d and frictional bond τ_0 in the fiber/matrix interface were enhanced by increased hydration products, thereby resulting in the increase of the bridging stress σ_0 .

With the increase of age, the tensile strain capacity of ECC1 has a rough decrease trend. For example, the maximum tensile strain of ECC1 is 4.13% at 6 hours, and it is reduced to 3.36% at 60 days. This is because that the increase of matrix fracture toughness K_m leads to the strengthening of the crack tip toughness J_{tip}' . On the other hand, the complementary energy J_b' is reduced by the change of fiber/matrix interfacial properties, resulting in the decrease of J_b'/J_{tip}' .

4.3. *Micromechanics-Based Design of Domestic HES-ECC.* The domestic BHL fiber has no enough long available length, only REC-15 fiber and PE fiber can be applied in single-fiber pullout test to obtain related micromechanical parameters.

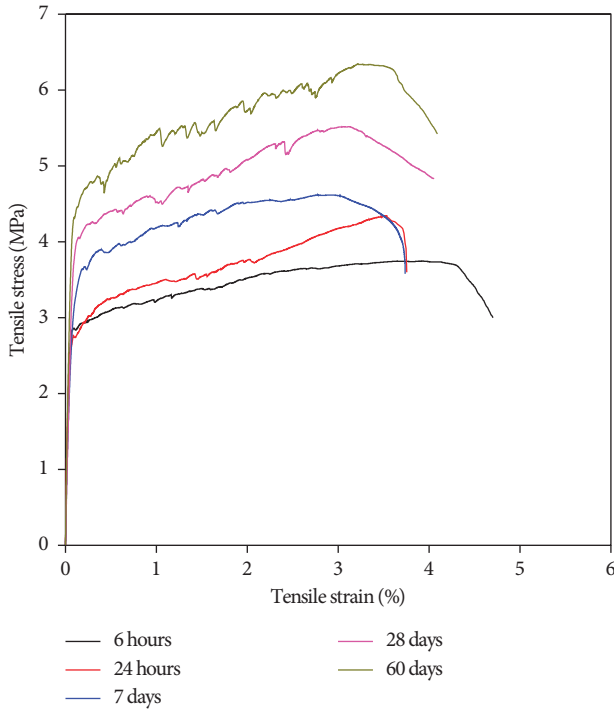


FIGURE 6: Tensile behaviors of the controlled mixture ECC1 with local ingredients and imported fiber (REC-15).

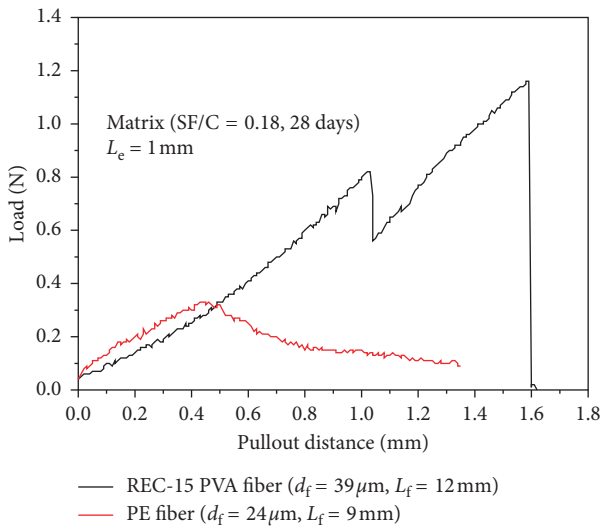


FIGURE 7: Typical pullout curve of single fiber from matrix: (a) REC-15 fiber; (b) PE fiber.

Figure 7 shows the typical pullout load-distance relationship of two different fibers from the same matrix. The microscopic mechanical parameters in the fiber/matrix interface from these figures, including chemical bond G_d , frictional strength τ_0 , and slip-hardening coefficient β , both can be calculated. As shown in Figure 7(a), for PVA fiber, when fiber starts to bear the tensile force, the force value firstly rises to P_a during fiber/matrix debonding stage, and then suddenly drops to P_b , indicating the chemical bond G_d in the

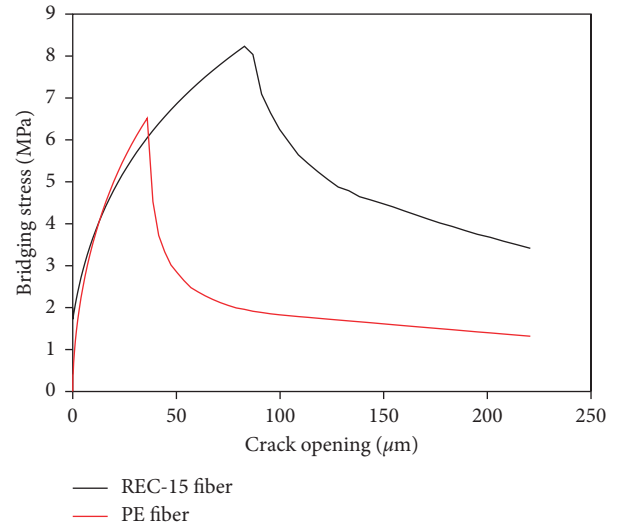


FIGURE 8: Computed fiber bridging stress-crack opening relationship ($\sigma - \delta$) of ECC with REC-15 fiber and PE fiber.

fiber/matrix interface has been destroyed. After, the fiber is in a pullout stage under the action of frictional strength τ_0 and strain-hardening capacity, the force value gradually increases to the second peak and drops until the fiber is broken. In case of fiber without chemical bond, such as PE fiber, P_a can be approximately equated with P_b . When the force value reaches to only one peak P_{peak} ($P_{peak} = P_b$), the buried fiber end is justly debonded, and the pullout force value is provided by frictional bond strength τ_0 (in Figure 7(b)). Based on these microscopic parameters, the fiber bridging stress-crack opening displacement curve can be calculated by using MATLAB [28] (in Figure 8). The complementary energy J'_b can also be obtained from this figure.

For the abovementioned related cases, Redon et al. [38] indicate that polymer fiber tends to reveal either slip-hardening, constant friction, or slip-softening effect when pulled out from the matrix, defined as β , which can be a positive value, 0 or a negative value [39]. In this study, slip-hardening coefficient β was derived from both REC-15 fiber and PE fiber.

Li et al. [40] have proved that the load carried by the fiber was magnified in both debonding and pullout phases at nonzero inclination angles due to the snubbing effects between the inclined fiber and matrix; the snubbing coefficient f was introduced to describe this behavior. In this investigation, for PVA fiber, the snubbing coefficient f was defined as 0.2 according to Yang et al. [28]. The snubbing coefficient f of PE fiber is computed from the peak loads of five specimens with inclined fibers. Li et al. [40] indicated that the snubbing effects can be modeled as

$$\ln \left[\frac{P_{peak}(\phi)}{P_{peak}(0)} \right] = f\phi, \quad (7)$$

where $P_{peak}(\phi)$ and $P_{peak}(0)$ are the peak force for a specimen with fiber inclination angle of ϕ and 0, respectively. In the case of zero degree, the fibers are perpendicular to the crack plane. The left side of (7) was

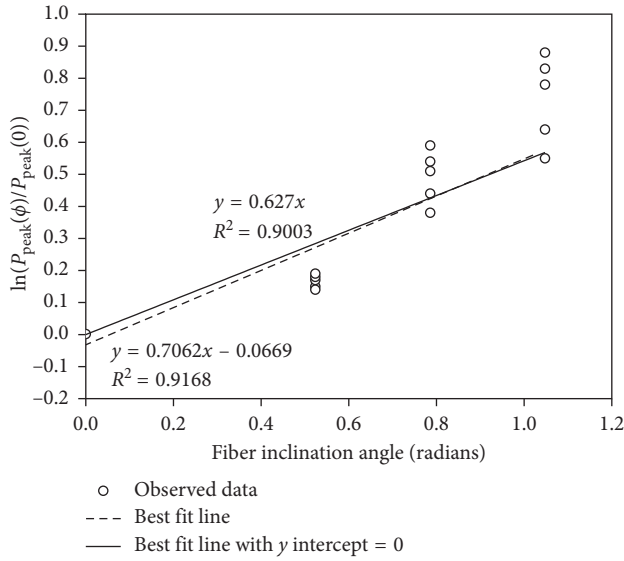


FIGURE 9: Deduction of snubbing coefficient f using inclined PE fiber pullout specimens.

plotted in Figure 9 to find the best-fit curve (dashed line) through four different fiber-inclined angles. To meet the requirement of the model in (7), another best-fit curve (solid line) with zero y -intercept is computed. As seen in Figure 9, the considered inclination angle is 0° , 30° , 45° , and 60° , respectively. The snubbing coefficient f of PE fiber in this study is determined as 0.63.

Figure 10 shows the influence of curing ages on the fiber/matrix interface micromechanical parameters in ECC1 with REC-15 fiber. The chemical bond G_d , frictional strength τ_0 , and slip-hardening coefficient β have a stable growth trend with the increase of age. This is mainly because the nonhydrated cement in ECC continues to hydrate and due to the nucleating effect of silica fume [41], making the hydration products sustain a stable growth, resulting in the increase of interfacial chemical bond G_d ; on the other hand, the interfacial frictional strength τ_0 is enhanced by the denser matrix. Figure 11 shows the influence of curing age on elastic modulus E_m and fracture toughness K_m in the matrix. As shown in Figure 11, the elastic modulus E_m and the fracture toughness K_m increase with the increase of age. It can be explained that the density of the matrix is enhanced by more hydration products, the result of combination of nonhydrated cement with the nucleating effect of silica fume, resulting in the increase of value.

Figure 12 shows the influence of curing ages on micromechanical parameters in ECC3 with PE fiber. Due to the hydrophobic nature of PE fiber, the chemical bond G_d can be approximately equal to zero. The frictional strength τ_0 and slip-hardening coefficient β have also a stable increase trend with the increase of age. The larger interfacial frictional bond strength τ_0 is generated by the densely packed ECC matrix. Due to the high strength of PE fiber, the continuous increase of the fiber bridging capacity is resisted by τ_0 .

Based on the strain-hardening criterion mentioned in Section 2, the strain-hardening performance index (σ_0/σ_{fc} , J'_b/J'_{tip}) of ECC with different fiber is calculated and listed in Table 4. As seen in Table 4, the first cracking strength σ_{fc} is obtained from direct tensile test for the specimen without fiber. The fiber bridging stress σ_0 and the maximum complementary energy J'_b can be measured from the relationship between fiber bridging strength and crack-opening displacement curve. The crack tip toughness J'_{tip} was calculated by (3) using K_m and E_m .

As shown in Table 4, it can be seen that both J'_b/J'_{tip} and σ_0/σ_{fc} are larger than critical values for strain-hardening conditions in case of ECC1 and ECC3 according to Wu [30] and Kanda [31], which ensure that both ECC materials can develop strain-hardening behavior. Nevertheless, the corresponding values of ECC3 are much smaller than that of ECC1 due to small fiber volume of 0.5% PE in ECC3 as opposed to 2% PVA in ECC1. Had the mixing issue of domestic PE fiber been overcome and more PE fibers could be mixed, it is very likely that PE ECC can have a better performance index than PVA ECC. The above analysis suggests that for the utilization of local ingredients in ECC production, it is feasible to replace imported fiber with domestic PE fiber to certain extent, even though its strain-hardening performance may be lower due to inability to mix 2% PE fiber in the cement matrix.

4.4. Domestic Composites Tensile Properties. Figure 13 shows the time-dependent tensile behavior of two domestic fibers. As shown in Figure 13, the significant strain-hardening behavior occurs in ECC2 and ECC3. Based on the domestic PVA fiber, the tensile strain capacity of ECC2 at all ages is less than 2%, indicating the weak micromechanical parameters that occur in the domestic fiber/matrix interface. Compared with the imported fiber (seen in Figure 6), the tensile properties of ECC2 with domestic fiber is lower than ECC1 during all ages. Based on the domestic PE fiber, the ultimate tensile strain of ECC3 gradually reduced from 3.9% at 6 hours to 3.1% at 60 days. The result from ECC3 is consistent with the decrease in the ratio of J'_b/J'_{tip} for ECC3 as discussed before.

It can be seen from Table 4 that the fiber bridging stress σ_0 increases with the increase of age. The same growth trend that occurs in the ultimate tensile strength is shown in Figure 14(a). Meanwhile, the maximum tensile strength of all high-early-strength ECC at 28 days is still able to reach more than 4 MPa. In addition, ECC3 based on PE fiber materials attains a lower maximum tensile strength due to much smaller fiber volume.

Generally, the uniaxial tensile test confirmed that a reasonable tensile ductility can be achieved for ECCs with domestic fibers. The experimental data shows that the domestic ECC2 based on BHL fiber can obtain a good compressive strength and ultimate tensile strain at the same time, while a relatively lower strain capacity may limit its application. For the ECC containing 0.5% PE fiber, it is able to provide a high ductility, but its tensile strength is somewhat sacrificed, with about 4 MPa at 28 days. Based on the PE

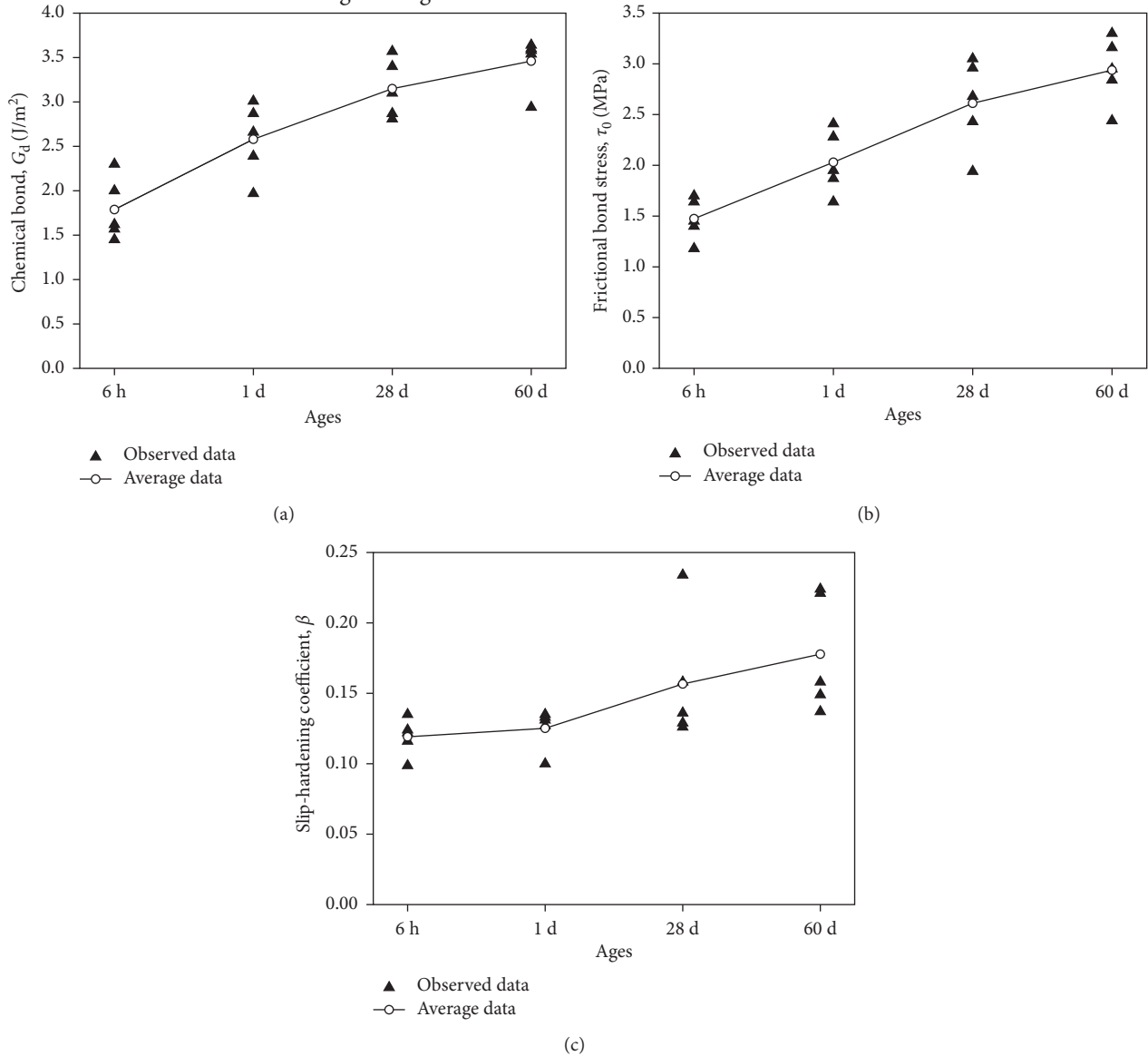


FIGURE 10: Influence of curing ages on REC-15 fiber/matrix interfacial parameters: (a) G_d ; (b) τ_0 ; (c) β .

fiber, the domestic ECC3 cannot meet the strength requirement of engineering applications due to its low ultimate tensile strength. Therefore, the author attempts to increase the fiber volume content and overcome this defect in the next section.

4.5. Domestic HES-ECC with Different Fiber Content. As commonly known, increase in fiber volume can effectively enhance the fiber bridging ability and therefore the ultimate tensile strength. Nevertheless, it is difficult to mix 1% PE fiber into the ECC matrix due to the fast setting time of sulfoaluminate cement (SAC) and smaller fiber diameter. Therefore, this study attempts to use a relatively higher fiber content (0.8% by volume) to produce the domestic HES-ECC.

The performance indices (σ_0/σ_{fc} , J'_b/J'_{tip}) of the strain-hardening behavior of HES-ECCs containing PE fibers are listed in Tables 5 and 6. The details of derivation of various

parameters are the same as before. It can be seen from Tables 5 and 6 that the fiber bridging capacity σ_0 and complementary energy J'_b increase significantly when the PE fiber content increases from 0.5% to 0.8% by volume, resulting in greatly improved J'_b/J'_{tip} and σ_0/σ_{fc} . Theoretically, larger strain-hardening indices should lead to a better strain-hardening behavior, assuming all fibers are randomly distributed.

Figures 13(b), 15, and 16 show the effect of different fiber contents on the tensile mechanical properties of ECC3 and ECC4. As shown in Figures 15 and 16(b), the domestic ECC4 exhibits an excellent high ductility. Compared with ECC3, the ultimate tensile strain of ECC4 increases by 18% at 60 days (from 3.2% to 3.8%). Also, the maximum tensile strength of ECC4 reaches to 5.6 MPa at 60 days, an increase of 23% compared with ECC3. Figure 16(a) shows that the maximum tensile strength is enhanced by increasing the fiber content from 0.5% to 0.8%, an increase of 167% at 6 hours (from 1.5 MPa to 2.5 MPa). However, the compressive

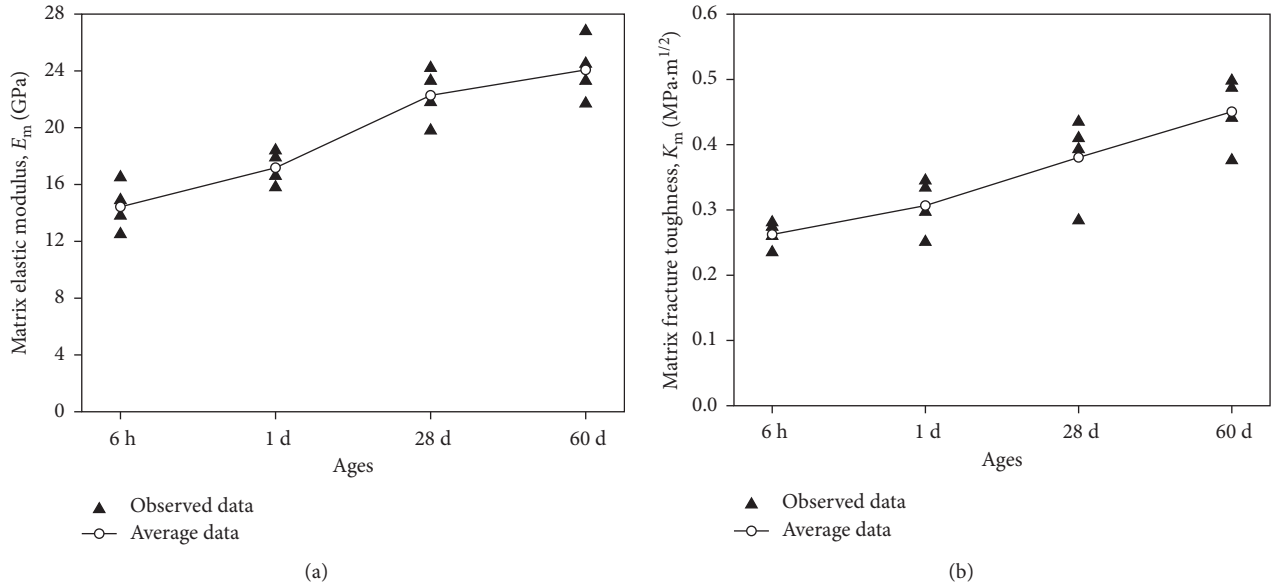
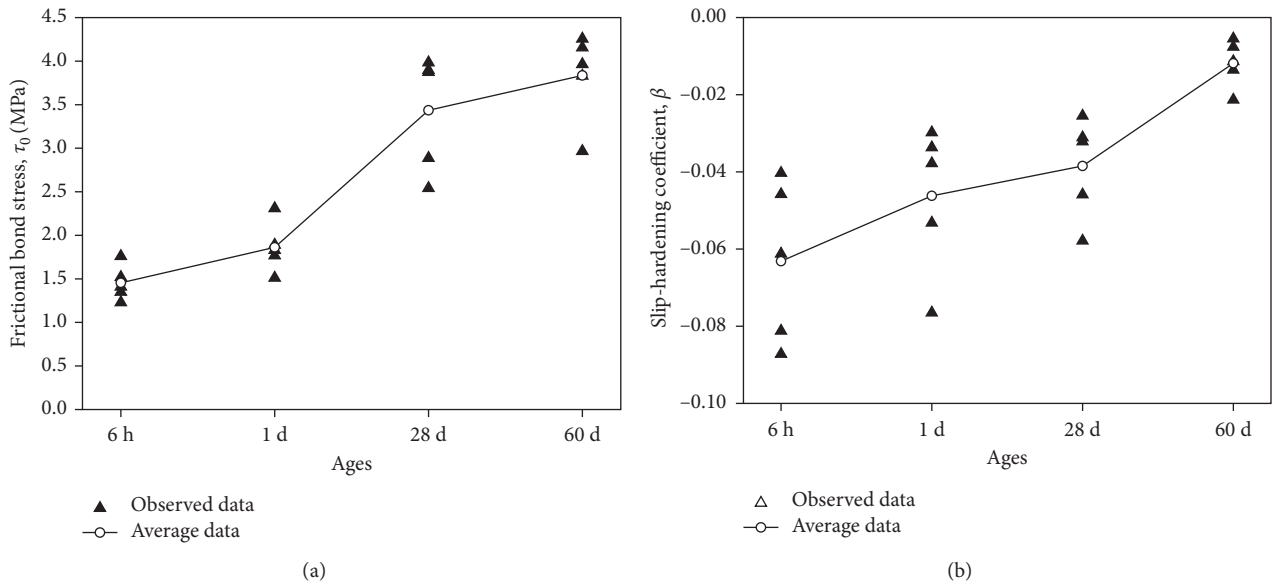
FIGURE 11: Influence of curing ages on matrix parameters: (a) E_m ; (b) K_m .FIGURE 12: Influence of curing ages on PE fiber/matrix interfacial parameters: (a) τ_0 ; (b) β .

TABLE 4: Strain-hardening performance index of HES-ECCs with different fiber.

Mixture ID	Curing ages	σ_0 (MPa)	σ_{fc} (MPa)	J'_b (J/m ²)	J'_{tip} (J/m ²)	J'_b/J'_{tip}	σ_0/σ_{fc}
ECC1	6 h	6.1	1.9	193.4	4.9	39.47	3.21
	1 d	7.3	2.3	179.0	5.6	31.96	3.17
	28 d	8.2	3.2	183.2	6.6	27.76	2.56
	60 d	8.8	3.4	190.9	8.7	21.94	2.59
ECC3	6 h	2.6	1.9	33.5	4.9	6.84	1.37
	1 d	3.0	2.3	39.9	5.6	7.13	1.30
	28 d	4.1	3.2	46.2	6.6	7.00	1.28
	60 d	4.2	3.4	45.2	8.7	5.20	1.24

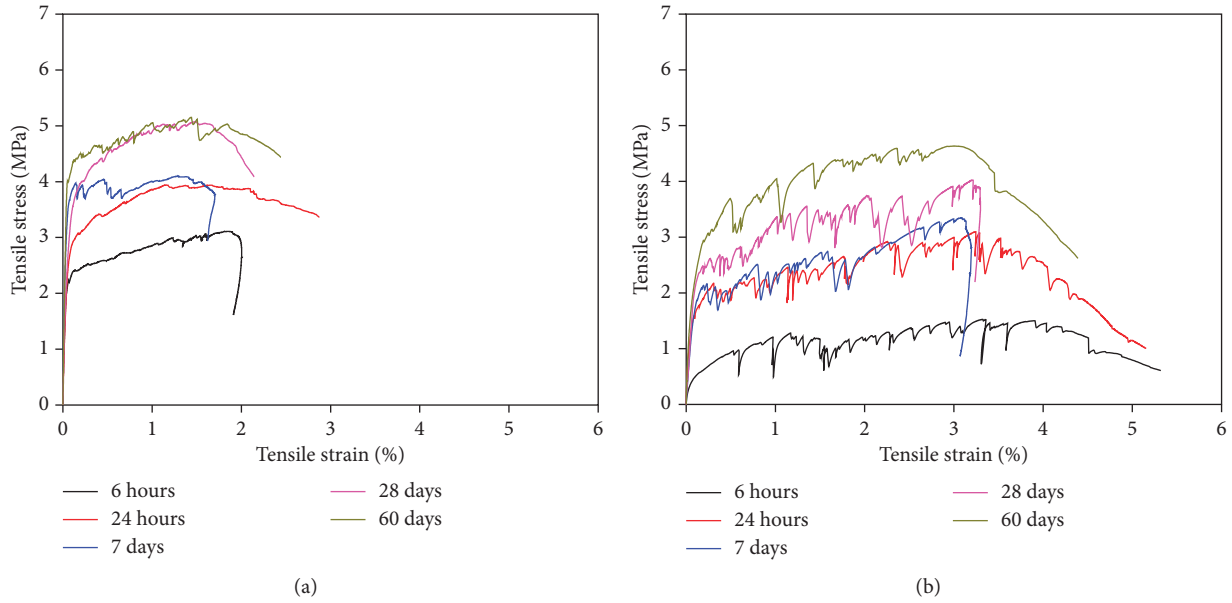


FIGURE 13: Uniaxial tensile stress-strain curves of HES-ECCs with different curing ages: (a) ECC2; (b) ECC3.

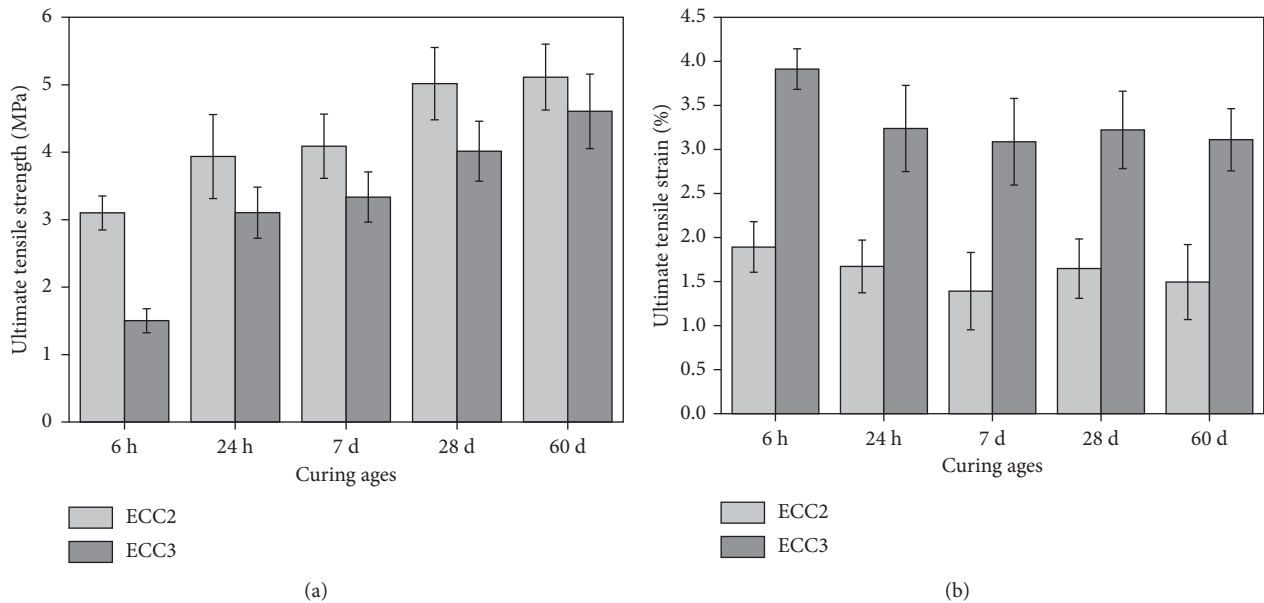


FIGURE 14: Comparison of tensile properties of HES-ECCs with different fibers at different ages: (a) ultimate tensile strength; (b) ultimate tensile strain.

TABLE 5: Performance indices of strain-hardening for HES-ECCs when PE fiber content is 0.5% (ECC3).

Curing ages	σ_0 (MPa)	σ_{fc} (MPa)	J'_b (J/m ²)	J'_{tip} (J/m ²)	J'_b/J'_{tip}	σ_0/σ_{fc}
6 h	2.6	1.9	33.5	4.9	6.84	1.37
1 d	3.0	2.3	39.9	5.6	7.13	1.30
28 d	4.1	3.2	46.2	6.6	7.00	1.28
60 d	4.2	3.4	45.2	8.7	5.20	1.24

strength at 6 hours has no increase when the fiber content increases to 0.8%, above 25 MPa. Therefore, the mechanical properties of ECC4 satisfy the minimum traffic compressive strength requirement.

Compared with ECC3, the first cracking strength and maximum tensile strength is enhanced by increasing the fiber content in ECC4 (seen in Figures 13(b) and 15). Meanwhile, the tensile strain capacity of ECC4 in general is

TABLE 6: Performance indices of strain-hardening for HES-ECCs when PE fiber content is 0.8% (ECC4).

Curing ages	σ_0 (MPa)	σ_{fc} (MPa)	J'_b (J/m ²)	J_{tip} (J/m ²)	J'_b/J_{tip}	σ_0/σ_{fc}
6 h	4.2	1.9	53.5	4.9	10.92	2.21
1 d	4.9	2.3	64.0	5.6	11.43	2.13
28 d	6.5	3.2	74.2	6.6	11.24	2.03
60 d	6.7	3.4	72.6	8.7	8.34	1.97

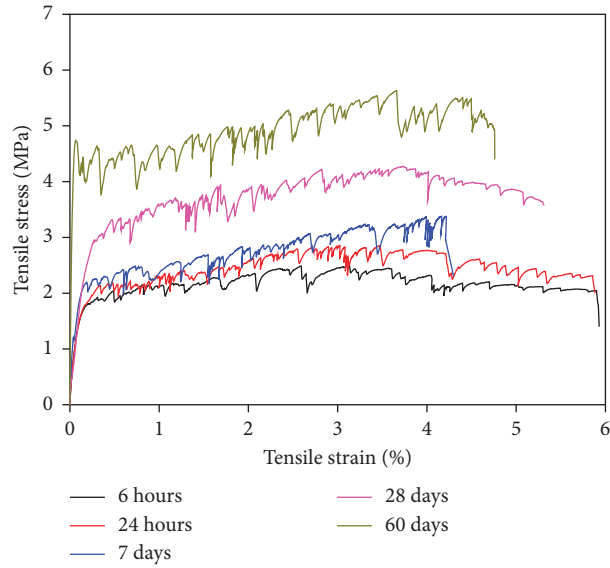


FIGURE 15: Tensile stress-strain curves of ECC4 with different curing ages.

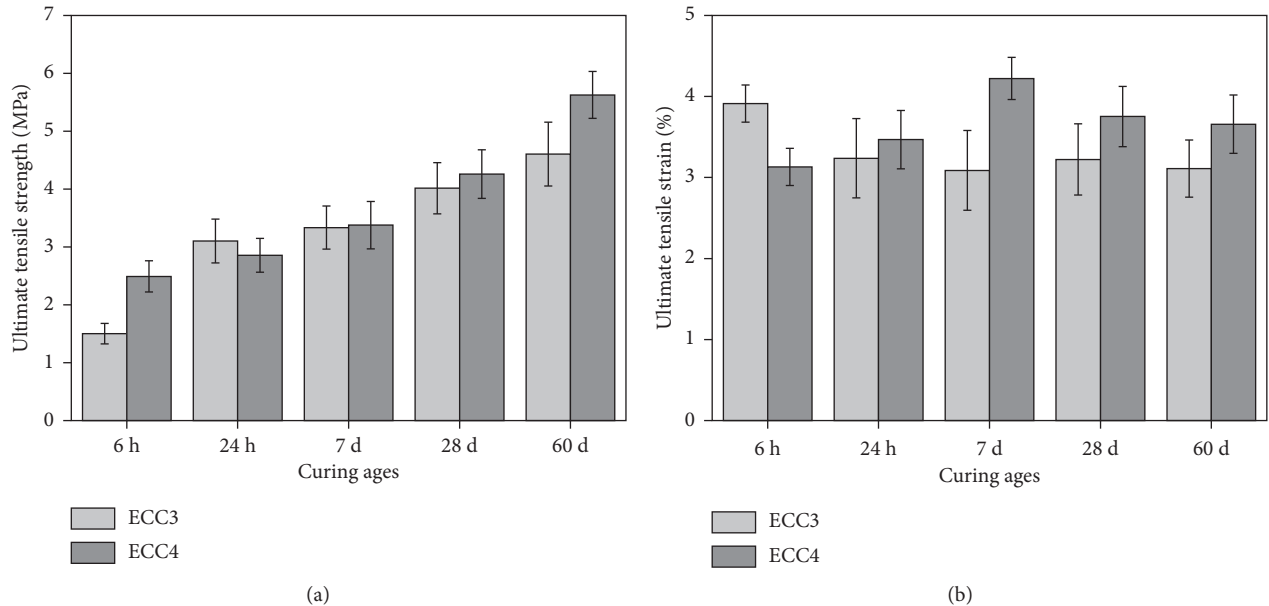


FIGURE 16: Comparison of tensile properties of PE HES-ECCs at different ages: (a) ultimate tensile strength; (b) tensile strain capacity.

better when compared with ECC3 (Figure 16(b)), which is consistent with the increase of strain-hardening performance index J'_b/J_{tip} for ECC4.

Figure 17 shows the influence of imported fiber and domestic fiber on tensile properties of ECC1 and ECC4. As

shown in Figure 17, the ultimate tensile strength of ECC4 with domestic PE fiber at all ages is less than that of controlled ECC1 with imported REC-15 fiber, approximately three-quarters of ECC1, due to a relative lower fiber content. However, the domestic ECC4 exhibits an excellent tensile

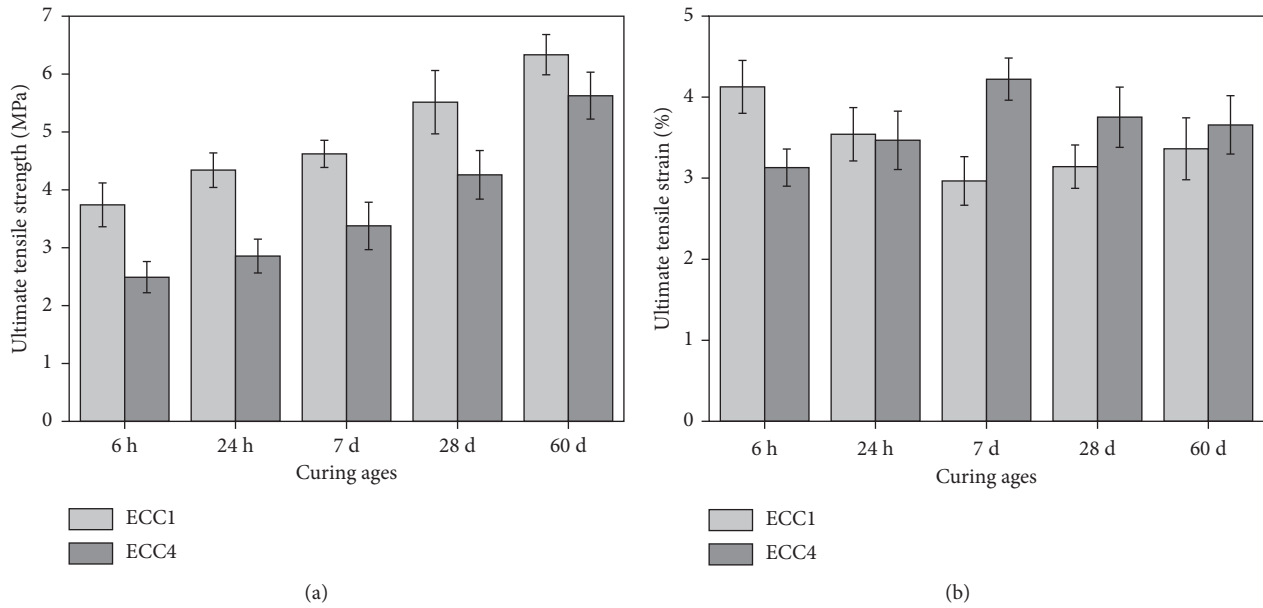


FIGURE 17: Comparison of tensile properties of ECC1 and ECC4 at different ages: (a) ultimate tensile strength; (b) tensile strain capacity.

strain capacity with only 0.8% fiber content. The ultimate tensile strain of ECC4 is more than that of ECC1 after 7 days with over 3%, increasing by more than 120%. It is indicated that 2% of imported REC-15 fiber can be replaced by 0.8% of domestic PE fiber in the process of preparing HES-ECC.

The domestic fiber can substitute for the imported fiber due to the lower cost. The price of REC-15 fiber and PE fiber is 225 yuan/kg and 150 yuan/kg in China (in Table 2), respectively. For large-scale applications, for example, the production of 10,000 cubic metre HES-ECCs need the imported REC-15 fiber of 260 kg or the domestic PE fiber of 104 kg, and then, the cost of imported fiber is 58,500 yuan. However, the cost of domestic fiber is only 15,600 yuan, about 27% of REC-15 fiber. Therefore, it is feasible to produce ECC materials with a lower domestic fiber, while maintaining high-early-strength and higher material ductility simultaneously.

The average crack width of ECC1, ECC2, ECC3, and ECC4 at 28 days is 61, 58, 55, and 49 μm respectively. The reduction of crack width after load removal can be contributed to more fiber bridging capacity from the PE fiber/matrix interface. It should be noted that the crack width at the very early age of 24 hours is as low as 50 μm (for ECC4), whereas the tensile strain capacity is as high as 3.2%. This high tensile ductility and very tight crack width at an early age of HES-ECC provide a high resistance to early-age cracking.

5. Conclusions

This study aims at the production of high-early-strength ECC with excellent mechanical properties using all domestic ingredients, including matrix materials and PE fiber. According to the principle of ECC micromechanics and fracture mechanics design, the interfacial micromechanical parameters were analyzed, and the high ductile ECC materials were designed and adjusted by the replacement of

fiber and the increase of fiber content. The final recommendation of high-early-strength ECC is ECC4, which contains 0.8% of PE fiber by volume, meeting both strain-hardening criteria (strength criterion and energy criterion). The main conclusions were as follows:

- (1) To realize the localization of high-early-strength ECC, a combination of sulfoaluminate cement, silica fume, and domestic fibers is found to be helpful for attaining higher compressive strength and tensile properties at early ages. The compressive strength of more than 25 MPa and tensile strain capacity of 1.8% within 6 hours of all high-early-strength ECCs can be obtained in this study.
- (2) Using BHL fiber at 2%, it was found that ultimate tensile strength of 5 MPa and compressive strength of 40 MPa at 28 days can be achieved, with a modest tensile strain capacity of about 2%.
- (3) It was found that an excellent strain-hardening behavior can be achieved when HES-ECCs use the domestic PE fiber with only 0.5% content, but with ultimate tensile strength less than 1.5 MPa within 6 hours.
- (4) When 0.8% PE fiber was used, domestic HES-ECC (ECC4) can also obtain a good tensile strain capacity of 3% and ultimate tensile strength of 2.5 MPa within 6 hours. Meanwhile, the ultimate tensile strength of more than 5 MPa and ultimate tensile strain of more than 3.5% after 60 days can be easily achieved. The compressive strength for this mixture exceeds 49 MPa at 60 days.
- (5) When 2% of imported REC-15 fiber was replaced by 0.8% of domestic PE fiber, the cost of all materials was significantly reduced, approximately up to 70%.

Conflicts of Interest

The authors declare that there are no conflicts of interest regarding the publication of this paper.

Acknowledgments

The authors would like to thank the National Natural Science Foundation of China (no. 51278097) and the Nanyang Technological University for providing a start-up grant (M4081208).

References

- [1] N. J. Delatte, *Concrete Pavement Design, Construction, and Performance*, E & FN Spon, New York, NY, USA, 2007.
- [2] S. S. Seehra, S. Gupta, and S. Kumar, "Rapid setting magnesium phosphate cement for quick repair of concrete pavements-characterization and durability aspects," *Cement and Concrete Research*, vol. 23, no. 2, pp. 254–266, 1993.
- [3] D. Knofel and J. F. Wang, "Properties of three newly developed quick cement," *Cement and Concrete Research*, vol. 24, no. 5, pp. 801–812, 1994.
- [4] D. Whiting and M. Nagi, "Strength and durability of rapid highway repair concretes," *Concrete International*, vol. 16, no. 9, pp. 36–41, 1994.
- [5] M. M. Sprinkel, *Very-High-Strength Latex-modified Concrete Overlay. Report No. VTRC99-TAR3*, Virginia Department of Transportation, Richmond, VA, USA, 1998.
- [6] P. D. Baraguru and D. Bhatt, *Rapid Hardening Concrete. Report No. FHWA NJ2001-3*, New Jersey Department of Transportation, Trenton, NJ, USA, 2000.
- [7] F. Parker and M. L. Shoemaker, "PCC pavement patching materials and procedures," *Journal of Materials in Civil Engineering*, vol. 3, no. 1, pp. 29–47, 1991.
- [8] S. Kurtz, P. Balaguru, G. Consolazio, and A. Maher, *Fast Track Concrete for Construction Repair. Report No. FHWA NJ2001-015*, New Jersey Department of Transportation, Trenton, NJ, USA, 1997.
- [9] J. Anderson, J. Daczko, and J. Luciano, "Producing and evaluating Portland cement-based rapid strength concrete," *Concrete International*, vol. 25, no. 8, pp. 77–82, 2003.
- [10] A. M. Vaysburd, C. D. Brown, B. Bissonnette, and P. H. Emmons, "'Realcrete' versus 'labcrete'," *Concrete International*, vol. 26, no. 2, pp. 90–94, 2004.
- [11] S. Wang and V. C. Li, "High early strength engineered cementitious composites," *ACI Materials Journal*, vol. 103, no. 2, pp. 97–105, 2006.
- [12] M. Li and V. C. Li, "High-early-strength engineered cementitious composites for fast, durable concrete repair-material properties," *ACI Materials Journal*, vol. 108, no. 1, pp. 3–12, 2011.
- [13] Y. M. Lim and V. C. Li, "Durable repair of aged infrastructures using trapping mechanism of engineering cementitious composites," *Journal of Cement and Concrete Composites*, vol. 19, no. 4, pp. 373–385, 1997.
- [14] V. C. Li, H. Horii, P. Kabele, T. Kanda, and Y. M. Lim, "Repair and retrofit with engineering cementitious composites," *Engineering Fracture Mechanics*, vol. 65, pp. 317–334, 2000.
- [15] V. C. Li, "High performance fiber reinforced cementitious composites as durable material for concrete structure repair," *International Journal for Restoration of Buildings and Monuments*, vol. 10, no. 2, pp. 163–180, 2004.
- [16] K. Wang, D. C. Jansen, S. Shah, and A. F. Karr, "Permeability study of cracked concrete," *Cement and Concrete Research*, vol. 27, no. 3, pp. 381–393, 1997.
- [17] Y. Hiraishi, T. Honma, M. Hakoyama, and S. Miyazato, "Steel corrosion at bending cracks in ductile fiber reinforced cementitious composites," in *Proceeding of the JCI Symposium on Ductile Fiber Reinforced Cementitious Composites (DFRCC)*, Tokyo, Japan, 2003, in Japanese.
- [18] V. C. Li and M. Lepech, "Crack resistant concrete material for transportation construction," in *Proceeding of the Transportation Research Board 83rd Annual Meeting*, Washington, DC, USA, January 2004.
- [19] S. Wang and V. C. Li, "Polyvinyl alcohol fiber reinforced engineered cementitious composites: material design and performances," in *Proceedings of International Workshop on HPFRCC in Structural Applications*, pp. 23–26, Honolulu, HI, USA, 2005.
- [20] Z. Zhang and S. Qian, "The feasibility of engineered cementitious composites with local compositions," in *Proceedings of the 2nd International RILEM Conference on Strain Hardening Cementitious Composites*, pp. 323–328, Rio de Janeiro, Brazil, December 2011.
- [21] H. Ma, S. Qian, Z. Zhang, Z. Lin, and V. C. Li, "Tailoring Engineered cementitious composites with local ingredients," *Construction and Building Materials*, vol. 101, pp. 584–595, 2015.
- [22] Z. Pan, C. Wu, J. Liu, W. Wang, and J. Liu, "Study on mechanical properties of cost-effective polyvinyl alcohol engineered cementitious composites (PVA-ECC)," *Construction and Building Materials*, vol. 78, pp. 397–404, 2015.
- [23] V. C. Li, "From micromechanics to structural engineering—the design of cementitious composites for civil engineering application," *Journal of Structural Engineering/Earthquake Engineering*, vol. 10, no. 2, pp. 37–48, 1993.
- [24] V. C. Li and C. K. Y. Leung, "Steady state and multiple cracking of short random fiber composites," *Journal of Engineering Mechanical*, vol. 188, no. 11, pp. 2246–2264, 1992.
- [25] V. C. Li and H. C. Wu, "Conditions for pseudo strain-hardening in fiber reinforced brittle matrix composites," *Applied Mechanics Reviews*, vol. 45, no. 8, pp. 390–398, 1992.
- [26] Z. Lin, T. Kanda, and V. C. Li, "On interface property characterization and performance of fiber reinforced cementitious composites," *Concrete Science and Engineering*, vol. 1, pp. 173–184, 1999.
- [27] T. Kanda and V. C. Li, "Practical design criteria for saturated pseudo strain hardening behavior in ECC," *Journal of Advanced Concrete Technology*, vol. 4, no. 1, pp. 59–72, 2005.
- [28] E. H. Yang, S. Wang, Y. Yang, and V. C. Li, "Fiber-bridging constitutive law of engineered cementitious composites," *Journal of Advanced Concrete Technology*, vol. 6, no. 1, pp. 181–193, 2008.
- [29] D. B. Marshall and B. N. Cox, "A J-integral method for calculating steady-state matrix cracking stresses in composites," *Mechanical Materials*, vol. 8, pp. 127–133, 1988.
- [30] C. Wu, *Micromechanical Tailoring of PVA-ECC for Structural Applications in Departmental of Civil and Environmental Engineering*, University of Michigan, Ann Arbor, MI, USA, 2001.
- [31] T. Kanda, *Design of Engineered Cementitious Composites for Ductile Seismic Resistant Elements*, in *Department of Civil and Environmental Engineering*, University of Michigan, Ann Arbor, MI, USA, 1998.

- [32] JC/T2282-2014, *Quick Setting and Rapid Hardening Sulphoaluminate Cement*, China Building Materials Industry Press, Beijing, China, 2014, in Chinese.
- [33] GB/T27690-2011, *Silica Fume for Cement Mortar and Concrete*, China Standards Press, Beijing, China, 2011, in Chinese.
- [34] R. Ranade, V. C. Li, M. D. Stults, W. F. Heard, and T. S. Rushing, "Composite properties of high-strength, high-ductility concrete," *ACI Materials Journal*, vol. 110, no. 4, pp. 413–422, 2013.
- [35] A. Katz and V. C. Li, "A special technique for determining the bond strength of carbon fibers in cement matrix by pullout test," *Journal of Materials Science Letters*, vol. 15, pp. 1821–1823, 1996.
- [36] ASTM E399-12, *Standard Test Method for Linear-Elastic Plane-Strain Fracture Toughness K_{IC} of Metallic Materials*, ASTM, West Conshohocken, PA, USA, 2012.
- [37] JSCE, *Recommendations for Design and Construction of High Performance Fiber Reinforced Cement Composites with Multiple Fine Cracks (HPFRCC)*, Japan Society of Civil Engineers, Tokyo, Japan, 2008.
- [38] C. Redon, V. C. Li, C. Wu, H. Hoshiro, T. Saito, and A. Ogawa, "Measuring and modifying interface properties of PVA fibers in ECC matrix," *Journal of Materials in Civil Engineering*, ASCE, vol. 13, no. 6, pp. 399–406, 2001.
- [39] Z. Lin and V. C. Li, "Crack bridging in fiber reinforced cementitious composites with slip-hardening interfaces," *Journal of Mechanics and Physics of Solids*, vol. 45, no. 5, pp. 763–787, 1997.
- [40] V. C. Li, Y. Wang, and S. Backer, "Effect of inclining angle, bundling and surface treatment on synthetic fibre pullout from cement matrix," *Composites Journal*, vol. 20, no. 2, pp. 132–140, 1990.
- [41] B. W. Langana, K. Wengb, and M. A. Warda, "Effect of silica fume and fly ash on heat of hydration of Portland cement," *Cement and Concrete Research*, vol. 32, pp. 1045–1451, 2002.

Research Article

Flexural Behavior of RC Slabs Strengthened in Flexure with Basalt Fabric-Reinforced Cementitious Matrix

Sugyu Lee,¹ Kinam Hong ,¹ Yeongmo Yeon,¹ and Kyusan Jung²

¹Department of Civil Engineering, Chungbuk National University, 1 Chungdae-ro, Seowon-Gu, Cheongju, Chungbuk 28644, Republic of Korea

²Structural Engineering Research Institute, Korea Institute of Civil Engineering and Building Technology, 283 Daehwa-dong, Goyangdae-ro, Ilsanseo-gu, Goyang-si, Gyeonggi-do 10223, Republic of Korea

Correspondence should be addressed to Kinam Hong; hong@cbnu.ac.kr

Received 22 August 2017; Accepted 26 November 2017; Published 11 February 2018

Academic Editor: Doo-Yeol Yoo

Copyright © 2018 Sugyu Lee et al. This is an open access article distributed under the Creative Commons Attribution License, which permits unrestricted use, distribution, and reproduction in any medium, provided the original work is properly cited.

This paper presents both experimental and analytical research results for predicting the flexural capacity of reinforced concrete (RC) slabs strengthened in flexure with basalt fabric-reinforced cementitious matrix (FRCM). A total of 13 specimens were fabricated to evaluate the flexural behavior of RC slabs strengthened with basalt FRCM composite and were tested under four-point loading. The fiber type, tensile reinforcement ratio, and the number of fabric layers were chosen as experimental variables. The maximum load of FRCM-strengthened specimens increased from 11.2% to 98.2% relative to the reference specimens. The energy ratio and ductility of the FRCM-strengthened specimens decreased with the higher amount of fabric and tensile reinforcement. The effective stress level of FRCM fabric can be accurately predicted by a bond strength of ACI 549 and Jung's model.

1. Introduction

Reinforced concrete structures experience degradation due to design errors, construction errors, aging, and increased loads caused by changes in usage [1]. These deteriorated structures can recover their load bearing capacity through strengthening [2, 3]. Strengthening methods are largely divided into enlargement of concrete section, externally bonded reinforcement (EBR), and near-surface mounted reinforcement (NSMR) [4]. Particularly, the EBR method is easy to apply because reinforcing materials such as steel plate and fiber are adhered to the concrete surface by an epoxy resin and also exhibit excellent strengthening effect [5]. Steel plates were used mainly as the EBR strengthening material 20 to 30 years ago. However, it had been known that steel plates attached to the outside of concrete structures are vulnerable to corrosion and fire and greatly increase the weight of the structure [6]. Thus, at present, sheets or plates made up of carbon fiber-reinforced polymer (CFRP), glass fiber-reinforced polymer (GFRP),

and aramid fiber-reinforced polymer (AFRP) are used as strengthening materials in replace of steel plates. The FRP strengthening material has a high strength-to-weight ratio and has excellent corrosion resistance, chemical resistance, and endothelial strength [7, 8]. Despite these many advantages, FRP strengthening material attached to the exterior of the structure by the epoxy resin is prone to damage by fire and ultraviolet radiation [9]. Additionally, epoxy used as adhesive has the following limitations: (1) difficult to control quality in wet condition, difficult to harden at low temperatures in winter, and very low fire resistance due to the lower glass transition temperatures and (2) due to the epoxy resin matrix kept the moisture at interface between the concrete surface and the epoxy resin matrix, the strengthening material might be debonded from the concrete surface [3, 10].

Since inorganic cementitious matrix has a higher glass transition temperature than the organic epoxy resin, it is excellent in stability at high temperature, can be used under wet conditions due to hydration reaction, and also can

prevent the fiber damage due to the ultraviolet ray [11]. In order to compensate the disadvantages of the epoxy resin, a fabric-reinforced cementitious matrix (FRCM) method, which is a strengthening method using the cementitious matrix as an adhesive, has been studied [4, 8–10, 12, 13]. Babaeidarabad et al. [12] conducted a bending test considering the number of polybenzoxazole (PBO) fabric layers and the concrete compressive strength as experimental variables. The experimental test results were compared with the flexural strengths predicted by ACI 549 [14]. The comparison results showed that the predicted flexural strengths were lower than the experimental values, but the criterion had an appropriate accuracy [12]. Ombres [7] performed a four-point bending test for FRCM-strengthened beams considering the tensile reinforcement ratio and the number of FRP fabric layers as experimental variables in order to analyze the flexural behavior, ultimate strength, deflection, ductility, and failure mode. Experimental test results showed that the ultimate strengths of strengthened specimens increased by 10% to 44% compared to the reference specimen. The specimen strengthened with one FRP fabric layer failed by flexural behavior, and the specimen with more than two FRP fabric layers failed due to FRP debonding at the midspan. In addition, the predicted value for maximum load is significantly different from the experimental test value when the specimen was destroyed by FRCM peeling [7]. D'Ambrisi et al. [11] conducted flexural tests on FRCM-strengthened beams considering the type of fiber, the number of fabric layers, and the fixing method as experimental variables. From the experimental results, it was confirmed that the PBO fabric is more efficient than the CFRP fabric in the FRCM method. Furthermore, the specimens strengthened with FRCM were destroyed due to the loss of reinforcing effect caused by peeling of the FRCM composite [11]. Azam and Soudki [15] conducted an experimental study to investigate the strengthening performance of beams strengthened in shear with the FRCM method. Three-point loading tests were carried out on FRCM shear-strengthened beams considering the type of fibers and reinforcement as experimental variables. Experimental results showed that the ultimate load increase of 19% to 105% from the type of fibers and strengthening type has no significant effect on failure mode and failure load of the specimen [15]. Jung et al. [16] conducted flexural tests on FRCM-reinforced beams by varying the type of fabric and the number of fabric layers. Experimental results showed that FRCM-reinforced specimens increased by 131.7% to 219.8% compared to the reference specimen and all of FRCM-strengthened specimens were destroyed by FRCM composite peeling. Additionally, Jung et al. [16] suggested a bonding strength model for considering the bond-slip behavior between the BFRP fabric and the cementitious matrix on FRCM.

PBO fabric, CFRP fabric, and GFRP fabric were used as reinforcing materials in most studies regarding the FRCM composites [17, 18]. However, due to decomposition of epoxy matrix, the tensile strength of CFRP and GFRP at 600°C decreased to less than 60% of the strength measured

at room temperature, and the tensile strength of PBO fabric at 500°C decreased to less than 40% of the strength measured at room temperature [17, 19]. Therefore, even if the epoxy is replaced with a cementitious matrix, it should be considered that the sufficient fire resistance cannot be secured if these fabrics are used as strengthening materials. Unlike other fibers, basalt fiber is known to have more than 90% of the tensile strength measured at room temperature even at 600°C [3]. However, only few researchers have reported the application of the basalt fiber as a material of FRCM composites [3, 20, 21]. Therefore, this study reports the flexural performance of FRCM-strengthened beams with basalt fiber-reinforced polymer (BFRP) fabric. Moreover, the strength prediction model for FRCM-strengthened beams was examined for FRCM-strengthened slab structure.

2. Experimental Program

2.1. Test Specimens. A total of 13 specimens were fabricated to evaluate the flexural behavior of RC slabs strengthened with FRCM composite. The type of fibers, tensile reinforcement ratio, and the number of fabric layers were chosen as experimental variables. The specimens had a rectangular cross section of 400 mm × 200 mm, and their cover concrete depth was constantly 30 mm. The total length and net span of the specimen were 3,400 mm and 3,000 mm, respectively. Two deformed steel bars with nominal diameter of 10 mm were placed as compressive reinforcement in all specimens. Deformed steel bars with nominal diameter of 10 mm, 13 mm, and 16 mm were utilized as the variable of tensile reinforcement in the specimens.

Also, in order to prevent the occurrence of shear failure before flexural failure, U-shaped stirrups with nominal diameter of 10 mm were placed at 200 mm intervals on the specimens. Specimen details are presented in Figure 1.

2.2. Materials. The specimens were fabricated by using ready-mixed concrete with the design strength of 30 MPa. In order to confirm the mechanical properties of concrete, nine cylinders of Ø100 mm were manufactured in accordance with ASTM C39/39M [22] at the time of concrete casting. The cylinders were cured under the same condition as the specimens. The average compressive strength of specimens was 33.8 MPa at 28 days. The mixture properties of the concrete used are presented in Table 1. Symbols in Table 1 are water-cement ratio (W/C), sand percent of total aggregate by solid volume (S/a), water (W), cement (C), sand (S), gravel (G), and water-reducing admixture (Ad).

Deformed steel bars with nominal diameters of 10 mm, 13 mm, and 16 mm were used in specimen fabrication. Their mechanical properties were determined in accordance with ASTM A370 [23], and the test results are shown in Table 2.

BFRP and CFRP fabrics were used in this study. The used CFRP fabric in this research was manufactured in Switzerland, consisting of carbon fiber in the warp direction and glass fiber in the weft direction.

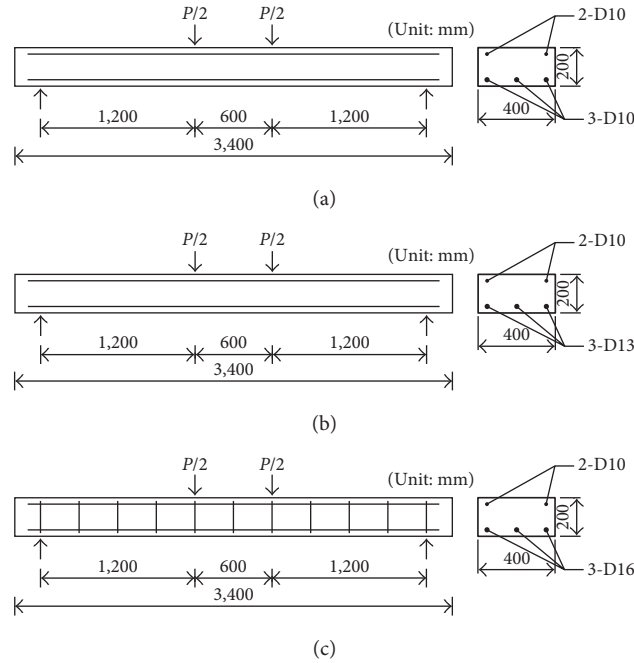


FIGURE 1: Details of test specimens. (a) R41. (b) R55. (c) R87.

TABLE 1: Mixture properties of concrete.

W/C (%)	S/a (%)	W	Unit weight (kg/m ³)			
			C	S	G	Ad
46.7	48.1	168	360	860	949	2.02

The spacing of the carbon fiber strips and the glass fiber strips was 15 mm and 30 mm, respectively. The BFRP fabric has excellent fire resistance performance compared to the CFRP fabric, while its tensile strength is 30% of CFRP strength. The fire resistance of the basalt fabric is 1.5 times greater than the fire resistance of the CFRP or GFRP fabric [24]. Thus, a direct tensile test as shown in Figure 2 was conducted as a preliminary experiment to determine the amount of BFRP fabrics having an equivalent to tensile strength of the CFRP fabric. Thus, as a preliminary test, direct tensile test as shown in Figure 2 was conducted to determine the required amount of BFRP fabrics with an equivalent to tensile strength of the CFRP fabric.

As a result, the thickness of the BFRP fabric with the same tensile strength as the CFRP fabric in the warp direction was determined to be 4.88 times the thickness of the CFRP fabric. The BFRP fabric consisted of basalt fiber in both warp and weft directions. Also, the spacing of warp and weft strips of BFRP fabric was 15 mm and 30 mm, respectively. Table 3 and Figure 3 present the mechanical properties and shapes of the fabrics used as a strengthening material in this research.

Cementitious matrix used as binder consisted of silica sand, polypropylene fiber, cement, fly ash, and polymer powder. The compression test for the cementitious matrix was performed at the curing age of 28 days in accordance

with ASRM C109/C109M [25]. Its compression strength was 46.3 MPa.

2.3. Experimental Variables. The experimental variables tested were tensile reinforcement ratio (0.41%, 0.55%, and 0.87%), different strengthening materials (CFRP fabric and BFRP fabric), and different number of fabric layers (1-layer, 2-layers, and 3-layers). Test parameter details are given in Table 4. The nomenclature of the specimens follows the experimental variables used. In this research, unstrengthened specimen was fabricated as a reference specimen.

A single specimen strengthened with the CFRP fabric was tested to compare its behavior to a behavior of reinforced concrete slab with the BFRP fabric with the tensile reinforcement ratio of 0.41%. The comparison of the global behavior between the slabs reinforced with the CFRP fabric and BFRP fabric presents feasibility of the BFRP fabric as the reinforcement material.

The tensile reinforcement ratio of the specimen was labeled using a letter abbreviation and an Arabic number. The first letter, R, represents the tensile reinforcement ratio. The following Arabic number, 41, 55, or 87, represents the tensile reinforcement ratios of 0.41%, 0.55%, and 0.87%, respectively. Next to the symbol “-”, the letter, N, C, and B represent the nonstrengthened CFRP fabric, and BFRP fabric, respectively. The following Arabic numbers, 1, 2, and 3, represent the 1-layer, 2-layers, and 3-layers of fabric, respectively. For example, “R55-B3” denotes a strengthened specimen with the tensile reinforcement ratio of 0.55% and 3-layers of BFRP fabric.

TABLE 2: Material properties of the used steel.

Nominal diameter (mm)	Yield stress (MPa)	Ultimate stress (MPa)	Modulus of elasticity (GPa)
10	487	621	204
13	469	671	199
16	449	622	194



FIGURE 2: Direct tensile test of FRP fabric.

2.4. Specimen Preparation. Prior to strengthening the concrete slab by FRCM composite, the concrete specimens were rotated 180° so that the strengthening surface of specimens would be the upper surface. The laitance on their strengthening surface was removed using sandblaster and washed with high pressure water.

FRCM strengthening was proceeded as follows: (a) apply the cementitious matrix on the strengthening surface with a thickness of 5 mm by using a shotcrete machine; (b) place the FRP fabric on the matrix; and (c) apply the cementitious matrix with a thickness of 5 mm on FRP fabric. For the specimens with 2-layers and 3-layers of BFRP fabric, the above procedure was repeated two and three times, respectively. The flexural test was conducted after 28 days of strengthening procedure, so that the cement matrix would have enough time to develop its strength.

2.5. Test Setup. The specimens were loaded with a 2,000 kN capacity actuator at a stroke speed of 3 mm/min. The test was carried out under a four-point loading system, and the distance between loading points was 600 mm. Two linear variable differential transformers (LVDTs) were installed on the lower surface of the specimen to measure the deflection

of the specimen at midspan. Additionally, the strain values of the concrete, tensile steel bar, compression steel bar, and fabric of FRCM composite were measured by the strain gages installed at the midspan section of specimens. The measured strain values were recorded at a frequency of 1 second by a data logger.

3. Test Result and Discussion

3.1. Failure Mode. Figure 4 shows the deformed shape of the representative specimens after test. Reference specimens R41-NN, R55-NN, and R87-NN were failed by the yielding of tensile rebar followed by the concrete crushing of the compression zone. All of the FRCM-strengthened specimens had fabric slippage in FRCM composite after the maximum load and were ultimately failed by the tensile fracture of the fabric followed by the concrete crushing of the compression zone. Additionally, it should be noted that the peeling failure of the FRCM composite did not occur in any specimen. Figure 5 shows the crack pattern at the midspan of R55-B1, R55-B2, and R55-B3 specimens. It can be seen from Figure 5 that the flexural cracks were developed at regular intervals in the midspan and propagated toward the compression zone. Furthermore, the FRCM composite was broken with a concrete hammer after the end of the test to investigate the BFRP fabric if the fabric was damaged. It was confirmed that about 60% of the basalt fabric was broken.

3.2. Load-Displacement Curves. Table 5 and Figure 6 show the summary of test results and the comparison of load-displacement curves for all specimens, respectively. Figure 6(a) shows the comparison of the load-displacement curves of R41-C1 and R41-B1 specimens strengthened with 1 layer of CFRP fabric and BFRP fabric, respectively. They show very similar flexural behavior before yielding of steel rebar. After yielding of steel rebar, the load of R41-C1 strengthened with CFRP fabric with relatively high elastic modulus increased more rapidly than that of R41-B1. However, the maximum loads of R41-C1 and R41-B1 were increased by 30.7% and 40.9%, respectively, compared with that of R41-NN. This is because the CFRP fabric has about 8 times higher elastic modulus than the BFRP fabric, resulting in the slip of R41-C1 earlier than R41-B1.

Figure 6(b) shows a comparison of the load-displacement curves of the specimens strengthened with the 1, 2, and 3 layers of BFRP fabric, respectively, all of which had the same tensile reinforcement ratio of 0.41%. As the number of fabric layers increased, the initial crack load

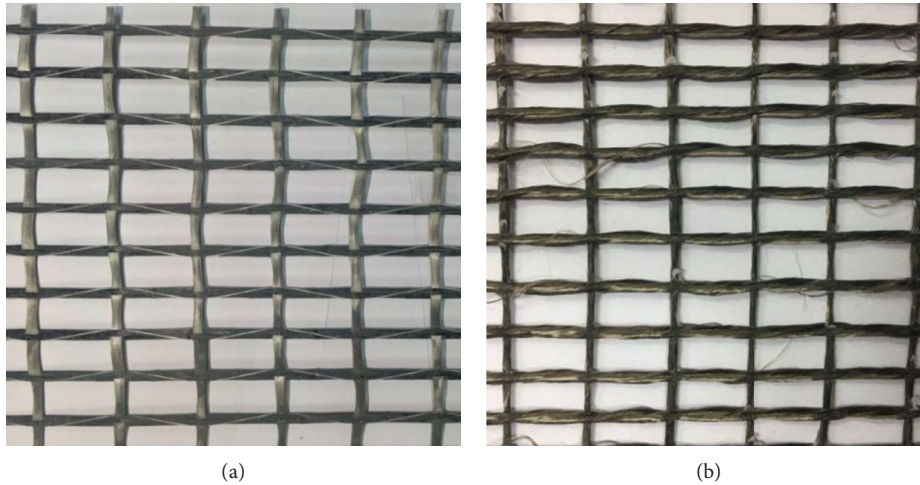


FIGURE 3: FRP fabrics. (a) CFRP fabric. (b) BFRP fabric.

TABLE 3: Material properties of FRP fabric.

Fabric	Nominal thickness (mm ² /mm)	Ultimate tensile strain	Ultimate tensile stress (MPa)	Modulus of elasticity (GPa)
BFRP fabric	0.522	0.023	274.85	11.84
CFRP fabric	0.107	0.014	1314.68	94.85

TABLE 4: Test parameter details.

Specimen	Tensile reinforcement ratio (%)	Strengthening material	Number of fabric layers
R41-NN	0.41	None	0
R41-C1	0.41	CFRP	1
R41-B1	0.41	BFRP	1
R41-B2	0.41	BFRP	2
R41-B3	0.41	BFRP	3
R55-NN	0.55	None	0
R55-B1	0.55	BFRP	1
R55-B2	0.55	BFRP	2
R55-B3	0.55	BFRP	3
R87-NN	0.87	None	0
R87-B1	0.87	BFRP	1
R87-B2	0.87	BFRP	2
R87-B3	0.87	BFRP	3

increased. The yielding load of R41-B1, R41-B2, and R41-B3 increased to 27.1%, 25.3%, and 43.6%, respectively, compared with that of R41-NN. The slope of the curve increased steeply in proportion to the number of fabric layers after yielding of steel rebar. The maximum loads of R41-B1, R41-B2, and R41-B3 were increased to 40.9%, 52.0%, and 98.2%, respectively, compared with R41-NN.

Figure 6(c) shows a comparison of the load-displacement curves of the specimens strengthened with the 1, 2, and 3 layers of BFRP fabric, all of which had the same tensile

reinforcement ratio of 0.55%. As with specimens with a tensile reinforcement ratio of 0.41%, the initial crack loads and yielding loads of specimens with a tensile reinforcement ratio of 0.55% increased in proportion to the number of fabric layers. In addition, the flexural rigidity of the specimens was not improved significantly before yielding of steel rebar but improved in proportion to the number of fabric layer after yielding of steel rebar. The maximum load of R51-B1, R51-B2, and R51-B3 increased to 17.1%, 40.2%, and 62.8%, respectively, compared with that of R51-NN.

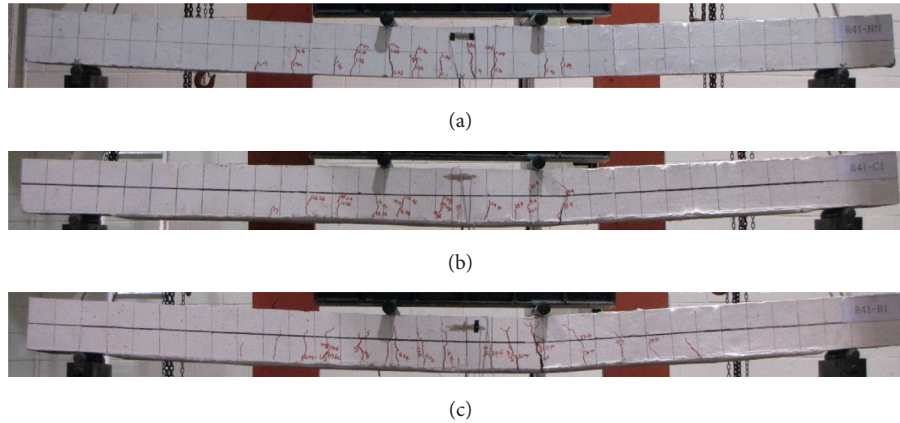


FIGURE 4: Deformed shapes of specimens after testing. (a) R41-NN. (b) R41-C1. (c) R41-B1.

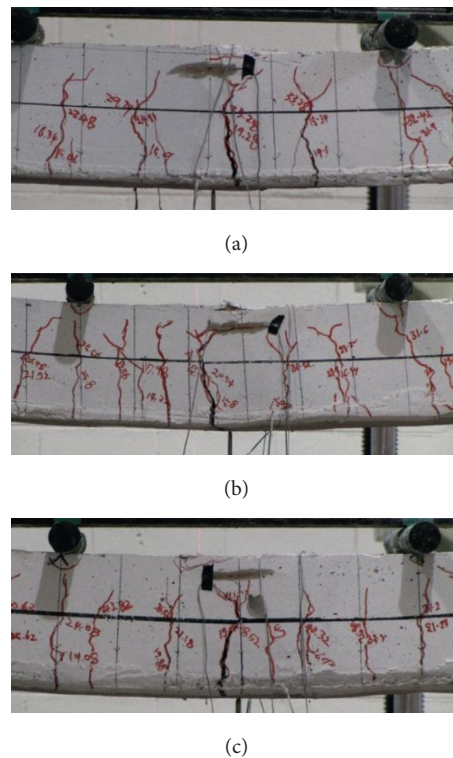


FIGURE 5: Crack pattern at midspan. (a) R55-B1. (b) R55-B2. (c) R55-B3.

Figure 6(d) shows a comparison of the load-displacement curves of the specimens strengthened with the 1, 2, and 3 layers of BFRP fabric, all of which had the same tensile reinforcement ratio of 0.87%. As with specimens with other tensile reinforcement ratios, the flexural rigidity of the specimens was not improved significantly before yielding of steel rebar, but improved in proportion to the number of fabric layer after yielding of steel rebar. The maximum load of R87-B1, R87-B2, and R87-B3 increased to 11.2%, 29.0%, and 48.8%, respectively, compared with that of R51-NN. It should also be noted that the increasing ratio of maximum load decreases as the tensile reinforcement ratio increases.

3.3. Load-Strain Curves. Figure 7 shows the strain distribution along the depth at a midspan cross section of representative specimens. The strains of concrete, tensile reinforcement, and FRP fabric were evaluated at representative load stages. It can be observed from Figure 7 that the strain distribution is linear at the low load level, while it becomes nonlinear and the slippage between FRP fabric and the cementitious matrix occurs after 60% of the maximum load. From 80% of the ultimate load stages, the strains of the FRP fabric were reduced compared to the strains of steel, which might be because the cementitious matrix was broken and slippage occurred between FRP fabric and cementitious

TABLE 5: Summary of test results.

Specimens	Yielding load (kN)	Maximum load (kN)	Load increase over reference (%)
R41-NN	28.94	34.90	—
R41-C1	39.70	45.60	30.7
R41-B1	36.82	49.16	40.9
R41-B2	36.26	53.06	52.0
R41-B3	41.36	69.16	98.2
R55-NN	43.28	50.42	—
R55-B1	47.50	59.06	17.1
R55-B2	49.14	70.70	40.2
R55-B3	54.22	82.08	62.8
R87-NN	64.84	70.72	—
R87-B1	66.08	78.66	11.2
R87-B2	74.56	91.20	29.0
R87-B3	75.54	105.24	48.8

material. Consequently, it should be noted that the strain distribution at low load level can be assumed to be linear, but it cannot be considered as linear at the high load level due to the slippage between FRP fabric and cementitious matrix. Thus, the slippage between FRP fabric and cementitious material needs to be taken into account in order to accurately predict the flexural performance of FRCM-strengthened slabs.

3.4. Ductility. Ductility is generally expressed as the ratio of the deflection at the time of steel yielding to the ultimate deflection. In this research, the fracture mode of the specimen was determined by the ductility index “ μ ” proposed by Jeong [26] shown in Figure 8. The ductility index is expressed in (1):

$$\mu = \frac{1}{2} \left(\frac{E_{\text{tot}}}{E_{\text{el}}} + 1 \right), \quad (1)$$

$$E_{\text{tot}} = E_{\text{in}} + E_{\text{el}}, \quad (2)$$

where μ is the ductility index, E_{tot} is the total energy which is calculated as the area under the load-displacement curve up to the failure load, E_{el} is the elastic energy which is a part of the total energy, and E_{in} is the inelastic energy, as illustrated in Figure 8.

Based on the ductility index proposed by Jeong [26], Grace et al. [27] developed failure modes depending on the energy ratio. The energy ratio ($E_{\text{in}}/E_{\text{tot}}$) is classified into a range of 75% or more, 70% to 75%, or 70% or less and is defined as the ductile, semibrittle, or brittle failure mode, respectively. Table 6 shows the failure mode evaluation results of each specimen defined by this criterion. For nonreinforced specimens, the total energy and elastic energy increase while the energy ratio decreases as the tensile steel reinforcement ratio increases. The energy ratios of the R41-NN, R55-NN, and R87-NN were 83.5%, 76.5%, and 69.3%, which

are defined as the ductile mode, ductile mode, and brittle mode, respectively.

The ductile fracture mode absorbs a large amount of energy before fracture, which was shown in R41-NN, R41-B1, and R55-NN. With increase of the tensile reinforcement ratio, the failure mode was changed from the ductile to the brittle mode. The brittle fracture was shown in the R41-C1, R41-B3, R55-B2, R55-B3, R87-B1, R87-B2, and R87-B3. All of those mentioned specimens failed by the debonding of the FRP fabric with the broken cementitious matrix.

Compared to the R41-NN, the total energy of the R41-C1 specimen with a layer of CFRP fabric was reduced by 28.2%, while the elastic energy was increased by 74.4%. The energy ratio of R41-C1 was 60.3%, confirming that the failure mode of this specimen was brittle failure. However, for the R41-B1 specimen with a layer of BFRP fabric, both the total energy and the elastic energy increased compared with those of R41-NN, and its energy ratio was 76.0%, indicating ductile failure.

For the specimens with the tensile reinforcement ratio of 0.41%, the energy ratio decreased with the increase of the number of BFRP fabric layers. The energy ratios of the R41-B1, R41-B2, and R41-B3 were 76.0%, 70.9%, and 63.6%, which are defined as the ductile mode, semiductile mode, and brittle mode, respectively.

For the specimens with the tensile reinforcement ratio of 0.55%, the energy ratio and the total energy decreased with the increase of the number of BFRP fabric layers. The energy ratios of the R55-B1, R55-B2, and R55-B3 were 74.0%, 67.0%, and 65.1%, which are defined as the ductile mode, brittle mode, and brittle mode, respectively.

For the specimens with the tensile reinforcement ratio of 0.87%, the energy ratio and the total energy decreased with the increase of the number of BFRP fabric layers. The energy ratios of the R87-B1, R87-B2, and R87-B3 were 67.4%, 61.2%, and 56.5%, which are defined as brittle mode.

Also, it can be seen that the ductility of the FRCM-strengthened specimens decreased with the higher amount of fabric and the higher tensile reinforcement ratio.

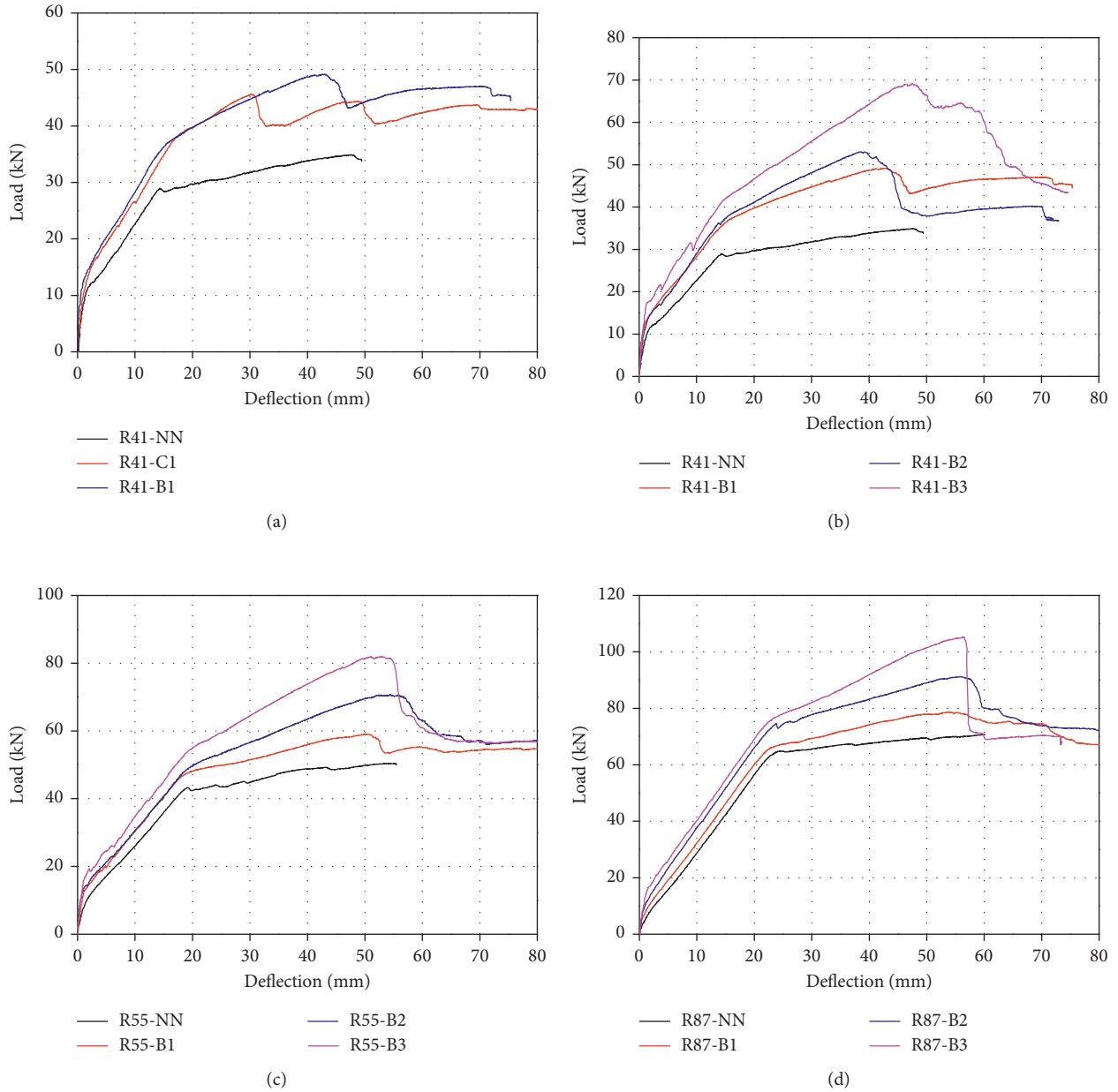


FIGURE 6: Comparison of load-deflection curves. (a) Specimens with CFRP and BFRP fabric. (b) Specimens with the tensile reinforcement ratio of 41%. (c) Specimens with the tensile reinforcement ratio of 55%. (d) Specimens with the tensile reinforcement ratio of 87%.

4. Numerical Approach

4.1. Effective Tensile Stress Level of FRCM Fabric

4.1.1. *ACI 549*. In ACI 549 [14], the effective tensile strain level in the FRCM fabric attained at failure, ϵ_{fe} , is limited to the design tensile strain of the FRCM fabric, ϵ_{fd} , as defined in

$$\epsilon_{fe} = \epsilon_{fd} \leq 0.012. \quad (3)$$

Also, the effective tensile stress level in the FRCM fabric attained at failure, f_{fe} , in the FRCM composite is calculated in accordance with

$$f_{fe} = E_f \epsilon_{fe}, \quad (4)$$

where E_f is the elastic modulus of FRCM fabric.

4.1.2. *Jung Model*. Jung et al. [16] proposed the FRCM bond strength model with regard to both the slippage and the debonding phenomenon of the FRCM composite by (5), based on the FRCM research performed by D'Ambrishi et al. [18] and the model proposed by Teng et al. [28]. The effective tensile stress level in the FRCM fabric at failure can be computed by the following equations:

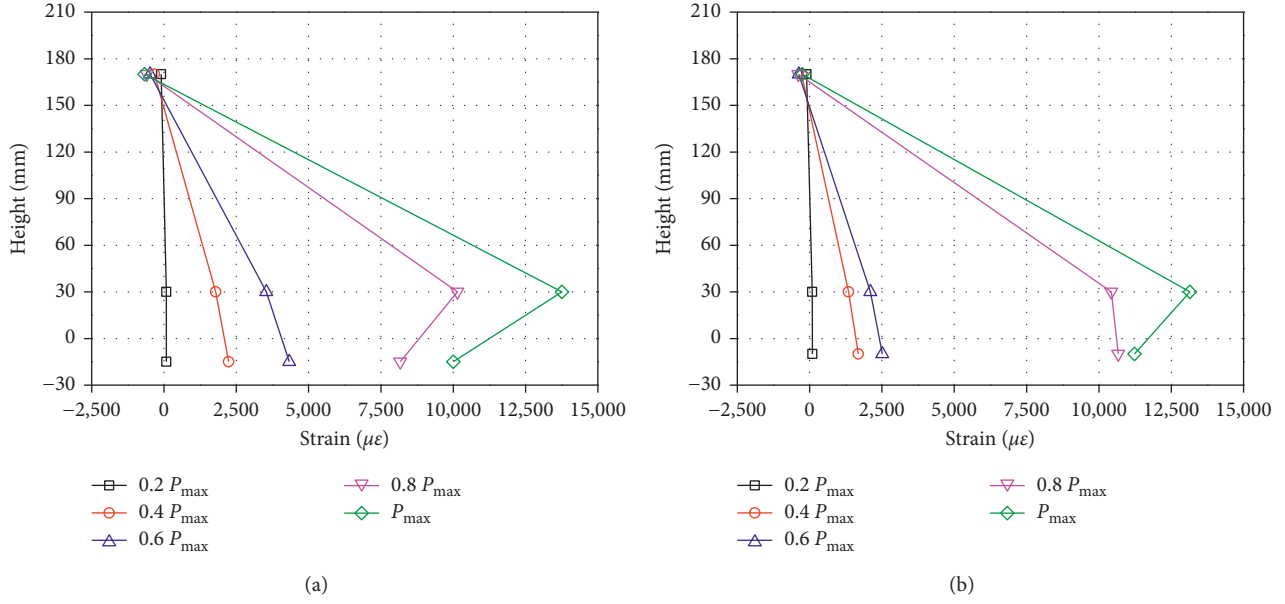


FIGURE 7: Load-strain relation. (a) R55-B1. (b) R55-B3.

$$f_{fe} = \alpha \beta_F \beta_L \sqrt{\frac{E_F \sqrt{f'_c}}{t_1 \sqrt{n}}},$$

$$\beta_F = \sqrt{\frac{2 - b_F/b_c}{1 + b_F/b_c}},$$

$$\beta_L = \begin{cases} 1, & \text{if } L \geq L_e \\ \sin \frac{\pi L}{2L_e}, & \text{if } L < L_e, \end{cases} \quad (5)$$

$$L_e = \sqrt{\frac{E_F t_F}{f'_c}},$$

where b_F is the width of the FRCM fabric, b_c is the width of the specimen, L is the bond length, L_e is the effective bond length, E_F is the elastic modulus of the FRCM fabric, t_F is the total thickness of the FRCM fabric, f'_c is the cylinder compressive strength for concrete, and α is the reduction factor and given as 0.727 for FRCM by Jung et al. [16]. Additionally, t_1 is the nominal thickness of a layer of the FRCM fabric and n is the number of fabric layers.

4.2. Nominal Flexural Strength. Nominal flexural strength was calculated by using ACI 318 [13] and ACI 549 [14]. First, the neutral axis depth, c_u , satisfying the internal force equilibrium expressed by (6), (7) was determined by the trial and error method:

$$T_f + T_s = C, \quad (6)$$

where

$$T_s = A_s f_y,$$

$$T_f = n A_f f_{fe},$$

$$C = \alpha_1 f'_c \beta_1 c_u b,$$

$$\alpha_1(c_u) = \frac{3 \epsilon'_c \epsilon_c(c_u) - [\epsilon_c(c_u)]^2}{3 \beta_1(c_u) \epsilon_c'^2},$$

$$\beta_1(c_u) = \frac{4 \epsilon'_c - \epsilon_c(c_u)}{6 \epsilon_c' - 2 \epsilon_c(c_u)}, \quad (7)$$

$$\epsilon'_c = \frac{1.7 f'_c}{E_c},$$

$$E_c = 4700 \sqrt{f'_c},$$

$$\epsilon_{fe} = \frac{f_{fe}}{E_f},$$

$$\epsilon_c = \frac{c_u}{h - c_u} \epsilon_{fe},$$

where T_s , T_f , C , A_s , A_f , f_y , n , α_1 , β_1 , ϵ'_c , ϵ_c , E_c , f_{fe} , ϵ_{fe} , and E_f are the tensile force provided by tensile rebar, tensile force provided by the FRCM composite, compressive force provided by concrete, area of tensile steel rebar, area of the FRP fabric, yielding strength of steel rebar, number of FRP fabrics, concrete stress block factor, compressive strain attained in the maximum compressive strength of unconfined

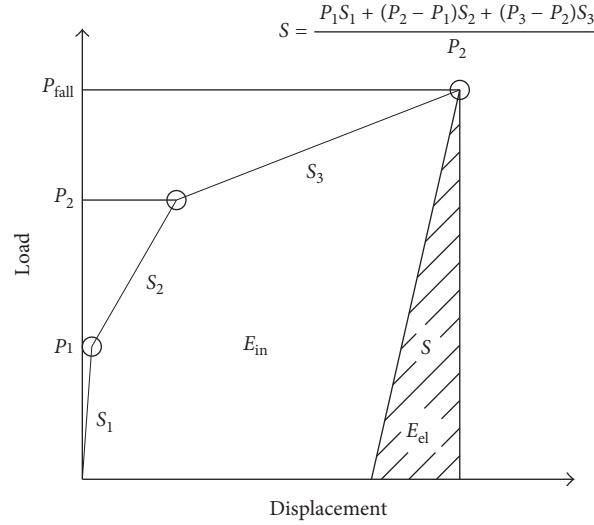


FIGURE 8: Definition of ductility index [17].

TABLE 6: Results of ductility evaluation.

Specimen	E_{el} (J)	E_{in} (J)	E_{tot} (J)	μ_{energy}	Energy ratio (%)	Failure mode
R41-NN	217	1100	1317	3.53	83.5	Ductile
R41-C1	379	575	954	1.76	60.3	Brittle
R41-B1	372	1175	1547	3.53	76.0	Ductile
R41-B2	413	1006	1419	2.22	70.9	Semiductile
R41-B3	808	1409	2217	1.87	63.6	Brittle
R55-NN	506	1641	2146	2.62	76.5	Ductile
R55-B1	581	1653	2234	2.42	74.0	Semiductile
R55-B2	880	1786	2665	2.01	67.0	Brittle
R55-B3	1027	1912	2939	1.93	65.1	Brittle
R87-NN	995	2250	3245	2.13	69.3	Semiductile
R87-B1	1005	2078	3082	2.03	67.4	Brittle
R87-B2	1414	2235	3649	1.79	61.2	Brittle
R87-B3	1754	2275	4029	1.65	56.5	Brittle

concrete, strain in the concrete, elastic modulus of concrete, strength of the FRCM composite, strain in the FRCM composite, and elastic modulus of the FRCM composite.

The nominal flexural strength, M_n , can be calculated in accordance with the following equations:

$$M_n = M_s + M_f,$$

$$M_s = A_s f_y \left(d - \frac{\beta_1 c_u}{2} \right), \quad (8)$$

$$M_f = A_f b f_{fc} \left(h - \frac{\beta_1 c_u}{2} \right),$$

where d and h are the effective depth and height of specimen cross section, respectively.

4.3. Prediction of Nominal Flexural Strength. Table 7 shows the comparisons of nominal flexural strength predicted by

ACI 549 [14] and the Jung model [16]. The ratios of the test result to the predicted flexural strength by ACI 549 were ranged from 0.97 to 1.14. The mean and standard deviation of the ratios of the test result to the prediction value by ACI 549 were 1.08 and 0.05, respectively. The ratios of the test result to the predicted value by Jung model were ranged from 0.94 to 1.14. The mean and standard deviation of the ratios of the test result to the predicted value by the Jung model were 1.05 and 0.06, respectively. Consequently, the Jung model predicts the effective stress level more accurately than ACI 549. However, it can be noted that both ACI 549 and the Jung model predict the effective stress level of the FRCM fabric with the sufficient accuracy to be applied for the FRCM strengthening design of the RC slab.

5. Conclusion

The following conclusions are drawn from the results:

TABLE 7: Comparison of nominal flexural strength.

Specimen	Nominal flexural strength			Test/ACI 549	Test/Jung model
	Test (kN)	ACI 549 (kN)	Jung model (kN)		
R41-B1	29.50	27.33	29.18	1.08	1.01
R41-B2	31.84	32.69	33.94	0.97	0.94
R41-B3	41.50	38.00	38.08	1.09	1.09
R55-B1	35.44	32.97	34.80	1.07	1.02
R55-B2	42.42	38.25	39.48	1.11	1.07
R55-B3	49.25	43.47	43.55	1.13	1.13
R87-B1	47.20	45.39	46.94	1.04	1.01
R87-B2	54.72	50.44	51.52	1.08	1.06
R87-B3	63.14	55.37	55.43	1.14	1.14
				Mean: 1.08, SD: 0.05	Mean: 1.05, SD: 0.06

- (1) All of the FRCM-strengthened specimens had fabric slippage in FRCM composite after the maximum load and were ultimately destroyed by the tensile fracture of the fabric followed by the concrete crushing of the compression zone.
- (2) The initial crack loads and yielding loads of specimens with three tensile reinforcement ratio of 0.41%, 0.55%, and 0.87% showed increasing trend in proportion to the number of fabric layers. Also, the maximum loads of FRCM-strengthened specimens increase from 11.2% to 98.2% relative to the reference specimens. Additionally, it should be noted that the increasing ratio of maximum load over the reference specimen decreases as the tensile reinforcement ratio increases.
- (3) The strain distribution of the FRCM-strengthened specimen is linear at the low load level, while it becomes nonlinear after 60% of maximum load, resulting from the slippage between FRP fabric and the cementitious matrix. Thus, the slippage between FRP fabric and cementitious material needs to be considered in order to accurately predict the flexural performance of the FRCM-strengthened slabs.
- (4) The energy ratio and ductility of the FRCM-strengthened specimens decreased with the higher amount of fabric and the higher tensile reinforcement. With the higher amount of fabric, the fracture mode was changed from ductile failure to brittle failure.
- (5) The Jung model predicts the effective stress level more accurately than ACI 549. However, it can be noted that both ACI 549 and the Jung model predict the effective stress level of the FRCM fabric with sufficient accuracy to be applied for FRCM strengthening design of the RC slab.

Conflicts of Interest

The authors declare no conflicts of interest.

Acknowledgments

This work was supported by the Korea Science and Engineering Foundation (KOSEF) grant funded by the Korea government (MOST) (no. 2015R1D1A1A01057453).

References

- [1] K. Kovler and V. Chernov, "Types of damage in concrete structures," in *Failure, Distress and Repair of Concrete Structures*, pp. 32–56, Woodhead Publishing Limited, Cambridge, UK, 2009.
- [2] G. Loreto, L. Leardini, D. Arboleda, and A. Nanni, "Performance of RC slab-type elements strengthened with fabric-reinforced cementitious-matrix composites," *Journal of Composites for Construction*, vol. 18, no. 3, 2014.
- [3] H. M. Elsanadedy, T. H. Almusallam, S. H. Alsayed, and Y. A. Al-Salloum, "Flexural strengthening of RC beams using textile reinforced mortar—experimental and numerical study," *Composite Structures*, vol. 97, pp. 40–55, 2013.
- [4] S. W. Kim, *Experimental Study on Bond Flexural Behavior of RC Members Using CFRP-Bar NSM System*, Ph.D. thesis, pp. 1–4, Yeungnam University, Gyeongsan, Republic of Korea, 2015.
- [5] H. J. Kim, *Failure Behavior of Reinforced Concrete Beams with Flexural Strengthened by Steel Plates*, Ph.D. thesis, pp. 17–22, Chonnam University, Gwangju, Republic of Korea, 2005.
- [6] J. Y. Park, *Behavior Characteristics and Strengthening Design of Reinforced Concrete Beam Strengthened with Carbon Fiber Reinforced Polymer Plate*, Ph.D. thesis, pp. 1–3, Chungbuk University, Cheongju, Republic of Korea, 2003.
- [7] L. Ombres, "Flexural analysis of reinforced concrete beams strengthened with a cement based high strength composite material," *Composite Structures*, vol. 94, no. 1, pp. 143–155, 2011.
- [8] H. H. Lee and E. S. Koo, "A study on the strength and the deformation capacity of RC beams strengthened with aramid fiber sheet," *Journal of the Korea Concrete Institute*, vol. 10, pp. 151–158, 1998.
- [9] T. C. Triantafillou and C. G. Papanicolau, "Shear strengthening of reinforced concrete members with textile reinforced mortar (TRM)," *Materials and Structures*, vol. 39, no. 1, pp. 93–103, 2006.

- [10] H. Ko, S. Matthys, A. Palmieria, and Y. Sato, "Development of simplified bond stress-slip model for bonded FRP-concrete interfaces," *Construction and Building Materials*, vol. 68, pp. 142–157, 2014.
- [11] A. D'Ambrisi and F. Focacci, "Flexural strengthening of RC beams with cement-based composites," *Journal of Composites for Construction*, vol. 15, no. 5, pp. 707–720, 2011.
- [12] S. Babaeidarabad, G. Loreto, and A. Nanni, "Flexural strengthening of RC beams with an externally bonded fabric-reinforced cementitious matrix," *Journal of Composites for Construction*, vol. 18, no. 5, 2014.
- [13] American Concrete Institute (ACI), *Building Code Requirements for Reinforced Concrete (ACI 318)*, American Concrete Institute, Farmington Hills, MI, USA, 2011.
- [14] American Concrete Institute (ACI), *Design and Construction Guide of Externally Bonded FRCM System for Concrete and Masonry Repair and Strengthening (ACI 549)*, American Concrete Institute, Farmington Hills, MI, USA, 2013.
- [15] R. Azam and K. Soudki, "FRCM strengthening of shear-critical RC beams," *Journal of Composites for Construction*, vol. 18, no. 5, 2014.
- [16] K. Jung, K. Hong, S. Han, J. Park, and J. Kim, "Prediction of flexural capacity of RC beams strengthened in flexure with FRP fabric and cementitious matrix," *International Journal of Polymer Science*, vol. 2015, Article ID 868541, 11 pages, 2015.
- [17] T. Kuroki, Y. Tanaka, T. Hokudoh, and K. Yabuki, "Heat resistance properties of poly (p-phenylene-2,6-benzobisoxazole) fiber," *Journal of Applied Polymer Science*, vol. 65, no. 5, pp. 1031–1036, 1997.
- [18] A. D'Ambrisi, L. Feo, and F. Focacci, "Experimental analysis on bond between PBO-FRCM strengthening materials and concrete," *Composites Part B: Engineering*, vol. 44, no. 1, pp. 524–532, 2013.
- [19] G. P. Lignola, C. Caggegi, F. Ceroni et al., "Performance assessment of basalt FRCM for retrofit applications on masonry," *Composites Part B: Engineering*, vol. 128, pp. 1–18, 2017.
- [20] J. Sim, C. Park, and D. Y. Moom, "Characteristics of basalt fiber as a strengthening material for concrete structures," *Composites Part B: Engineering*, vol. 36, no. 6-7, pp. 504–512, 2005.
- [21] Q. Liu, M. T. Shaw, R. S. Parnas, and A. M. McDonnell, "Investigation of basalt fiber composite mechanical properties for applications in transportation," *Polymer Composites*, vol. 27, no. 1, pp. 41–48, 2006.
- [22] ASTM International, *Standard Test Method for Compressive Strength of Cylindrical Concrete Specimens (ASTM C39/C39M)*, ASTM International, West Conshohocken, PA, USA, 2013.
- [23] ASTM International, *Standard Test Method and Definitions for Mechanical Testing of Steel Products (ASTM A370)*, ASTM International, West Conshohocken, PA, USA, 2013.
- [24] V. Dhand, G. Mittal, K. Y. Rhee, S. J. Park, and D. Hui, "A short review on basalt fiber reinforced polymer composites," *Composites Part B: Engineering*, vol. 73, pp. 166–180, 2015.
- [25] ASTM International, *Standard Test Method for Compressive Strength of Hydraulic Cement Mortars (ASTM C109/C109M)*, ASTM International, West Conshohocken, PA, USA, 2013.
- [26] S. M. Jeong, *Evaluation of Ductility in Prestressed Concrete Beams Using Fiber Reinforced Plastic Tendons*, Ph.D. thesis, University of Michigan, Ann Arbor, MI, USA, 1994.
- [27] N. F. Grace, A. K. Soliman, G. Abdel-Sayed, and K. R. Saleh, "Behavior and ductility of simple and continuous FRP reinforced beams," *Journal of Composites for Construction*, vol. 2, no. 4, pp. 186–194, 1998.
- [28] J. G. Teng, S. Y. Smith, J. Yao, and J. F. Chen, "Intermediate crack-induced debonding in RC beams and slabs," *Journal of Construction and Building Materials*, vol. 17, no. 6-7, pp. 447–462, 2003.

Research Article

Feasibility of Reduced Lap-Spliced Length in Polyethylene Fiber-Reinforced Strain-Hardening Cementitious Composite

Wonchang Choi ¹, Seok-Joon Jang,² and Hyun-Do Yun ²

¹Department of Architectural Engineering, Gachon University, Seongnam-si, Gyeonggi-do, Republic of Korea

²Department of Architectural Engineering, Chungnam National University, Daejeon, Republic of Korea

Correspondence should be addressed to Hyun-Do Yun; wiseroad@cnu.ac.kr

Received 26 July 2017; Revised 16 November 2017; Accepted 4 December 2017; Published 29 January 2018

Academic Editor: Doo-Yeol Yoo

Copyright © 2018 Wonchang Choi et al. This is an open access article distributed under the Creative Commons Attribution License, which permits unrestricted use, distribution, and reproduction in any medium, provided the original work is properly cited.

This research investigates the interfacial behavior between polyethylene (PE) fiber-reinforced strain-hardening cement composite (PE-SHCC) and reinforcing bars that are spliced in the tension region to determine feasibility of reduced lap-spliced length in PE-SHCC. Twenty test specimens were subjected to monotonic and cyclic tension loads. The variables include the replacement levels of an expansive admixture (0% and 10%), the compressive strength of the SHCC mixtures (40 MPa and 80 MPa), and the lap-spliced length in the tension region (40% and 60% of the splice length recommended by ACI 318). The PE-SHCC mixture contains polyethylene fiber to enhance the tensile strength, control the widths of the cracks, and increase the bond strength of the lap splice reinforcement and the calcium sulfo-aluminate- (CSA-) based expansive admixture to improve the tension-related performance in the lap splice zone. The results have led to the conclusion that SHCC mixtures can be used effectively to reduce the development length of lap splice reinforcement up to 60% of the splice length that is recommended by ACI 318. The addition of the calcium sulfo-aluminate-based expansive admixture in the SHCC mixtures improved the initial performance and mitigated the cracking behavior in the lap splice region.

1. Introduction

Many research studies have been carried out to investigate the force transfer from the reinforcement to the concrete in a splice zone in both tension and compression [1–7]. It has been established that the bond strength is governed by the mechanical properties of the concrete, concrete cover, the presence of confining reinforcement, reinforcement geometry, and so on. Ganesan et al. [6] reported that the confinement and bridging effect of hybrid fibers enhanced the bond strength of deformed reinforcing bars embedded in hybrid fiber-reinforced high-performance concrete (HFRHPC) composites when compared to plain high-performance concrete (HPC). They concluded from their test results that the anchorage length requirement for deformed bars can be reduced by the usage of HFRHPC.

Recently, Hosseini et al. [8] investigated the bond behavior of deformed steel reinforcement bars connected by a grouted spiral connection for linking precast member to member. The axial and flexural pullout test results indicated that the load transfer within the connected bars is dependent on the mechanical interlocking mechanism enhanced by the spiral confinement. The tensile resistance of spliced bars can be increased by better confinement in the spliced region.

Conventionally, the use of deformed reinforcement is an efficient way to improve the bond strength and ductility of concrete structures in order to mitigate bond failure as well as to enhance the energy absorption and dissipation in the splice zone in compression and tension. The bond strength between the concrete and spliced reinforcement increases as the length of the deformed reinforcement

TABLE 1: Design of the conventional concrete and SHCC mixtures.

Mixture ID	W/B	f'_c (MPa)	Fibers (%)		Unit weight (kg/m ³)						
			PE	Cement	Water	Silica fume	EXA	S	G	AE	T
C30	0.50	30	—	350	175	—	—	770	981	—	—
C100	0.18	100	—	800	160	89	—	546	835	—	—
xxP40/00*	0.45	30	1.50	1,075	484	—	—	430	—	—	—
xxP40/10				968	489	—	108	430	—	—	—
xxP80/00	0.19	100	1.50	1409	319	245	—	163	—	33	7
xxP80/10				1268	319	245	141	163	—	33	7

*xxP40/00 (mixture ID example): xx = percent of spliced length; P = reinforced fiber type (P is polyethylene fiber); 40 = compressive strength of concrete (40 MPa); 00 = expansive admixture (EXA) replacement level (0%). The other specimen ID "C" is control concrete. W/B = water-to-binder ratio; PE = polyethylene fiber; EXA = expansive admixture; S = sand; G = gravel; AE = air-entraining agent; T = antifoaming agent.

TABLE 2: Mechanical properties of polyethylene (PE) fiber.

Fiber	Specific gravity	Length l (mm)	Diameter d (μ m)	Aspect ratio l/d^*	Tensile strength (MPa)	Young's modulus (GPa)
Polyethylene fiber	0.97	12	12	1000	2500	75

* l/d is length-to-diameter ratio.

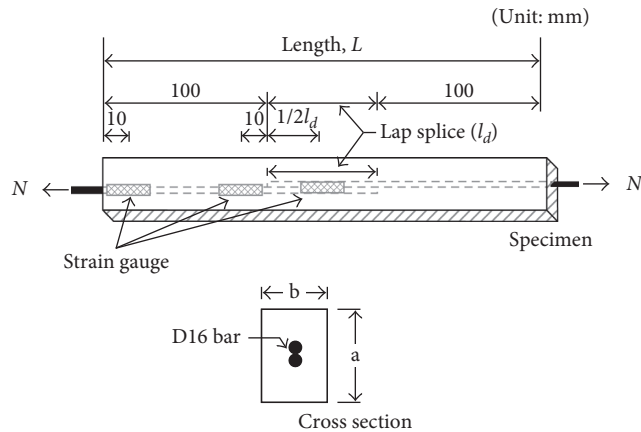


FIGURE 1: Schematic drawing for specimens.

increases, such that splitting failure converts to pullout failure [9].

Several investigations have been carried out to study the effect of fiber as an alternative method for improving the bond strength between concrete and reinforcement. The lap splice length of the reinforcement in a fiber-reinforced strain-hardening cement composite (SHCC), which has strain-hardening behavior and a capacity to control macrocracks in direct tension, can be lesser (shorter) than that of reinforcement used in conventional concrete. The reduction in the length of the reinforcement used for joints between precast concrete members would lead to construction efficiency as well as time and cost savings. Hamad and Itani [10] converted a concrete structure from brittle failure character to ductile failure character by adding steel fibers to the concrete mixture. The fibers play a role similar to that of confinement reinforcement in a splice region, with bridging effects to the cracks that delay the propagation of cracks.

Research findings indicate that the brittle failure that occurs after reaching the maximum tensile load can be controlled by using fibers in the splice region in tension [6, 7, 11]. Yazici and Arel [7] concluded that pullout loading is increased by 7% to 16% when the amount of steel fiber and the aspect ratio in the steel fiber concrete mixtures are increased in comparison to concrete mixtures without steel fiber. The pullout loads of the deformed steel reinforcement are affected by the mechanical properties of the concrete mix, concrete cover, amount of steel fibers, and the aspect ratio of the steel fibers. A study carried out by Haddad [12] similarly showed that the bond strength of concrete with steel fibers added by 2% volume was increased by 23% of the bond strength of plain concrete.

Fischer and Li [13] investigated the tensile characteristics of a polyvinyl alcohol (PVA) fiber in an engineered cementitious composite (ECC) mixture to compensate for the brittle nature of concrete. In the Fischer study, tension members reinforced with PVA fibers showed superior tensile performance after forming initial cracks. However, the initial cracks at the hardening stage in the rich mix design of the ECC mixture led to lower tensile stress than for a conventional cement mixture.

Similarly, SHCCs reinforced with fiber also show superior tensile performance, which includes the control of crack propagation, but considerable shrinkage was observed due to the rich mix design [14]. This study investigated the effects of the expansive admixture, compressive strength, and the reduced lap splicing length associated with the bond performance in the splice region. It is likely that the initial shrinkage cracks adversely affect the tensile strength, lap splice length, and bond behavior in the splice region. Therefore, shrinkage cracking needs to be considered in SHCC mix design. To compensate for the excessive shrinkage of the SHCC mixtures, the cement was replaced with an expansive admixture [15].

TABLE 3: Details of test specimens.

¹ b × a (mm)	² Splice length (mm)	Specimen ID	40% of spliced length		Specimen ID	60% of spliced length	
			L (mm)	³ 40% of l_d (mm)		L (mm)	⁴ 60% of l_d
80 × 100	440	C40	640	—	—	—	—
	240	C80	440	—	—	—	—
	440	40P40/00	380	180	60P40/00	460	260
	440	40P40/10	380	180	60P40/10	460	260
	240	40P80/00	300	100	60P80/00	340	140
	240	40P80/10	300	100	60P80/10	340	140

¹See Figure 1 for cross section; ²splice lengths were calculated using ACI 318-11 equation; ³40% of splice length (SHCC specimens); ⁴60% of splice length (SHCC specimens).

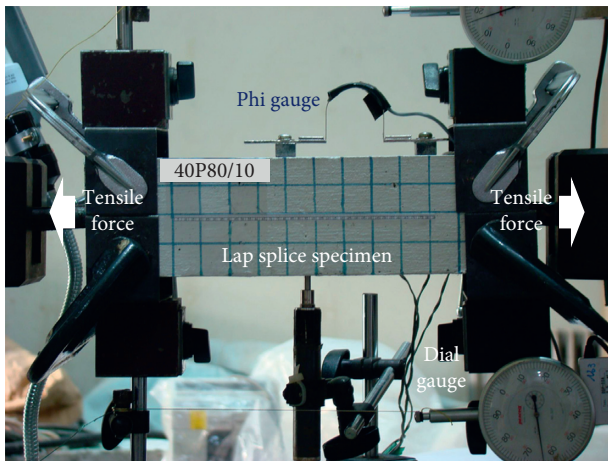


FIGURE 2: Test setup of spliced specimens in the direct tension.

2. Experimental Program

2.1. Preparation. Twenty test specimens were fabricated in order to examine the bond performance in tension in terms of the following parameters. The variables include the replacement levels of an expansive admixture (0% and 10%), the compressive strength of the SHCC mixtures (40 MPa and 80 MPa), and the length of the lap splice in the tension region (40% and 60% of the splice length recommended by ACI 318). In order to reduce the excessive shrinkage of the SHCC mixtures, 10% of the cement was replaced with a CSA-based expansion admixture [15].

Table 1 presents the design of the concrete and SHCC mixtures used in this study. For example, the designation P30/10 indicates that the compressive strength of SHCC mixture is 30 MPa and includes 10% expansive admixture.

Table 2 presents the mechanical properties of the polyethylene (PE) fibers used in the mixtures. SHCC mixtures are affected significantly by shrinkage and also show strain-hardening effects and broadly dispersed cracks in the tension zone. In order to determine the mechanical properties of the SHCC mixtures used in this study, test specimens were fabricated specially for shrinkage, compressive strength, and tensile strength. A prismatic specimen 100 mm × 100 mm × 400 mm was used to test for shrinkage. After placing the mixture, a shrinkage gauge was installed in the middle of the specimen, and then the

specimen was cured in an environmental chamber at 20°C ± 1°C and 50% ± 1% relative humidity. Three cylindrical specimens 100 mm × 200 mm for each SHCC mixture were fabricated for compressive strength testing according to KS F2405. The direct tensile strength of each SHCC mixture was determined using dumbbell-shaped specimens according to JSCE-E-53110. A specimen for each mixture was tested separately under monotonic loading and cyclic loading.

Figure 1 presents a schematic illustration of a test specimen that includes details for the three strain gauges that were attached at the splice region and both ends of the steel reinforcement. In addition, a crack gauge was installed at the end of the splice region to measure the crack width, also shown in Figure 1. The overall deformation of the specimen and strain of the reinforcement were measured using dial gauges attached at both ends of the specimen. Table 3 presents detailed information for the specimens associated with the spliced length in this study.

The reinforcement used for the splice region is D16 reinforcement with a nominal diameter of 16 mm. The yield stress (f_y), strain at yielding (ϵ_y), and the elastic modulus (E_s) of the reinforcement are 528 MPa, 2750 μ m, and 193 GPa, respectively.

2.2. Experimental Procedure. Twenty SHCC specimens were fabricated to examine the tensile performance in the lap splice zones; the tensile performance was based on the mechanical characteristics of the reinforcing fibers and mixing conditions. The splice lengths for the concrete specimens (C40 and C80) were computed using the equation found in ACI 318. Monotonic and cyclic direct tension loads were applied using a universal testing machine with a capacity of 50 kN as shown in Figure 2.

For the cyclic tensile tests, the number of cracks and the crack widths were measured at maximum stress so that the dispersion and mitigation of the cracks that developed in the spliced zone could be examined. The cyclic loads, which were controlled using two displacement gauges installed at the ends of the specimens, were repeatedly applied at 500 μ , 1000 μ , and 2000 μ .

3. Experimental Results

3.1. Mechanical Properties of the SHCC Mixtures. Table 4 presents the experimental results for the mechanical

TABLE 4: Material properties of concrete and SHCC mixtures.

Mixture type	Strain 1 day after casting (μ)	Compressive strength (MPa)	Young's modulus (GPa)	Tensile strength (MPa)	Tensile strain capacity* (%)
C40	-134	32.9	22.5	—	—
C80	-443	84.7	35.4	—	—
P40/00	-316	39.4	13.4	5.88	2.78
P40/10	330	39.5	13.4	6.61	1.12
P80/00	-446	81.7	27.4	7.83	0.93
P80/10	229	86.7	25.9	6.65	1.11

Note. The compressive and tensile strength results are the averages for three and five specimens, respectively. *Tensile strain at the peak tensile stress.

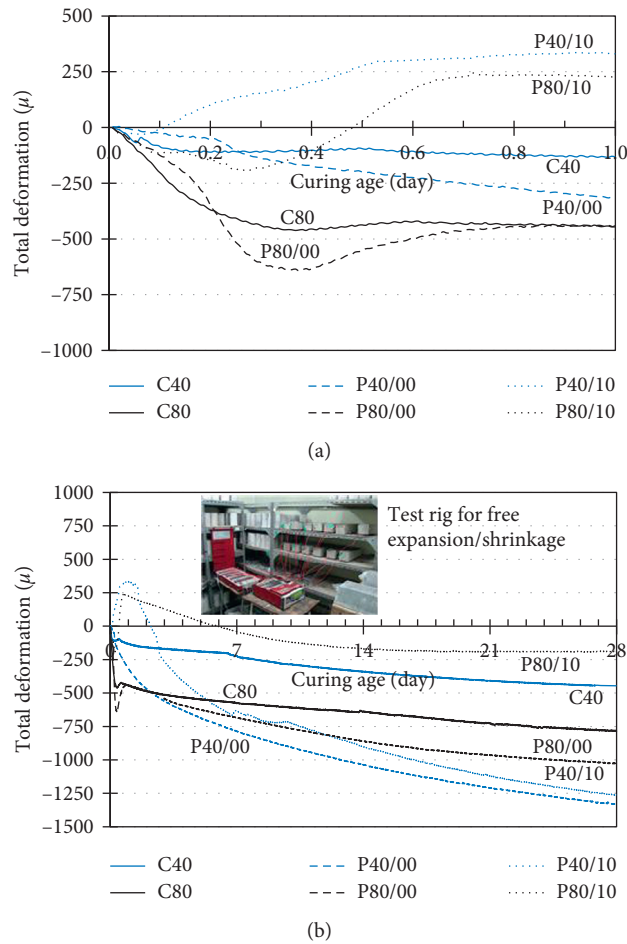


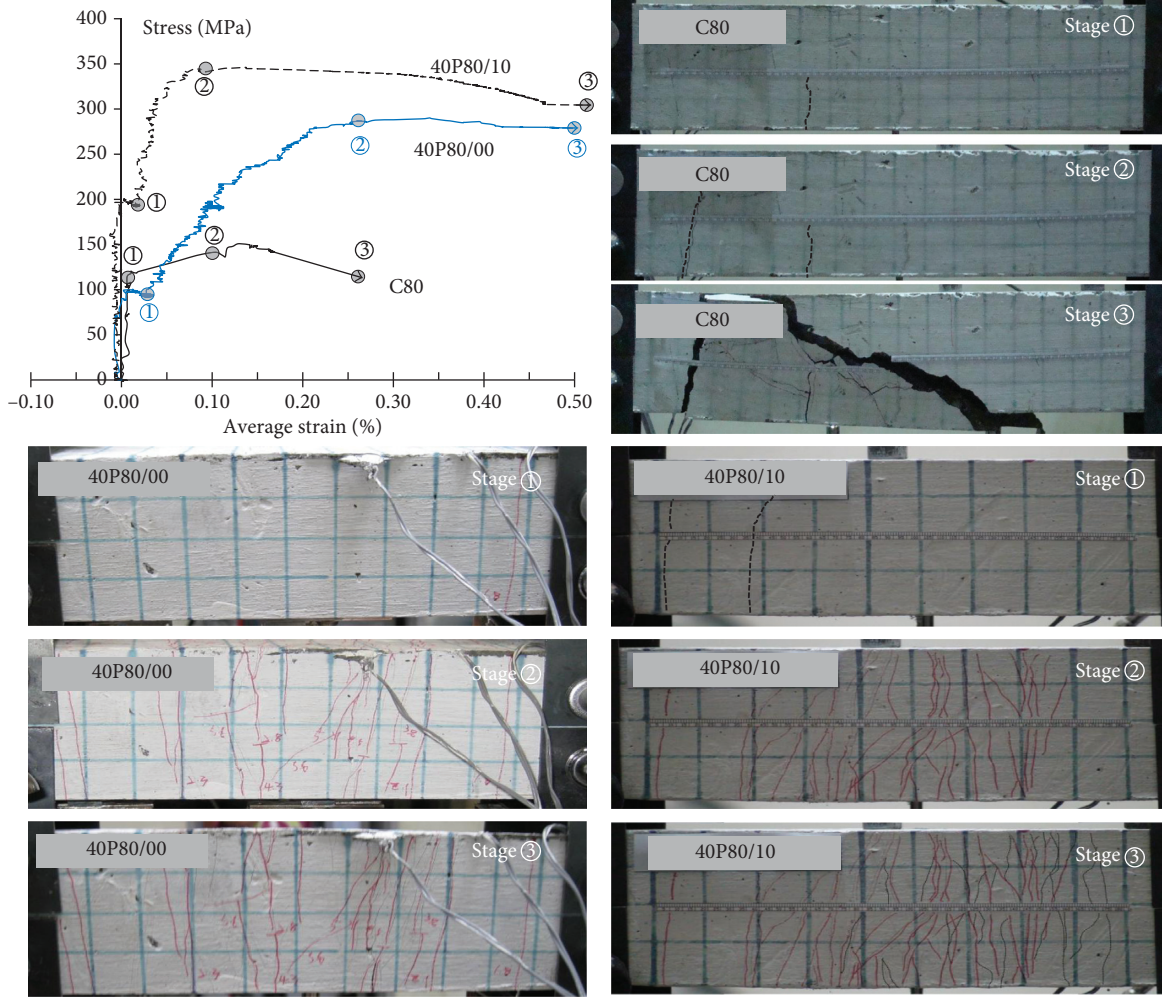
FIGURE 3: Free expansion-shrinkage strain of concrete and PE-SHCC prisms. (a) Free strain history during 1 day. (b) Free strain history during 28 days.

properties, which include shrinkage, compressive strength, elastic modulus, and tensile strength and strain for each SHCC mixture.

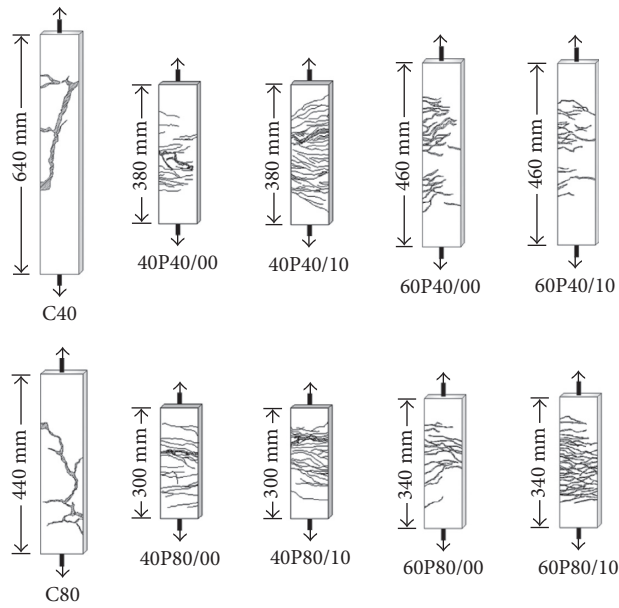
Figures 3(a) and 3(b) show the shrinkage that was monitored over 1 day and 28 days, respectively, after casting the SHCC mixtures. The shrinkage for each mixture was measured in an environmental chamber at a temperature of $20^{\circ}\text{C} \pm 1^{\circ}\text{C}$ and at $60\% \pm 1\%$ relative humidity. The amounts of the free length change for the polyethylene fiber-reinforced SHCC (i.e., PE-SHCC) specimens during 1 day

are higher than that for the plain concrete specimens. The shrinkage was turned into expansion with respect to the presence of the expansive admixture. In particular, the levels of early age shrinkage within 1 day for specimens C80 and P80/00 are higher than for the other specimens, which is due to the relatively large amount of cement and the presence of 17% silica fume.

The C40 and C80 specimens shrank rapidly over half day after placement, and then the shrinkage increased gradually. The PE-SHCC specimens, however, tended to shrink



(a)



(b)

FIGURE 4: Typical cracking patterns of spliced specimens. (a) Typical crack propagation. (b) Cracking patterns at failure.

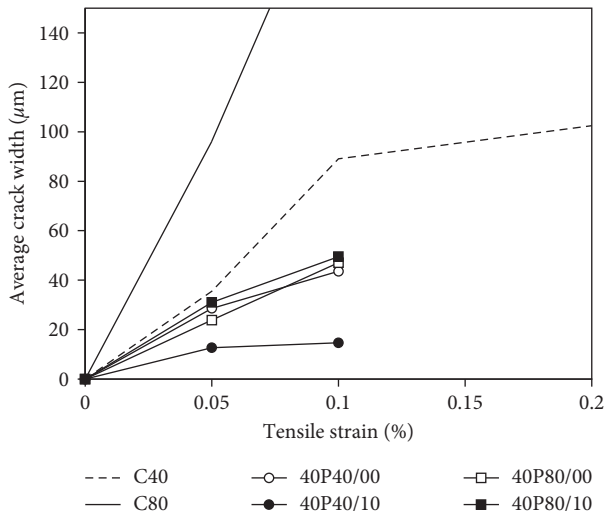


FIGURE 5: Average crack widths in lap splice for the specimens with 40% l_d .

radically after 1 day. This tendency can be observed especially for specimens P40 and P80 in Figure 3.

The SHCC mixtures containing the expansive admixture exhibited greater compressive strength than those without the expansive admixture. Among those mixtures, the high-strength PE-SHCC mixture had a relatively high increasing rate of compressive strength with the presence of the expansive admixture.

All of the tensile specimens of the PE-SHCC mixture exhibited over 1% strain at maximum loading, and microcracks were distributed throughout the specimens. With respect to the presence of the expansive admixture, the tensile strength of the normal-strength PE-SHCC mixture increased, but the strain capacity decreased at the maximum stress level. Conversely, the tensile strength of the high-strength PE-SHCC mixture decreased with the addition of the expansive admixture, and the mixture showed relatively ductile behavior.

Ductile behavior was also observed in the high-strength mixtures, similar to the PE-SHCC mixture, without any significant change in tensile strength. The expansion of the high-strength PE-SHCC mixtures that contained the expansive admixture adverse effect on ductility caused low tensile strength.

3.2. Cracking Pattern and Failure Character. Figure 4(a) shows the crack propagation patterns for each load stage of the specimens with the high-strength PE-SHCC mixture. For the specimen C80, the first crack was presented at the end of spliced reinforcement, and the maximum load was reached without forming any new cracks. Finally, the splitting cracks were developed rapidly at failure. Several hairline cracks form along the spliced region in the specimens 40P80/0 and 40P80/10 after presenting initial cracks because of the increment of tensile strength. The strength and deformation capacity along the spliced region tends to be increased significantly.

In particular, forming initial cracks was delayed in the specimen containing 10% of an expansive admixture (40P80/10), and the cracks were distributed widely as similar as that for the dumbbell-shaped specimen in the PE-SHCC mixture. This phenomenon was remarkable in the high-strength specimen with design compressive strength of 80 MPa containing the relatively large amount of cement.

Figure 4(b) shows typical crack patterns at failure of the specimens for this study. The crack widths were measured using a microscope with 60 magnifications. The average crack widths were computed by measuring all the cracks at each level of deformation.

Figure 5 presents the average crack widths that correspond to the tensile strain of the reinforcement in the splice zones of the concrete and SHCC mixtures. The average crack widths of the SHCC specimens are 50% smaller than those of the concrete specimens. For the specimens that contained SHCC, the crack widths of the specimens with normal strength are wider than those of the specimens with high strength, whereas for the control specimens, the crack width of the high-strength concrete specimen (C80) is wider than that of the specimen with conventional concrete strength (C40). Table 5 indicates that the tensile strength and strain levels of the high-strength specimens are lower than those of the normal-strength specimens, which results in fewer instances of crack formation and development.

Figure 5 also shows that large splitting cracks, which are due to the bond failure in a splice region, were observed for the high-strength specimens. However, many vertical microcracks subsequently transformed to splitting cracks in the normal-strength specimens.

The polyethylene fiber is shown to perform well to control microcracking as well as low strength and large deformations. The cracks of the PE-SHCC specimens were fewer in number and less wide due to the presence of the expansive admixture.

3.3. Tensile Performance in Lap Splice Zone. Figure 6 presents the tensile stress-strain relationship in the lap splice zone when the specimens were subjected to monotonic and cyclic loading. The figure also includes the material properties of the reinforcement (D16). The experimental results are summarized in Table 5 and include (1) tensile strength, (2) tensile strain, (3) average crack width at 0.2% tensile strain, and (4) average bond strength (u) determined by summing the forces parallel to the reinforcement axis, assuming that the bond stress levels are distributed uniformly over this length [3], as follows:

$$u_{\text{avg}} = \frac{f_s \cdot d_b}{4 \cdot L_s}, \quad (1)$$

where d_b is the nominal diameter of the reinforcement, L_s is the splice length, and f_s is the stress of the spliced reinforcement at failure.

Similar initial cracking strength levels were obtained for all the specimens. The tensile strength of the SHCC specimens for Class B in the ACI 318 specifications exceeded the 50% yield strength of the reinforcement (264 MPa). This

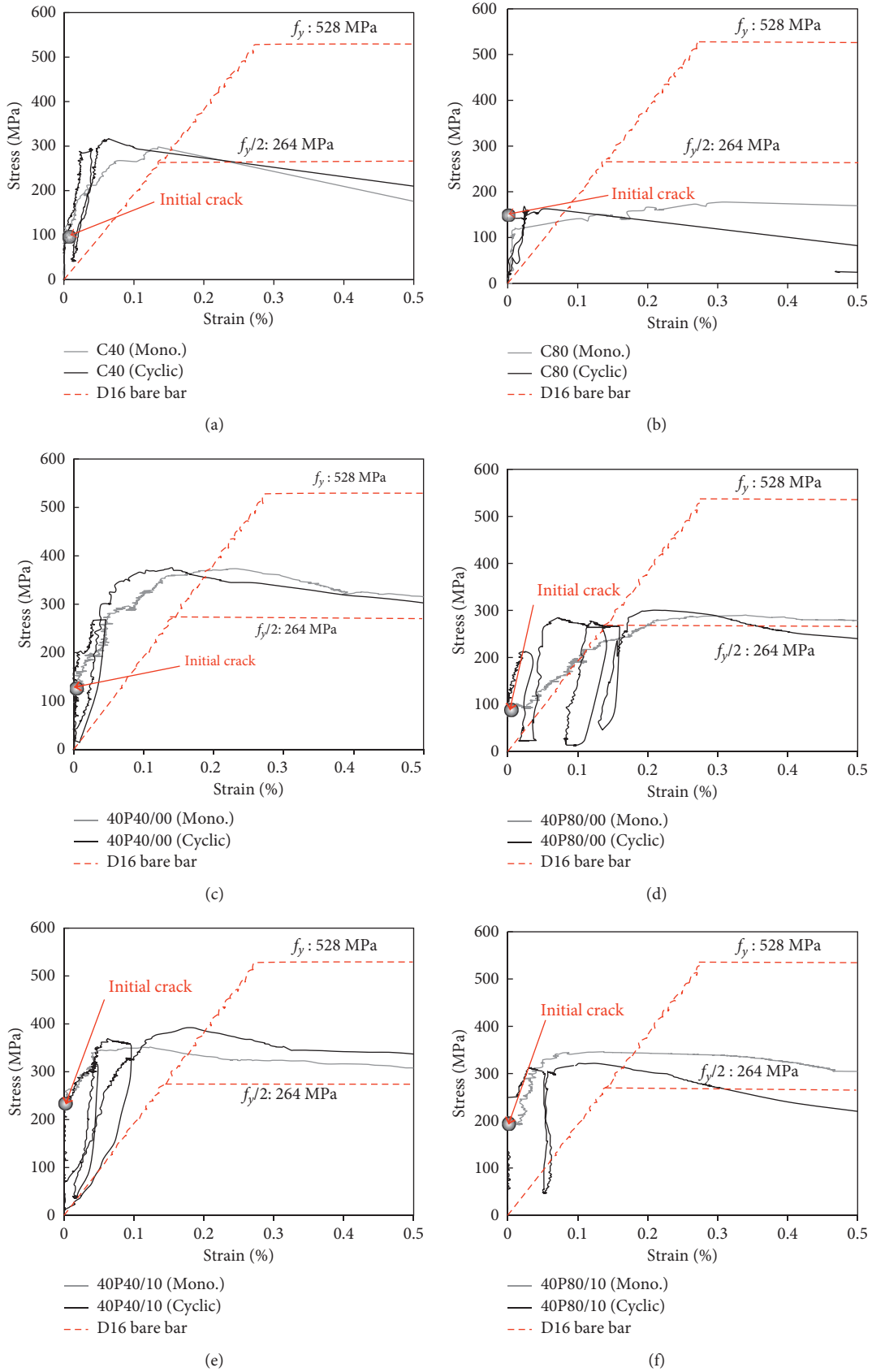


FIGURE 6: Continued.

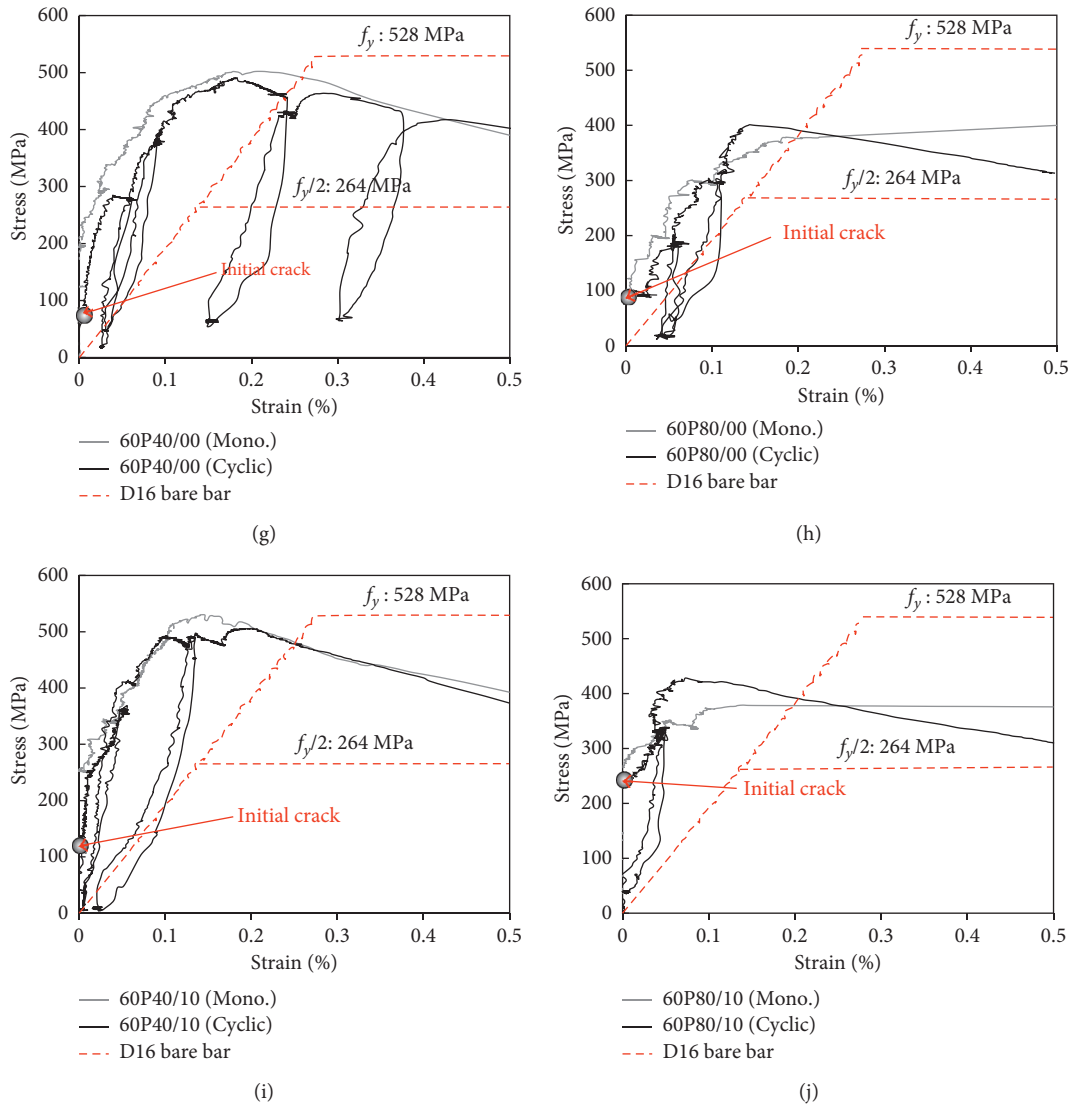


FIGURE 6: Tensile responses of lap splice specimens. (a) C40. (b) C80. (c) 40P40/00. (d) 40P80/00. (e) 40P40/10. (f) 40P80/10. (g) 60P40/00. (h) 60P80/00. (i) 60P40/10. (j) 60P80/10.

result indicates that 60% of the lap splice length required by the ACI code equation can be used safely.

The tensile strength in the lap splice region for the high-strength SHCC specimens was 10% lower than for the normal-strength SHCC specimens. Azizinamini [16] reported that the bond strength between a concrete surface and the reinforcement does not increase, even if the lap splice length increases with compressive concrete strength above 70 MPa. Therefore, the high-strength SHCC specimens used in this study (80 MPa) have a similar result in which the concrete and SHCC mixtures did not contribute significantly to the tensile strength in the splice region. In addition, Kaklauskas et al. [17] reported that the cracking resistance can be reduced by the shrinkage-induced stresses in the concrete due to the restraining action of bar reinforcement. In this study, the early age shrinkage within 24 hours of the high-strength SHCC specimens was greater

than that of the normal-strength SHCC specimens. This outcome led to shrinkage cracking in the cement matrix, which then affected the cracking resistance in the splice region.

Substituting the expansive admixture in the PE-SHCC mixture increased the tensile strength and initial stiffness under monotonic loads and cyclic loads. In particular, the stiffness of the high-strength SHCC specimens substantially increased more than for the normal-strength SHCC specimens. This outcome is due to the characteristic nature of expansive admixture in high-strength SHCC specimens, whereby initial cracking is controlled and stress is redistributed [15].

Figure 7 presents the role of cement composites as part of the tensile strength development in the splice region for each specimen subjected to axial tensile force. The tensile strength of the cement composites was computed by subtracting the

TABLE 5: Experimental test results.

Specimen ID	Initial cracking		Tensile strength (MPa)	Tensile strain (%)	Average crack width at 0.1% tensile strain (μm)	Average bond strength by (1) (MPa)
	Strength (MPa)	Strain (%)				
C40	95	0.008	316	0.06	89	2.69
C80	149	0.002	168	0.06	214	2.72
40P40/00	125	0.003	375	0.83	43	7.67
40P40/10	235	0.002	391	1.78	14	8.10
40P80/00	89	0.005	316	2.13	47	11.80
40P80/10	196	0.002	321	0.50	49	10.76
60P40/00	73	0.005	491	0.18	43	8.24
60P40/10	124	0.001	506	0.20	25	7.76
60P80/00	89	0.003	401	0.14	34	11.54
60P80/10	240	0.002	428	0.07	29	13.76

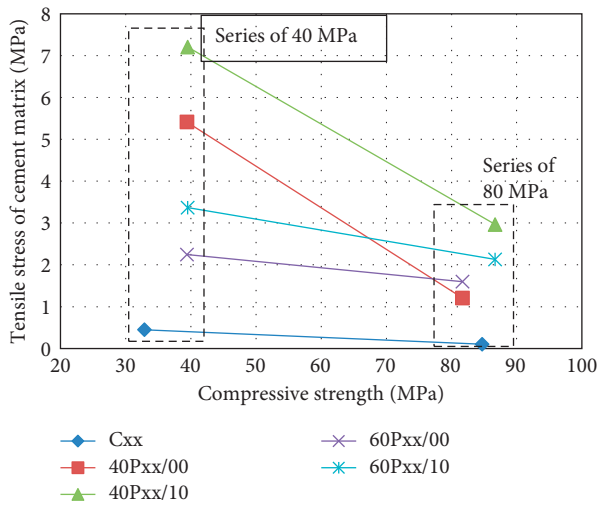


FIGURE 7: Tensile stress of cement matrix in lap splice specimens.

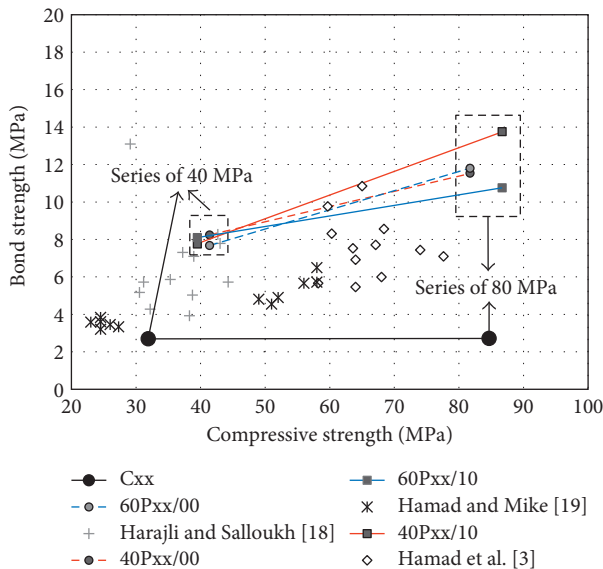


FIGURE 8: Bond strength of lap splice reinforcement [3, 18, 19].

tensile strength of the reinforcement (D16) from the tensile strength of each specimen.

The concrete specimens shown in Figure 7 are seen to contribute slightly only to the tensile strength of the reinforcement. For the SHCC specimens, however, the tensile strength levels of the SHCC mixtures in the splice region are over three times that of the concrete. The tensile stress levels of the cement matrix in the normal-strength SHCC mixtures are 30% higher than in the high-strength SHCC mixtures. Substituting the expansive admixture increased the tensile stress of the SHCC in the splice region. Furthermore, the use of cement composite enhanced the tensile strength of the specimens, which then led to improvement in terms of strength and deformation. The reduced spliced length, as opposed to the length recommended by the ACI specifications, was able to ensure the required tensile strength.

3.4. Bond Stress. Figure 8 presents a comparison between the bond strength and compressive strength of each specimen. The bond strength in the splice region increases as the compressive strength increases [1].

This study found that the bond strength slightly increases when an expansive admixture is substituted into the mix. Replacement with expansive admixture induces the reduction of shrinkage cracking and redistributes the tensile stress in the specimen, which serves to improve the compressive strength as well as the bond performance in the splice zone.

4. Conclusions

In order to evaluate the feasibility of the reduced lap-spliced length in the PE-SHCC mixture, direct tensile tests were performed for SHCC mixtures with lap-spliced lengths that were 40% and 60% shorter than those recommended in the ACI provisions. The following results have been obtained.

Initial cracking, stress, stiffness, and maximum strength levels increased due to the substitution of the expansive admixture into the SHCC mixtures. The tensile performance

in the lap splice region of the high-strength SHCC mixtures was worse than that of the normal-strength SHCC mixtures. The PE-SHCC mixture effectively controlled macrocracks so that the stress was distributed and numerous microcracks developed throughout the specimens. This behavior was evident in the specimens that contained the expansive admixture, which is used to control initial cracks. Moreover, the direct tensile test results show that the tensile strength values of all the SHCC specimens were above the allowable stress level for Class B splices and also show steady strength reduction and ductile behavior after reaching maximum strength.

Conflicts of Interest

The authors declare that there are no conflicts of interests regarding the publication of this paper.

Acknowledgments

This work was supported by the Energy Research & Development of the Korea Institute of Energy Technology Evaluation and Planning (KETEP) grant funded by the Korea Government Ministry of Trade, Industry & Energy (No. 20161120200190).

References

- [1] J. Zuo and D. Darwin, "Splice strength of conventional and high relative rib area bars and high strength concrete," *ACI Structural Journal*, vol. 97, no. 4, pp. 630–641, 2000.
- [2] S. Yazici, G. Inan, and V. Tabak, "Effect of aspect ratio and volume fraction of steel fiber on the mechanical properties of SFRC," *Construction and Building Materials*, vol. 21, no. 6, pp. 1250–1253, 2007.
- [3] B. S. Hamad, M. H. Harajli, and G. Jumaa, "Effect of fiber reinforcement on bond strength of tension lap splices in high-strength concrete," *ACI Structural Journal*, vol. 98, no. 5, pp. 638–647, 2001.
- [4] L. Yerex, T. H. Wenzel, and R. Davies, "Bond strength of mild steel in polypropylene fiber reinforced concrete," *ACI Journal Proceedings*, vol. 82, no. 1, pp. 40–45, 1985.
- [5] M. H. Harajli, B. S. Hamad, and A. A. Rteil, "Effect of confinement on bond strength between steel bars and concrete," *ACI Structural Journal*, vol. 101, no. 5, pp. 595–603, 2004.
- [6] N. Ganesan, P. V. Indira, and M. V. Sabeena, "Bond stress slip response of bars embedded in hybrid fibre reinforced high performance concrete," *Construction and Building Materials*, vol. 50, no. 15, pp. 108–115, 2014.
- [7] S. Yazici and H. S. Arel, "The effect of steel fiber on the bond between concrete and deformed steel bars in SFRCs," *Construction and Building Materials*, vol. 40, pp. 299–305, 2013.
- [8] S. J. A. Hosseini, A. B. A. Rahman, M. H. Osman, A. Saim, and A. Adnan, "Bond behavior of spirally confined splice of deformed bars in grout," *Construction and Building Materials*, vol. 80, pp. 180–194, 2015.
- [9] D. Darwin and E. K. Graham, "Effect of deformation height and spacing on bond strength of reinforcing bars," *ACI Structural Journal*, vol. 90, no. 6, pp. 646–657, 1993.
- [10] B. S. Hamad and M. S. Itani, "Bond strength of reinforcement in high-performance concrete: the role of silica fume, casting position and super plasticizer dosage," *ACI Materials Journal*, vol. 95, no. 5, pp. 499–511, 1998.
- [11] A. El-Azab, H. M. Mohamed, and A. Farahat, "Effect of tension lap splice on the behavior of high strength self-compacted beams," *Alexandria Engineering Journal*, vol. 53, no. 2, pp. 319–328, 2014.
- [12] R. H. Haddad, R. J. Al-Saleh, and N. M. Al-Akhras, "Effect of elevated temperature on bond between steel reinforcement and fiber reinforced concrete," *Fire Safety Journal*, vol. 4, no. 5, pp. 334–343, 2008.
- [13] G. Fischer and V. C. Li, "Influence of matrix ductility on tension-stiffening behavior of steel reinforced engineered cementitious composites (ECC)," *ACI Structural Journal*, vol. 99, no. 1, pp. 104–111, 2002.
- [14] V. C. Li, S. Wang, and C. Wu, "Tensile strain-hardening behavior of polyvinyl alcohol engineered cementitious composites (PVAECC)," *ACI Materials Journal*, vol. 98, no. 6, pp. 483–492, 2001.
- [15] W. C. Choi and H. D. Yun, "Effect of expansive admixtures on the shrinkage and mechanical properties of high-performance fiber-reinforced cement composites," *Scientific World Journal*, vol. 2013, Article ID 418734, 11 pages, 2013.
- [16] A. Azizinamini, R. Pavel, E. Hatfield, and S. K. Ghosh, "Behavior of lap-spliced reinforcing bars embedded in high-strength concrete," *ACI Structural Journal*, vol. 96, no. 5, pp. 826–835, 1999.
- [17] G. Kaklauskas, V. Gribniak, D. Bacinskas, and P. Vainiunas, "Shrinkage influence on tension stiffening in concrete members," *Engineering Structures*, vol. 31, no. 6, pp. 1305–1312, 2009.
- [18] M. H. Harajli and K. A. Salloukh, "Effect of fibers on development/splice strength of reinforcing bars in tension," *ACI Structural Journal*, vol. 94, no. 4, pp. 317–324, 1997.
- [19] B. S. Hamad and J. A. Mike, "Experimental investigation of bond strength of hot-dip galvanized reinforcement in normal- and high-strength concrete," *ACI Structural Journal*, vol. 100, no. 4, pp. 465–470, 2003.

Research Article

Air-Cured Fiber-Cement Composite Mixtures with Different Types of Cellulose Fibers

Ali Murat Soydan ¹, Abdul Kadir Sari,² Burcu Duymaz,² Recep Akdeniz,² and Bahadır Tunaboğlu³

¹Gebze Technical University, Institute of Energy Technologies, Gebze, Turkey

²Department of Materials Science and Engineering, Gebze Technical University, Gebze, Turkey

³Department of Industrial Engineering, Istanbul Sehir University, Dragos Kampusu Orhantepe Mahallesi, Turgut Ozal Bulvarı, No. 21, Dragos, Kartal, Istanbul, Turkey

Correspondence should be addressed to Ali Murat Soydan; asoydan@gtu.edu.tr

Received 24 August 2017; Revised 31 October 2017; Accepted 9 November 2017; Published 28 January 2018

Academic Editor: Rishi Gupta

Copyright © 2018 Ali Murat Soydan et al. This is an open access article distributed under the Creative Commons Attribution License, which permits unrestricted use, distribution, and reproduction in any medium, provided the original work is properly cited.

This present study was carried out to check the feasibility of different cellulose fibers obtained from cropped virgin cellulose, bleached eucalyptus, and araucaria pulps through different new environmentally friendly curing processes for fiber-cement production. The aim is to introduce the different sources of cellulose fibers with lower cost to produce the “fiber-cement without autoclave” (FCWA). The slurries used in the experiments contain approximately 8% wt. of cellulose. The influence of the waste marble powder addition to the cement mixture was also studied. The physical and mechanical properties of the products which were prepared with this method under different curing conditions were investigated. The mechanical properties of eucalyptus cellulose appear to offer the best combination, especially after longer air-cure cycles. The results showed that the production of FCWA is very economical by using waste marble powders. And moreover, two new types of cellulose fibers (eucalyptus and araucaria celluloses; EuC and ArC, resp.), which provide a better density and packing in the fiber-cement leading to better modulus of rupture (MOR) and modulus of elasticity (MOE) values as virgin cellulose (ViC), are very usable for production of the fiber-cement in industrial scale.

1. Introduction

Cellulosic fibers contribute to the development of high-quality fiber-reinforced cement composites [1–4]. Fiber-reinforced cement (FC) is used in a wide range of applications from building facade cladding systems to advertising and promotional and decorative applications, and it is becoming increasingly common throughout the day. Information on the use of natural fibers as reinforcements in composites has increased in the 2000s [5, 6]. Natural fiber-based fiber-cement sheets are used in all kinds of interior and exterior coverings. Flat-shaped and wooden-patterned fiber-cement panels are hardened in autoclaves. FC products are produced in two different production methods in the industry. The first method is hardening with high pressure and temperature in autoclaves, and the other one is in nonautoclave systems. The

fiber-cement produced by nonautoclave systems has been termed as “fiber-cement without autoclave” (FCWA). Prescription to be used in production of FC: there are two different curing methods. First one is air/humid curing, and the other curing is at high-temperature and high-pressure conditions in autoclaves [7]. Autoclave production method is well known across the world, and commercially, they are widely used in the construction industry [8]. When producing FCWA, the synthetic PVA (polyvinyl-alcohol) fibers are generally used due to increasing distortion and abrasion resistance [9]. PVA fibers have been used in dramatically low amounts, <1% in this study, as compared to the content of total cellulosic fibers. Environmentally friendly cellulosic fibers, derived from renewable materials, are produced with a low-cost fiber-cement production method, air-curing in this study. General practice, however, involves

use of autoclaves, processing at high temperatures which increases cost in manufacturing of fiber-cement.

Wood fibers have many advantages such as nonhazardous, relatively low costs, biodegradability, renewability, and recyclability. They are also widely used in cementitious composites due to easy manufacturing process [10]. Wood fibers are examined in two categories such as softwood and hardwood fibers, which have long and short length, respectively. Characteristically, eucalyptus as a hardwood fiber has short fiber length and is dispersed better than pinus which is known as a softwood fiber with long fiber length in the sludge matrix and contains more cellulose fibers per unit volume [10, 11]. Therefore, the amount of paper clay obtained from one gram of softwood fiber is greater than the amount of paper clay obtained from one gram of hardwood fiber [12]. Eucalyptus can be used to produce the FCWA materials which are cheaper than other fiber cements in the market, and raw materials are easily available. FCWA is harmless since it contains renewable materials [13].

FC materials offer several advantages compared to conventional construction materials. These advantages are widespread resource availability, high fiber strength, advanced fiber extracting technology, and relatively low cost [14]. The primary problem in the production of the fiber cement by air-cured nonautoclave system is the increase of the material and manufacturing costs [15]. The most important reasons for the increase of the production cost in the conditions of Turkey are the high cost of virgin cellulose (ViC) used as raw material and autoclave costs. In this study, eucalyptus and araucaria celluloses (EuC and ArC, resp.), which are cheaper than relatively virgin cellulose, were produced without autoclaving in order to reduce the cost of raw materials. The characteristics of the produced FCWA products were also compared. PVA is used in minimal proportions, and its strength contribution is assumed by other fibers in the system.

2. Experimental

2.1. Materials. Three different types of American (Brazilian and Canadian) and European (Spaniard, Portuguese, and Swedish French) fibers were selected to produce the fiber-cement materials. Virgin, eucalyptus, and araucaria celluloses (ViC, EuC, and ArC) were used in this study as different cellulose sources. And the recycling water (pH = 13) was used to prepare the mixture. The virgin, eucalyptus, araucaria celluloses, and PVA fibers were supplied by Cellulose Lerox International, Kombassan, and Kordsa. Powder materials such as cement CEM I 42.5 R and waste marble powder (WMP) were supplied by Cimsa and Durmus Mermer which is a producer in the Bilecik region.

2.2. Characterization of the Raw Materials. The chemical analysis of the raw materials, cement, and waste marble powders used in the experiments was performed by XRF analysis. Particle size and distribution of the raw materials were measured by Mastersizer from Malvern Instrument. The specific surface area (SSA) of the raw materials was determined by Quanta Chrome Autosorb 1B using the nitrogen adsorption BET method. The structure and morphology of the raw

materials, fibers, and products were investigated using a Philips XL30 SFE scanning electron microscope (SEM). Samples were dried first and then coated with gold. Each sample was examined with the SEM at different magnifications. The crystal structure of the materials was identified by X-ray diffraction (XRD) recorded on a Rigaku Dmax 2200 diffractometer using Cu-K α radiation with a characteristic wavelength of $\lambda = 1.5406 \text{ \AA}$ ($2\theta = 10\text{--}80^\circ$) at room temperature.

2.3. The Properties and Microstructural SEM Analysis of the Raw Materials: Fibers, Cement, and Waste Marble Powders. The chemical XRF analysis of the cement material and waste marble powders (WMPs) is shown in Table 1. WMP contains CaO as main phase only, but the cement contains the main phases CaO (63.50%), SiO $_2$ (19.35%), and Al $_2$ O $_3$ (4.74%). The XRD analysis results of WMP and the cement material, shown in Figure 1, are in accordance with the XRF analysis (Table 1). This means that WMP consists of calcium carbonate, and the used cement materials consist of calcium silicate, aluminium silicate, and alumina as crystalline phase.

Particle size and size distribution analysis of WMP and cement is given in Figure 2. The median sizes (d_{50}) of the cement and WMP were measured as $16.08 \mu\text{m}$ and $5.52 \mu\text{m}$, respectively, as shown in Figure 2. The measuring results of the specific surface area of the cement and WMP are $1.23 \text{ m}^2\cdot\text{g}^{-1}$ and $2.17 \text{ m}^2\cdot\text{g}^{-1}$, respectively. It is an expected result that the cement material with large grain size has a specific surface area less than WMP.

The SEM images of the CEM I 42.5 R cement from Cimsa and PVA fibers from Kordsa used in the experiments are shown in Figures 3(a) and 3(b). The scaled SEM images of the natural fibers, papers, and pulps according to the cellulose types were taken to determine the structure and diameters of natural fibers (ViC, EuC, and ArC) as shown in Table 2. The diameters of the natural fibers (ViC, EuC, and ArC) and also the average diameters/thickness were determined as shown in Table 3. Table 4 shows the measured freedom degrees of natural fibers (ViC, EuC, and ArC). Moisture measurements of powder materials, PVA, and all kinds of fibers were determined using a moisture analyzer. The results are shown in Table 5.

3. Preparation of the Samples

Different ratios of fiber have been tried in the prescription. The fiber ratio was tried between 2 and 12% and optimized to 8% [16]. The ratio of water used is between 25 and 40% in many concrete works. The water/cement ratio is optimized to 30%, and these ratios were used in these experiments [17]. The cellulose pulps, PVA, cement, waste marble powder (WMP), and recycling water with the pH value of 13 were used in the desired proportions as shown in Table 6 to prepare the FCWA slurry used for the production of the fiber-cement composite materials in the experiments.

First step of the production is preparing mixture of the fiber-cement sludge. After that, the sludge is poured into the vacuum box. The excess water in the slurry is discharged out of the press with the help of vacuum pump. Following the

TABLE 1: XRF analysis of powder materials.

Number	Component	Cement	WMP
1	Na ₂ O	0.38	—
2	MgO	1.88	1.69
3	Al ₂ O ₃	4.74	—
4	SiO ₂	19.35	0.27
5	P ₂ O ₅	0.08	—
6	SO ₃	2.72	—
7	K ₂ O	0.53	—
8	CaO	63.50	54.27
9	TiO ₂	0.36	—
10	Cr ₂ O ₃	0.11	—
11	MnO	0.08	—
12	Fe ₂ O ₃	3.29	0.22
13	LOI	3.01	43.55

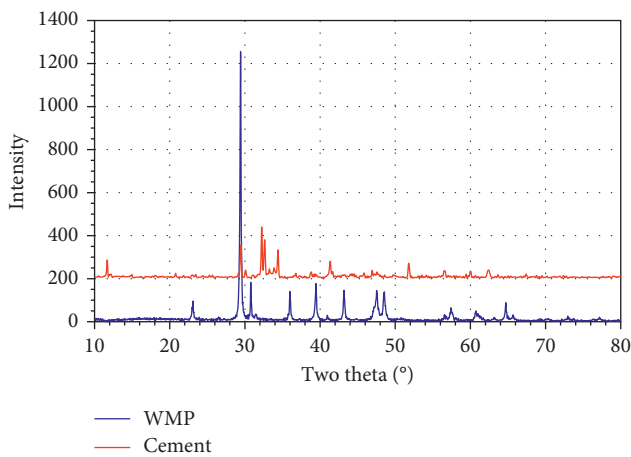


FIGURE 1: XRD analysis of the raw materials.

vacuuming process, the fiber-cement samples are placed in the press machine and compressed with a pressure of 7 MPa for 120 seconds. Thus, 10 specimens were produced for each fiber type. Figure 4 shows the flow chart of the fiber-cement production. All prepared samples were cured in the air by itself. However, the samples were allowed to cure after curing the samples at 30°C for 6 hours in order to maintain the stability of each sample.

4. Tests on the Materials: Freeness Test

The degree of freedom is defined as the measurement of the drainage rate at the discharge of the wood pulp suspension (3 g of pulp in 1 L of water). The drainage rate and the degree of freedom help determine the behavior of the fibers in the cement matrix or determine the fiber elasticity of the fibers or fine particle content of the fiber. According to the results of the measurements, stock preparation depends on the temperature, surface properties, and water quality [18, 19]. It is often referred to as Canadian Standard Freedom (CSF) because it was developed by the Canadian Cellulose and

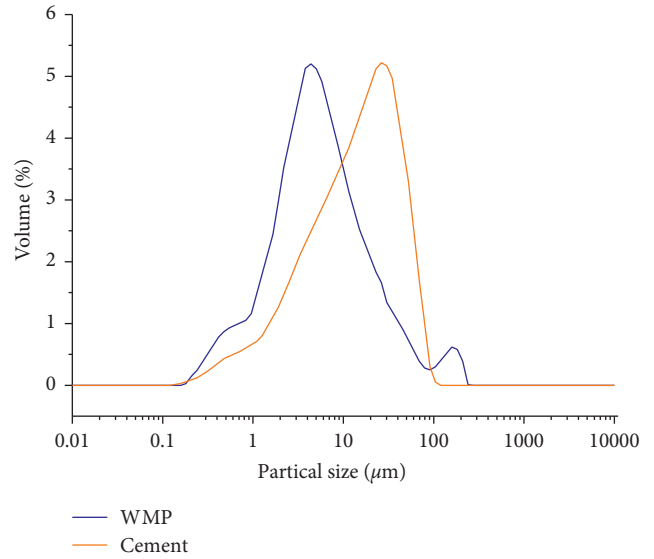
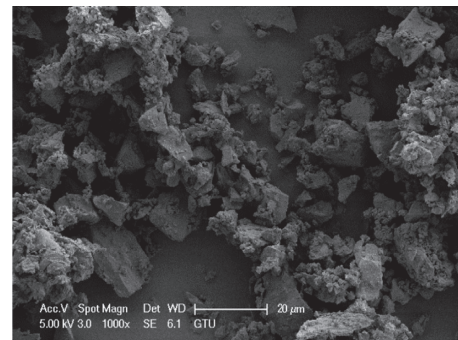
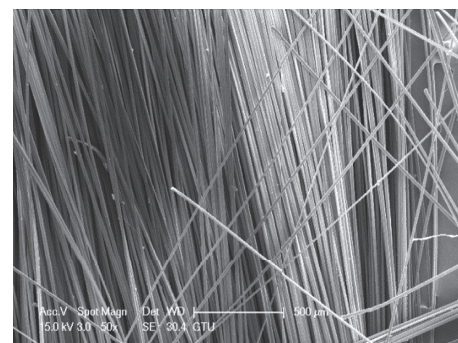


FIGURE 2: Particle size distribution of cement (Cimsa) and waste marble powder (Durmus Mermer).



(a)

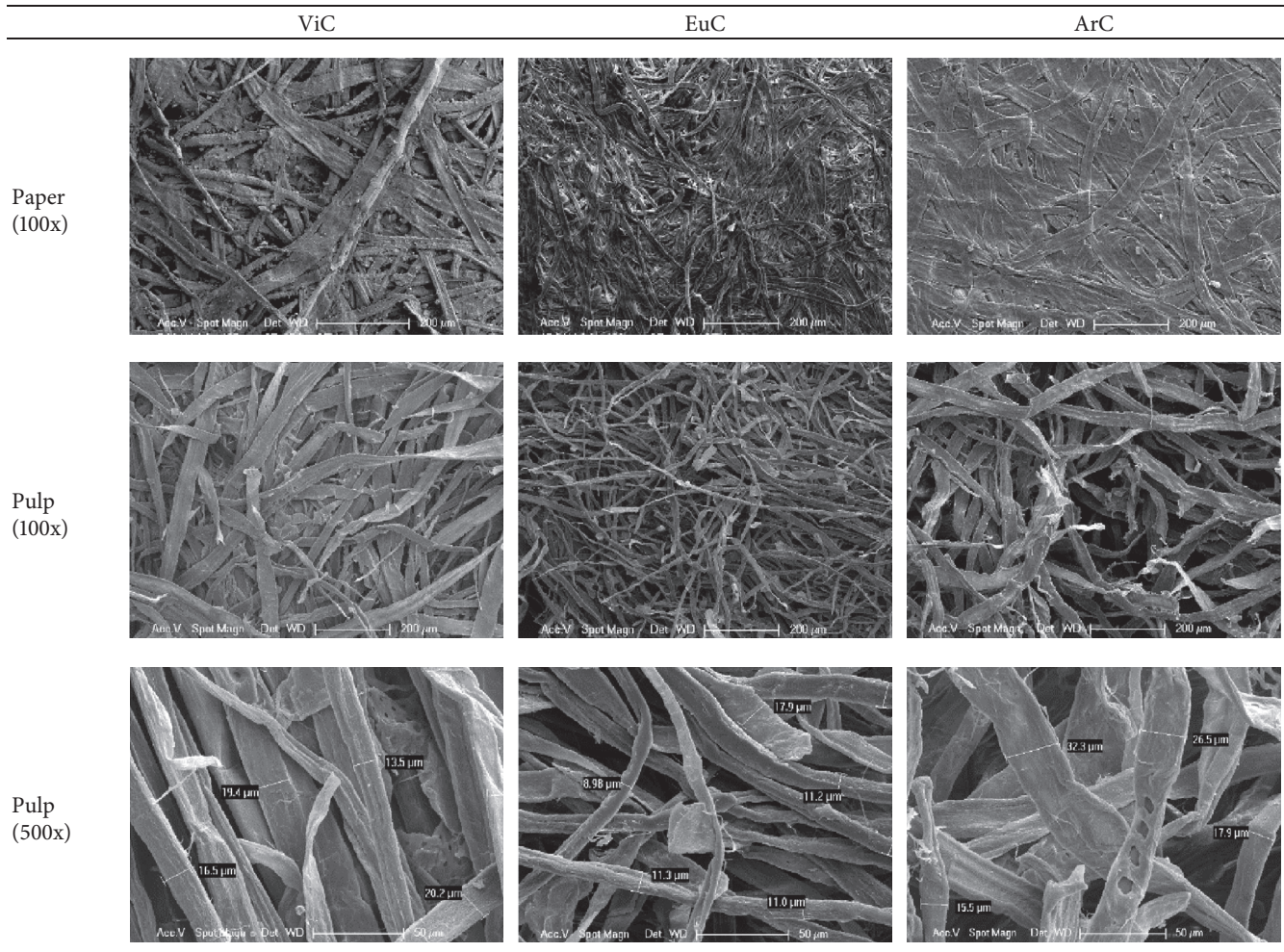


(b)

FIGURE 3: SEM micrographs of CEM 1 42.5 R cement (a) and of PVA fibers (b).

Paper Research Institute [18, 19]. Figure 5 shows a test machine according to the CSF. The freeness degree of celluloses pulp such refined fibers as ViC, EuC, and ArC was measured using a CSF, according to ISO 5257/2. In this study, the degree of freedom and drying rate of ViC, EuC, and ArC are measured.

TABLE 2: SEM micrographs of papers and pulps according to the cellulose types.



5. Tests on the Materials: Three-Point Bending, Strain-Stress Test

The effects of the fiber-cement produced without autoclaving on the physical and mechanical properties of all three fiber types were investigated. All fiber types were used 8% wt. in the mixtures to investigate differences in fiber's physical properties. The modulus of rupture (MOR) and modulus of elasticity (MOE) were determined using the three-point bending configuration for the mechanical characterization of the produced fiber-cements. Tests were performed using the Intelli Jack 6 kN device. The equations required to calculate the modulus of rupture (MOR) and the modulus of elasticity (MOE) with the three-point bending configuration are given in (1). Five flexural specimens were tested for each composite formulation during the experiments:

$$\text{MOR (MPa)} = \left(\frac{L_{\text{Max}}}{b \cdot h^2} \right) \cdot (S_{\text{down}} - S_{\text{up}}),$$

$$\text{MOE (GPa)} = tg\alpha \cdot \left(\frac{L_{\text{Max}}}{\delta} \right) \cdot \frac{(S_{\text{down}} - S_{\text{up}})^3}{b \cdot h^3} \times 10^6, \quad (1)$$

TABLE 3: Fiber wideness according to SEM analysis.

	ViC	EuC	ArC	
Average thickness of cellulose (μm)	L_{Avr}	30.34	9.79	43.55
	L_{Max}	48.27	21.7	59.1
	L_{Min}	17.2	4.18	27.8

TABLE 4: Freeness of fibers.

Properties	ViC	EuC	ArC
Drainage rate	30–50	73	68
% drying rate	80 ± 2	94.1	93.52
% humidity	3.98	5.9	6.48

where L_{Max} is the maximum stress of the linear portion of the stress-strain curve, $(S_{\text{down}} - S_{\text{up}})$ is the major span, b and h are the specimen width and thickness, respectively, $tg\alpha$ is the initial slope of the stress-strain curve, and α is the deflection of the composite. The mechanical properties of the samples were measured 7, 15, and 28 days after the production of the sheet [9].

TABLE 5: Drying mass and humidity of components.

Samples	% drying mass	% humidity
PVA	97.2	2.8
Waste marble powder (WMP)	99.2	0.8
CEM 1 cement (Cimsa)	100	0.0

TABLE 6: Usage rates of raw materials.

Raw materials	Mass rate (%)
Celluloses (eucalyptus, araucaria, and virgin cellulose)	8.0
PVA	0.6
CaCO ₃ (reduce of marble powder)	31.4
Cement (Cimsa CEM I)	60

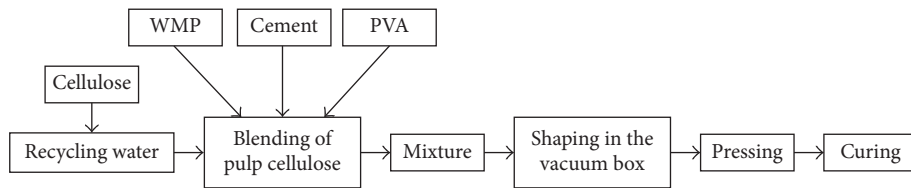


FIGURE 4: The production flow chart of fiber-cement sheets.

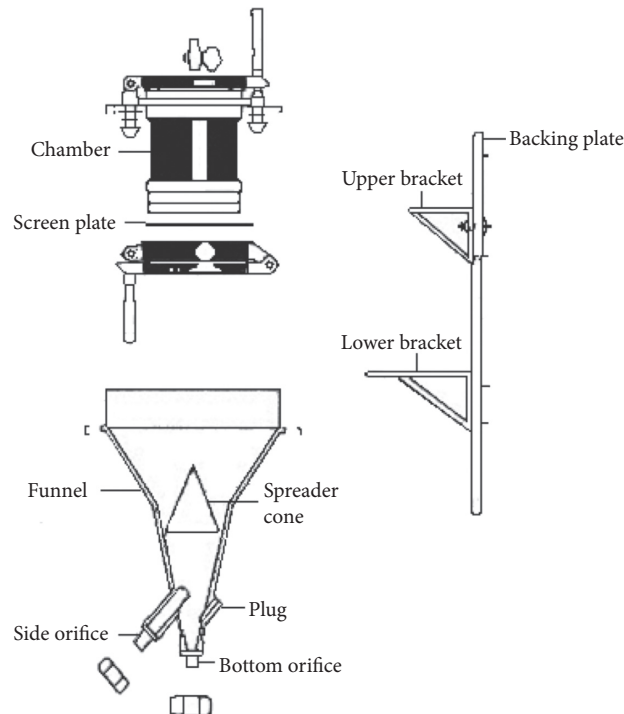
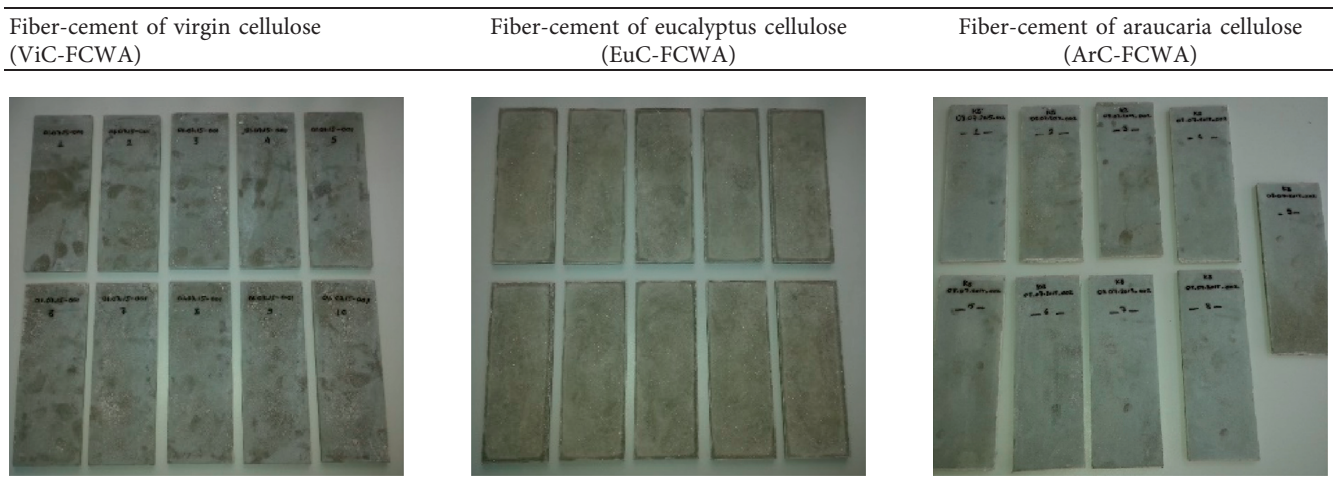


FIGURE 5: Freeness test machine [18].

TABLE 7: Nonautoclave products: ViC-FCWA, EuC-FCWA, and ArC-FCWA.



6. Tests on the Materials: Determination of Bulk Density and Water Absorption

Archimedes test was performed to determine the density of the produced samples. Their bulk density and water absorption values were measured. The samples were dried in the oven until their weight get stable and scaled first (W1). Thereafter, the samples were kept in the water for 48 hours and waited until they had not changed their weight and the samples get scaled in the water with the Archimedes scale (W2). The samples were taken out from water to determine their saturated weights (W3). The bulk density and water absorption values of the samples were determined by the following equations:

$$\text{Bulk density} = \frac{W1}{(W1 - W2)} \times 100, \tag{2}$$

$$\text{Water absorption \%} = \frac{(W3 - W1)}{W1} \times 100,$$

where W1 is the dried weight in the oven, W2 is the weight in water, and W3 is the saturated weight (the surface of the sample removed from the water is weighed in the air by wiping with a moist cloth).

7. Results and Discussion

The densities of the produced samples were measured: dry density is 1.4g/cm³ and saturated samples density is 1.8g/cm³ according to ASTM C1185 standard [13]. The dimensions of these fiber-cements produced in the laboratory are measured as 210 mm × 76 mm × 8 mm. Table 7 shows the plates of the produced fiber cements in the laboratory environment.

The effects of the fiber-cement produced without autoclaving on the physical and mechanical properties of all three fiber types were investigated. All fiber types were used 8% wt. in the mixtures to investigate differences in fiber's

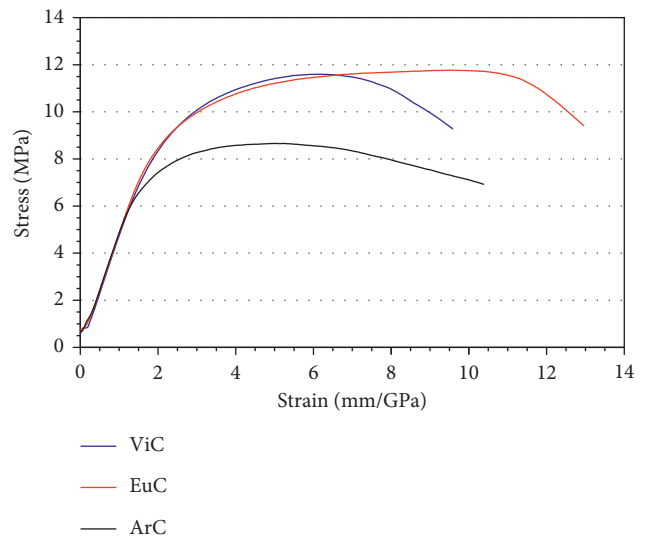


FIGURE 6: Stress-strain measure.

TABLE 8: Mechanical result of produced samples.

		ViC-FCWA	EuC-FCWA	ArC-FCWA
7-day results	MOR (MPa)	11.24	11.94	13.13
	MOE (GPa)	4.70	4.65	5.43
15-day results	MOR (MPa)	9.76	13.97	12.16
	MOE (GPa)	3.79	5.76	5.66
28-day results	MOR (MPa)	9.76	17.57	17.39
	MOE (GPa)	3.79	5.28	4.89

physical properties. Stress-strain measure graphic appears in Figure 6. It is seen that all fiber cements have the same stability under the strain up to 2 GPa. But, after 2 GPa, EuC and ViC have similar values of stress, while ArC has a lower value. EuC and ViC exhibit the same properties according to the stress-strain test. Stress-strain diagram is shown in Figure 6.

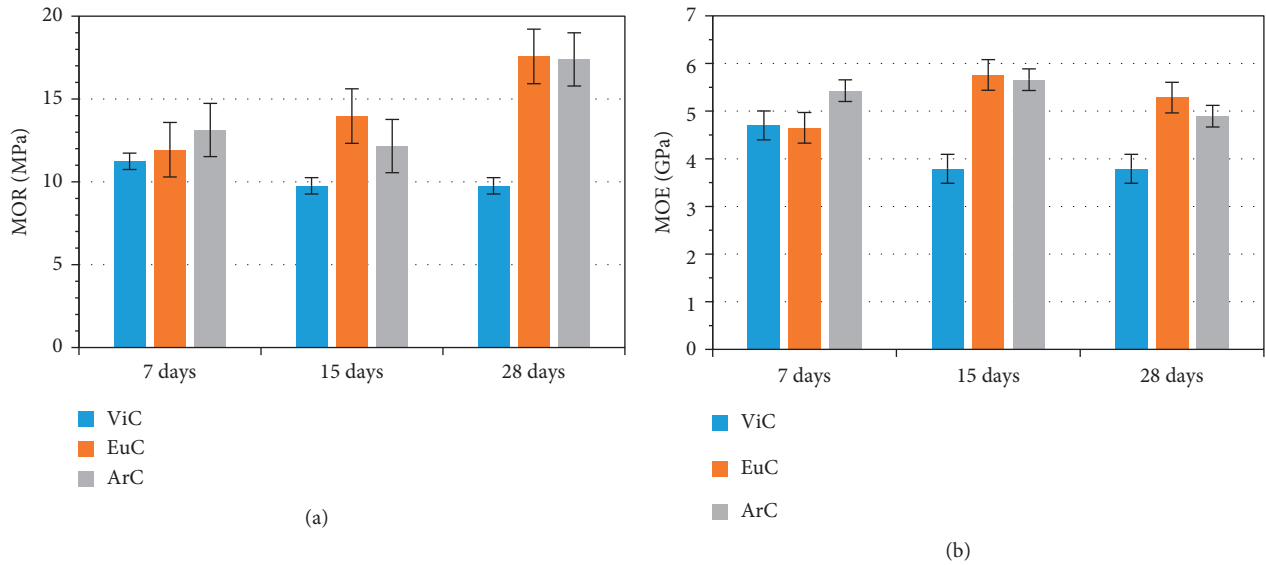
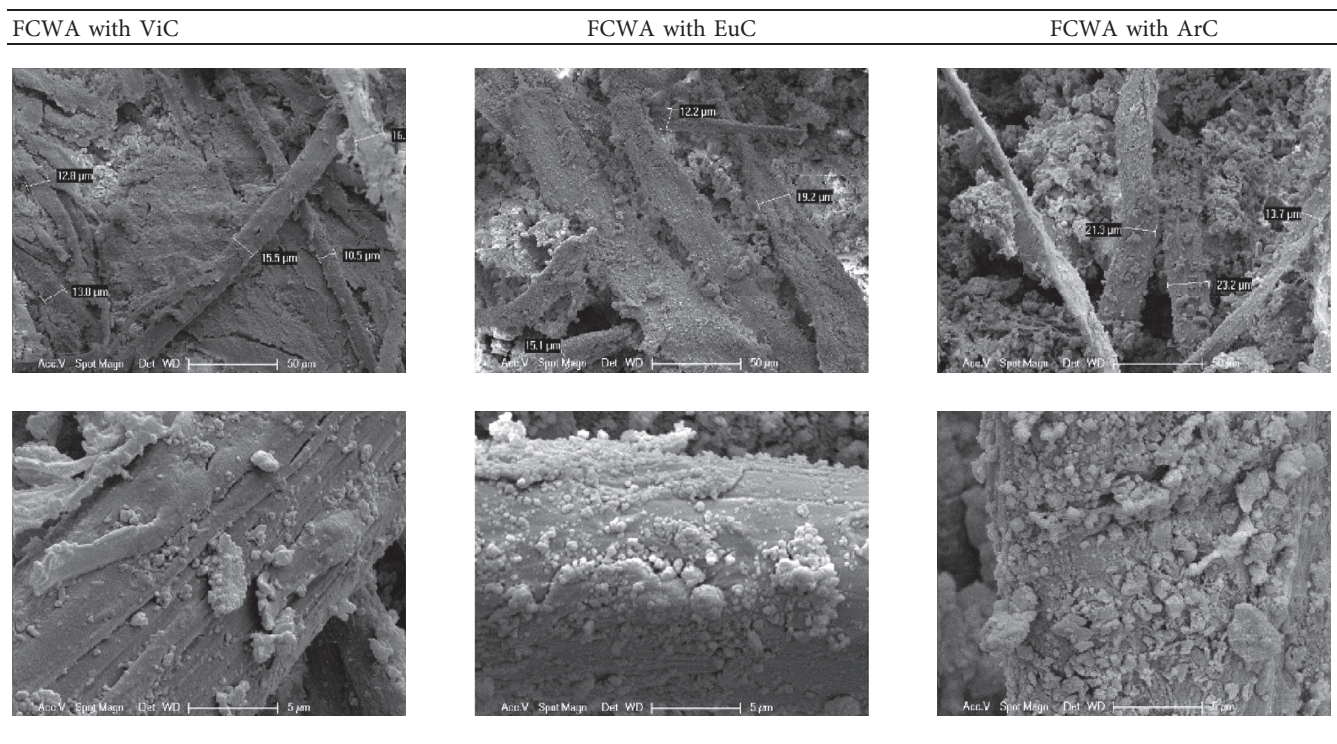


FIGURE 7: The mechanical properties of FCWA according to cellulose fiber type: (a) modulus of rupture and (b) modulus of elasticity.

TABLE 9: SEM images of the produced samples with magnification of 500x and 5000x.



In Table 8, mechanical property test results for samples cured for 7, 15, and 28 days are provided. It was observed that MOR and MOE values of the ViC-FCWA samples remained relatively constant, but a slight drop in properties was observed from 7-day to 15-day and 28-day processes. The rupture values of EuC-FCWA samples were observed to increase from 11.94 MPa, 13.97 MPa, and 15.57 MPa, with MOE values rising from 4.65 GPa to 5.76 GPa and stabilizes

at 5.28 GPa for 7-, 15-, and 28-day curing, respectively. The MOR values of ArC-FCWA samples were observed to be 13.13 MPa, 12.16 MPa, and 17.39 MPa for 7-, 15-, and 28-day curing, respectively. There was a significant improvement in the MOR value after the 28-day process. MOE values of ArC-FCWA samples were 5.43 GPa, 5.66 GPa, and 4.89 GPa, respectively. Figure 7 shows a graphical representation of the MOR and MOE values. There was an appreciable

TABLE 10: 28-Day results of FCWA products.

	ViC-FCWA	EuC-FCWA	ArC-FCWA
Humidity (%)	9.00	8.90	9.60
Bulk density (g/cm ³)	1.52	1.55	1.56
Water absorption (%)	14.00	14.62	14.89

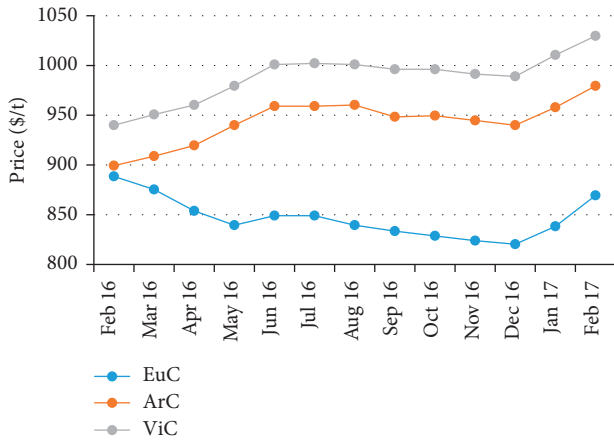


FIGURE 8: The tonnage cost of cellulose types.

improvement in MOR values as the cure duration increased in the process.

Microstructural analysis was performed on the specimens by taking SEM images of the produced fiber-cements. The morphology, size, and distributions of natural fibers are shown in Table 9. It has been observed that the cement and fibers have very good interaction, the fibers are homogeneously distributed in the matrix of the cement, and also the fibers have partly lamellar structure.

In Table 10, the bulk density of the ViC-FCWA sample was measured as 1.52 g/cm³, and the water absorption was 14%. The value for EuC-FCWA sample was 1.55 g/cm³, with the water absorption of 14.62%. The density value of ArC-FCWA sample was 1.56 g/cm³, while water absorption was 14.89%. The humidity of ViC-FCWA, EuC-FCWA, and ArC-FCWA was determined to be 9.0, 8.9, and 9.6, respectively.

In addition, the energy consumed by the autoclave in production increases the cost considerably. In this study, it has been shown that fiber-cement can be produced without autoclaving. However, this process increased the curing time of the products. According to the results of physical and mechanical tests, the properties of fiber-cement are mainly influenced by properties of the fibers. The mechanical strengths of eucalyptus and araucaria cellulose were found to be close to each other, which is considerably higher than virgin cellulose, for the cure time of 28 days. When comparing the desired properties with cost of the fiber-cement, the ones produced using eucalyptus will be more advantageous in terms of cost and mechanical performance. The cure optimization must be done based on different fiber types for optimal properties of fiber-cement products.

The biggest problem in fiber-cement technology is increasing material and manufacturing costs [15]. Approximately,

40% of the fiber-cement cost is the cellulose cost of the producers. The tonnage costs of cellulose in US dollars are shown in Figure 8 [20]. However, the cellulose prices may vary depending on the countries where they are produced and the logistics distance.

8. Conclusion

It was found from our studies that mechanical properties of FC produced using EuC and ArC are superior to ViC, especially after longer air-cure cycles. This study proposes more economical FCWA method and two new types of cellulose fibers for fiber-cement. It was believed that finer structures of EuC and ArC fibers compared to ViC provide a higher density and packing in the fiber-cement leading to better MOR and MOE values. EuC-reinforced fiber-cement offers the optimal solution in terms of shorter cure time and best mechanical properties. As a recommendation, it would be explanatory to try different curing conditions according to different fiber types.

Conflicts of Interest

The authors declare that there are no conflicts of interest regarding the publication of this paper.

Acknowledgments

The authors thank the staff members Adem Sen and Ahmet Nazım of Gebze Technical University for their assistance in their studies. The authors extend their thanks also to Uğur Arslan from Vefa Holding for his assistance during the experiments. The authors gratefully acknowledge Vefa Holding and A. Ş. Ekobord for their support.

References

- [1] R. Coutts, "Flax fibres as a reinforcement in cement mortars," *International Journal of Cement Composites and Lightweight Concrete*, vol. 5, no. 4, pp. 257–262, 1983.
- [2] R. Coutts and M. Campbell, "Coupling agents in wood fibre-reinforced cement composites," *Composites*, vol. 10, no. 4, pp. 228–232, 1979.
- [3] H. Savastano, P. G. Warden, and R. S. P. Coutts, "Brazilian waste fibres as reinforcement for cement-based composites," *Cement and Concrete Composites*, vol. 22, no. 5, pp. 379–384, 2000.
- [4] R. MacVicar, *Mechanical and Physical Changes Associated with Aging of Cellulose Fiber Reinforced Cement Composites*, National Library of Canada/Bibliothèque Nationale du Canada, Ottawa, Canada, 1997.
- [5] H. Savastano, S. Santos, M. Radonjic, and W. Soboyejo, "Fracture and fatigue of natural fiber-reinforced cementitious composites," *Cement and Concrete Composites*, vol. 31, no. 4, pp. 232–243, 2009.
- [6] F. de Andrade Silva, R. D. Toledo Filho, J. de Almeida Melo Filho, and E. de Moraes Rego Fairbairn, "Physical and mechanical properties of durable sisal fiber-cement composites," *Construction and Building Materials*, vol. 24, no. 5, pp. 777–785, 2010.

- [7] R. Coutts and P. Warden, "Air-cured, wood pulp, fibre cement composites," *Journal of Materials Science Letters*, vol. 4, no. 1, pp. 117–119, 1985.
- [8] R. S. P. Coutts, "Sticks and stones," *Forest Products News Letter*, vol. 2, no. 1, pp. 1–4, 1988.
- [9] J. A. Rabi, S. F. Santos, G. H. Tonoli, and H. Savastano Jr., "Agricultural wastes as building materials: properties, performance and applications," in *Agriculture Issues and Policies Series*, p. 219, Nova Science Publishers, Hauppauge, NY, USA, 2006.
- [10] M. Khorami and E. Ganjian, "Comparing flexural behaviour of fibre-cement composites reinforced bagasse: wheat and eucalyptus," *Construction and Building Materials*, vol. 25, no. 9, pp. 3661–3667, 2011.
- [11] G. Tonoli, H. Savastano, E. Fuente, C. Negro, A. Blanco, and F. R. Lahr, "Eucalyptus pulp fibres as alternative reinforcement to engineered cement-based composites," *Industrial Crops and Products*, vol. 31, no. 2, pp. 225–232, 2010.
- [12] O. Onuaguluchi and N. Banthia, "Plant-based natural fibre reinforced cement composites: a review," *Cement and Concrete Composites*, vol. 68, pp. 96–108, 2016.
- [13] R. MacVicar, L. Matuana, and J. Balatinecz, "Aging mechanisms in cellulose fiber reinforced cement composites," *Cement and Concrete Composites*, vol. 21, no. 3, pp. 189–196, 1999.
- [14] B. Mohr, N. El-Ashkar, and K. Kurtis, "Fiber-cement composites for housing construction: state-of-the-art review," in *Proceedings of the NSF Housing Research Agenda Workshop*, pp. 112–128, Orlando, FL, USA, 2004.
- [15] D. J. Merkley and C. Luo, "Fiber cement composite materials using cellulose fibers loaded with inorganic and/or organic substances," Google Patents, 2004.
- [16] A. Bentur and S. Mindess, *Fibre Reinforced Cementitious Composites*, CRC Press, Boca Raton, FL, USA, 2006.
- [17] R. Jarabo, E. Fuente, M. Monte, H. Savastano, P. Mutjé, and C. Negro, "Use of cellulose fibers from hemp core in fiber-cement production. Effect on flocculation, retention, drainage and product properties," *Industrial Crops and Products*, vol. 39, pp. 89–96, 2012.
- [18] TAPPI, *Freeness of Pulp (Canadian Standard Method), Testing Methods T 227 om-94*, TAPPI Press, Peachtree Corners, GA, USA, 1999.
- [19] International Organization for Standardization (ISO), "Determination of drainability part 2: "Canadian standard" freeness method," in *Paper, Board and Pulps*, ISO 5267-2, International Organization for Standardization, Geneva, Switzerland, 2001.
- [20] Monitor Paper & Packaging, 800-45-Great 237, pp. 1–15, 2017, <http://www.greatamerican.com>.

Research Article

Mechanical Properties and Durability of Latex-Modified Fiber-Reinforced Concrete: A Tunnel Liner Application

Joo-Ha Lee,¹ Hwang-Hee Kim,² Sung-Ki Park,² Ri-On Oh,² Hae-Do Kim,³ and Chan-Gi Park ⁴

¹Department of Civil Engineering, University of Suwon, Hwaseong 18323, Republic of Korea

²Research Center, Contecheng Co., Ltd., Seongnam 13636, Republic of Korea

³Rural Research Institute, Korea Rural Community Corporation, Ansan 15634, Republic of Korea

⁴Department of Rural Construction Engineering, Kongju National University, Yesan 32439, Republic of Korea

Correspondence should be addressed to Chan-Gi Park; cgpark@kongju.ac.kr

Received 22 August 2017; Revised 8 November 2017; Accepted 14 November 2017; Published 21 January 2018

Academic Editor: Young Hoon Kim

Copyright © 2018 Joo-Ha Lee et al. This is an open access article distributed under the Creative Commons Attribution License, which permits unrestricted use, distribution, and reproduction in any medium, provided the original work is properly cited.

This study assessed the mechanical properties and durability of latex-modified fiber-reinforced segment concrete (polyolefin-based macrosynthetic fibers and hybrid fiber-macrosynthetic fiber and polypropylene fiber) for a tunnel liner application. The tested macrosynthetic fiber-reinforced concrete has a better strength than steel fiber-reinforced concrete. The tested concrete with blast furnace slag has a higher chloride ion penetration resistance (less permeable), but its compressive and flexural strengths can be reduced with blast furnace slag content increase. Also, the hybrid fiber-reinforced concrete has higher compressive strength, flexural strength, chloride ion water permeability resistance, impact resistance, and abrasion resistance than the macrosynthetic fiber-reinforced concrete. The modified fiber improved the performance of concrete, and the hybrid fiber was found to control the formation of micro- and macrocracks more effectively. Therefore, overall performance of the hybrid fiber-reinforced concrete was found superior to the other fiber-reinforced concrete mixes tested for this study. The test results also indicated that macrosynthetic fiber could replace the steel fiber as a concrete reinforcement.

1. Introduction

Utility tunnels in urban areas are generally constructed using *drill and blast* and mechanized tunneling methods. Although tunnel excavation using the *drill and blast* method is economically feasible, environmental restrictions and ground conditions must be carefully considered for a tunnel construction method selection [1]. Noise, vibration, impact on the existing infrastructures, and environmental issues are typical concerns for the tunnel construction in urban spaces [1, 2]. For these reasons, a mechanized tunneling (e.g., shield TBM) is more favorable for an urban tunneling (e.g., subways, electric power, communications, and water tunnels) [2, 3]. Shield TBM tunnels typically use steel and concrete segmental liner for tunnel supports. Steel segments were initially used exclusively [4]. However, as concrete performance

improved, reinforced concrete (RC) segmental liners have been increasingly used due to their enhanced corrosion resistance and cost-effectiveness compared to steel liners [4]. In urban areas, tunnels are usually located within the public road right of way (ROW). They tend to follow the road's alignment, and relatively sharp curves are also required to minimize tunnel intrusions into private properties [1]. For this case, edges of a reinforced concrete (RC) segmental liner can be damaged by the TBM thrust force and load eccentricity. Therefore, considerations have been given to the steel segmental liners to mitigate this type of damage. However, steel segmental liners are known to be corrosive when they are exposed to an aggressive environment (Figure 1).

Recent studies have explored alternatives to minimize the steel reinforcement of RC segmental liner using steel fiber reinforcement [4, 5]. Steel fiber-reinforced concrete



FIGURE 1: Corrosion of steel segments.

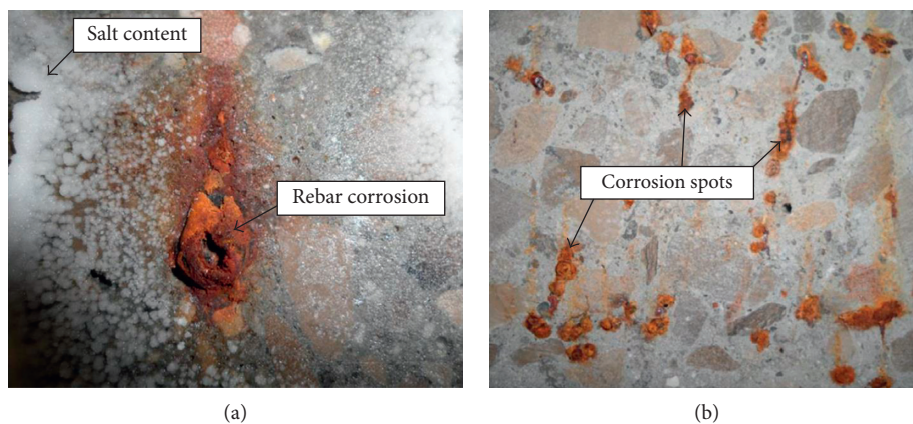


FIGURE 2: Corrosion of steel rebar and steel fiber exposed to 10% Cl^- solution. (a) RC beam specimen. (b) SFRC beam specimen.

segmental liners have a better performance than typical RC segmental liners. However, durability of the steel fiber-reinforced concrete segmental liner was questioned due to the internal corrosion of the steel reinforcement (Figure 2) [6]. According to the study done by Abbas, RC and steel fiber-reinforced concrete (SFRC) segments can be corroded when they are exposed to a chloride ion environment [6]. There are two mitigation measures to the corrosion issue of steel rebar and steel fiber reinforcement: (1) improve the water permeability resistance by compacting the concrete and/or (2) use noncorrosive reinforcing materials. This study evaluated the utilization of noncorrosive polyolefin-based macrosynthetic fiber and hybrid fiber as a replacement of steel fiber and steel reinforcement commonly used in concrete segmental tunnel liners. Latex and blast furnace slag (an industrial by-product) were also used to improve the water permeability resistance. Many studies have discussed the use of polyolefin-based macrosynthetic fiber in various applications such as marine structures, shotcrete, and concrete tunnel liners due to its corrosion resistance and higher impact/static strength than steel fiber. These properties translate to better corrosion resistance and higher rebound stability than steel fiber in shotcrete [7–10]. However, the fluidity decreases as volume fraction increases

due to poorer fiber dispersibility in fiber-reinforced concrete, which leads to poorer segmental concrete liner performance [11, 12]. This study used latex to increase the fluidity and water permeability resistance. When latex is added to the concrete mix, it improves the water permeability resistance due to the formation of a latex film, fiber dispersibility, and fluidity of fiber-reinforced concrete [13, 14]. Also, the waterproofness of concrete containing fine particles of blast furnace slag improves as the generated calcium-silicate-hydrate (C-S-H) gel improves the pore system and subsequently the sulfate and chloride ion penetration resistance [15–17]. To evaluate the feasibility of replacing commonly used steel fiber-reinforced concrete with latex-modified fiber-reinforced concrete for a tunnel liner application, this study tested the compressive strength, flexural strength, and chloride ion penetration as a function of volume fraction with fine particles of blast furnace slag, steel fiber, and macrosynthetic fiber. A mix suitable for a latex-modified segment concrete was used, to which macrosynthetic fiber and a hybrid fiber, consisting of a combination of macrosynthetic fiber + polypropylene fiber, were added. The reinforced concrete was then tested for compressive strength, flexural strength, chloride ion penetration, impact strength, and abrasion resistance. Previous research

TABLE 1: Properties of cement.

Type of cement	Fineness (cm ² /g)	Density (g/mm ³)	Stability (%)	Setting time		Compressive strength (MPa)		
				Initial (min)	Final (min)	3 days	7 days	28 days
ASTM type 1	3200	3.15	0.02	220	400	20.3	30.2	38.7

indicated that the hybrid fiber is effective at macro- and microinternal crack formation prevention in segmental concrete liners.

2. Materials

2.1. Materials. This study used ASTM Type I cement, and its properties are given in Table 1. Fine particles of blast furnace slag were added to improve the durability and waterproofness of concrete. The blast furnace slag composition is listed in Table 2. Crushed aggregate having a maximum size of 25 mm was used as the coarse aggregate, and Table 3 gives the physical properties of the coarse aggregate. The fine aggregate had a density of 2.62 g/mm³. For the reinforcing fiber, bundled end-hook-type steel fiber (30 mm (length) × 0.5 mm (diameter)) and polyolefin-based macrosynthetic fiber (30 mm (length) × 1 mm (diameter)) were used; Table 4 and Figure 3 provide details. The polyolefin-based macrosynthetic fiber (macrosynthetic fiber) is a monofilament fiber with polypropylene and polyethylene combined (Nycon Materials Co., Seoul, Republic of Korea). In this study, polypropylene fiber was applied. The polypropylene microfibers (polypropylene fiber) consisted of 100% percent virgin homopolymer polypropylene multifilament fibers containing no reprocessed olefin materials.

The report published by the 548 Technical Committee of the American Concrete Institute (ACI) indicated that pores ranging from 10 to 1000 nm in diameter damage concrete in the long term through a capillary effect [18]. Polymers with a particle size of 100 nm effectively fill these internal pores. In this study, it was difficult to ensure the pore filling during the mixing or sample fabrication due to low initial fluidity caused by the fiber reinforcement. Styrene-butadiene (SB) latex was used to improve durability and initial fluidity [18]. Table 5 summarizes the SB latex properties.

2.2. Mix Proportions. This study evaluated the performance of latex-modified fiber-reinforced concrete as a function of type and volume fraction of reinforcing fiber and the use of fine particles of blast furnace slag. The mechanical properties and durability of the concrete were measured for the mixes containing steel fiber and macrosynthetic fiber with fiber volume fractions at 0.0, 0.25, 0.5, and 1.0% and with fine particles of blast furnace slag substituted at 30%. Latex was included at 10% of the binder weight. The design compressive strengths of the concrete mixes were 40 and 60 MPa at a material age of 28 days. Tables 6 and 7 give the mix designs.

TABLE 2: Chemical compositions of blast furnace slag.

Chemical composition (%)							
SiO ₂	Al ₂ O ₃	Fe ₂ O ₃	CaO	MgO	MnO	TiO	S
33.1	13.9	0.29	42.4	6.1	0.4	0.96	0.66

TABLE 3: Physical properties of coarse aggregate.

Type of aggregate	Specific density (g/mm ³)			Absorption (%)	FM
	Bulk	Bulk (SSD)	Apparent		
Crushed coarse aggregate	2.80	2.65	2.83	0.35	6.92

3. Test Methods

The compressive strength, flexural strength, and chloride ion penetration resistance of the latex-modified fiber-reinforced segment concrete were measured using standard test methods. Impact resistance and abrasion resistance tests were also carried out to measure the durability of the mixes.

3.1. Compressive Strength. Compressive strength was determined in accordance with ASTM C 39 “Testing Methods for Compressive Strength of Concrete Standard” [19]. Specimens of dimensions 100 mm (diameter) × 200 mm (length) were made. Three specimens were tested at the material age of 28 days. The specimen was located at the center of the platen in the universal testing machine and loaded at constant speed until failure. The maximum load for each specimen was divided by its cross-sectional area, and the average value was reported as the compressive strength. Specimens were cured for 1 day at 23 ± 2°C and a relative humidity of 50%, followed by water curing in a constant temperature bath at 23 ± 2°C. Testing was done in duplicate.

3.2. Flexural Strength. Flexural strength was evaluated using the ASTM C 496 “Testing Methods for Flexural Strength of Concrete Standard” [20]. Concrete was placed in a rectangular mold (100 mm × 100 mm × 400 mm) to form three specimens for this test at the material age of 28 days. After initial curing, the specimens were immersed in a constant temperature water bath at 23 ± 2°C. Testing was done in duplicate.

3.3. Chloride Ion Penetration. Permeability is the most important contributor to the strength and durability of concrete. Increased permeability lowers the strength via

TABLE 4: Properties of fibers.

Type of fiber		Elastic modulus (GPa)	Density (g/mm ³)	Length (mm)	Diameter (mm)	Tensile strength (MPa)	Aspect ratio (L/d)
Steel	Bundled type	200	7.8	30	0.5	1100	60
Polypropylene	Fibrillated bundle type	4	0.91	6	0.1	600	60
Macrosynthetic	Crimped type (monofilament)	10	0.91	30	1	550	30

crack expansion and reduces the durability through freezing, thawing, and abrasion. In this study, a permeability test was conducted in accordance with standard ASTM C 1202-94 [21]. Two cylindrical specimens (100 mm (diameter) × 200 mm (length)) were prepared for each composition and tested at the material age of 28 days. The centers of the specimens were lowered to a thickness of 50 mm and then placed in a desiccator. Vacuum was applied for 3 hours to remove the trapped air, and then water was introduced into the desiccator to saturate the specimens with water. The vacuum was reapplied for 1 hour. The vacuum pump was then turned off, and the specimens were maintained fully immersed in water for 18 ± 1 hours. Following this process, a specimen was fixed in an applied voltage cell, where the positive pole was filled with 0.3 N NaOH solution, and the negative pole was filled with 3% NaOH solution. A potential of 60 V was applied, and the current was measured over a 6-hour period. The test was repeated twice with three specimens having the material age of 28 days. Figure 4 shows the chloride ion penetration resistance setup. Table 8 (from the ASTM standard) ranks the chloride ion permeability level as a function of the charge passed.

3.4. Impact Resistance. The ACI Committee 544 Test Method was used to evaluate impact resistance. According to this method, a rigid body of dimensions 150 mm (diameter) × 60 mm (length) is freely dropped [22]. Three specimens were produced for each material age, cured for 1 day in a curing room ($23 \pm 2^\circ\text{C}$, 50% relative humidity) and then cured in a water bath at a constant temperature of $23 \pm 2^\circ\text{C}$. The test was repeated twice for three specimens at the material age of 28 days. Figure 5 shows the device used for the impact resistance test.

3.5. Abrasion Resistance. Four cylindrical specimens were made with dimensions 150 mm (diameter) × 300 mm (length) in accordance with the ASTM C 944 standard [23]. The specimens were cured in a curing room at $23 \pm 2^\circ\text{C}$ and a relative humidity of 50% for 1 day, demolded, and then cured in water for 28 days in a constant temperature bath at $23 \pm 2^\circ\text{C}$. The abrasion test was performed in duplicate. The test setup is shown in Figure 6.

4. Results and Discussion

4.1. Compressive Strength. Figure 7 shows the compressive strength results for the mix formulations containing



(a)



(b)



(c)

FIGURE 3: Geometry of reinforcing fibers. (a) Bundled end-hook-type steel fibers. (b) Macrosynthetic fibers. (c) Polypropylene fiber.

various amounts of fine particles of blast furnace slag. The blast furnace slag content increase in the mixes lowered the compressive strength of concrete, and similar results were found regardless of the fiber type or volume fraction for all design strengths of 40 and 60 MPa. The fine particles of blast furnace slag behaved as a quasi-pozzolanic material. The design strength was achieved for all mixes.

Figures 8 and 9 show the compressive strength results as a function of reinforcing fiber type. This study evaluated the

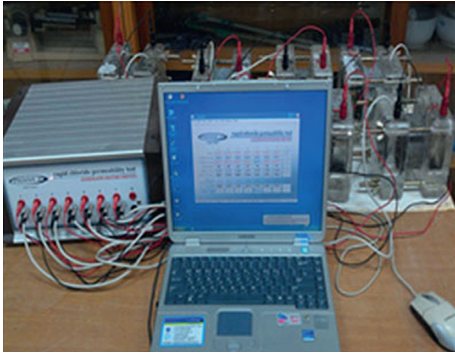


FIGURE 4: Chloride ion permeability setup.

TABLE 8: Standard of permeability levels by ASTM.

Charge passed (Coulombs)	Chloride permeability
>4000	High
2000~4000	Moderate
1000~2000	Low
100~1000	Very low
<100	Negligible

possible use of macrosynthetic fiber to replace the settle fiber as a mitigation measure to the steel fiber corrosion in the reinforced concrete structures. Concrete mixes containing steel fiber and macrosynthetic fiber showed similar compressive strength, regardless of volume fraction. The fiber type did not appear to affect the compressive strength, which indicated that the macrosynthetic fiber can replace the steel fiber.

The compressive strength increased as fiber volume fraction increased. Generally, concrete fluidity decreases with increasing fiber volume fraction due to poorer fiber dispersibility. This leads to a decrease in compressive strength. However, latex was added to the mixes to ensure fluidity, and the fiber was tempered for 2.5 minutes after the injection to increase its dispersibility. No compressive strength decrease was observed for the latex-added concrete mixes.

4.2. Flexural Strength. The flexural strength of concrete under a load is more critical than its compressive strength for a tunnel liner application. Figures 10–12 show the flexural strength results of the concrete with blast furnace slag. The blast furnace slag content increase in the mixes lowered the flexural strength of concrete; this was observed for the design strengths of 40 and 60 MPa, regardless of the fiber type or volume fraction. As a quasi-pozzolanic material, the fine particles delayed strength development. Consequently, flexural strength decreased.

The flexural strength increased with increasing fiber volume fraction. The effect of macrosynthetic fiber was slightly greater than that of steel fiber: the flexural strength was higher at a given volume fraction because the lower density of the macrosynthetic fiber indicated a higher number of fibers per unit volume. The flexural



FIGURE 5: Impact resistance test setup.



FIGURE 6: Abrasion test setup.

strength results showed that macrosynthetic fiber can replace steel fiber.

4.3. Chloride Ion Penetration. Figures 13–15 show the chloride ion penetration resistance results of the concrete containing reinforcing fiber and fine particles of blast furnace slag. The penetration decreased in those mixes containing fine particles of blast furnace slag because the fine particles filled the micropores of the concrete matrix.

The water permeability resistance increased with decreasing chloride ion penetration in the mixes containing macrosynthetic fiber, while the chloride ion penetration resistance improved with increasing fiber volume fraction. The high strength (60 MPa) concrete mix containing the macrosynthetic fiber had the highest resistance, while 0.5

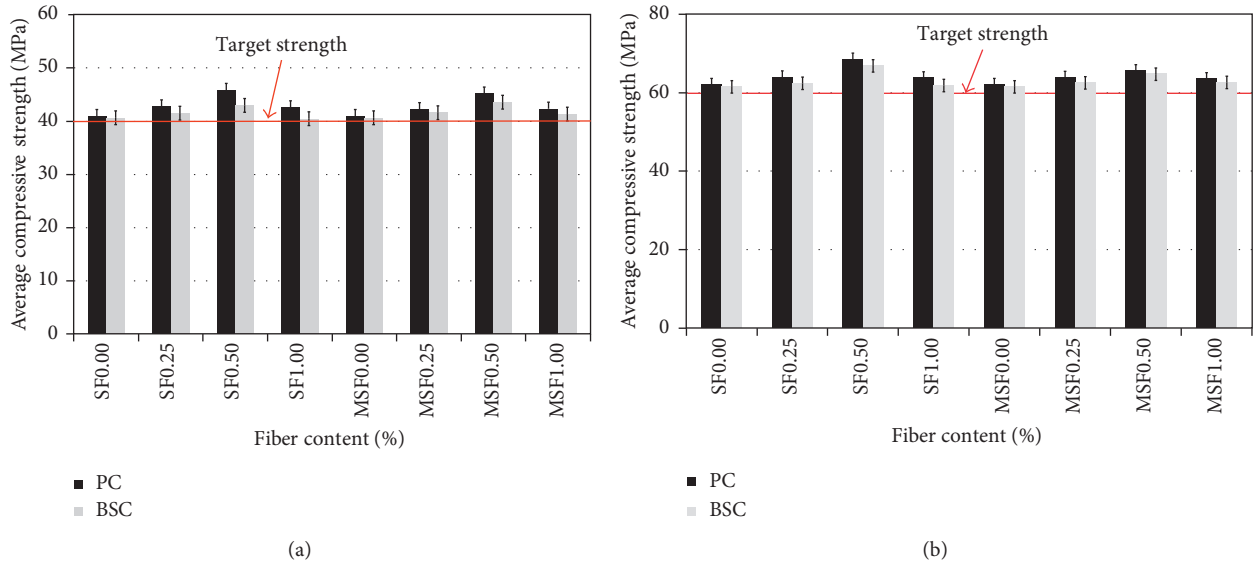


FIGURE 7: Compressive strength with fiber volume fraction. (a) Target strength 40 MPa. (b) Target strength 60 MPa.

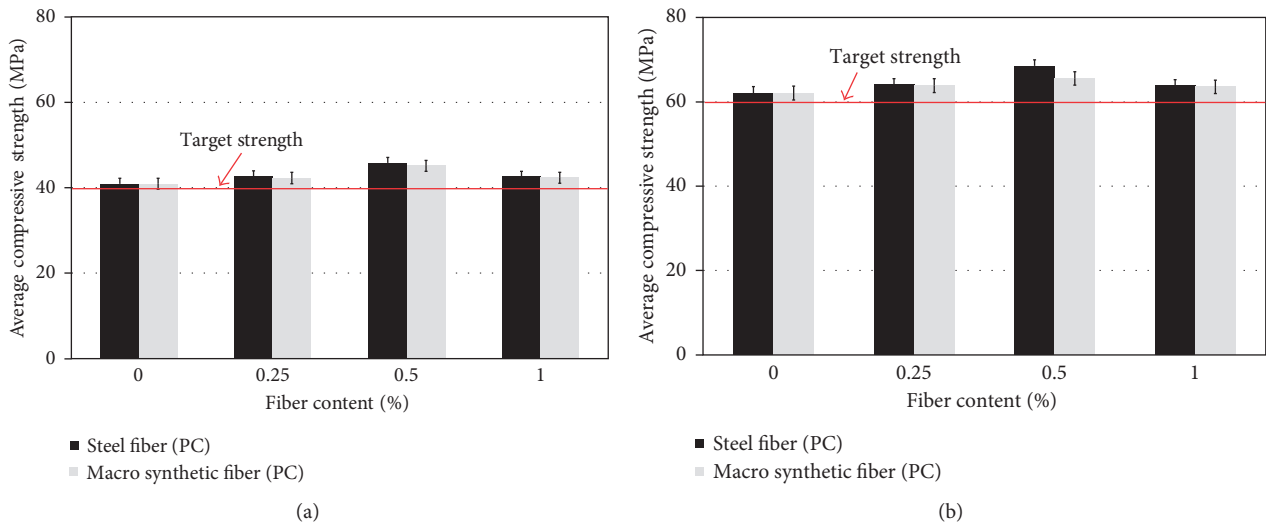


FIGURE 8: Compressive strength of PC segment with reinforcing fiber type. (a) Target strength 40 MPa. (b) Target strength 60 MPa.

and 1.0% volume fraction of the macrosynthetic fiber with fine particles of blast furnace slag resulted in a “very low” rating, according to the ASTM standard 1202. All other mixes scored “low” for the water permeability with an equal value throughout its range. Those 40 MPa mixes containing macrosynthetic fiber all had “low” ratings, while the mixes with added steel fiber scored the “low” rating only at the 1.0% substitution level. All the other mixes had “moderate” water permeability. Additionally, both steel fiber and macrosynthetic fiber mixes that also included fine particles of blast furnace slag had “low” water permeability. Macrosynthetic fiber performs better than steel fiber to enhance the water permeability resistance; other mixes that included fine

particles of blast furnace slag also showed higher water permeability resistance.

5. Determination and Performance of the Optimum Mix

5.1. *Determination of the Optimum Mix Proportions.* The macrosynthetic fiber, steel fiber, and fine particles of blast furnace slag were used as variables to identify the optimum concrete mix design. The fine particles of blast furnace slag improved the chloride ion penetration resistance but reduced the initial compressive and flexural strengths. Nevertheless, all of the mixes met the design

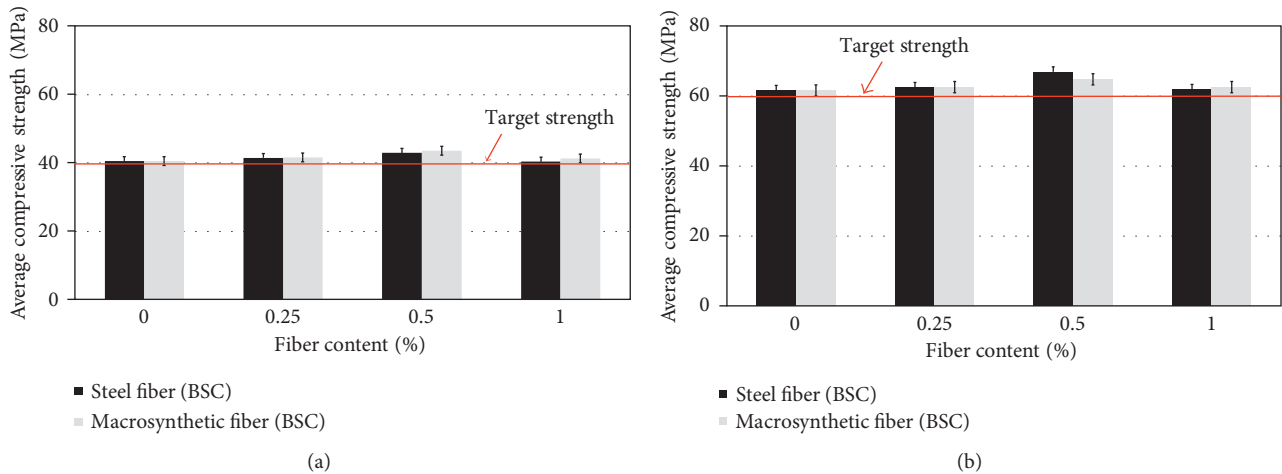


FIGURE 9: Compressive strength of BSC segment with reinforcing fiber type. (a) Target strength 40 MPa. (b) Target strength 60 MPa.

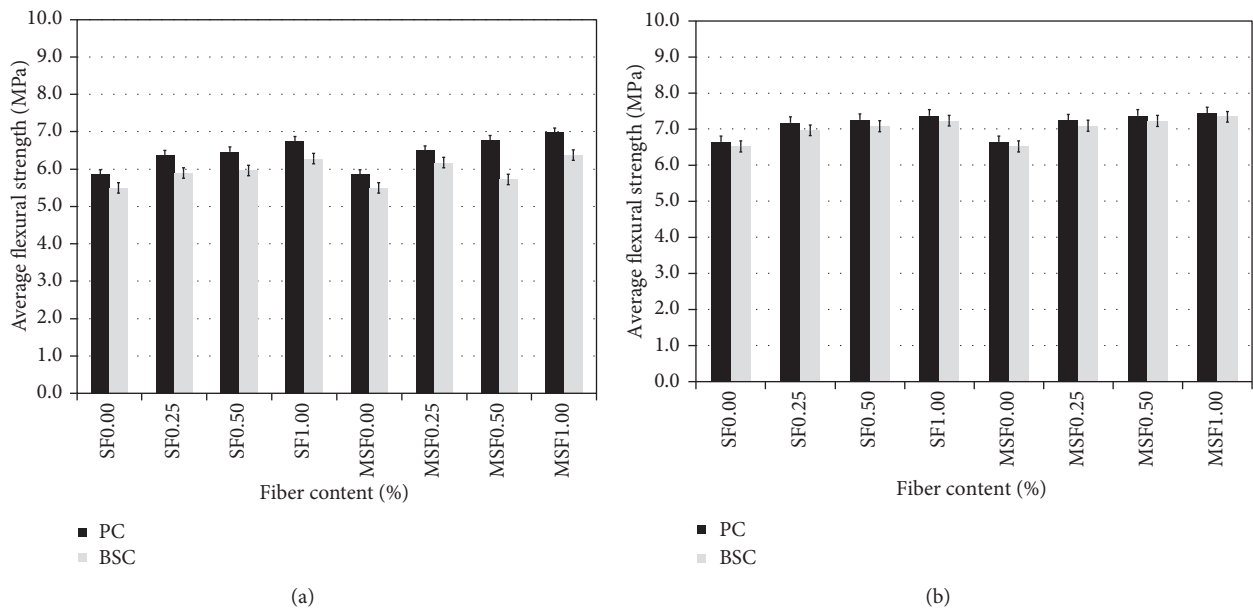


FIGURE 10: Flexural strength with fiber volume fraction. (a) Target strength 40 MPa. (b) Target strength 60 MPa.

strengths of 40 and 60 MPa. Hence, fine particles of blast furnace slag were added to all of the mixes. A steel fiber was not used for the optimum mix design determination due to its known corrosion issues. The properties of mixes containing 0.1% volume ratio of polypropylene fiber-added mix were measured, and this fiber addition prevented the formation of micro- and macrocracks. The mix proportions of the various tests were summarized in Table 9.

5.2. Evaluation of the Optimum Mix. This study compared and evaluated the mechanical properties and durability of the control mix (no reinforcing fiber) with the other mixes containing macrosynthetic fiber or hybrid fiber.

Figure 16 shows the test results for the compressive strength of the final optimum mix proportions. The mixes containing the hybrid fiber showed the highest strength, followed sequentially by those containing the macrosynthetic fiber and control fiber; the trends were the same for the 40 and 60 MPa cases. Generally, mixing with reinforcing fiber affects the flexural strength to a greater degree than the compressive strength. It was also noted that the compressive strength did not increase significantly. All of the mixes achieved the 40 and 60 MPa design strengths.

Figure 17 shows the flexural strength results for the optimum mix. The mix containing the hybrid fiber had the

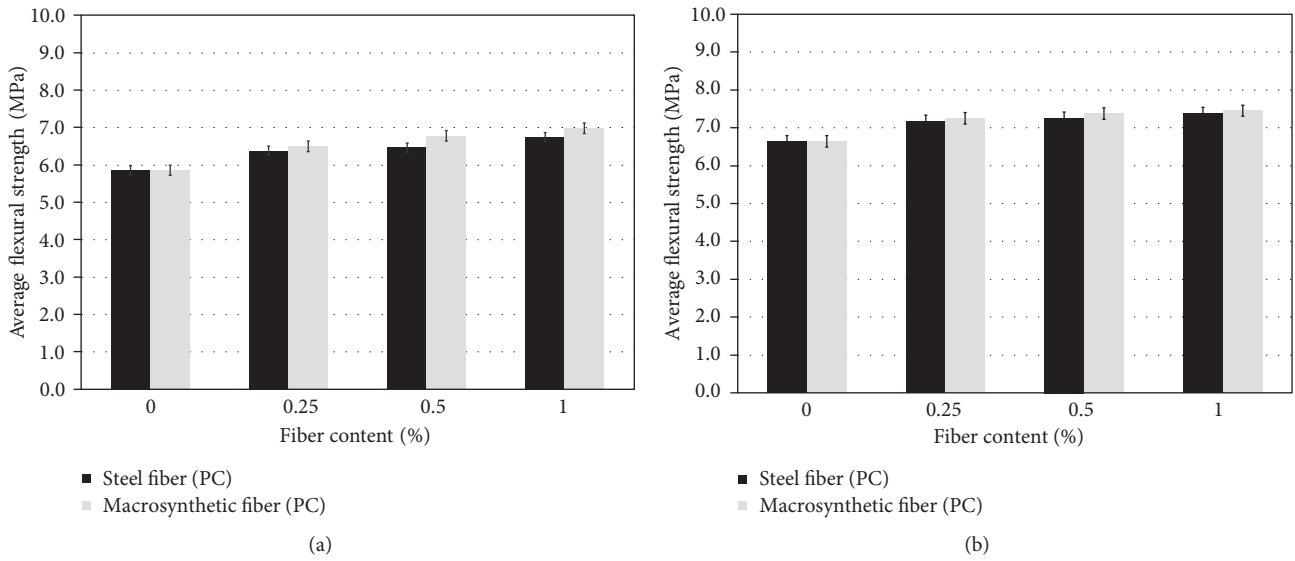


FIGURE 11: Flexural strength of PC segments with reinforcing types. (a) Target strength 40 MPa. (b) Target strength 60 MPa.

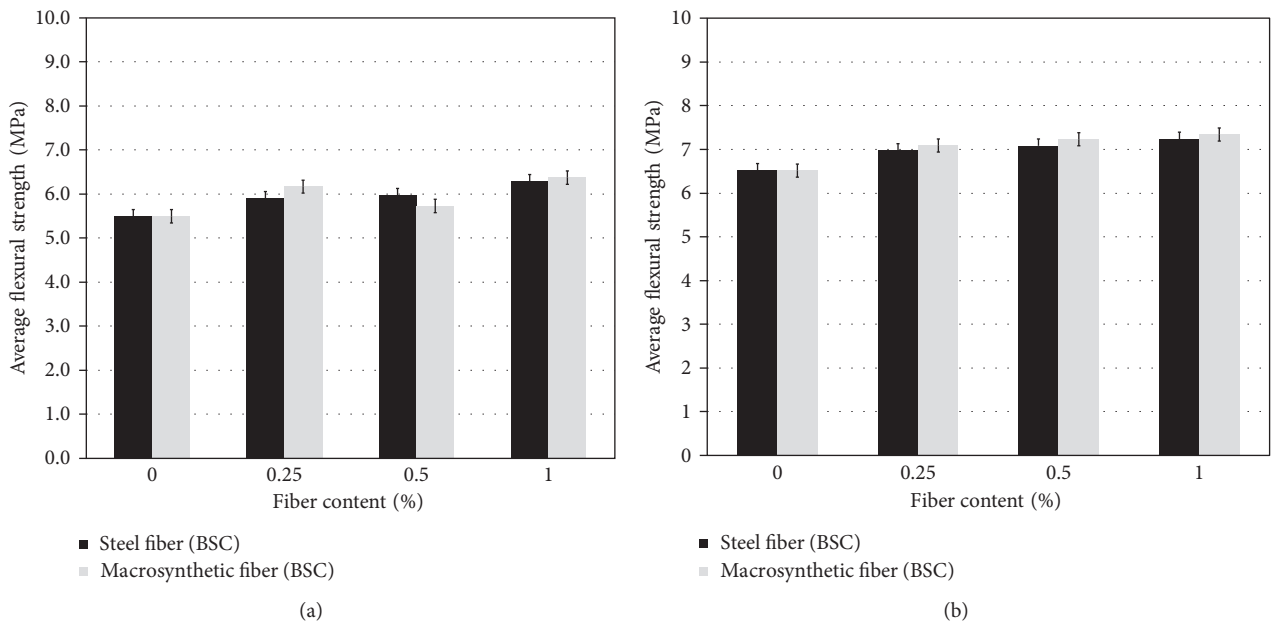


FIGURE 12: Flexural strength of BSC segments with reinforcing types. (a) Target strength 40 MPa. (b) Target strength 60 MPa.

highest flexural strength, followed by the macrosynthetic fiber and control mixes. This was because the hybrid fiber mix used a blend of macrosynthetic and polypropylene fibers to effectively control micro- and macrocrack formation in the concrete. The macrosynthetic fiber mix also had a higher flexural strength than the control mix and also controlled crack formation more effectively than the control mix.

Figure 18 shows the chlorine ion penetration results for the final mix composition. The mix containing the hybrid fiber had the lowest penetration, followed by that containing the macrosynthetic fiber and the control. For the designed 40 MPa mixes, the control mix with its value

greater than 2000 C indicated moderate permeability, while the macrosynthetic fiber and hybrid fiber mixes had low permeability and very low permeability, respectively. For the designed 60 MPa mixes, the control mix had a low water permeability (1500 C or higher) while the addition of macrosynthetic or hybrid fibers provided very low water permeability. The permeability resistance of latex-modified segment concrete was increased by adding reinforcing fibers. Also, mixes with hybrid fiber had a better permeability resistance than the mix with the macrosynthetic fiber, because the presence of polypropylene fiber controls the crack formation.

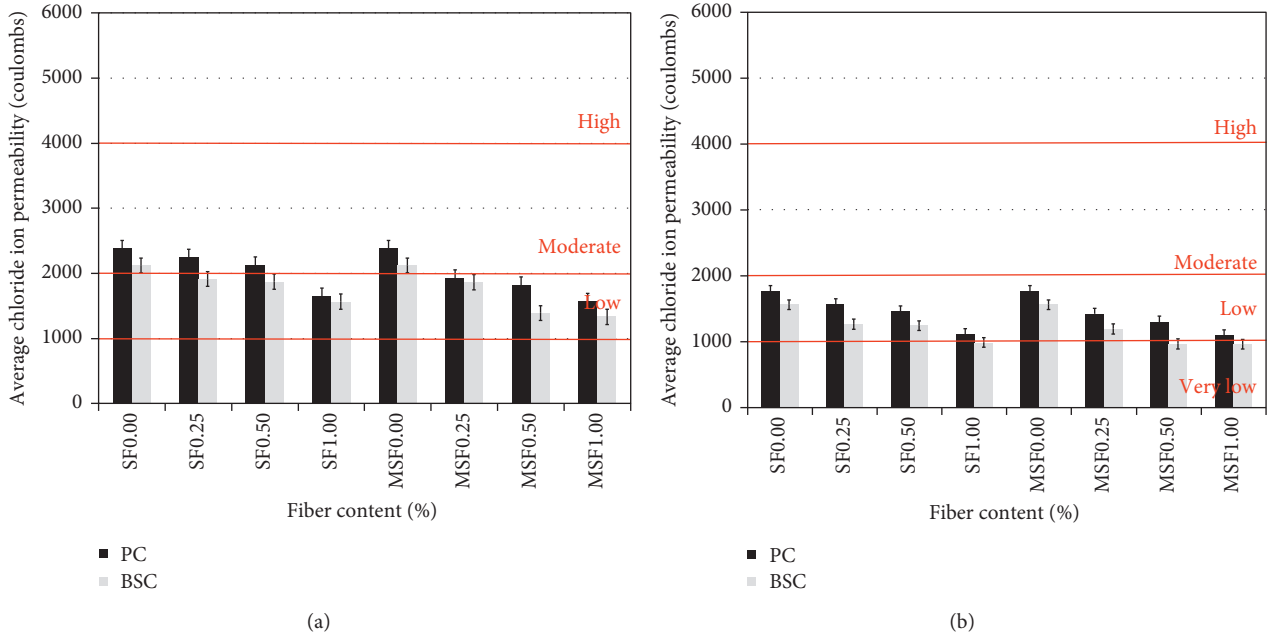


FIGURE 13: Chloride ion penetration test results of concrete segments with fiber volume fraction. (a) 40 MPa. (b) 60 MPa.

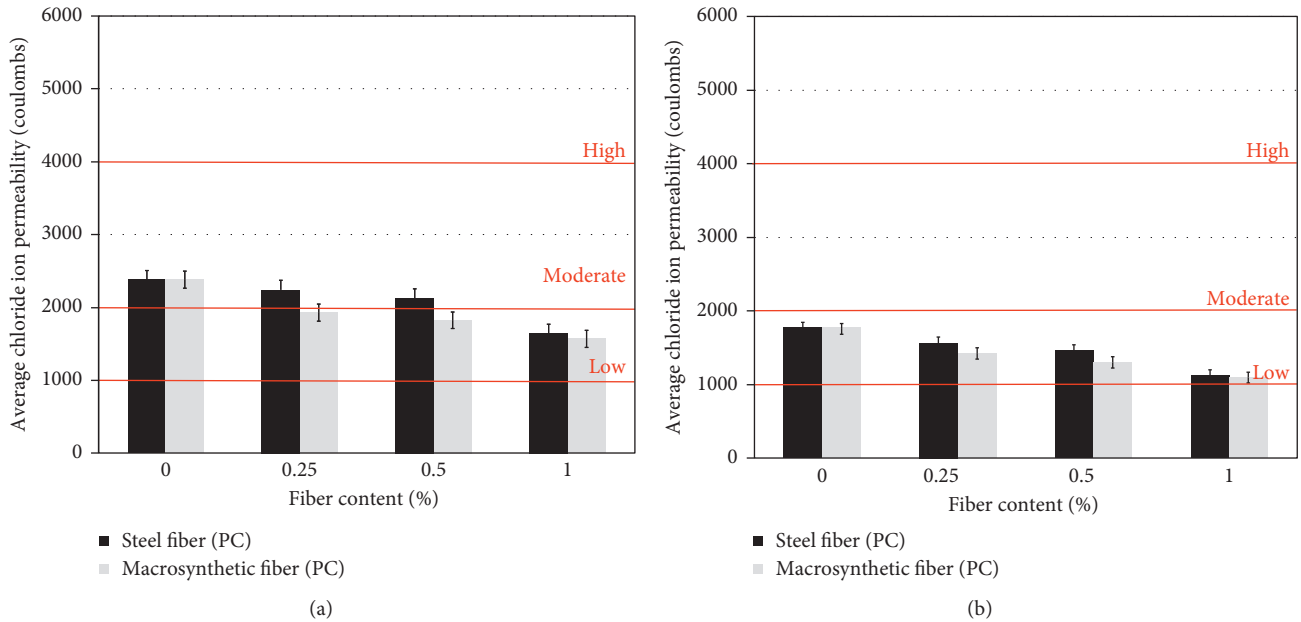


FIGURE 14: Chloride ion penetration of PC segments with reinforcing types. (a) 40 MPa. (b) 60 MPa.

Figure 19 shows the impact resistance results of the optimum mix. The improvement followed the order of control mix < macrosynthetic fiber mix < hybrid fiber mix, because adding a reinforcing fiber helped to absorb the impact. A fiber reinforcement of concrete improves flexural toughness and energy absorption capacity through complex steps of pullout, debonding, bridging, and fracture and consequently, increases impact resistance. Therefore, mixes with macrosynthetic fiber had

better impact resistance than those lacking reinforcing fiber. Moreover, using the hybrid blend of macrosynthetic fiber with polypropylene fiber suppressed the formation of micro- and macrocracks, thereby increasing the energy absorbing capacity and impact resistance. Figure 20 has photographs of impact test specimens after the test. The optimum mix containing fiber only got the microcracks. Mixes lacking reinforcing fiber displayed microcracks in the 40 MPa design case but macrocracks in the 60 MPa

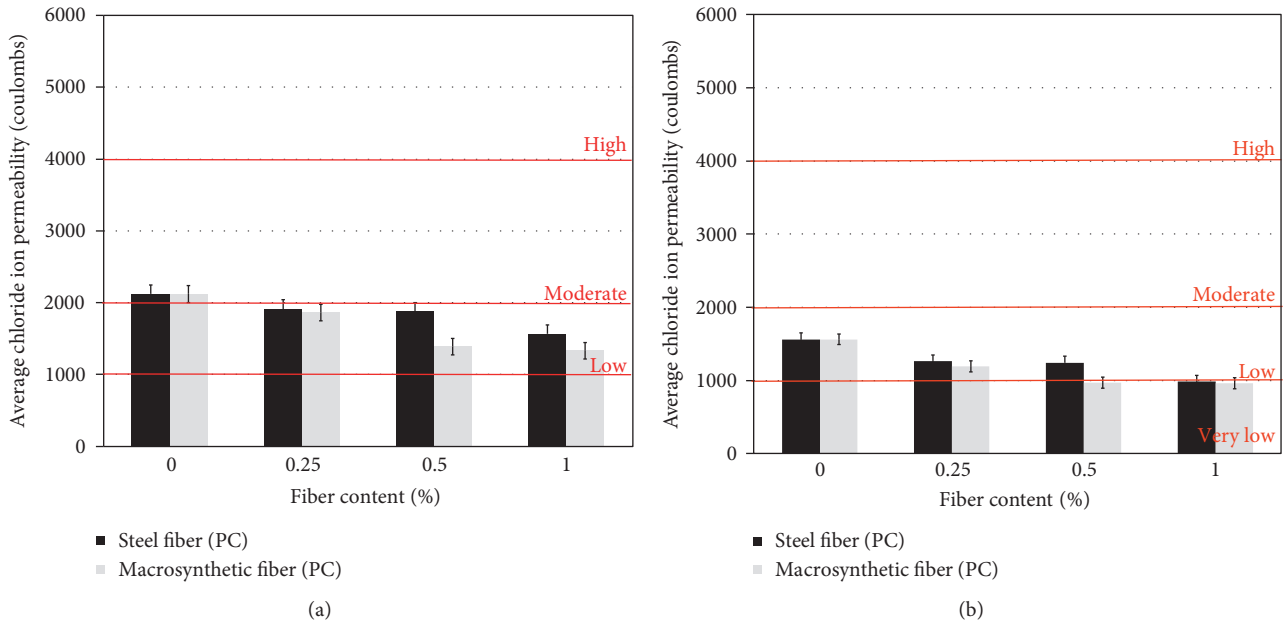


FIGURE 15: Chloride ion penetrations of BSC segments with reinforcing types. (a) 40 MPa. (b) 60 MPa.

TABLE 9: Mixing ratio for optimum mix proportions determination.

Design strength (MPa)	Type of mix	Unit weight (kg/m ³)							
		W	C	BFS	G	S	Latex	Macrosynthetic fiber	Polypropylene fiber
40	Control								
	Macrosynthetic fiber	150	350	150	1184	466	50	9	—
	Hybrid fiber							9	0.9
60	Control								
	Macrosynthetic fiber	143	437	188	1087	467	62	9	—
	Hybrid fiber							9	0.9

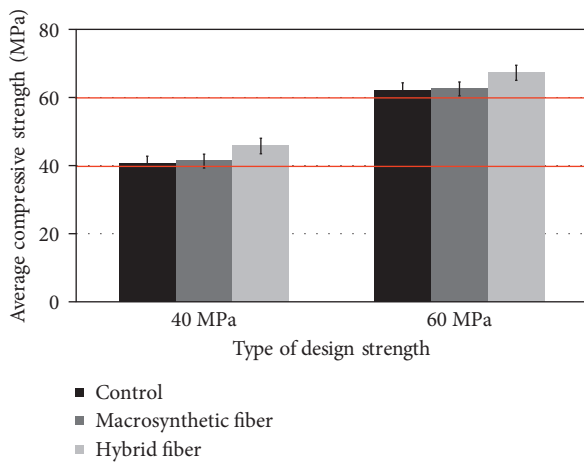


FIGURE 16: Compressive strength of optimum mix ratio.

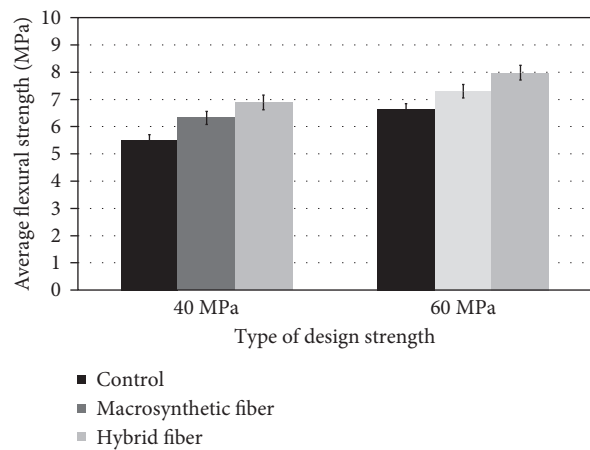


FIGURE 17: Flexural strength of optimum mix ratio.

design case. The higher strength was accompanied by increased brittleness, leading to macrocracks and ultimately failure. However, stronger specimens require

higher numbers of impacts until failure; the crack width and number of impacts were accordingly higher for the 60 MPa design mixes in this study.

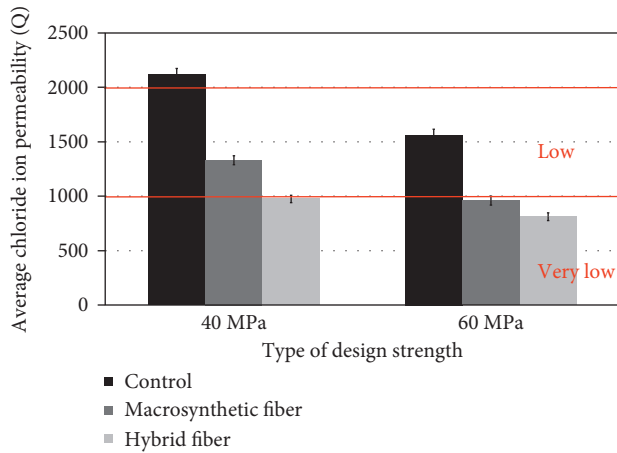


FIGURE 18: Chloride ion penetration of optimum mix ratio.

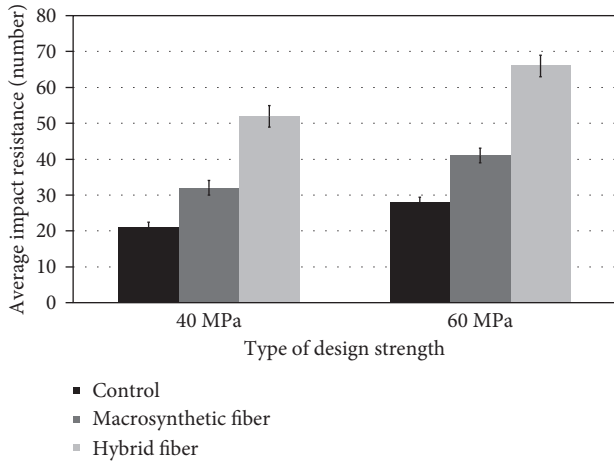
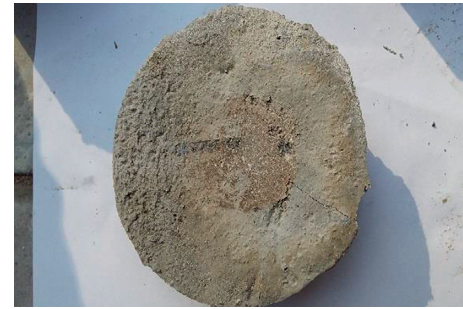


FIGURE 19: Impact resistance of optimum mix ratio.

Figure 21 shows the abrasion resistance results for the optimum mix. The resistance improved in the order of control mix < macrosynthetic fiber mix < hybrid mix. The hybrid mix comprising a blend of macrosynthetic fiber and polypropylene fiber increased the abrasion resistance through a crosslinking effect as the fiber resisted separation of concrete powder and pieces during the abrasion process. Notably, for the hybrid mix, macrocracks created on the normal concrete surface by abrasion were controlled by the macrosynthetic fiber, while microcracks were mitigated by the polypropylene fiber, providing an overall improvement in abrasion resistance. Figure 22 shows the specimens after the abrasion test. Surface abrasion was less for the mixes containing macrosynthetic and hybrid fibers than the control mix.

As a result of evaluating the mechanical performance and durability of the optimum mix according to the type of fiber, the hybrid fiber application showed the best performance. Generally, hybrid fiber is effective to suppress microcrack and macrocrack simultaneously in concrete [12]. A microfiber of small length and diameter inhibits the generation and growth of microcracks. Macrofiber with a large length and diameter



(a)



(b)



(c)



(d)

FIGURE 20: Photographs of fracture shape after impact test. (a) 40 MPa (control). (b) 40 MPa (optimum). (c) 60 MPa (control). (d) 60 MPa (optimum).

inhibits the initiation and growth of microcracks. Therefore, the addition of hybrid fibers to concrete improves the mechanical performance and durability of concrete by simultaneously controlling microcracks and macrocracks. In this study, polypropylene fibers were used for fibers of small length and diameter (microfiber), and macrosynthetic fibers were applied for fibers of long length and diameter

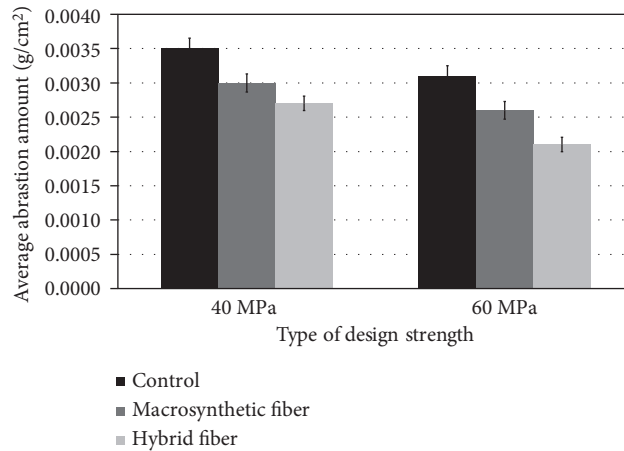


FIGURE 21: Abrasion resistance of optimum mix ratio.

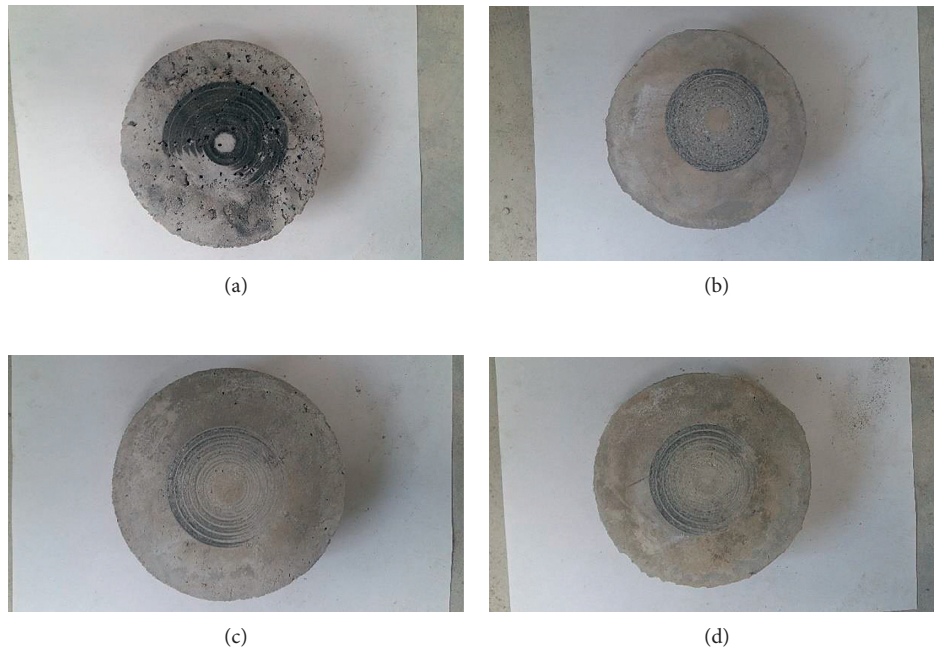


FIGURE 22: Photo of abrasion specimens after abrasion. (a) 40 MPa (control). (b) 40 MPa (optimum). (c) 60 MPa (control). (d) 60 MPa (optimum).

(macrofiber). Therefore, mechanical properties (compressive strength and bending strength), permeability, impact resistance, and abrasion resistance were improved compared to concrete without macrosynthetic fiber and concrete without fiber. That is, polypropylene fiber was added to concrete to suppress the generation and growth of microcracks, and macrosynthetic fiber to suppress macrocracks, thereby improving concrete performance.

6. Conclusions

This study evaluated the mechanical properties and durability of latex-modified fiber-reinforced concrete as an alternative to conventional steel fiber-reinforced concrete. Macrosynthetic, steel, and hybrid (macrosynthetic + polypropylene) fibers

were used as reinforcing fibers. The results of the study are summarized as follows:

- (1) Adding fine particles of blast furnace slag decreased the compressive strength. The effect of reinforcing fiber and fiber volume fraction were not significant. All mixes achieved the design strengths of 40 and 60 MPa.
- (2) Adding fine particles of blast furnace slag decreased flexural strength. However, the strength increased with increasing volume fraction of reinforced fiber. Macrosynthetic fiber provided a slightly better flexural strength than steel fiber.
- (3) Adding fine particles of blast furnace slag decreased the chloride ion penetration, which indicated improved water permeability resistance. Chloride ion

penetration decreased with increasing fiber volume fraction. Macrosynthetic fiber provided a better water permeability resistance than did steel fiber.

- (4) The compressive strength, flexural strength, and chloride ion penetration resistance results were used to obtain the optimum mix composition. The optimum mix contained fine particles of blast furnace slag and macrosynthetic fiber.
- (5) The mechanical durability was assessed for the optimum mix by varying the reinforcing fiber type, that is, no reinforcing fiber (control), macrosynthetic fiber, and hybrid fiber (macrosynthetic fiber + polypropylene fiber). The compressive strength, flexural strength, chloride ion water permeability test, impact resistance, and abrasion resistance are followed in the order of the control mix < macrosynthetic fiber mix < hybrid fiber mix.
- (6) The addition of hybrid fiber effectively controlled the formation of macro- and microcracks.
- (7) Macrosynthetic fiber is also a feasible replacement for steel fiber in the latex-modified concrete.

Conflicts of Interest

The authors declare that they have no conflicts of interest.

Acknowledgments

This research was supported by a grant (15SCIP-B105148-01) from the Construction Technology Research Program funded by the Ministry of Land, Infrastructure, and Transport of the Korean Government.

References

- [1] S. J. You and C. S. You, "A study on the member forces of segmental linings considering key segments," *Journal of Korean Tunneling and Underground Space Association*, vol. 17, no. 3, pp. 363–382, 2015.
- [2] S. H. Chang, G. P. Lee, S. W. Choi, and G. J. Bae, "State of the art of segment lining in shield tunnel and statistical analysis of its key design parameters," *Journal of the Korean Society for Rock Mechanics*, vol. 21, pp. 427–438, 2011.
- [3] W. G. Lee, H. I. Kim, B. C. Jung, J. I. Kim, and H. Woo, "A construction plan of double shield TBM in steep tunnel and fault zone," *Korean Tunneling and Underground Space Association*, vol. 21, pp. 427–438, 2008.
- [4] C. S. You and H. M. A. Jeon, "Comparative study on methods for shield tunnel segment lining sectional forces," *Korean Tunneling and Underground Space Association*, vol. 14, pp. 159–181, 2012.
- [5] G. Tiberti, G. A. Plizzari, J. C. Walraven, and C. B. M. Blom, *Concrete Tunnel Segments with Combined Traditional and Fiber Reinforcement*, Taylor & Francis Group, London, UK, ISBN 978-0-415-47535-8, 2008.
- [6] S. Abbas, *Structural and Durability Performance of Precast Segmental Tunnel Linings*, University of Western Ontario, London, ON, Canada, 2014.
- [7] J. P. Won, C. G. Park, Y. J. Kim, and K. H. Park, "Bond properties of synthetic and steel single fiber in high strength cement based composites," *Journal of the Korean Society for Civil Engineers*, vol. 27, pp. 609–616, 2007.
- [8] J. P. Won, C. G. Park, Y. J. Kim, and C. W. Lee, "Pullout behavior of polyolefin synthetic fibers with hydrophilic surface treatment in cement matrix," *Journal of the Korean Society for Civil Engineers*, vol. 27, pp. 453–460, 2007.
- [9] N. Banthia, P. Gupta, C. Yan, and D. R. Morgan, "How tough is fiber reinforced shotcrete? Part 1. Beam tests," *Concrete International*, vol. 21, pp. 59–62, 1999.
- [10] N. Banthia, P. Gupta, C. Yan, and D. R. Morgan, "How tough is fiber reinforced shotcrete? Part 2. Plate tests," *Concrete International*, vol. 21, pp. 62–69, 1999.
- [11] R. Chris, M. Kyran, and J. S. Pei, *Fiber-Reinforced Concrete and Bridge Deck Cracking*, University of Oklahoma Graduate College, Norman, OK, USA, 2006.
- [12] J. H. Lee and C. G. Park, "Effect of natural jute fiber on bond between polyolefin based macro fiber and cement matrix," *Journal of the Korean Society for Civil Engineers*, vol. 31, pp. 251–260, 2011.
- [13] H. B. Wagner and D. G. Grenley, "Interphase effects in polymer-modified hydraulic cements," *Journal of Applied Polymer Science*, vol. 22, no. 3, pp. 813–822, 1978.
- [14] Y. Ohama, "Study on properties and mix proportioning of polymer-modified mortars for buildings," in *Report of the Building Research Institute*, p. 65, Building Research Institute, Tokyo, Japan, 1973.
- [15] H. W. Song, S. J. Kwon, S. W. Lee, and K. J. Byun, "A study on resistance of chloride ion penetration in ground granulated blast-furnace slag concrete," *Journal of the Korea Concrete Institute*, vol. 15, pp. 400–408, 2003.
- [16] D. Hester, C. McNally, and M. G. Richardson, "Study of influence of slag alkali level on the alkali-silica reactivity of slag concrete," *Construction and Building Materials*, vol. 19, no. 9, pp. 661–665, 2005.
- [17] F. Leng, N. Feng, and X. Lu, "An experiment study on the properties of resistance to diffusion of chloride ions of fly ash and blast furnace slag concrete," *Cement and Concrete Research*, vol. 30, no. 6, pp. 989–992, 2000.
- [18] American Concrete Institute, *Guide for the Use of Polymers in Concrete*, ACI Committee 548, Detroit, MI, USA, 1997.
- [19] ASTM C39, *Standard Test Method for Compressive Strength of Cylindrical Concrete Specimens*, American Society for Testing and Materials, Philadelphia, PA, USA, 2015.
- [20] ASTM C 78/C78M, *Standard Test Method for Flexural Strength of Concrete (Using Simple Beam with Third-Point Loading)*, American Society for Testing and Materials, Philadelphia, PA, USA, 2015.
- [21] ASTM C 1202–94, *Standard Test Method for Electrical Indication of Concrete's Ability to Resist Chloride Ion Penetration*, American Society for Testing and Materials, Philadelphia, PA, USA, 1997.
- [22] American Concrete Institute, *State-of-the-Art Report on Fiber Reinforced Concrete*, ACI Committee 544, Detroit, MI, USA, 2002.
- [23] ASTM C 944, *Standard Test Method for Abrasion Resistance of Concrete or Mortar Surfaces by the Rotating-Cutter Method*, American Society for Testing and Materials, 2005.

Research Article

Effects of Reinforcing Fiber and Microsilica on the Mechanical and Chloride Ion Penetration Properties of Latex-Modified Fiber-Reinforced Rapid-Set Cement Concrete for Pavement Repair

Woong Kim,¹ Jong-Chan Jeon,² Byung-Hwan An,² Joo-Ha Lee,³ Hae-Do Kim,⁴
and Chan-Gi Park²

¹Department of Bio-Industry Mechanical Engineering, Kongju National University, Yesan 32439, Republic of Korea

²Department of Rural Construction Engineering, Kongju National University, Yesan 32439, Republic of Korea

³Department of Civil Engineering, University of Suwon, Hwaseong 18323, Republic of Korea

⁴Rural Research Institute, Korea Rural Community Corporation, Ansan 15634, Republic of Korea

Correspondence should be addressed to Chan-Gi Park; cgpark@kongju.ac.kr

Received 22 August 2017; Accepted 29 October 2017; Published 21 January 2018

Academic Editor: Young Hoon Kim

Copyright © 2018 Woong Kim et al. This is an open access article distributed under the Creative Commons Attribution License, which permits unrestricted use, distribution, and reproduction in any medium, provided the original work is properly cited.

This study evaluated the influence of reinforcement fiber type and microsilica content on the performance of latex-modified fiber-reinforced roller-compacted rapid-hardening cement concrete (LMFRCRSC) for a concrete pavement emergency repair. Experimental variables were the microsilica substitution ratio (1, 2, 3, and 4%), and the reinforcement fiber (jute versus macrosynthetic fiber). In the tests, compressive, flexural, and splitting tensile strength; chloride ion penetration resistance; and abrasion resistance were assessed. From the compressive and flexural strength tests with microsilica substitution, the 4-hour curing strength decreased as the microsilica substitution ratio increased. From the chloride ion penetration test, as the microsilica substitution ratio increased, chloride ion penetration decreased. The abrasion resistances increased with the substitution ratio of microsilica increase. Based on these test results, microsilica at a substitution ratio of 3% or less and macrosynthetic fiber as the reinforcement improved the performance of LMFRCRSC for a concrete pavement emergency repair and satisfied all of the target strength requirements.

1. Introduction

The repair of deteriorated concrete pavements, using roller-compacted latex-modified rapid-hardening cement concrete, has been studied recently [1]. A roller-compacted concrete (RCC) is a concrete with low fluidity [2–6]. RCC does not require a consistency for compacting, and it must be compacted with an external vibrator, such as a vibration roller or a vibration pressure tamper [2]. Roller-compacted concrete pavement (RCCP) offers a fast, successive construction and use of a wide range of construction equipment; thus, it has higher economic feasibility than other concrete pavements [2–6]. Compared with a general concrete

pavement, RCCP has a lower water-to-cement (W/C) ratio [2]. A lower W/C ratio has the effect of increasing the strength of concrete, and it may reduce the risk of contraction cracks due to moisture evaporation [2–6]. Thus, RCCP also has the advantage of increased durability of pavement over the long term [2–6]. When RCC and latex are used with rapid-hardening cement for a concrete pavement, it is possible to achieve both easy construction and durability [1]. Currently, roller-compacted rapid-hardening cement concrete pavement uses up to 15% latex [1]. The use of latex up to 15% may delay the concrete's initial strength development. As such, it may be difficult to secure sufficient initial target strength [7, 8]. Economically, the overall concrete pavement

repair is more costly due to the high latex amounts. The latex-modified rapid-hardening cement offers superior workability, crack resistance, and durability compared to the general rapid-hardening cement concrete [8–15], but it has the problems of initial strength development delay and lower economic feasibility. Also, the increase in initial fluidity makes roller compaction difficult because latex-modified fiber-reinforced roller-compacted rapid-hardening cement concrete (LMFRCRSC) uses a mix that has low slump, due to the characteristics of RCC.

In the previous study [16], the performance of LMFRCRSC according to the type of fiber reinforcement was evaluated. The possibility of the roller compaction method was evaluated by measuring the slump value according to the type of fiber reinforcement. Mechanical properties such as compressive strength and flexural strength were evaluated, and durability such as permeability and abrasion resistance were evaluated. However, the using amount of rapid-hardening cement is not reduced, so there is a limit to solving the problems caused by the increase in hydration heat in the early age. Therefore, it is necessary to reduce the using amount of rapid-hardening cement. The study was conducted to apply microsilica as a substitute material for rapid-hardening cement in order to reduce the using amount of rapid-hardening cement. The addition of microsilica brings about the pozzolanic reaction and a fine pore-filling effect, providing increased strength and improved water tightness [16, 17]. Also, this study added macrosynthetic fibers and natural jute fibers which showed good results in the previous study. A fiber reinforcement minimizes crack formation and propagation in concrete through the fiber's fracture, pullout, debonding, and bridging effects [13–15]. As a result, the addition of the reinforcement fiber improves the tensile strength of concrete [13–15]. The influence of reinforcement fiber type and microsilica content on the performance of LMFRCRSC was evaluated for a concrete pavement emergency repair.

2. Materials

2.1. Materials. A rapid-hardening cement used was the product manufactured by Jungang Polytech, Korea. Physical and chemical characteristics of the rapid-hardening cement are shown in Table 1. A microsilica, a product from Micro Chemical, Korea, was used for this study, and its chemical compositions are shown in Table 2. Also, the microsilica consists of spherical particles with an average particle size of $0.15\ \mu\text{m}$ and a specific surface area of $20\ \text{m}^2/\text{g}$. The coarse aggregate was the crushed aggregate with a maximum diameter of 13 mm. The fine aggregate was river sand, with a specific gravity of 2.58. The physical characteristics of the aggregates are listed in Table 3. A styrene butadiene latex (SB latex) from Jungang Polytech, Korea, was used for this study, and its characteristics are given in Table 4. The macrosynthetic fiber and natural jute fiber were purchased from Nycontech, Korea, and the fiber characteristics are shown in Table 5. The shapes of the fibers are shown in Figure 1 [16].

TABLE 1: Chemical compositions of rapid-hardening cement.

SiO ₂ (%)	Al ₂ O ₃ (%)	Fe ₂ O ₃ (%)	CaO (%)	MgO (%)	K ₂ O (%)	SO ₃ (%)
13 ± 3	17.5 ± 3	3 >	50 ± 3	2.5 >	0.21	14 ± 3

TABLE 2: Chemical compositions of microsilica.

SiO ₂ (%)	Al ₂ O ₃ (%)	Fe ₂ O ₃ (%)	CaO (%)	Others (%)
90–98	0.4–0.9	1–2	0.2–0.7	2–3

TABLE 3: Physical properties of coarse aggregates.

Properties	Density (g/mm ³)	Absorption (%)	Fineness modulus
Value	2.61	0.35	6.92

2.2. Mix Proportions. In case of concrete pavement repaired using rapid-hardening cement, the traffic open time is specified as a 4-hour minimum curing time by the American Association of State Highway and Transportation Officials (AASHTO) [18], the road traffic administrations of each state in the United States, and the Korea Expressway Corporation [19]. The traffic open standard is a compressive strength of at least 21 MPa and a flexural strength of at least 3.5 MPa. After curing for 28 days, the compressive strength is required to be at least 35 MPa, with a flexural strength of 4.5 MPa and a splitting tensile strength of 4.2 MPa. The abovementioned strength criteria were used as target mix strengths for this study. In addition, permeability has the biggest influence on concrete pavement life cycle degradation. In terms of durability, a chloride ion penetration test result of ≤ 2000 Coulombs (C) after 28 days of curing was set as a target for permeability, based on the Korea Expressway Corporation's ASTM C1202 test method. Also, in this study, to ensure initial permeability, the target chloride ion penetration at 4 hours of curing was set at 4000 C or less.

The W/C ratio was set at 0.28, and latex at 5% (solid-based) of the binder (cement + microsilica) weight was used. In the preliminary study [16], it was decided to apply about 5%, considering the range of latex that can be roller compaction methods on the type of fiber reinforcement. The reinforcement fibers, macrosynthetic fiber and jute fiber, were added at a volume ratio of 0.10%. The addition of reinforcement fibers facilitates slump reduction for roller compaction and is effective for controlling crack formation/growth and reducing water penetration. Microsilica was substituted for cement at weights of 0, 1, 2, 3, and 4% to evaluate the influence of the addition of microsilica. The study mix ratios are shown in Table 6.

2.3. Manufacturing of Test Specimens. For test specimens of LMFRCRSC, this study manufactured specimens using a pressure tamper, which mimicked the roller compaction process. In the first step of specimen fabrication, one-third of the mixed latex-modified fiber-reinforced rapid-hardening

TABLE 4: Properties of styrene butadiene latex.

Solid content (%)	Styrene content (%)	Butadiene content (%)	pH	Specific gravity	Surface tension (dyne/cm)	Particle size (A)	Viscosity (cps)
49	34 ± 1.5	66 ± 1.5	11.0	1.02	30.57	1700	42

TABLE 5: Properties of fibers.

Properties	Macrosynthetic fiber	Natural jute fiber
Elastic modulus (GPa)	10	61
Density (g/mm ³)	0.91	1.26
Fiber length (mm)	30	3
Fiber diameter (mm)	1	0.015
Tensile strength (MPa)	550	510

cement concrete was poured for specimens, and the vibration and pressure tamper was used to apply vibration pressure for 30 s. Similarly, the second third was poured, and 30 s of pressure vibration compaction was carried out. The final third was poured, pressure vibration compaction was carried out, and the surface was finished. The specimens were then evaluated in terms of performance. Figure 2 shows the vibration and pressure tamper used and the specimens manufactured using the vibration and pressure tamper [16].

3. Test Methods

3.1. Compressive Strength Tests. Compressive strength tests were performed in accordance with the ASTM C 39 standard [20]. Tests were performed after 4 hours and 28 days of curing. Each variable was investigated using six specimens.

3.2. Splitting Tensile Tests. Splitting tensile tests were conducted in accordance with the ASTM C 496 standard [21]. Tests were performed after 4 hours and 28 days of curing. Specimens (Ø100 × 200 mm) were cured in water at 23 ± 2°C. Each variable was investigated using six specimens.

3.3. Flexural Tests. Flexural tests were conducted in accordance with the ASTM C 496 standard [22]. Tests were performed after 4 hours and 28 days of curing. Specimens (100 mm × 100 mm × 400 mm) were cured in water at 23 ± 2°C. Each variable was investigated using six specimens.

3.4. Chloride Ion Penetration Tests. Chloride ion penetration tests were conducted in accordance with the ASTM C 1202-94 standard [23]. Specimens, 150 mm × 50 mm in size, were tested after 28 days of curing. Each variable was investigated using six specimens. The test apparatus for the chloride ion penetration test is shown in Figure 3 [16].

3.5. Abrasion Tests. Abrasion tests were conducted in accordance with the ASTM C 944 standard [24]. Specimens,

150 mm × 60 mm in size, were tested after 7 days of curing. Each variable was investigated using six specimens. The test apparatus for the abrasion test is shown in Figure 4 [16].

4. Results and Discussion

4.1. Compressive Strength. Figure 5 shows the compressive strength test results of LMFRCRSC for a concrete pavement emergency repair according to the reinforcement fiber type and microsilica substitution ratio. Generally, when pressure vibration compaction is used, the resulting concrete is more dense and may show increased compressive strength. On mixing with jute fibers, the 4-hour curing target compressive strength of at least 21 MPa was satisfied up to a microsilica substitution ratio of 2%. Also, on mixing with macrosynthetic fibers, the target compressive strength was satisfied up to a microsilica substitution ratio of 3%. As the microsilica substitution ratio increased, the compressive strength decreased. Rapid-hardening cement promotes hydration, with an active reaction of 3CaO·SiO₂, generating acicular crystals of ettringite by the reaction of calcium silicate hydrate (CSH) gel and calcium sulfoaluminate (CSA); this increases the initial strength. With microsilica substituting for rapid-hardening cement, the 3CaO·SiO₂ ingredient is present in a smaller proportion, causing a delay in compressive strength development in the early stages. For the 4-hour compressive strength, in cases using jute fibers, as the microsilica substitution ratio increased from 0 to 1, 2, 3, and 4%, the compressive strengths were 22.1, 21.8, 21.3, 16.2, and 15.4 MPa, respectively. Using macrosynthetic fibers, as the microsilica substitution ratio increased from 0 to 1, 2, 3, and 4%, the compressive strengths were 27.5, 24.5, 23.0, 20.8, and 15.8 MPa, respectively. The cases using macrosynthetic fibers showed higher compressive strengths than those using jute fibers. Fiber-reinforcing materials can be classified into structural fibers to improve structural performance, such as strength, and nonstructural fibers to be used for crack control and durability improvement [15, 16]. In this study, macrosynthetic fibers, which can replace steel fibers as structural fibers, were applied, while jute fibers were incorporated as nonstructural fibers [15, 16]. Also, jute fiber is a natural fiber; thus, it is more difficult to maintain the quality. The jute fiber's main ingredient contains cellulose and a small amount of lignin. Lignin has the effect of delaying the concrete's compressive strength development.

The 28-day curing compressive strength results showed that the target of 35 MPa was satisfied by the results with all mixes. As the microsilica substitution ratio increased, compressive strength increased. The microsilica additive improved the performance of the concrete via the pozzolanic reaction and the fine pore-filling effect. These tendencies

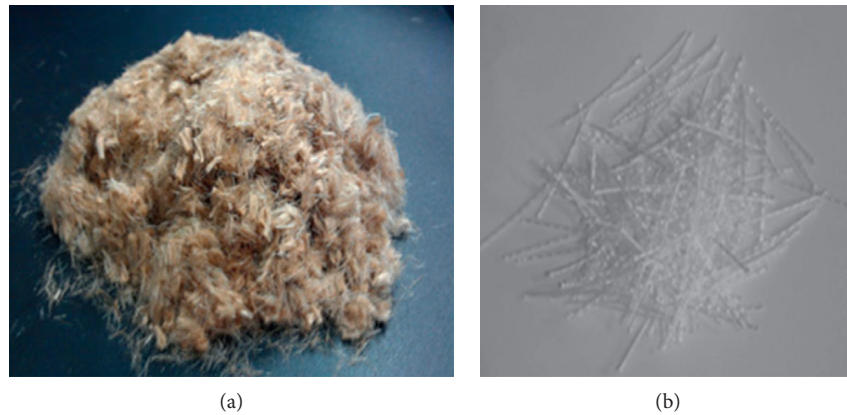


FIGURE 1: Geometry of fibers [16]. (a) Jute fiber. (b) Macrosynthetic fiber.

TABLE 6: Mix proportions of LMFRCRSC for a pavement repair.

Mix no.	W*/B** (%)	S/A (%)	W	C	Macrosilica	S	G	Unit weight (kg/m ³)				
								Latex (solid)	Water in latex	Macrosynthetic fiber	Jute fiber	
Macrosynthetic-0				400	0							
Macrosynthetic-1				396	4							
Macrosynthetic-2				392	8					0.91		—
Macrosynthetic-3				388	12							
Macrosynthetic-4	28	55	91	384	16							
Jute-0				400	0	1015	831	20	21			
Jute-1				396	4							
Jute-2				392	8						—	1.26
Jute-3				388	12							
Jute-4				384	16							

*W + water in latex. **Cement + macrosilica.

were also seen in the mixes with added jute and macrosynthetic fibers. The compressive strength was higher with macrosynthetic fibers than with jute fibers.

4.2. Flexural Strength. The flexural strength test results of LMFRCRSC for a concrete pavement emergency repair by reinforcement fiber types and the macrosilica substitution ratio are shown in Figure 6. On mixing with jute fibers, the results showed that the 4-hour curing target flexural strength of 3.5 MPa was satisfied up to a macrosilica substitution ratio of 2%. When the macrosynthetic fiber was included, the target flexural strength was satisfied up to a macrosilica substitution ratio of 3%. As the macrosilica substitution ratio increased, the flexural strength decreased. Rapid-hardening cement promotes hydration, with an active reaction of $3\text{CaO}\cdot\text{SiO}_2$, generating acicular crystals of ettringite by the reaction of CSH gel and CSA. With macrosilica substituting for rapid-hardening cement, the $3\text{CaO}\cdot\text{SiO}_2$ ingredient is present in a relatively lower proportion, causing a delay in strength development in the early stages. Thus, the strength is lower. The cases using macrosynthetic fibers showed higher flexural strengths than those using jute fibers. The

28-day curing flexural strength results showed that the target of 4.5 MPa was satisfied by all mixes. Generally, latex and reinforcement fibers have more influence on flexural strength than on compressive strength. Thus, in this study, latex and reinforcement fibers were used. The mix with no macrosilica added had the highest flexural strength. Moreover, pressure vibration compaction was used to densify the concrete structure; it was effective in increasing the concrete's strength. Thus, after curing for 28 days, the flexural strength satisfied the target strength of ≥ 4.5 MPa. As the macrosilica substitution ratio increased, the flexural strength increased slightly. Macrosilica improves the performance of the concrete, due to the pozzolanic reaction and the fine pore-filling effect. Thus, in the case of long-term strength, the flexural strength increased with the substitution ratio. This tendency was also seen in the mixes with added jute and macrosynthetic fibers. The flexural strength was slightly higher with macrosynthetic fibers than with jute fibers.

4.3. Splitting Tensile Strength. The splitting tensile strength results of LMFRCRSC for a concrete pavement emergency



(a)



(b)

FIGURE 2: Manufacturing of test specimens [16]. (a) Manufacturing of compressive strength specimens. (b) Manufacturing of flexural strength specimens.

repair by the reinforcement fiber type and the microsilica substitution ratio are shown in Figure 7. The results showed that the mixes satisfied the 28-day splitting tensile strength target of ≥ 4.2 MPa. In this study, pressure vibration compaction was used to densify the concrete structure and was effective in increasing the concrete's strength. Thus, after curing for 28 days, the splitting tensile strength satisfied the target of ≥ 4.2 MPa. The addition of latex and reinforcement fibers has more influence on tensile strength than on compressive strength. Thus, when latex and reinforcement fibers were added, splitting tensile strength also increased. All mixes satisfied the target of ≥ 4.2 MPa splitting tensile strength. Splitting tensile strength increased slightly as the microsilica substitution ratio increased; this was attributed to the pozzolanic reaction and filling of fine pores by the microsilica additive. The pozzolanic reaction has the effect of increasing the long-term strength. Moreover, while latex delays initial strength development, it increases the long-term strength. The splitting tensile strength was higher with macrosynthetic fibers than with jute fibers. This is because the macrosynthetic fiber is a structural fiber, which is used to replace the steel fiber and improves the structural performance of the concrete [16, 25, 26]. However, jute fibers are crack-control fibers, which are used to improve durability rather than structural performance [16, 27].

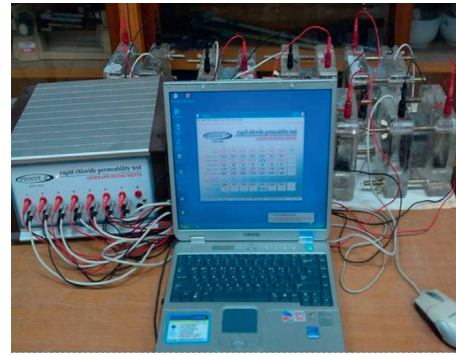
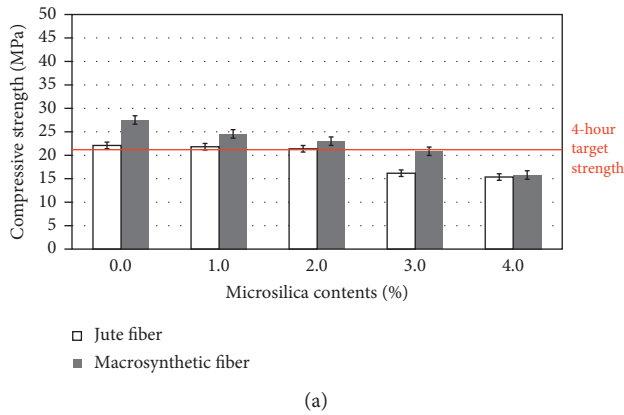


FIGURE 3: Chloride ion penetration test setup [16].

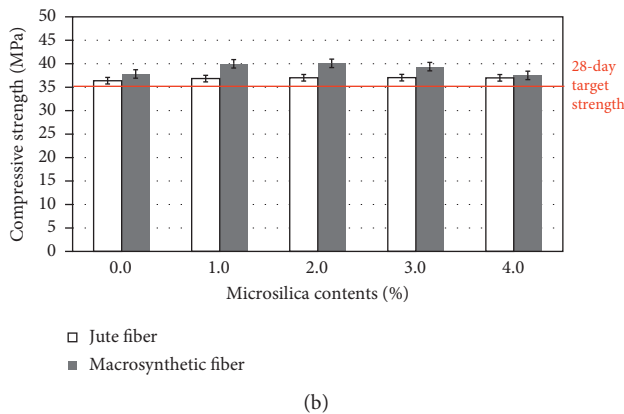


FIGURE 4: Abrasion test setup [16].

4.4. Chloride Ion Penetration. The chloride ion penetration resistance results of LMFRCRSC for a concrete pavement emergency repair by the reinforcement fiber type and the microsilica substitution ratio are shown in Figure 8. In the chloride ion penetration tests conducted after 28 days of curing, all mixes showed values lower than the target 2000 C. In this study, pressure vibration compaction was used to densify the concrete structure. Thus, with 28 days of curing, all mixes satisfied the target chloride ion penetration amount of ≤ 2000 C. Also, the target value of 4000 C or less at 4 h of curing was satisfied for all mix ratios. In the case of rapid-hardening cement concretes, cracks occur inside the cement due to high hydration heat in the early stages [1–3]. The addition of reinforcement fibers appeared to offset hydration heat-induced crack formation [5, 12]. Because the reinforcing fibers inhibit the internal cracks due to the generation of hydration heat before sufficient strength is developed, the chlorine ion penetration amount decreases. For the 4-hour curing stage, all mixes showed moderate water penetration properties. The reinforcing fibers inhibit internal crack formation due to the generation of hydration heat before sufficient strength develops. Therefore, it can be concluded that the addition of reinforcing fibers is effective in reducing chloride ion penetration at the initial curing period in the repair concrete. After curing for 28 days, all



(a)



(b)

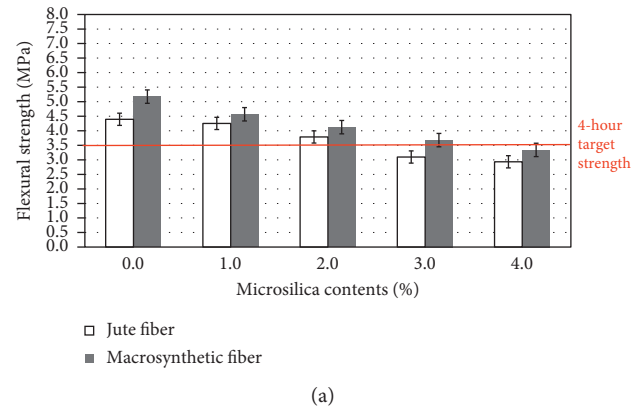
FIGURE 5: Compressive strength of LMFRCRSC. (a) 4-hour curing. (b) 28-day curing.

mixes showed low-level penetration at up to 2% microsilica content. When the microsilica content exceeded 3%, low-level permeability was observed. Also, the results showed decreased chloride ion penetration in cases using macrosynthetic fibers versus those using jute fibers. The main ingredient of the jute fiber is cellulose, plus a small amount of lignin. Lignin has the effect of delaying the concrete's strength development [16, 27]. Therefore, the hardening was insufficient, and the chloride ion permeability was enhanced.

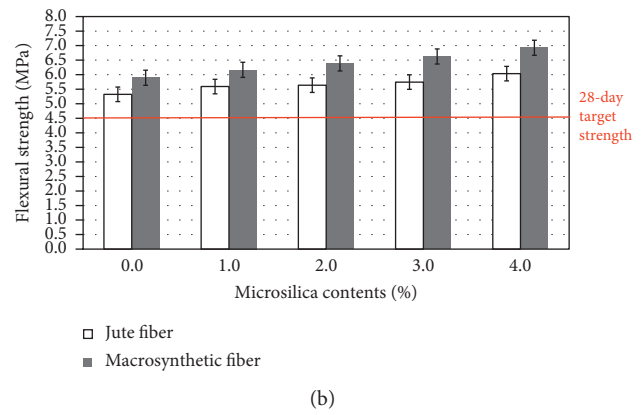
4.5. Abrasion Resistance. The abrasion test results of LMFRCRSC for a concrete pavement emergency repair by the reinforcement fiber type and the microsilica substitution ratio are shown in Figure 9. As the microsilica substitution ratio increased, the results showed decreased abrasion on the concrete surface. This is because when microsilica is added to the concrete, the pozzolanic reaction and the fine pore-filling effect create a more dense concrete structure with improved abrasion resistance. By the fiber reinforcement type, the results showed increased abrasion resistance in the cases using macrosynthetic fibers versus those using jute fibers. However, the difference in the results was not significant.

5. Conclusions

This study evaluated the influence of reinforcement fiber types and microsilica on the performance of LMFRCRSC for



(a)



(b)

FIGURE 6: Flexural strength of LMFRCRSC. (a) 4-hour curing. (b) 28-day curing.

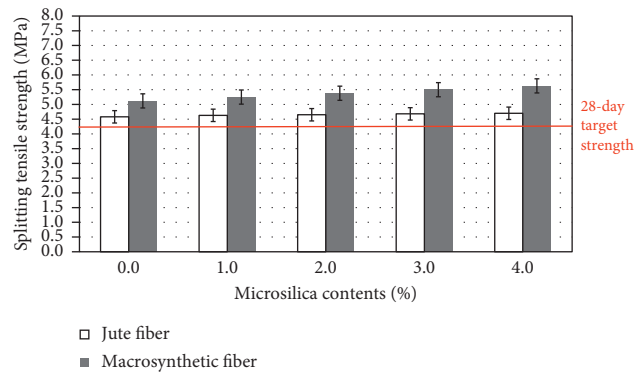


FIGURE 7: Splitting tensile strength of LMFRCRSC.

a concrete pavement emergency repair. A summary of the test results is given below:

- (i) In the compressive strength and flexural strength tests with curing for 4 h, the strength decreased as the microsilica substitution ratio increased. For the jute fiber-reinforced concrete mix with 4-hour curing, a target compressive strength of ≥ 21 MPa and target flexural strength of ≥ 3.5 MPa were achieved up to a microsilica substitution ratio of 2%. When the macrosynthetic fiber was mixed, the 4-hour curing target strength was satisfied up to a microsilica substitution ratio of 3%.

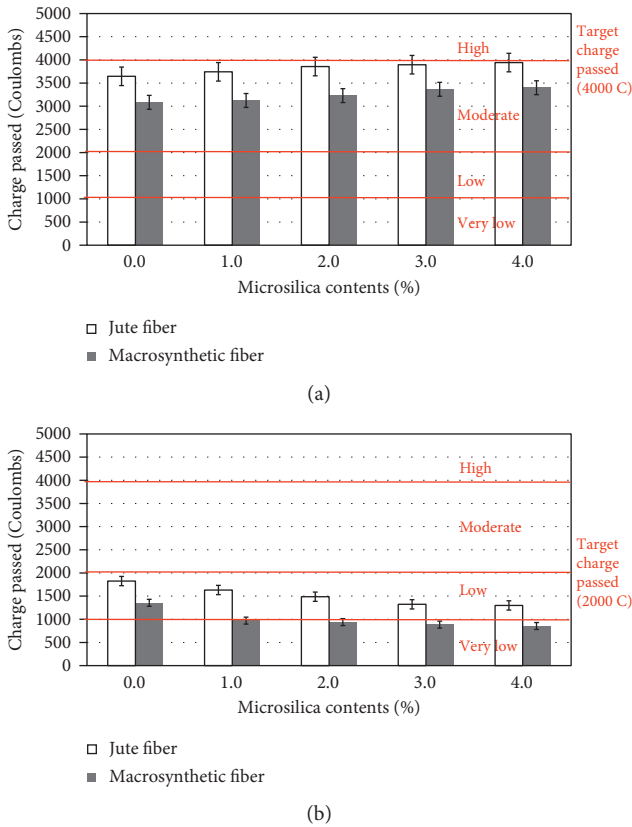


FIGURE 8: Chloride ion penetration of LMFRCRSC. (a) 4-hour curing. (b) 28-day curing.

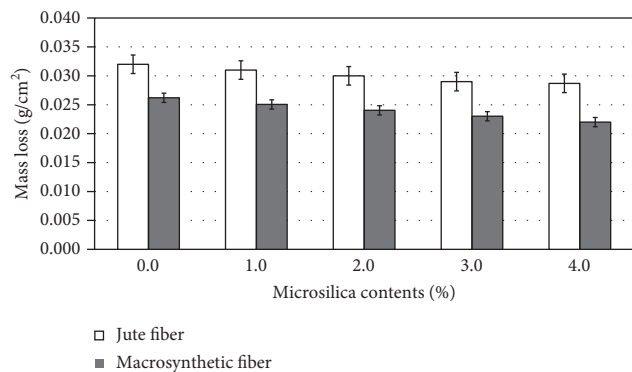


FIGURE 9: Abrasion resistance of LMFRCRSC.

- (ii) With curing for 28 days, the compressive strength, flexural strength, and splitting tensile strength increased as the microsilica substitution ratio increased. Also, with curing for 28 days, the target compressive strength (≥ 35 MPa), flexural strength (≥ 4.5 MPa), and splitting tensile strength (≥ 4.2 MPa) were all satisfied.
- (iii) In terms of compressive, flexural, and splitting tensile strength test results, cases with macrosynthetic fibers showed higher values than cases with jute fibers.
- (iv) From the chloride ion penetration tests, as the microsilica substitution ratio increased, the chloride

ion penetration decreased. All mixes satisfied the target chloride ion penetration of ≤ 2000 C after curing for 28 days. Regarding the reinforcement fiber, chloride ion penetration decreased more with macrosynthetic fibers than with jute fibers, but the difference was minor.

- (v) From the abrasion, as the microsilica substitution ratio increased, the abrasion resistance properties increased. With respect to the fiber type, the macrosynthetic fibers showed slightly better results than jute fibers.
- (vi) For mixes that satisfied both the target strength goals and the target chloride ion penetration amount, with improved abrasion resistance, the results showed that when the microsilica substitution ratio was 3% or less and macrosynthetic fiber was used as the reinforcement fiber, LMFRCRSC performance improved for a concrete pavement emergency repair and satisfied the target values. Also, the microsilica would likely be used because of the high cost of microsilica and the marginal increase in benefits with increasing amounts.

Conflicts of Interest

The authors declare that they have no conflicts of interest.

Acknowledgments

This work was supported by the research grant of the Kongju National University in 2017.

References

- [1] J. P. Won, J. M. Kim, S. J. Lee, S. W. Lee, and S. K. Park, "Mix proportion of high-strength, roller-compacted, latex-modified rapid-set concrete for rapid road repair," *Construction and Building Materials*, vol. 25, no. 4, pp. 1796–1800, 2011.
- [2] ACI, "State-of-the-art report on roller compacted concrete pavements," 2 Tech. Rep.32510R-95, American Concrete Institute, Farmington Hills, MI, USA, 1995.
- [3] J. La Hucik, S. Dahal, J. Roesler, and A. N. Amirhanian, "Mechanical properties of roller-compacted concrete with macro-fibers," *Construction and Building Materials*, vol. 135, pp. 440–446, 2017.
- [4] S. Krishna Rao, P. Sravana, and T. Chandrasekhar Rao, "Abrasion resistance and mechanical properties of roller compacted concrete with GGBS," *Construction and Building Materials*, vol. 114, pp. 925–933, 2016.
- [5] S. Krishna Rao, P. Sravana, and T. Chandrasekhar Rao, "Investigating the effect of M-sand on abrasion resistance of fly ash roller compacted concrete (FRCC)," *Construction and Building Materials*, vol. 118, pp. 352–363, 2016.
- [6] J. N. Karadelis and Y. Lin, "Flexural strengths and fibre efficiency of steel-fibre-reinforced, roller-compacted, polymer modified concrete," *Construction and Building Materials*, vol. 93, pp. 498–505, 2015.
- [7] J.-W. Han, J.-H. Jeon, and C.-G. Park, "Mechanical and permeability characteristics of latex-modified pre-packed

- pavement repair concrete as a function of the rapid-set binder content," *Materials*, vol. 8, no. 10, pp. 6728–6737, 2015.
- [8] J. P. Won, J. H. Kim, C. G. Park, and J. W. Kang, "Shrinkage cracking of styrene butadiene polymeric emulsion-modified concrete using rapid-hardening cement," *Journal of Applied Polymer Science*, vol. 112, no. 4, pp. 2229–2234, 2009.
- [9] M. Sprinkel, "Latex-modified concrete overlay containing type K cement," Tech. Rep. FHWA/VTRC 05–R26, Virginia Transportation Research Council, Charlottesville, VA, USA, 2005.
- [10] M. Sprinkel, "High early strength latex modified concrete overlay," Tech. Rep. VTRC 88–R12, Virginia Transportation Research Council, Charlottesville, VA, USA, 1998.
- [11] M. Sprinkel, "Very-early-strength latex-modified concrete over-lays," Tech. Rep. TAT99–TAR3, Virginia Transportation Research Council, Charlottesville, VA, USA, 1998.
- [12] Z. J. Ricardo, "Development of rapid, cement-based repair materials for transportation structures," M.S. thesis, The University of Texas at Austin, Austin, TX, USA, 2013.
- [13] D. H. Kim and C. G. Park, "Permeability, abrasion, and impact resistance of latex-modified fibre reinforced concrete for precast concrete pavement application," *Progress in Rubber, Plastics & Recycling Technology*, vol. 29, pp. 239–254, 2013.
- [14] R. O. Oh, D. H. Kim, and C. G. Park, "Durability performance of latex modified nylon fiber reinforced concrete for precast concrete pavement applications," *Indian Journal of Engineering and Materials Sciences*, vol. 21, pp. 49–56, 2014.
- [15] D. H. Kim and C. G. Park, "Strength, permeability and durability of hybrid fiber-reinforced concrete containing styrene butadiene latex," *Journal of Applied Polymer Science*, vol. 129, pp. 1499–1505, 2013.
- [16] S. K. Lee, M. J. Jeon, S. S. Cha, and C. G. Park, "Mechanical and permeability characteristics of latex-modified fiber-reinforced roller-compacted rapid-hardening-cement concrete for pavement repair," *Applied Sciences*, vol. 7, no. 7, p. 694, 2017.
- [17] A. Dousti, M. Shekarchi, R. Alizadeh, and A. Taheri-Motlagh, "Binding of externally supplied chlorides in micro silica concrete under field exposure conditions," *Cement and Concrete Composites*, vol. 33, no. 10, pp. 1071–1079, 2011.
- [18] AASHTO, *Standard Specification of Rigid Pavement*, American Association of State Highway and Transportation Officials, Washington, DC, USA, 1998.
- [19] Korea Expressway Corporation, *Construction Material Quality and Standard for Highway Construction*, Korea Expressway Corporation, Seongnam, Republic of Korea, 2005.
- [20] ASTM C39, *Standard Test Method for Compressive Strength of Cylindrical Concrete Specimens*, American Society for Testing Materials, Philadelphia, PA, USA, 2015.
- [21] ASTM C496/C496M, *Standard Test Method for Splitting Tensile Strength of Cylindrical Concrete Specimens*, American Society for Testing Materials, Philadelphia, PA, USA, 2011.
- [22] ASTM C 78/C78M, *Standard Test Method for Flexural Strength of Concrete (Using Simple Beam with Third-Point Loading)*, American Society for Testing Materials, Philadelphia, PA, USA, 2015.
- [23] ASTM C1202, *Standard Test Method for Electrical Indication of Concrete's Ability to Resist Chloride Ion Penetration*, American Society for Testing Materials, Philadelphia, PA, USA, 2012.
- [24] ASTM C944, *Standard Test Method for Abrasion Resistance of Concrete or Mortar Surfaces by the Rotating-Cutter Method*, American Society for Testing Materials, Philadelphia, PA, USA, 2012.
- [25] J. P. Won, D. H. Lim, C. G. Park, and H. G. Park, "Bond behavior and flexural performance of structural synthetic fiber reinforced concrete," *Magazine of Concrete Research*, vol. 28, no. 6, pp. 401–410, 2003.
- [26] J. P. Won, C. G. Park, S. W. Lee, C. I. Jang, and H. Y. Kim, "Performance of synthetic macrofibers in reinforced concrete for tunnel linings," *Magazine of Concrete Research*, vol. 61, no. 3, pp. 165–172, 2009.
- [27] A. Bentur and S. Mindess, *Fiber Reinforced Cementitious Composites*, Elsevier Applied Science, London, UK, 1992.

Research Article

Mechanical Attributes of Uniaxial Compression for Calcium Carbonate Whisker Reinforced Oil Well Cement Pastes

Yuanyi Yang,^{1,2} Shun Fu,³ and Xingkui Li²

¹College of Materials and Chemistry & Chemical Engineering, Chengdu University of Technology, Chengdu, China

²Department of Materials Engineering, Sichuan College of Architectural Technology, Deyang, China

³College of Administrative Science, Chengdu University of Technology, Chengdu, China

Correspondence should be addressed to Shun Fu; fs@cdut.edu.cn

Received 18 June 2017; Revised 11 August 2017; Accepted 6 September 2017; Published 23 November 2017

Academic Editor: Rishi Gupta

Copyright © 2017 Yuanyi Yang et al. This is an open access article distributed under the Creative Commons Attribution License, which permits unrestricted use, distribution, and reproduction in any medium, provided the original work is properly cited.

It is crucial for design and safety of the cementing sheath to develop better understanding of the CaCO₃ whisker reinforced oil well cement pastes. The uniaxial compression curve, mechanical constitutive relation, and reinforcing mechanism of the CaCO₃ whisker reinforced oil well cement pastes are studied in this script. The results indicate that the CaCO₃ whisker under the 10% dosage could improve the tensile strength of the cement paste significantly. The peak stress, elasticity modulus, and the energy at different stages of the stress-strain curve of the CaCO₃ whisker reinforced cement paste are reinforced with the increasing of CaCO₃ whisker. Afterward, the constitutive model of stress-strain curve, the toughness index, and capability coefficients index of the CaCO₃ whisker reinforced cement paste are established. A physical model of the interface layer is also established and the micromechanical reinforcement is related to the double film layer between the CaCO₃ whisker and cement matrix which could be bonded with much more fastness to the cement surface. The development of this script provides new ways to analyze the toughening mechanism of CaCO₃ whisker and establishes a correlation between basic material structure and the physical properties.

1. Introduction

With many advantages such as excellent mechanical properties, modest price, easy producing process, and natural compatibility with the cement, the application of inorganic crystal whiskers is developing rapidly in the industry. The application of inorganic crystal whiskers in the cement based composite not only is with high worth for academic research and good prospect of engineering employment but is also important for the energy conservation and sustainable development in the manufacture. The researches focused on the inorganic crystal whiskers reinforced cement pastes are gradually improved as a hotspot. Cao et al. [1, 2] have firstly explored the calcium carbonate whiskers in the cement based composite as reinforcing material, and the result of the study shows that the compressive strength, flexible strength, and tensile strength of the cement pastes with calcium carbonate whisker are increased. Cao et al. [3] have researched the cement pastes with hybrid fibers of calcium carbonate whisker and basalt fiber which displays that the hybrid effect

with different kinds of fibers could arise in the cement pastes and the mechanical property of the cement pastes would be improved further than with just single fiber. Simultaneously, with the perfect performance of high strength, high elasticity modulus, excellent heat-resisting, and heat insulation, the calcium carbonate whisker as a kind of desired filling material could fit the requests of the cementing and geological engineering in petroleum industry well [1, 4]. Li et al. [5, 6] have explored the workability of the cement slurry and the mechanical performance and the microstructure of the oil well cement pastes with hybrid fibers of calcium carbonate whisker and carbon fiber. The strengthening mechanism with hybrid fibers is elaborated as hybrid reinforcement. Ming et al. [7] have found that calcium carbonate whisker could not only reinforce mechanical performance of the oil well cement pastes but also develop the static gel strength conspicuously that could enhance the gas channeling prevention of the oil well cement slurry.

From the above, almost all the studies are focused on the traditional mechanical performances of cement pastes and

TABLE 1: Properties of CaCO₃ whisker.

Material	Density ratio	Relative molecular weight	Draw ratio	Appearance	Size	Origin
CaCO ₃ whisker	2.8 g/cm ³	100.09	20–30		20–80 μm	China, Shandong Runxing Chemical Industry Co., Ltd.

TABLE 2: Mix proportions of cement pastes.

CaCO ₃ whisker dosage	Cement (g)	Defoaming agent (g)	Water reducer (g)	Water (g)	CaCO ₃ whisker (g)	Water-cement ratio
0	800	1	8	352	0	0.44
3%	776	1	8	352	24	0.44
5%	760	1	8	352	40	0.44
8%	736	1	16	352	64	0.44
10%	720	1	16	352	80	0.44

workability of the cement slurry. Meanwhile, the constitutive relation is based on the mechanical properties of cement pastes and the macroscopic constitutive model of cement paste could be established through the experimental data as a kind of continuous state material. As a key basic property, the uniaxial compression of cement pastes is important to research of the bearing capacity and the deformability of cement sheath. And the stress-strain diagram is also a reflection of comprehensive capability of the cement material. The arising of the plastic deformation, producing and extending of the microcrack, peak strength, and the ultimate deformation of the cement pastes all appeared in the stress-strain diagram as the most important factors account for the compressive capacity and nonlinear process [8–11]. Nevertheless, the researches appearing in studies of the constitutive relation and stress-strain diagram of uniaxial compression focused on the CaCO₃ whisker reinforced oil well cement pastes are quite insufficient.

The purpose of this study is to gain a better comprehending of the physical properties as well as the strengthening and toughening mechanism of the CaCO₃ whisker reinforced oil well cement pastes. Establishing the constitutive relation between the CaCO₃ whisker and oil well cement pastes, analyzing the stress-strain diagram, and calculating the physical model of interface layer are helpful for further research on the oil well cement based composite material. Therefore, the uniaxial compression curve, mechanical constitutive relation, and microreinforcing mechanism of the CaCO₃ whisker reinforced oil well cement pastes are tested and discussed in this script to elaborate the fundamental physical effect of CaCO₃ whisker reinforced oil well cement paste, which could

lead to a better design and more safer cementing sheath, to achieve desirable toughening effects and improve wellbore integrity.

2. Materials and Methods

The materials applying in this script were cement (G high sulfur resistant oil well cement, Sichuan, China), CaCO₃ whisker, water reducer (phenol and formaldehyde condensation polymer, Chengdu, China), defoaming agent (dibutyl phosphate, Chengdu, China), and pure water. The basic properties and chemical constituents of CaCO₃ whisker were shown in Table 1, respectively.

The cement slurry of CaCO₃ whisker was produced based on the Chinese standard “GB10238-2005 Oil Well Cement” and “GB/T19139-2012: The Application Performance and Test Methods of Oil-Well Cement.” Thereafter, the mix design was divided into three steps which were elucidated as follows.

Step 1. The water reducer was mixed with the cement powder for 5 min by cement mortar mixer as predispersing powder.

Step 2. The CaCO₃ whisker powder was mixed with the cement predispersing powder according to the quality fraction of the cement (as shown in Table 2) for 5 min before being agitated with water.

Step 3. All the mixed powder was transported to a high speed mixer for blending with water in 2 min and producing the cement slurry, whereby the mixing procedures were illustrated in Figure 1.

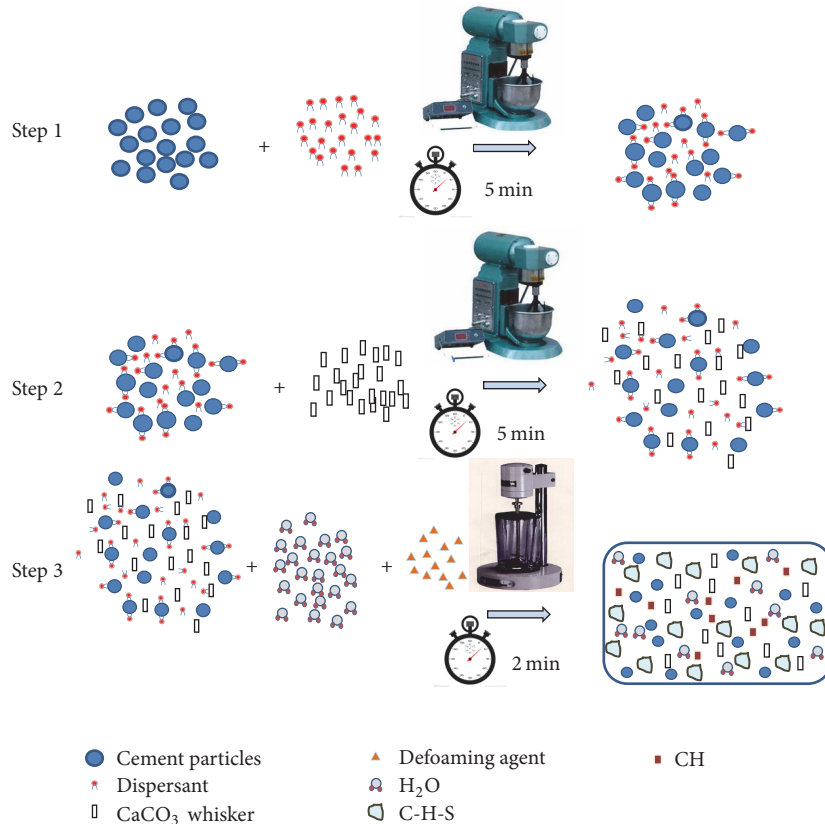


FIGURE 1: The mixing procedure for fresh cement paste mixtures.

Afterwards, the curing condition of the cement slurry was under the relative humidity 95% and 30°C for 7 days as preparation.

The split tensile strength of the cement pastes was test based on the Chinese standard “GB/T50081-2002: The Standard of Concrete Mechanics Performance Test Method” and the test specimen size of the cement pastes was 70.7 mm × 70.7 mm × 70.7 mm. The uniaxial compression experiment of cement pastes was tested by a CMT-300 universal testing machine with 300 kN maximum test load and 0.5 accuracy index, which was produced by the Shandong Jinan Lian Engineering Testing Technology, Co., Ltd. The test specimen size of the cement pastes for uniaxial compression experiment was 70.7 mm × 70.7 mm × 70.7 mm as well. The control mode of this experiment was displacement and the loading rate of the experiment was 0.06 mm/s; additionally the test data was collected by the computer software and the diagram of experimental facility as in Figure 2.

3. Results and Discussion

In this part, the macroscopic mechanical properties of split tensile strength, uniaxial compression strength, stress-strain curve, constitutive model, and fracture energy were studied and elucidated. Meanwhile the micrographs of cement pastes fracture with CaCO₃ whiskers and the reinforcing effect were also shown and elaborated as follows.

3.1. The Split Tensile Strength. Under the oil well, the cement sheath would be easily destroyed by the tensile stress. Therefore the split tensile strength of the cement pastes with different dosage of the CaCO₃ whisker was presented in Figure 3. With the increasing of the CaCO₃ whisker, the improving trend of cement pastes tensile strength has taken place. Thereafter, the dosage exceeded 10%; the tensile strength started to decrease significantly. At the 10% point, the growth of the tensile strength was increased by 54% as the highest comparing to the control sample. With high mechanical strength, the CaCO₃ whisker could fill in the cement and restrict the formation and propagation process of the microcrack [12, 13]. At the dosage of CaCO₃ whisker of 15%, the tensile strength of the cement pastes has fallen down seriously. Hereby, over this dosage, the CaCO₃ whisker could not be dispersed well and the cement material was decreased so that the CaCO₃ whisker could not be embraced homogeneously by the cement slurry. As in Figure 4, the white dots were marked by red circles, which were the CaCO₃ whiskers aggregating on the test-piece failure surface. Thus the added quantity of the CaCO₃ whisker was confined from 1% to 10% in the next test part of the uniaxial compression.

3.2. The Stress-Strain Curve. Incorporating with different dosages of CaCO₃ whisker, the stress-strain curves of the cement pastes were presented in Figure 5, used to assess the contribution of different dosage of CaCO₃ whisker. By increasing the CaCO₃ whisker, the peak compressive stress

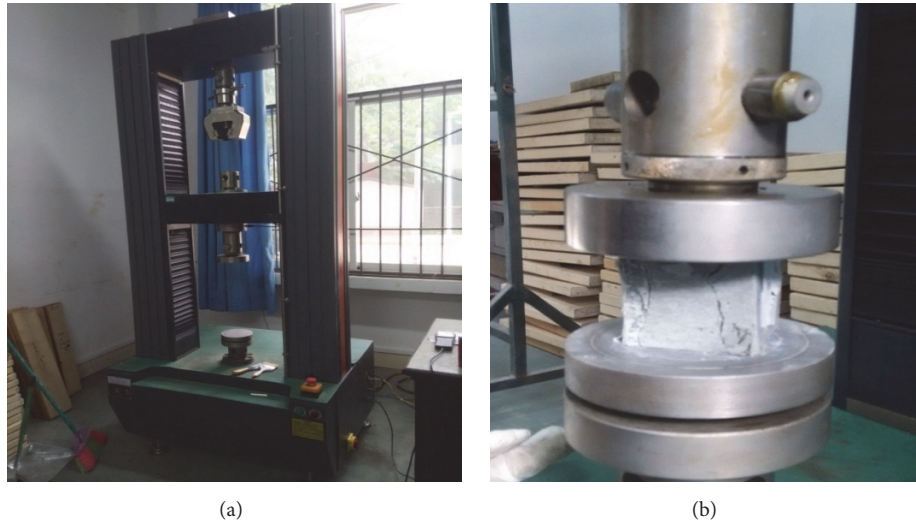


FIGURE 2: (a) Experimental facility. (b) Uniaxial compression fixture for cement pastes.

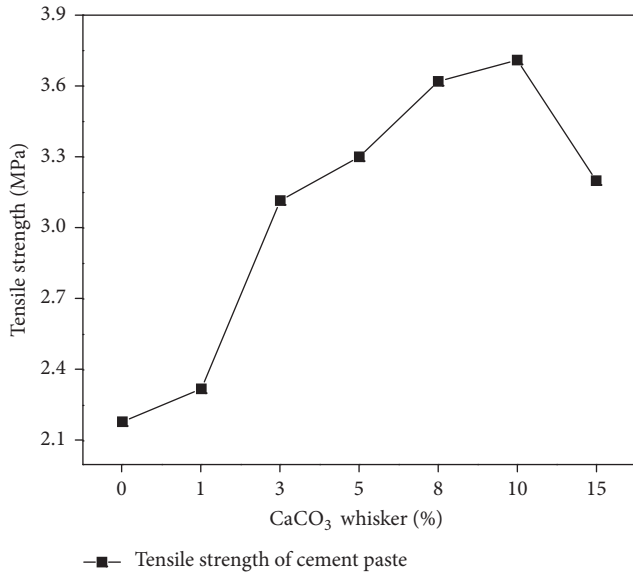


FIGURE 3: Tensile strength of CaCO₃ whisker.



FIGURE 4: The failure surface of test-piece reinforced cement pastes.

was improved effectively and each deforming phase was still obvious; hereby that was the possibility of establishing the mathematical model to understand the complete stress-strain process. By increasing the CaCO₃ whisker, the stiffness of the cement paste was also improved observably at the elastic stage comparing to the control sample; this improvement was caused by the curve slope and the elasticity modulus rising. Since the peak stress and peak strain were enhanced with the CaCO₃ whisker increasing, the deformation energy of the cement pastes could be improved at the elastic-plastic deformation stage and the energy analysis would be elucidated in Section 3.4 adequately. Afterward, beyond the ultimate high dosage, the dispersity of CaCO₃ whisker in cement slurry had been hindered for further improving. However, as the filling effect, the peak stress of cement paste with high CaCO₃ whisker quality could be still higher than the control sample but with reduction of the deformation energy.

The results of uniaxial compression test were shown in Table 3 and the mathematical fitting relationship between CaCO₃ whisker and the peak stress was expressed as formula (1). Thereby the fitted curve was shown in Figure 6 and the relationship between CaCO₃ whisker and the peak stress was approximately a linear function. This means that the peak stress of the cement paste was increasing with the CaCO₃ whisker. The fitting formula between CaCO₃ whisker and the elasticity modulus was shown as formula (2), and the fitted curve was shown in Figure 7. The relationship between the CaCO₃ whisker and elasticity modulus was likely monomial function; thus the CaCO₃ whisker had reinforced the elasticity modulus of the cement paste well. The relationship between the CaCO₃ whisker and peak strain was exhibited in Figure 8, which showed that the peak strain was fluctuated from 0.6 to 0.8 with different dosage of CaCO₃ whisker. Thereby it could not be ruled and the CaCO₃ whisker could hardly impact the peak strain of cement pastes.

$$F_c = 2.86N_f + 128.32 \tag{1}$$

TABLE 3: The result of uniaxial compression test.

Dosage of CaCO ₃ whisker	Peak stress (kN)	Peak strain (mm)	Elasticity modulus (N/mm ²)
0	128.80	1.89	1356.97
3%	136.50	1.41	1564.12
5%	140.40	1.69	1473.30
8%	155.70	1.87	1418.84
10%	154.50	2.03	1387.21

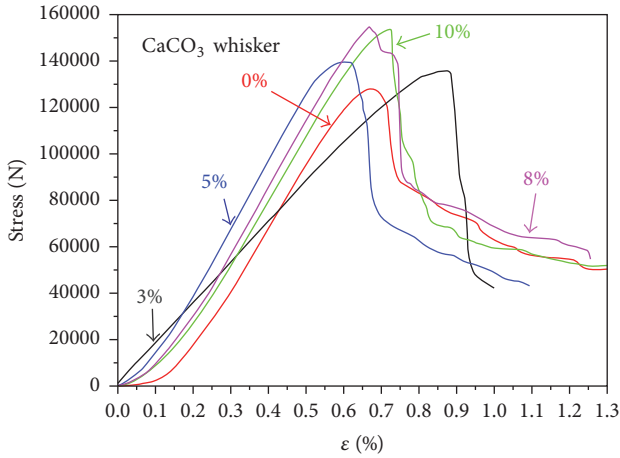


FIGURE 5: The stress-strain curve of different CaCO₃ whisker dosage cement pastes.

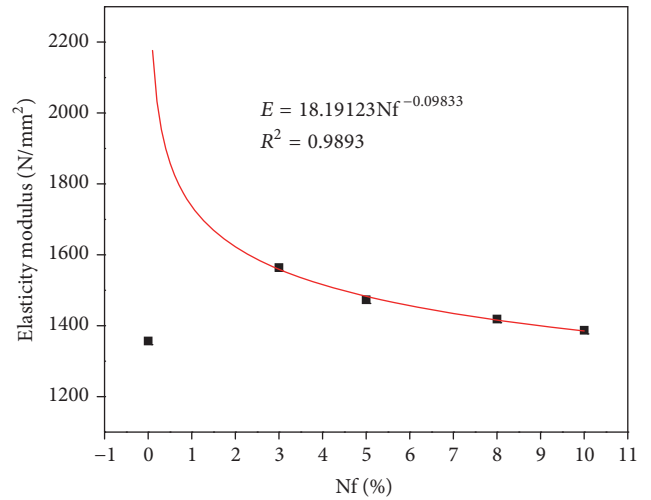


FIGURE 7: Plot of elasticity modulus against CaCO₃ whisker.

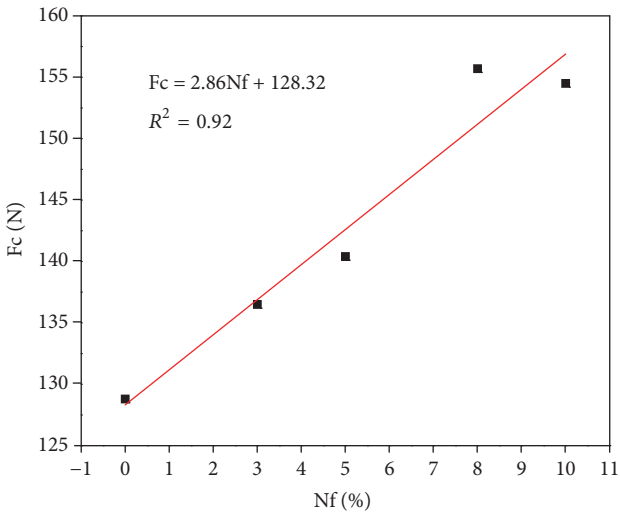
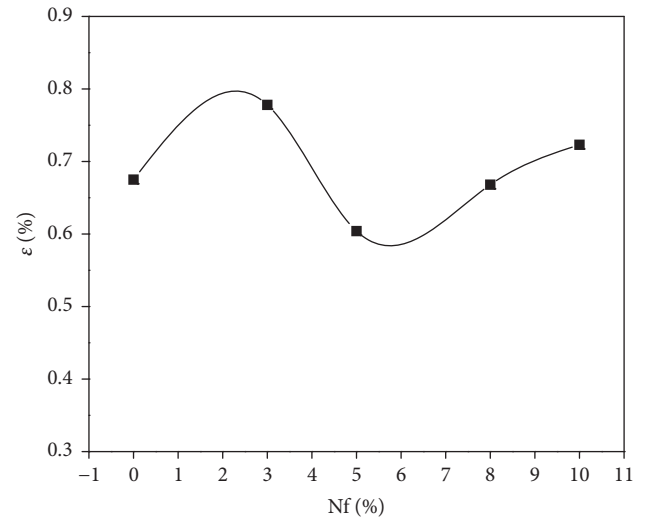


FIGURE 6: Plot of peak stress against CaCO₃ whisker.

$$E = 18.19Nf^{-0.10}, \quad (2)$$

where the F_c , N_f , and E were with respect to the peak stress, CaCO₃ whisker dosage, and elasticity modulus.

3.3. The Constitutive Model of Stress-Strain Curve. Figure 5 showed that although the stress-strain curves of CaCO₃



■ CaCO₃ whisker reinforced cement paste

FIGURE 8: Plot of peak strain against CaCO₃ whisker.

whisker were at different dosage, the basic geometrical characteristics and processes of the uniaxial compression test were similar. A test result of experiment was chosen to illustrate the typical fiber reinforced cement uniaxial stress-strain curve

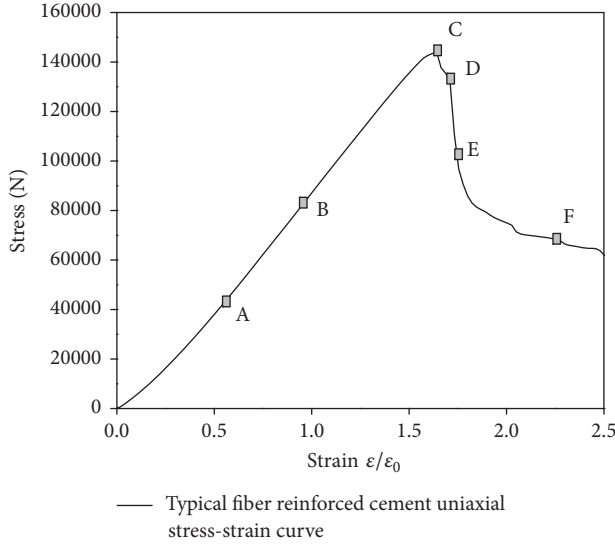


FIGURE 9: Typical fiber reinforced cement uniaxial stress-strain curve.

in Figure 9. Meanwhile the constitutive model of CaCO_3 whisker cement pastes stress-strain curve was established and analyzed in this part. A new mathematic relation was proposed in this part, which was enlightened by Zhenhai Guo from Tsinghua University [11].

(1) The stress-strain curve of CaCO_3 whisker reinforced cement paste was split into two parts as ascent stage and descent stage for fitting and analyzing as follows:

$$y = a_0 + a_1x + a_2x^5 + a_3x^6 \quad (3)$$

($x \leq 1$) the equation of ascent stage

$$y = \frac{x}{b_0 + b_1x + b_2x^2} \quad (4)$$

($x \geq 1$) the equation of descent stage,

where $x = \varepsilon/\varepsilon_p$, $y = \delta/\delta_p$, and ε and δ were the stress and strain. ε_p , δ_p were the peak strain and peak stress and $a_0, a_1, a_2, a_3, b_0, b_1, b_2$ were the calculating parameters of the curve.

(2) The ascent stage ($0 \leq x \leq 1$) is as follows.

As the stress-strain curve showed, a_0, a_1, a_2 , and a_3 should fit the geometrical feature as follows:

(A) The curve went through the origin and that meant when $x = 0$, then $y = 0$.

(B) When $0 \leq x < 1$, $\partial^2 y/\partial x^2 < 0$, the slope (dy/dx) of ascent stage decreased monotonously and with no inflection point.

(C) $x = 1$, $dy/dx = 0$, $y = 1$ was the necessary condition of the peak point C on the curve.

Taking (A), (B), and (C) conditions into (3), calculate the results as $a_0 = 0$, $a_2 = 6 - 5a_1$ and $a_3 = 4a_1 - 5$. Afterwards, to solve the problem was subject to calculating the independent parameter a_1 .

Then (3) was turned into

$$y = a_1x + (6 - 5a_1)x^5 + (4a_1 - 5)x^6. \quad (5)$$

From (3), when $x = 0$, then $dy/dx = a_1$.

Thus the following could be obtained:

$$a_1 = \left. \frac{dy}{dx} \right|_{x=0} = \left. \frac{d(\delta/\delta_p)}{d(\varepsilon/\varepsilon_c)} \right|_{x=0} = \frac{d\delta/d\varepsilon|_{x=0}}{\delta_p/\varepsilon_c} = \frac{E_0}{E_p}, \quad (6)$$

where the $E_0 = (d\delta/d\varepsilon)|_{x=0}$ (N/mm^2) was the elasticity modulus of initial tangent of the cement pastes and $E_p = \delta_p/\varepsilon_c$ (N/mm^2) was the ratio between the peak strength and peak strain as the secant modulus of the peak point of the curve, while a_1 was the ratio of the initial tangent modulus and secant modulus. The ascent stage of the curve could be calculated by E_c and E_p . Meanwhile the curve also fit condition (B), when $0 \leq x < 1$ and $\partial^2 y/\partial x^2 < 0$; then the following could be obtained:

$$\begin{aligned} \text{when } x = 1 \text{ as } \frac{\partial^2 y}{\partial x^2} &= 20(6 - 5a_1)x^4 + 30(4a_1 - 5)x^5 \leq 0 \\ (x = 1) \longrightarrow 20(6 - 5a_1) + 30(4a_1 - 5) &\leq 0 \\ \longrightarrow 20a_1 &\leq 30 \\ \longrightarrow a_1 &\leq 1.5 \end{aligned} \quad (7)$$

$$\text{also the } a_1 = \left(\frac{E_0}{E_p} \right) E_c > 0,$$

$$E_p > 0, \text{ then } a_1 > 0, 0 < a_1 \leq 1.5.$$

The plots of the calculated curves at the ascent stage with different a_1 were shown in Figure 10. When $a_1 > 1.5$, at the top part of the curve that was violated the actual test results were caused by $y > 1$. Simultaneously, the calculated results were contrasted with the actual test curves as Figure 11 (where the solid lines showed the calculation and the dashed lines showed the test samples). When $a_1 < 0.6$, the calculating curve could not fit the test result without an inflection point. Therefore, the data range of the a_1 could be suggested as

$$0.5 < a_1 \leq 1.5. \quad (8)$$

(3) The descent stage ($x \geq 1$) is as follows.

As the stress-strain curve showed, b_0, b_1 , and b_2 should fit the geometrical feature as follows:

(A) When $x = 1$, $dy/dx = 0$, and $y = 1$ the curve should reach peak point C.

(B) When $\partial^2 y/\partial x^2 = 0$, $x_D > 1.0$, hereby there was another inflection point as D.

(C) When $\partial^3 y/\partial x^3 = 0$, $x_E (> x_D)$, then the maximum curvature point of the descent stage was E.

(D) When $x \rightarrow \infty$, $y \rightarrow 0$ and $dy/dx \rightarrow 0$, the descent stage of the curve would be extended indefinitely and converged to coordinate axis without intersects; thus the whole curve should fit $x \geq 0, 0 < y \leq 1$.

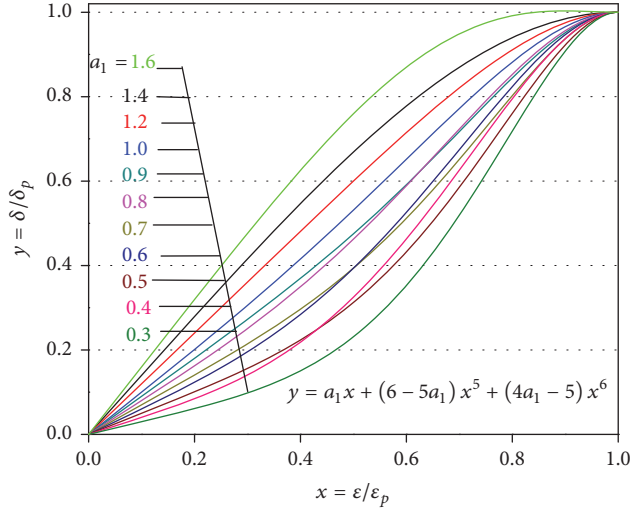
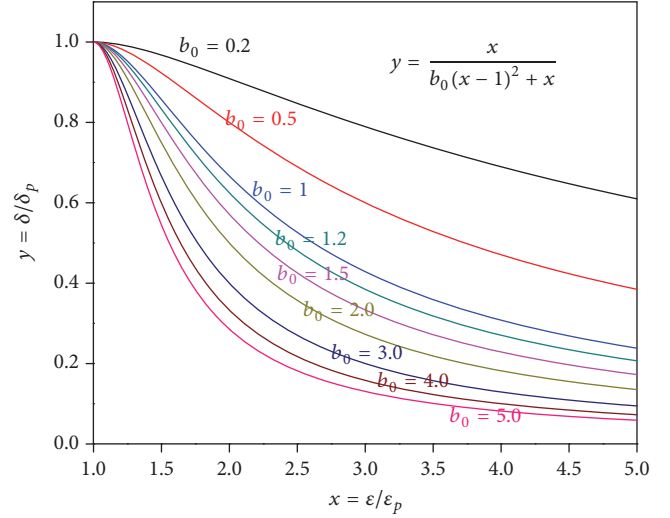
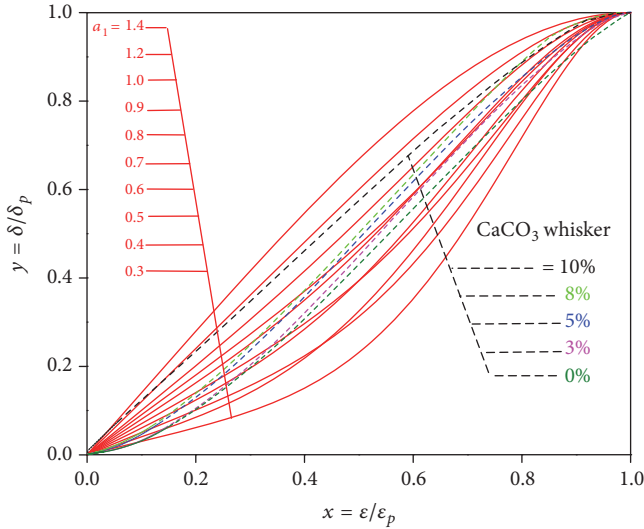

 FIGURE 10: a_1 and the calculated curve at the ascent stage.

 FIGURE 12: b_0 and the calculated curve at the descent stage.


FIGURE 11: The calculated curve contrast to the test curve.

To take (A) into (4) this would obtain the result as $b_1 = 1 - 2b_0$, $b_2 = b_0$ that could left the only parameter as b_0 . Then (4) would change as

$$y = \frac{x}{b_0(x-1)^2 + x} \quad x \geq 1. \quad (9)$$

Equation (9) should fit the conditions of (C) and (D). When $b_0 = 0$, then $y \equiv 1$.

As the curve presented when $b_0 \rightarrow \infty$, then $y \rightarrow 0$ and after peak point C, the residual stress of the cement paste was approaching 0 and at this time the cement paste would be considered as fragile material completely.

Based on condition (B), it could be calculated as

$$\frac{\partial^2 y}{\partial x^2} = \frac{2b_0 [x^3 - 3x + (2 - 1/b_0)]}{[b_0(x-1)^2 + x]^3} = 0. \quad (10)$$

Afterward, the value of point D could be calculated (when $x > 1$) based on condition (C) and that would be

$$\begin{aligned} \frac{\partial^3 y}{\partial x^3} &= \frac{-6b_0 [b_0^2 x^4 - 6b_0^2 x^2 + (8b_0^2 - 4b_0)x - (3b_0^2 - 4b_0 + 1)]}{[b_0(x-1)^2 + x]^3} \quad (11) \\ &= 0. \end{aligned}$$

Then the maximum curvature point E could be also calculated ($x_E > x_D$).

The descent stage of the curves against different b_0 was shown in Figure 12. When $b_0 = 0.2$ or $b_0 = 0.5$, the curve of the descent stage almost was linear, and inflection point D and maximum curvature point E were nonsignificant. Simultaneously, though the test-piece was deformed seriously, the spice was still with high strength which could not fit the actual test result.

The calculated curves were contrasted with the actual test curves in Figure 13. The shape of descent stage of the CaCO_3 whisker reinforced cement paste was complicated and the shape was effectively impacted by increasing the CaCO_3 whisker dosage. Figure 13 showed the descent stage was with a large range of residual stress, when the residual stress of the cement paste had fallen below 60% that would determine that the cement paste was complete failure in this script, which was because the cement paste was covered with macroscopic crack and destroyed seriously at this moment. From the above, the range of b_0 of the descent stage curve was suggested to belong to $5 < b_0 < 500$.

The above calculating equations of the stress-strain curve were focused on the CaCO_3 whisker reinforced cement paste and were under a definitive water-cement ratio. When the conditions were changed the equations should be amended as well.

(4) The complete curve is as follows.

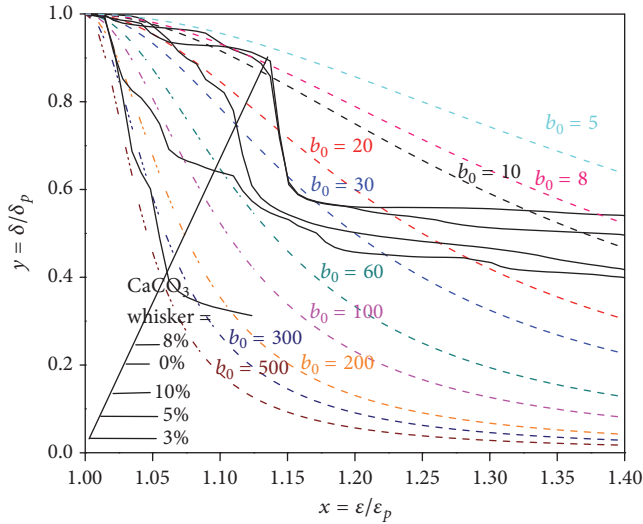


FIGURE 13: Calculating curve in contrast to the test curve.

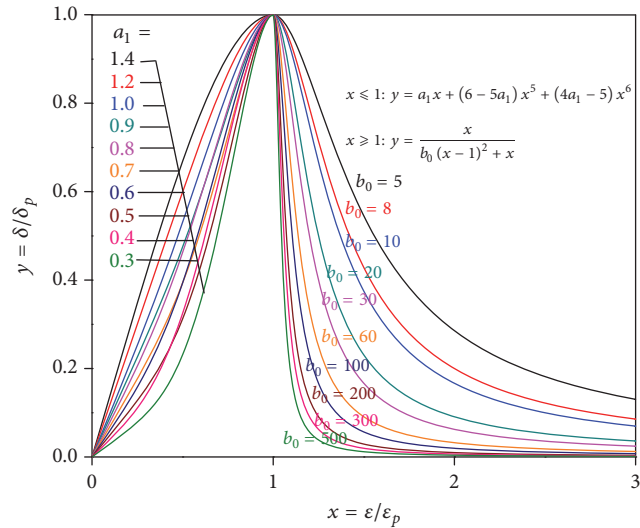


FIGURE 14: The calculating curve of constitutive model.

To sum up, the equations of (5) and (9) were combined together to represent the constitutive model of the stress-strain curves in Figure 14, and the constitutive model was contrasted to the test curves in Figure 15. The results of the experiment curves were all contained by the calculating curves, so the fitted equation would be effective, especially at the ascent stage and the descent stage before the stress below 60%. After the stress had fallen below 60%, the cement paste would be destroyed completely, which was considered to lose the research value.

The constitutive model of stress-strain curve of the CaCO₃ whisker reinforced cement paste could be described by (5) and (9) as

$$y = a_1x + (6 - 5a_1)x^5 + (4a_1 - 5)x^6, \quad 0 \leq x \leq 1$$

$$y = \frac{x}{b_0(x-1)^2 + x}, \quad x \geq 1, \quad (12)$$

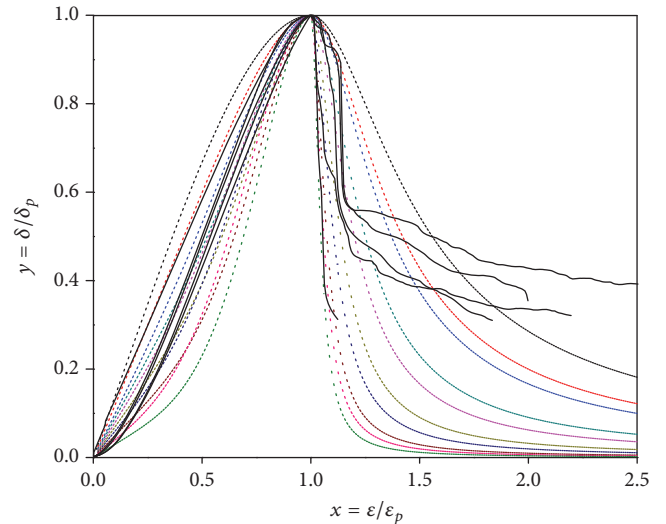


FIGURE 15: The integrated calculating curve in contrast to the complete test curve. The colored dotted lines referred to the incorporation of calculated results in Figures 11 and 13.

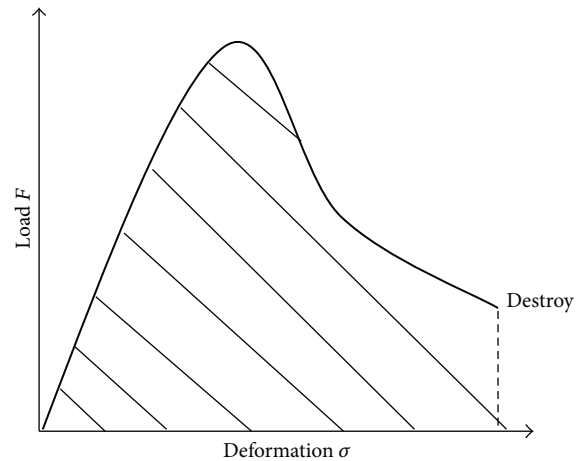


FIGURE 16: The toughness of the material.

where a_1 and b_0 were undecided parameters and the range of a_1 and b_0 of the CaCO₃ whisker reinforced cement paste was elaborated as $0.5 < a_1 \leq 1.5$, $5 < b_0 < 500$ in this script.

3.4. *Toughness of Uniaxial Compression.* The toughness of the cementitious material was focused on the ability of absorbing energy from initial loading to materials failure; the more the energy was absorbed, the more tough the cementitious material would be. The absorbing energy of the material under uniaxial compression was calculated by the area of the stress-strain curve in Figure 16. The work of the load could be calculated by

$$W = \int Fd\sigma, \quad (13)$$

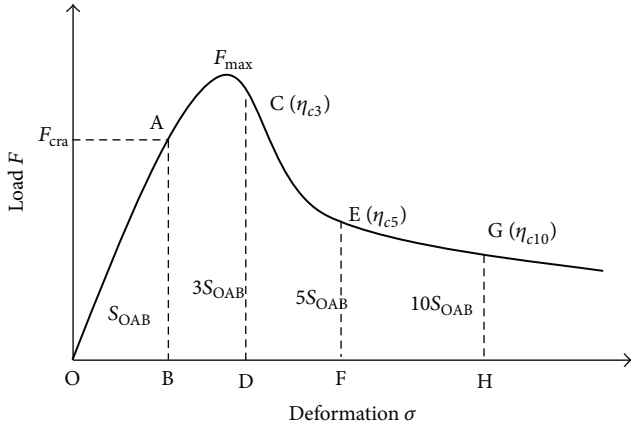


FIGURE 17: The stress-strain curve and toughness index.

where W , F , and σ were the load work, load, and the strain capacity.

The toughness of the cementitious material was related not only to the bearing capacity but also to the mechanical deformation capability. In this script, the toughness of the cementitious material which was calculated referring to the Chinese standard of “Steel Fiber Reinforced Concrete Testing Methods (CECS13: 2009)” and was elucidated as follows.

(1) The compression curve of the cement was divided into 4 parts in Figure 17, drawing a straight line through the x -axis at the point of F_{cra} (where $F_{cra} = 0.85 * F_{max}$; F_{max} was the peak stress), which was parallel to the y -axis and intersected the load curve at the critical point A. The x -axis of point A was the critical elastic deformation as σ_{cra} and the area of S_{OAB} was defined as critical toughness of S_{OAB} .

(2) Calculate the values of 1.2, 1.5, and 2.0 times of σ_{cra} , respectively, which were determined as the points D, F, and H on the load curve. The areas of S_{OAB} , S_{OACD} , S_{OAEF} , and S_{OAGH} were also calculated. Hereby, the toughness indexes were defined as follows:

$$\begin{aligned} \eta_{c1.0} &= \frac{S_{OF_{max}}}{S_{OAB}} \\ \eta_{c1.2} &= \frac{S_{OACD}}{S_{OAB}} \\ \eta_{c1.5} &= \frac{S_{OAEF}}{S_{OAB}} \\ \eta_{c2.0} &= \frac{S_{OAGH}}{S_{OAB}} \end{aligned} \quad (14)$$

(3) The capability coefficients index was defined as follows:

$$\zeta = \frac{\eta_{c,n} - a}{a - 1}, \quad (15)$$

where a was the deformation value as 1.2, 1.5, and 2.0 and $\eta_{c,n}$ was the toughness index relating to the deformation value in Table 4.

The relationships between the toughness index or capability coefficients index and the dosage of the $CaCO_3$ whisker

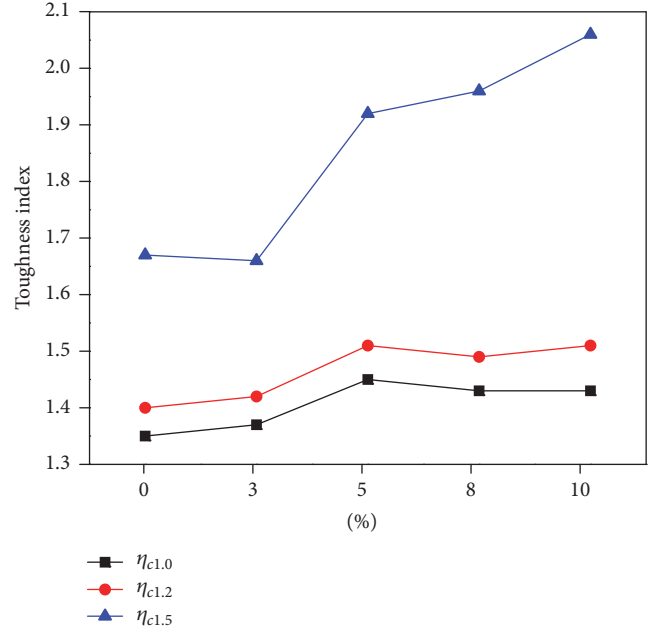


FIGURE 18: The toughness index of $CaCO_3$ whisker reinforced cement paste.

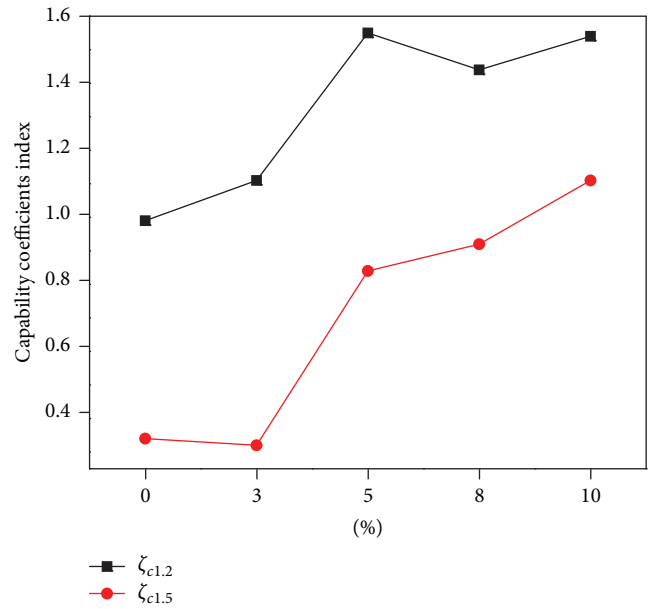


FIGURE 19: Capability coefficients index of $CaCO_3$ whisker reinforced cement paste.

were shown in Figures 18 and 19. The increasing trend of $\eta_{c1.0}$, $\eta_{c1.2}$, and $\eta_{c1.5}$ was shown in Figure 18. Additionally, the peak damage energy and the compressive toughness of the cement pastes were developed observably. The growth of $\eta_{c1.5}$ was most remarkable; at the point 10% it was improved 1.23 times the control sample. The increasing trend of capability coefficients index of the cement paste was also shown in Figure 19. $\zeta_{c1.2}$ and $\zeta_{c1.5}$ of point 5% were improved 1.57 and 2.47 times the control sample. $\zeta_{c1.2}$ and $\zeta_{c1.5}$ of point 10% were

TABLE 4: The toughness index and capability coefficients index.

CaCO ₃ whisker quality	$\eta_{c1.0}$	$\eta_{c1.2}$	$\eta_{c,n}$ $\eta_{c1.5}$	$\zeta_{c1.2}$	$\zeta_{c1.5}$
0%	1.35	1.40	1.67	0.99	0.34
3%	1.37	1.42	1.66	1.11	0.32
5%	1.45	1.51	1.92	1.55	0.84
8%	1.43	1.49	1.96	1.44	0.92
10%	1.43	1.51	2.06	1.54	1.11

improved 1.56 and 3.26 times the control sample. Thus the improvement of toughness of the cement paste was further characterized by the energy index as in Table 4.

3.5. Micromechanical Mechanisms

(1) *The Microstructure.* The CaCO₃ whiskers with sharp regularity were inset in the cement pastes which could be identified easily. From Figure 20(a), the cement paste was a kind of inhomogeneity material with small opening where the CaCO₃ whiskers with small size could fill in the microcracks and holes. Because of the CaCO₃ whiskers with rather higher mechanical strength, when the cement paste was under the stress damage, the CaCO₃ whiskers could support the stress as a bridge between the cracks in Figure 20(b), which could expend the destroying energy of the cement matrix by bridging toughening effect [14–16]. In Figure 20(c), caused by the rising stress, the collapsing strength of CaCO₃ whiskers far exceeded the cement paste cohesion strength; the crack could not break down the CaCO₃ whiskers; instead the CaCO₃ whiskers could be pulled out to consume the energy for rubbing action and stripping effect [15, 16]. Also the crack would be impeded by CaCO₃ whiskers [3, 17–20] as in Figure 20(d). This was marked by the red circle in Figure 20(e); over the ultimate high dosage, the CaCO₃ whiskers could be scattered unevenly; in reverse the whisker would ease the mechanical property of cement paste, whereby the strengthening effort of the CaCO₃ whiskers would be summed up as the destroying energy conservation and microcrack inhibiting and a physical model was stated in Figure 20.

(2) *Physical Model of Interface Layer.* With high draw ratio, the CaCO₃ whiskers were short fibers with different granulate material which could bear the longitudinal load. And that was confirmed in mechanical experiment above in this script. A physical interface layer model [21–23] was established to elaborate this mechanism in Figure 21. With a large specific surface area; when the CaCO₃ whiskers were blended with the cement slurry, a water molecule layer could be adhered to the surface of CaCO₃ whisker, which could promote the cement hydration. Furthermore the CH crystals would gather in this layer and form a specific fiber-matrix layer between the fiber and cement matrix; this layer consisted of double film layer, CH gathering layer, and porous layer. The thickness of the double film layer was about 1~2 μm , which was composed of CH crystals and C-S-H. Due to the small size of the CaCO₃ whiskers, the double film layer could be bonded with

much more fastness to the cement surface compared with the organic fiber which could raise the pull-out energy and inhibit the crack initiation and coalescence [21, 22]. With orienting CH gathering, the CH gathering layer was a weak link of the fiber-matrix layer for the loose structure. Another weak link of the fiber-matrix layer was the porous layer with abundant micropores and loose structure which consisted of CH crystals and C-S-H. The thickness of the fiber-matrix layer was about 10~100 μm and CH gathering layer and porous layer could firmly impact the mechanical strength of the cement paste as the loose structure and constitution. As the fiber spacing theory, the anticracking of the fiber was consanguineously related to the average distance between the reinforcing fiber and the cement matrix; thereby the distance was smaller and the anticracking was stronger. Since the distance was smaller, the thickness of the weak link of the fiber-matrix layer was thinner which indicated that the fiber could adhere the matrix with much fastness; this meant that the mechanical strength was well developed.

As assumed, the CaCO₃ whiskers were well dispersed in the three-dimensional direction in the cement paste and the equation of the average distance of the CaCO₃ whiskers was shown as follows [24–26]:

$$\bar{S} = 4.88 \frac{\sqrt{V_f}}{\text{FSS}}, \quad (16)$$

where \bar{S} , V_f , and FSS were the average distance (μm), fiber volume fraction (%), and the surface area of the fiber in the unit volume cement matrix (mm^2).

From (16), when the value of the FSS was increased, \bar{S} would be seriously reduced and the shape of the CaCO₃ whiskers was assumed as a uniform cylinder to calculate the FSS:

$$\text{FSS}_{\text{CaCO}_3\text{whisker}} = NP_f l_f = \frac{\pi d_f}{(\pi/4) d_f^2} V_f = \frac{4}{d_f} V_f, \quad (17)$$

where

$$N = \frac{V_f}{A_f l_f}, \quad (18)$$

$$P_f = \pi d_f,$$

where N was the number of fibers in unit volume cement matrix, P_f was the cross-sectional area of the CaCO₃ whiskers

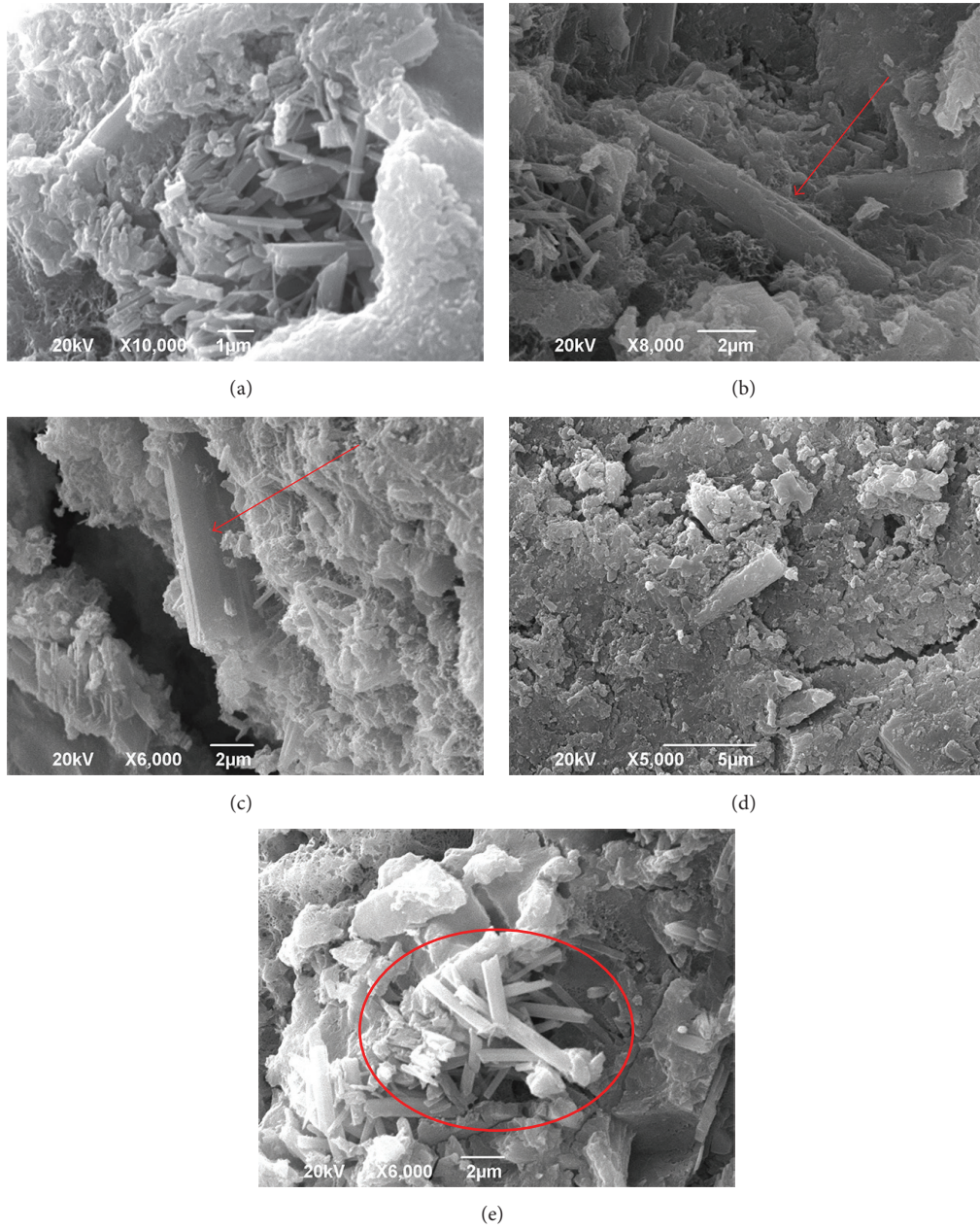


FIGURE 20: (a) The CaCO₃ whisker filling the crack. (b) The bridging effect of CaCO₃ whisker. (c) Pull-out effect of CaCO₃ whisker. (d) Confined crack developing. (e) the CaCO₃ whiskers scattered unevenly.

TABLE 5: The parameters of the physical model.

CaCO ₃ whiskers (%)	1	5	10	15
V_f (%)	0.67	3.40	6.60	14.80
FSS ($\mu\text{m}^2 \cdot \mu\text{m}^{-3}$)	0.027	0.136	0.264	0.592
\bar{S} (μm)	14.84	6.16	4.75	3.17

(mm^2), and d_f was the diameter of the reinforcing fiber (mm).

Under ideal dispersing, the parameters of different dosage of CaCO₃ whisker were calculated (where $L = 50 \mu\text{m}$ and $d_f = 1 \mu\text{m}$) in Table 5. \bar{S} was over $14 \mu\text{m}$ at 1% CaCO₃ whiskers

and the weak link of the fiber-matrix layer was at a relative large scale and the reinforcement of the CaCO₃ whiskers was not significant. With the CaCO₃ whisker increasing, \bar{S} was decreasing remarkably. And at 10% CaCO₃ whisker, \bar{S} was decreased to $4.75 \mu\text{m}$; hereby the fiber-matrix layer was

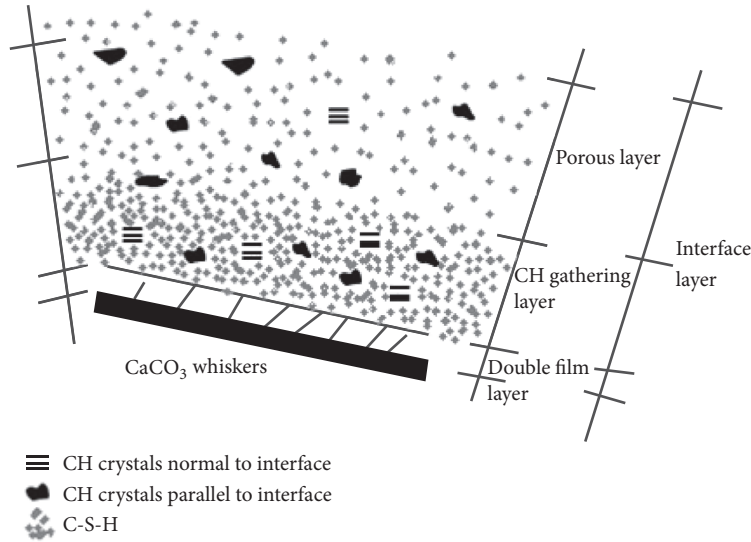


FIGURE 21: Physical model of interface layer.

compressed conspicuously and the tensile strength of the cement paste was well improved under the ideal condition. \bar{S} of the 15% was the lowest but the strength had still fallen down, because the CaCO_3 whiskers could not evenly be dispersed at this dosage; the CaCO_3 whiskers could be reunited and would decrease the cementation between the CaCO_3 whisker and cement matrix. Thus the fiber spacing theory would be invalid under this mixing condition.

(3) *XRD*. The results of XRD under 0%, 5%, and 10% of CaCO_3 whisker were shown in Figure 22. The types of the hydration products with CaCO_3 whiskers were not changed, whereas with the increasing trend of CaCO_3 whisker, the diffraction peaks of C_3S and the C_2S had fallen down; besides the diffracted intensity of the C-H-S and CH was increased significantly compared with the control sample. Because of the small size and large specific surface area, the CaCO_3 whisker was considered as a submicron material; the water molecule layer could be easily adhered to the whisker surface and formed a water film. The water on the surface of the CaCO_3 whisker could stimulate the cement hydration and the hydration products would fix the defect and strengthen the structure of the interface layer. Therefore, the physical model of interface layer had been demonstrated when the C-H-S and CH were increased significantly after adding CaCO_3 whisker.

4. Conclusion

(1) With high elasticity modulus and strength, the CaCO_3 whisker could improve the tensile strength of the cement paste significantly at the dosage of 10%.

(2) The peak stress, elasticity modulus, and the energy of different stage of the stress-strain curve of the CaCO_3 whisker reinforced cement paste were enforced with the increasing of CaCO_3 whisker, and the failure characteristics of each stage were observable. The mathematic relations between the peak stress, elasticity, peak strain, and the CaCO_3

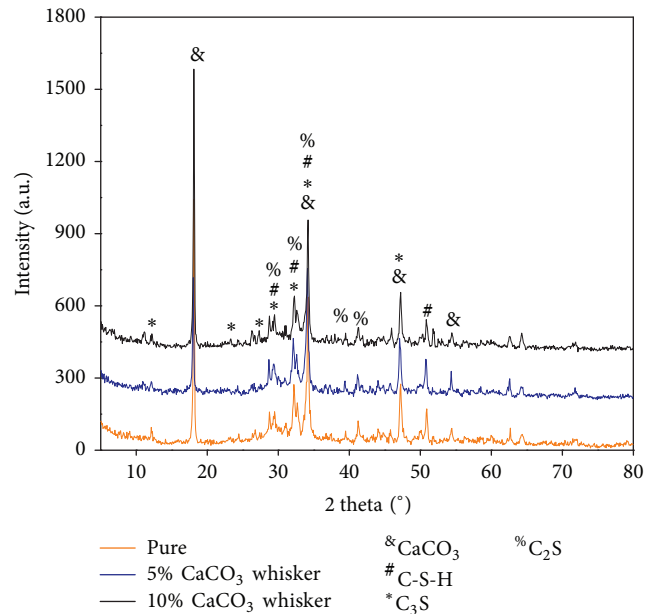


FIGURE 22: The XRD results of CaCO_3 whisker reinforce cement pastes.

whisker were discussed. The relation between the peak stress and the CaCO_3 whisker was linear relation. Besides, the relation between elasticity and the CaCO_3 whisker was power function and the relation between peak strain and CaCO_3 whisker was not so regular that the CaCO_3 whisker could impact the peak strain of the cement paste barely.

(3) The constitutive model of stress-strain curve of the CaCO_3 whisker reinforced cement paste was established in this paper which could describe the stress-strain properties and fit the experimental curve well.

(4) The toughness index and capability coefficients index of the CaCO_3 whisker reinforced cement paste were

established in this paper to elucidate that the CaCO_3 whisker could improve the toughness of the cement paste at different stages.

(5) The CaCO_3 whisker could develop the strength of cement pastes well and impede the microcracks initiation and coalescence in the cement paste. Caused by the pull-out and bridging effect, the CaCO_3 whisker could consume the damaging energy and toughen the cement paste. A physical model of interface layer was also established to elaborate the toughening effect. CaCO_3 whisker could form a water firm and the specific interface layer could compress the weak-link layer, improve the mechanical strength of the cement pastes, achieve desirable toughening effects, and improve wellbore integrity.

Conflicts of Interest

The authors declare that they have no conflicts of interest.

References

- [1] M. Cao, "Research progress of CaCO_3 whisker and application in composite materials," in *New Chemical Materials*, 2010.
- [2] M. Cao, J. Wei, and L. Wang, "Serviceability and reinforcement of low content whisker in portland cement," *Journal of Wuhan University of Technology-Mater*, vol. 26, no. 4, pp. 749–753, 2011.
- [3] M. L. Cao, H. Yao, and L. J. Wang, "Experimental study on CaCO_3 whisker-reinforced fiber cement mortar," *Key Engineering Materials*, vol. 477, pp. 245–251, 2011.
- [4] M. Cao, C. Zhang, and J. Wei, "Microscopic reinforcement for cement based composite materials," *Construction and Building Materials*, vol. 40, pp. 14–25, 2013.
- [5] M. Li, M. Liu, Y. Yang, Z. Li, and X. Guo, "Mechanical properties of oil well cement stone reinforced with hybrid fiber of calcium carbonate whisker and carbon fiber," *Petroleum Exploration and Development*, vol. 42, no. 1, pp. 104–111, 2015.
- [6] Y. Yuanyi, A well cementing toughening slurry system for gas storage, master thesis, Southwest Petroleum University, 2014.
- [7] L. I. Ming, M. Liu, Y. J. Yang, Y. Y. Yang, and X. Y. Guo, *Calcium Carbonate Whisker Improved the Performance of Oil and Gas Well Cement*, Bulletin of the Chinese Ceramic Society, 2014.
- [8] A. Caggiano, G. Etse, P. Folino, M. Ripani, and S. Vrech, *Constitutive Formulations for Concrete with Recycled Aggregates*, Springer International Publishing, 2017.
- [9] H. Chen, S. Wu, and F. Dang, The experimental research on the dynamic and static mechanical characteristics of dam concrete and the constitutive materials, 2016.
- [10] H. Qi, Y. Li, X. Chen, J. Duan, and J. Sun, Study of uniaxial constitutive model of concrete in code and development in ABAQUS, 2015.
- [11] G. Zhenhai, *The Strength of The Concrete and Constitutive Relation*, China Architecture and Building Press, 2004.
- [12] S. Grünwald and J. C. Walraven, "Parameter-study on the influence of steel fibers and coarse aggregate content on the fresh properties of self-compacting concrete," *Cement and Concrete Research*, vol. 31, no. 12, pp. 1793–1798, 2001.
- [13] Z. Wang and P. U. Xin, "Experimental study on the uniaxial compression properties and the stress-strain curves of UHS and HPC," *Journal of Chongqing Jianzhu University*, 2000.
- [14] F. J. Guild, A. C. Taylor, and J. Downes, *Composite Materials*, John Wiley Sons, 2017.
- [15] R. Talreja, "Matrix and fiber-matrix interface cracking in composite materials," *Modeling Damage, Fatigue and Failure of Composite Materials*, pp. 87–96, 2015.
- [16] W. J. Yin Hongfeng, *Composite Materials*, Press of Metallurgy Industry, 2012.
- [17] K. T. Faber and A. G. Evans, "Crack deflection processes—I. Theory," *Acta Metallurgica*, vol. 31, pp. 565–576, 1983.
- [18] H. R. Pakravan, M. Latifi, and M. Jamshidi, "Hybrid short fiber reinforcement system in concrete: A review," *Construction and Building Materials*, vol. 142, pp. 280–294, 2017.
- [19] B. H. Tekle, A. Khennane, and O. Kayali, "Bond of spliced GFRP reinforcement bars in alkali activated cement concrete," *Engineering Structures*, vol. 147, pp. 740–751, 2017.
- [20] L. Yang, Z. Wu, D. Gao, and X. Liu, "Microscopic damage mechanisms of fibre reinforced composite laminates subjected to low velocity impact," *Computational Materials Science*, vol. 111, pp. 148–156, 2016.
- [21] R. B. Jewell, K. C. Mahboub, T. L. Robl, and A. C. Bathke, "Interfacial bond between reinforcing fibers and calcium sulfoaluminate cements: fiber pullout characteristics," *ACI Materials Journal*, vol. 112, no. 1, pp. 39–48, 2015.
- [22] A. Medeiros, X. Zhang, G. Ruiz, R. C. Yu, and M. D. S. L. Velasco, "Effect of the loading frequency on the compressive fatigue behavior of plain and fiber reinforced concrete," *International Journal of Fatigue*, pp. 342–350, 2015.
- [23] J. Qiu, X.-N. Lim, and E.-H. Yang, "Fatigue-induced deterioration of the interface between micro-polyvinyl alcohol (PVA) fiber and cement matrix," *Cement and Concrete Research*, vol. 90, pp. 127–136, 2016.
- [24] C. Q. Shen Rongxi, *New type of fiber reinforced cement matrix composites*, Press of China Building Industry, 2004.
- [25] C. Carloni, D. A. Bournas, F. G. Carozzi et al., *Fiber Reinforced Composites with Cementitious (Inorganic) Matrix*, Springer Netherlands, 2016.
- [26] J. Zhang, Z. Wang, Q. Wang, and Y. Gao, "Simulation and test of flexural performance of polyvinyl alcohol-steel hybrid fiber reinforced cementitious composite," *Journal of Composite Materials*, vol. 50, no. 30, pp. 4291–4305, 2016.

Research Article

Mechanical Properties of Fiber-Reinforced Concrete Using Composite Binders

Roman Fediuk, Aleksey Smoliakov, and Aleksandr Muraviov

Far Eastern Federal University, Vladivostok 690950, Russia

Correspondence should be addressed to Roman Fediuk; roman44@yandex.ru

Received 14 June 2017; Revised 12 September 2017; Accepted 19 September 2017; Published 26 October 2017

Academic Editor: Rishi Gupta

Copyright © 2017 Roman Fediuk et al. This is an open access article distributed under the Creative Commons Attribution License, which permits unrestricted use, distribution, and reproduction in any medium, provided the original work is properly cited.

This paper investigates the creation of high-density impermeable concrete. The effect of the “cement, fly ash, and limestone” composite binders obtained by joint grinding with superplasticizer in the varioplanetary mill on the process of structure formation was studied. Compaction of structure on micro- and nanoscale levels was characterized by different techniques: X-ray diffraction, DTA-TGA, and electron microscopy. Results showed that the grinding of active mineral supplements allows crystallization centers to be created by ash particles as a result of the binding of $\text{Ca}(\text{OH})_2$ during hardening alite, which intensifies the clinker minerals hydration process; the presence of fine grains limestone also leads to the hydrocarboaluminates calcium formation. The relation between cement stone neoplasms composition as well as fibrous concrete porosity and permeability of composite at nanoscale level for use of composite binders with polydispersed mineral supplements was revealed. The results are of potential importance in developing the wide range of fine-grained fiber-reinforced concrete with a compressive strength more than 100 MPa, with low permeability under actual operating conditions.

1. Introduction

Concrete on cementitious binder and natural aggregates is widely used as structural material in construction industry. Worldwide, the large-capacity ash waste and crushing of the rocks are generated as a result of activity of the fuel and energy sector and mining industry enterprises. It seems necessary to optimize the processes of concrete mixtures structure formation by using industrial waste. Traditional types of concrete have insufficient properties of gas permeability and vapor permeability. At the same time, it is necessary to improve the strength and deformability quality of composite to achieve fine-grained fiber-reinforced concrete.

Leading scientific schools in the field of building materials science have developed a number of concrete types with enhanced operational properties.

Textile-reinforced concrete is a type of reinforced concrete in which the usual steel reinforcing bars are replaced by textile materials. Materials with high tensile strengths with negligible elongation properties are reinforced with woven or nonwoven fabrics. The fibers used for making the fabric are

of high tenacity like Jute, glass fiber, Kevlar, polypropylene, polyamides (nylon), and so forth.

Mechanical properties of high-strength concrete incorporate copper slag as a fine aggregate and concluded that less than 40% copper slag as sand substitution can achieve high-strength concrete comparable to or better than the control mix, beyond which, however, its behaviors decreased significantly [1–3].

Glass fiber-reinforced concrete consists of high-strength, alkali-resistant glass fiber embedded in a concrete matrix. In this form, both fibers and matrix retain their physical and chemical identities, while offering a synergistic combination of properties that cannot be achieved with either of the components acting alone.

High-performance fiber-reinforced cementitious composites (HPFRCCs) [4, 5] are a group of fiber-reinforced cement-based composites which possess the unique ability to flex and self-strengthen before fracturing. Strain hardening, the most coveted capability of HPFRCCs, occurs when a material is loaded past its elastic limit and begins to deform plastically. This stretching or “straining” action

actually strengthens the material. The basis for the engineered design of different HPRCCs varies considerably despite their similar compositions. For instance, the design of one type of HPRCC called Engineered Cementitious Composite (ECC) stems from the principles of micromechanics. ECC, also called bendable concrete, is an easily molded mortar-based composite reinforced with specially selected short random fibers, usually polymer fibers [6, 7]. Unlike regular concrete, ECC has a strain capacity in the range of 3–7%, compared to 0.01% for ordinary Portland cement (OPC). ECC, therefore, acts more like a ductile metal than a brittle glass (as does OPC concrete), leading to a wide variety of applications [8, 9].

Ultrahigh-performance concrete (UHPC) is a new type of concrete that is being developed by agencies concerned with infrastructure protection [10–14]. UHPC is characterized by being a steel fiber-reinforced cement composite material with compressive strengths in excess of 150 MPa, up to and possibly exceeding 250 MPa. UHPC is also characterized by its constituent material make-up: typically fine-grained sand, silica fume, small steel fibers, and special blends of high-strength Portland cement. Note that there is no large aggregate. The current types in production differ from normal concrete in compression by their strain hardening, followed by sudden brittle failure. Ongoing research into UHPC failure via tensile and shear failure is being conducted by multiple government agencies and universities around the world.

The high-strength self-consolidating (self-compacting) concrete technology is made possible by the use of polycarboxylates plasticizer instead of older naphthalene-based polymers and viscosity modifiers to address aggregate segregation [15, 16].

Combination of microsilica and nanosilica (colloidal silica) is considered to design high-strength self-consolidating concrete [1, 20, 21]. The results also revealed that 7% substitution of microsilica showed the same effect as 2% nanosilica replacement [1, 22, 23].

The fiber-matrix interfacial transition zone (ITZ) at nanoscale plays an important role in determining the mechanical performance of hybrid steel-polypropylene fiber-reinforced concrete at upper scales. This topic [24] presents the elastic behavior of the ITZ between steel/polypropylene fiber and pure cement paste through nanoindentation for different water/cement ratios.

Thus, the fine-grained structure with high homogeneity is characterized by increase of the integrated strength between aggregate and cement stone and decrease of specific stress in the contact area. Adhesion of sand component increases significantly with increase of contact area; these conditions were realized when creating the fine-grained concrete based on composite binders by using crushed granite from Wrangel deposit (Russian Far East). The aim of the study was to develop the concrete matrix dense structure with high gas, water, and vapor impermeability. Composite binders, obtained by cogrinding of Portland cement, fly ash, crushed limestone, and superplasticizer, have been proposed to achieve this aim. One of the ways to improve the properties of concrete and to reduce permeability parameters is the use of highly active additives of various compositions and genesis

at micro- and nanosized levels, which contribute to the optimization of structure formation processes by initiating the formation of hydrated compounds. The efficiency of use of the active mineral additives of nanostructured silica-modifier composition has been proven in topics [1, 20, 21, 23]. The possibility of the permeability reduction of the concrete by mechanically grinding the composite binders components was also studied previously [17]. However, the protective properties (impermeability parameters) and efficiency of high-density impermeable concrete (HDIC) produced on the basis of composite binder were not considered previously.

An assumption about the possibility of HDIC is obtained by varying the amount and type of additives, fineness of the composite binder components, and hardening conditions [18, 25]. The purpose of this work is to improve impermeability and strength characteristics of the fiber-reinforced concrete through use of composite binders obtained by cogrinding of Portland cement, superplasticizer, fly ash of a thermal power station, and crushing screenings limestone.

2. Materials and Methods

To achieve this goal, the following tasks were completed in this work:

- (i) Study of mineral composition, particle size distribution, and physical and mechanical characteristics of the binders components and fillers for concrete
- (ii) Research of the effect of mineral and organic additives on the properties of composite binders
- (iii) Study of the properties of fiber-reinforced concrete, depending on the characteristics of the composite binder taking into account peculiarities of structure formation to improve the impermeability and strength characteristics, research on characteristics of water absorption and gas, water, and vapor permeability of developed concrete, and experimental industrial testing of the proposed compositions

The science work included grinding of composite binder components in a varioplanetary mill. Ordinary Portland cement (OPC), fly ash (FA), limestone crushing waste (LCW), and superplasticizer were used as ground components.

The chemical and mineralogical compositions of the raw materials obtained by means of X-ray fluorescence (on D8 ADVANCE powder diffractometer from Bruker AXS) are presented in Tables 1 and 2.

In the varioplanetary mill, the rotational speeds of the grinding jars and the support disc can be set completely independently. The movement and the trajectory of the grinding balls can be influenced by varying the gear ratio, so that the balls strike horizontally on the inner wall of the grinding jar (by high impact energy), approach tangentially (by high friction), or simply roll over the inner wall of the grinding jar (by centrifugal mills). All intermediate stages and combinations between pressure friction and impact can be freely set (Figure 1). Accordingly, grinding by the varioplanetary mills is more energy-efficient than that by the ball mills and the vibratory mills. In addition, due to the

TABLE 1: The chemical compositions of the fly ashes, Portland cement, and limestone crushing wastes.

The predominant type of coal	Fly ash				Portland cement	LCW
	Primorye TPP Luchegorsk and Bikinsky	Vladivostok TPP Primorsky brown (Pavlovsky section)	Artem TPP Coal	Partizansk TPP Neryungrinsky coal		
Content of elements in terms of oxides, %						
SiO ₂	55.3	63	48.1	47.4	20.2–20.9	7.49
TiO ₂	0.5	0.5	0	0.9		0.24
Al ₂ O ₃	12.6	21.4	29.3	22.3	6.0–6.7	3.33
Fe ₂ O ₃	10.7	7.5	6.5	19.6	3.5–4.0	0.24
CaO	12.5	3.4	9.7	4.8	66.2–67	44.21
MgO	3.5	2.1	1.8	2.8	1.4–2.0	2.57
K ₂ O	1	1.3	1.2	0.1		
Na ₂ O	0.4	0.3	0.2	0.4		
SO ₃	3.4	0.6	2.3	1.62		
LOI	2.3	1.4	0.6	<5	0.18	38.71

TABLE 2: The mineral compositions of Spassky Portland cement.

Mineral composition	C ₃ S	C ₂ S	C ₃ A	C ₄ AF
Content [%]	58–67	8–15	10–12	10.5–12.5

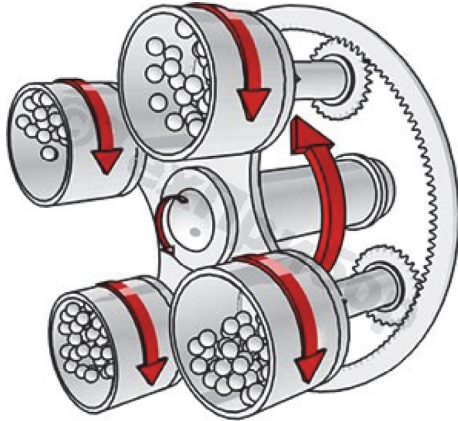


FIGURE 1: Operating principle of a varioplanetary mill.

joint action of shock, centrifugal shock, and abrasive forces, it becomes possible to achieve more highly disperse powders [26–29].

The reliability of results is provided by a systematic study with standard tools and methods for measuring, the mix of modern physical and chemical methods of analysis, X-ray diffraction and DTA, electron microscopy, and a sufficient amount of raw data and research results. The tasks of the scientific work were accomplished by implementing a systematic approach in the triad “composition (raw materials), structure, and properties” [30–32]. The studies were conducted with use of conventional physical-mechanical and physical-chemical

methods of quality assessment of raw materials and synthesized materials as well as finished products.

The fly ashes of largest thermal power plants (TPPs) of Russia (Vladivostok TPP (Figure 2), Artem TPP, Primorye TPP, and Partizansk TPP) were used as components of composite binders. The important factor is the possibility of dry ash selection, which is currently realized for these TPPs.

Taking into consideration the fact that the focus of the paper is the development and use of environmentally friendly materials, the ashes’ radioactivity has been evaluated (Table 3).

Thermal studies of the ash showed that, in the range of low temperatures, physically bound water is removed from it. Exothermic effect with the maximum at about 400°C indicates burnout of organic substances and endotherm effect at 712°C indicates dissociation of calcite to CaO and CO₂, which was confirmed by X-ray diffraction data (Figure 3).

Optimization of structure formation processes at hydration of the composite binder components creates the matrix dense structure which is necessary for creating increased impermeability composites. This can be realized by cogrinding of the Portland cement and the polyfunctional mineral admixtures and by reducing the concrete mix water-cement ratio through use of superplasticizers.

To reduce the water demand of concrete mix, the superplasticizers were used. They were selected of six most common construction material markets in the Far East. Cement paste shrinkage was measured by Hagerman cone. The Spassky cement CEM I 42.5N was used as grout. Water-cement ratio was 0.3. Plasticizer dosage was 0.3%. Time of measurement of shrinkage cone is recorded after the end of the cement paste mixing.

Achievement of high values of shrinkage cone is marked in the raw mix of binder and superplasticizer PANTARHIT PCI160 Plv (Table 4).

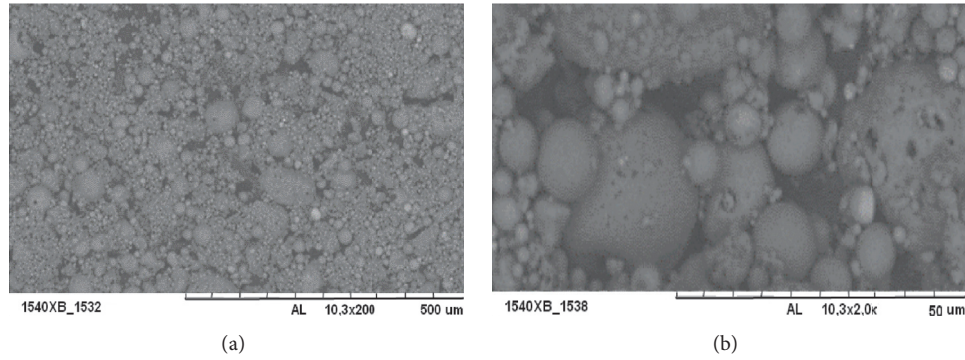


FIGURE 2: The Vladivostok TPP’s fly ash micrographs: (a) ×200; (b) ×2000.

TABLE 3: Specific effective activity of fly ash depending on the composition [19].

Name of indicator	The measurement result (A) [Bq/kg]			
	Primorye TPP	Vladivostok TPP	Artem TPP	Partizansk TPP
Activity ⁴⁰ K	496.9 ± 101	362 ± 89	342 ± 68	516.9 ± 101
Activity ²³² Th	153.6 ± 20.3	31.5 ± 19.7	29.5 ± 15.7	193.2 ± 22.3
Activity ²²⁶ Ra	163.1 ± 9.36	37.63 ± 6.32	27.23 ± 5.93	113.1 ± 6.37
$A_{eff} = A_{Ra} + 1.31A_{Th} + 0.085A_K$	>398	80 ± 30	93 ± 20	>410

TABLE 4: Shrinkage of the cement paste with different superplasticizers.

Time [min]	Melflux 1641 F	Melflux 5581 F	PANTARHIT PC160 Plv	FOX™-8H	PC-1030	JK-04 PPM
	Shrinkage [mm]					
0	290	350	370	250	240	130
5	380	390	400	260	280	120
30	390	350	390	240	190	98

Time: the time since beginning of measurement.

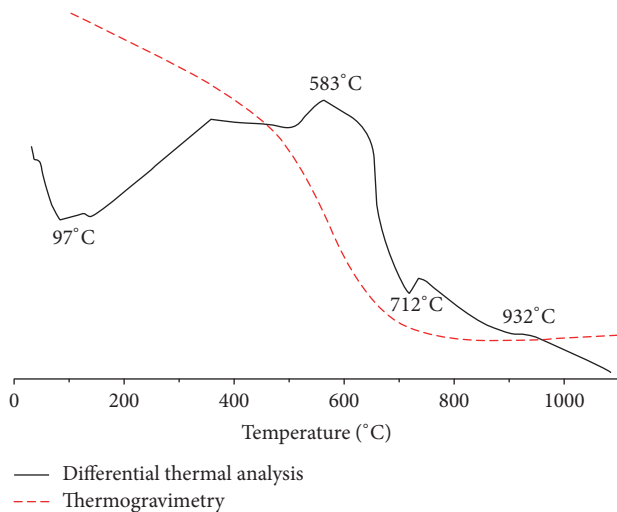


FIGURE 3: The DTA and TG results of the Vladivostok TPP fly ash [17–19].

The raw components were milled and mixed in various proportions (OPC 30–100%, FA 0–50%, LCW 0–20%, and superplasticizer 0.3%) in a varioplanetary mill for one hour.

The materials mixing was carried out using cyclic and continuous flow dispensers with automatic control with a maximum weighing cycle duration of 45–90 s, with a weighing accuracy of 1–3%. All raw materials were dosed by mass, with the exception of water and liquid additives (if any) dosed by volume. In our research, there were no liquid additives. Water was added at the last stage, during the mortar preparation.

The control samples were made from a composite paste without addition of sand and fiber. Number of specimens was fabricated to determine the optimum composition of the binder.

The flowability of the concrete mix was evaluated using Hagerman cone molded from a concrete mix. Water-binder ratio was 0.3. The inverted cone was filled with a freshly prepared concrete mix without sealing. 90 seconds after filling, the cone rose upward. Immediately the stopwatch was turned on. As the mixture reached a diameter of 500 mm and also after the spreading process was completed, the time was fixed. After the flow was completed, the maximum diameter of the spread of the concrete mix was determined.

The compressive strength and the modulus of elasticity of the specimens were researched on 70 mm cubes at the 28th day; however, 100 × 100 × 500 mm prisms were prepared for four-point bending to obtain flexural strength of the



FIGURE 4: Bruker BioSpin NMR Spectroscopy.



FIGURE 5: Bruker D8 ADVANCE powder X-ray diffractometer.

specimens with effective span of 400 mm. Mechanical tests were performed with Servo-hydraulic Fatigue and Endurance Tester Shimadzu Servopulser U-type with capacity of 200 kN and as per BS EN 12390-3:2002. The compressive strength was calculated as the arithmetic average of the six samples.

The porosity of the hardened specimens was determined on $1 \times 1 \times 3$ cm and $3 \times 3 \times 3$ cm specimens. The structure of the cement stone was investigated at the age of 28 days. The porosity was determined by a number of mutually complementary methods, namely,

- (i) proton magnetic resonance with a pore measurement range of $1 \times 10^{-3} \dots 1 \times 10^{-1} \mu\text{m}$ in diameter (using Bruker BioSpin NMR Spectroscopy (Figure 4));
- (ii) small-angle X-ray diffraction with a measurement range of $2 \times 10^{-3} \dots 3 \times 10^{-1} \mu\text{m}$ (on D8 ADVANCE powder diffractometer from Bruker AXS (Figure 5));
- (iii) mercury porosimetry with a measurable range of $1 \times 10^{-1} \dots 4 \times 10 \mu\text{m}$ (using PoreMaster GT (Figure 6));
- (iv) optical microscopy of thin sections with a measuring range of $4 \times 10 \dots 1 \times 10^3 \mu\text{m}$.

X-ray phase analysis determined the degree of cement hydration and the content of low-base calcium hydrosilicates, CSH (I). The phases were identified by the international JCPDS table. The degree of hydration was determined from the intensity of the main C_3S reflex. The amount of CSH (I) was established by comparing the intensity of the main β -CS reflex obtained on samples of hardened cement sintered at 1000°C with a standard sample (quartz).

3. Experimental Part

Seven binder composites were developed for further research (Table 5). Superplasticizer PANTARHIT PC160 Plv at quantity 0.3% was added to each of them. The binder : sand ratio is 1 to 3. To determine the optimal dosage of components in



FIGURE 6: PoreMaster GT.

the “cement-limestone-ash” system, it was necessary to grind them to specific surface of $600 \text{ m}^2/\text{kg}$ at various ratios.

According to Table 5, positive dynamics of strength growth of the composite binder under the joint influence of the ash fine constituents, limestone crushing wastes, and superplasticizer with maximum increase in the activity of the binder at 62% were found.

This is due to the fact that active mineral components of the composite binder contribute to the binding of $\text{Ca}(\text{OH})_2$ produced during cement hydration, which results in formation of additional amount of hydrosilicate neoplasms. At the same time, optimizing the process of structure formation is achieved by composite polydispersed components. Highly dispersed spherical ash particles act as crystallization centers

TABLE 5: Compositions and strength of composite binders.

Number	Cement content, by weight [%]	Fly ash content, by weight [%]		Limestone content, by weight [%]	Compressive strength [MPa]		
		Vladivostok TPP	Artem TPP		3 d.	7 d.	28 d.
1	100	—	—	—	17	32.5	47.5
2	30	—	50	20	30.2	40.1	50.4
3	35	45	—	20	34.2	43.1	53.2
4	40	—	45	15	36.6	48.2	56.6
5	45	45	—	10	39.2	50.1	59.2
6	50	—	40	10	45.1	54.9	65.8
7	55	40	—	5	47.2	54.1	70.2
8	100	—	—	—	60.3	81	103.2

Note. The prototype is number 1 (without final grinding); compositions numbers 2–8 are ground to $S_{sp} = 600 \text{ m}^2/\text{kg}$.

TABLE 6: Bond between compressive strength [MPa] of the cement stone samples and the specific surface area of the composite binder [4].

Hardening time [d.]	Specific surface area of the composite binder [m^2/kg]					
	500	550	600	700	800	900
3	46.1	47.4	47.2	46.0	45.6	45.5
7	50.3	54.2	54.1	49.1	48.6	48.4
28	68.1	77.3	70.2	65.8	55.0	65.0

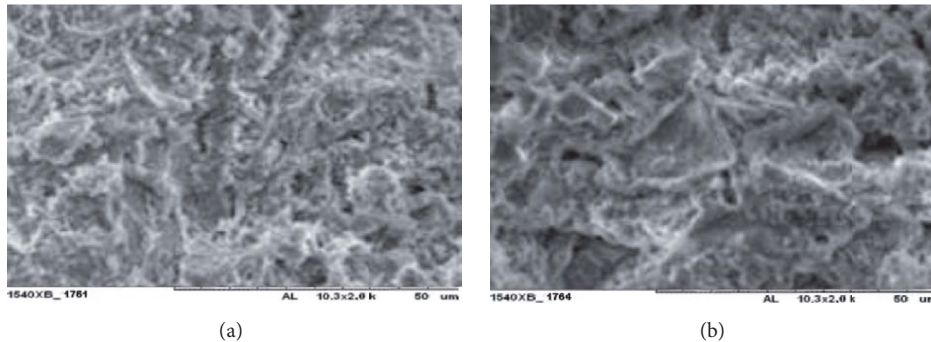


FIGURE 7: The cement stone microstructure: (a) CEM I 42.5N based; (b) composite binder based (composition number 7 in Table 5).

and are used as filler at the nano- and microlevels. In conjunction with the larger particles of the mineral component, denser filling of intergranular spaces is noted in concrete cement stone structure with reduction in number of pores and microcracks.

This is confirmed by micrographs of composite cement paste derived by joint grinding of clinker and industrial wastes of the Russian Far Eastern region. Cement stone structure is very dense packing of small grains in the crystalline neoplasms total mass (Figure 7). The additional amount of hydrated crystalline phases contributes to filling of the voids at the microlevel in the crystalline matrix of calcium hydrosilicates at the boundary of the contact area, increasing adhesion degree of binder with filler.

In order to determine the optimum particle size, the Portland cement, the superplasticizer, the ashes, and the limestone were ground (dosage according to composite number 7 of

Table 5) to different specific surface area (S_{sp}): 500, 550, 600, 700, 800, and 900 m^2/kg (Table 6).

According to Table 6, the 550–600 m^2/kg specific surface area (S_{sp}) of binder is optimal. Increasing S_{sp} above these values does not lead to further significant increase in strength. Reduction of start setting time of binder to 35–40 minutes by intensifying the hydration process under the influence of highly active components of the composite [17–19] should be noted.

Thus, the optimum parameters chosen for binder composition are specific surface area of 550 m^2/kg , the particle size of 0.15–500 microns, and average particle diameter of the grains of 0.65–11.2 mm [33, 34].

The most important task in creating HDIC is the rational formation and optimization of the pore space structure [35, 36]. In general, the overall reduction in porosity of compositions modified by the technogenic waste more than

TABLE 7: Influence of the composition of the composite binder to the cement stone porosity.

Composition according to Table 5	Technological (macroscopic level)	Porosity [%]		
		Capillary (microscopic level/submicroscopic level)	Gel (supramolecular level)	Total
1	1.2	4.6/2.3	8.2	16.3
2	2.6	1.7/4.5	1.6	10.4
3	1.3	1.1/5.0	3.5	10.8
4	1.4	1.9/2.3	4.4	9.6
5	3.6	1.7/2.5	1.6	9.4
6	3.2	1.1/1.0	3.5	8.8
7	1.0	0.9/1.8	4.4	8.1

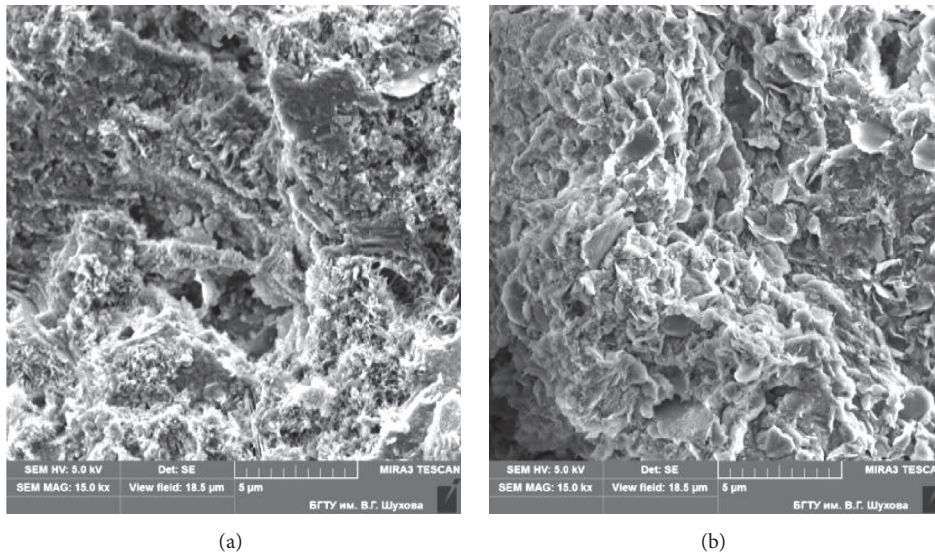


FIGURE 8: The neoplasms micrographs: (a) cement stone without any additives; (b) cement stone based on composite binders.

2 times (from 16.3% to 8%) should be noted. Fluctuations of different diameter pores which depend on nature of their formation should also be noted (Table 7).

Existence of a large quantity of hydrosilicate connections is confirmed by decreasing of the gel pores in crystalline bunch in conjunction with modified composites on molecular level with porosity maximum reduction more than 5 times [37, 38]. Although the maximum strength is 77.3 MPa in the optimal composition of binder (by grinding to specific area of 550 m²/kg), the gel porosity of the composite fell almost in 2 times. In this case, high strength is influenced by the complex actions: reduction of capillary porosity due to the intensification of the processes of growth of primary crystals of hydrosilicate phases [39, 40], due to possible formation of secondary recrystallization and crystals creation, due to filling the space at the micro- and submicrolevels of structural organization composite with them, and in conjunction with reduction technological porosity on 17% due to the formation of dense packing of the grain structure at the macrolevel, with the participation of spherical fine components of fly ash and limestone crushing wastes.

Denser structure of the binder composition with lower porosity is confirmed by microstructural studies. In phase of the modified binder formation, the amount of gel-like hydrate new formation increases on the surface of the filler particles (Figure 8(b)), there are no visible portlandite crystals, and it shows a decline of its share in the total mass of ligament hydrosilicate [41, 42].

By varying the percentage of added ash, it is possible to control number and size of ettringite crystals, which further define the properties of composite binder and concrete [43, 44]. The carbonates also have close contacts with cement stone, which is explained by the emergence of bonds between the cement hydration products and limestone [45, 46]. Growth of crystals of “needle-like” and “stem-like,” low-basic hydrosilicates is observed [47, 48]; there are also plate-like calcium crystals, allegedly hydrocarboaluminates (Figure 8(b)), in the structure of the modified binder. Synthesis of these compounds is the result of interaction during hydration of clinker minerals Ca(OH)₂ with active mineral ingredients of ash and limestone [49, 50]. Growth of needle-shaped crystals contributes to reinforcement of the composite

structure on nano- and microlevels, reduction of porosity, and improvement of the composite complex strength [51, 52].

The greatest effect [53–55] is achieved through the synergistic impact of man-made pozzolanic additives (fly ash) and sedimentary-origin natural materials (limestone) at the content of OPC, 55 wt.%; LCW, 5 wt.%; and FA, 40 wt.%.

In this proportion, the composite material reaches the compressive strength of 77.3 MPa (by grinding to $S_{sp} = 550 \text{ m}^2/\text{kg}$), at 45% replacement of cement with industrial waste. Thus, the effect of “cement, fly ash, and limestone” composite binder obtained by cogrinding with superplasticizer in the varioplanetary mill to structure formation process is determined. Ground active mineral supplements are the crystallization centers of neoplasms. Ash nanoparticles contribute to the binding of $\text{Ca}(\text{OH})_2$, produced during the hydration of clinker minerals, intensifying binder hydration with forming needle-shaped crystals of low-basic hydrosilicate. Existence of the fine grains of limestone leads to forming hydrocarboaluminates. Implementation of the fiber-reinforced concrete potential is only possible by creating the material optimal structure, formation of which is determined by the following basic parameters: type and quality of raw materials, technology and preparation of concrete mixes, and quantitative relation between the components of fiber-reinforced concrete mixture.

4. Results and Discussions

Study of physical-mechanical properties of fine-grained concrete showed that use of the composite binder obtained by cogrinding of Portland cement, fly ash, limestone powder, and superplasticizer allowed increasing the compressive strength of fine concrete by 21%, while reducing almost in 2 times the proportion of cement. Prism strength and elastic modulus in the researched concrete types are significantly higher than in control samples (Table 8).

To optimize the fine-grained concrete structure forming on the macrolevel, steel fiber was used.

Taking into consideration previous studies [17–19], composition number 3 was adopted for the prototype (Table 8), to which fiber in an amount of 24 to 45 kg/m^3 , that is, 2% of the total weight of the mixture in increments of 0.2%, was added. It was found that the structure optimization at the macrolevel improves the compressive strength by 24% (Table 9).

Addition of the domestically produced basalt fiber instead of the steel anchor fiber has not led to substantial improvement of physical and mechanical properties of concrete, so, for further investigations, fiber-reinforced concrete number 5 (1.6% reinforcement) is taken.

On basis of the research, it was revealed that the addition of the fly ash and the limestone waste to the composite binder promotes structural and phase changes in the formation of high-density composite impermeable structures.

The fine-grained fiber-reinforced types of concrete on the developed composite binder compositions number 2 and number 3 (Table 10), which achieve compressive strength of 100.2–100.9 MPa with the diffusion coefficient of $1.34 \cdot$

$10^{-4} - 1.39 \cdot 10^{-4} \text{ cm}^2/\text{s}$, have the best physical and mechanical properties (Table 11).

It is revealed that, for fine-grained structure of concrete, in addition to high homogeneity, it is also characteristic to reduce specific stresses in the contact zone and increase the integral adhesion force between the cement stone and aggregate. The structure-forming role of the fine aggregate is most evident with an increase in the interaction surface; these conditions are realized in fine-grained types of concrete with the use of screening of granite crushed stone on the basis of composite astringents which, due to the highly developed surface, allow intensifying the processes of structure formation and accelerating the strength of concrete and also consolidating the structure.

As can be seen from the test results (Tables 10 and 11), composite binder of cement, fly ash from thermal power plants, and limestone at all dosages reduces the water permeability and air permeability of concrete. Thus, there is a clearly defined relationship between the properties of concrete and the features of the structure of cement stone: increasing the number of low-basic calcium hydrosilicates as well as increasing gel content and, correspondingly, reducing capillary porosity, especially at the submicroscopic level, predetermine the increase in strength and decrease in the permeability of concrete.

The maximum decrease in impermeability parameters was found in composition number 2 with the replacement of the proportion of cement in the binder mixture by 45% with the technogenic waste (FA and LCW). The air permeability of concrete decreased by 2 times (to $0.0253 \text{ cm}^3/\text{s}$), which according to GOST 12730.5 (Russian regulatory requirements) corresponds to mark W14 on permeability. The fiber-reinforced concrete's dense structure provides humidity resistance and reduces water absorption by volume in almost 2.5 times. These patterns are reflected in the water vapor permeability characteristics, which reaches the limit of $0.021 \text{ mg}/(\text{m}\cdot\text{h}\cdot\text{Pa})$ in the humid climate. The concrete's diffusion permeability was determined on the basis of data on the concrete neutralization rate (carbonation) by carbon dioxide in the absence of gradient of common air-gas pressure at the difference between the concentration of carbon dioxide in the concrete and that in environment at the time when the neutralization process is limited by the speed of carbon dioxide diffusion into the concrete porous structure. The experimental procedure is intended for use in the technology development and the designing of concrete compositions that provide long-term maintenance-free operation in the construction in nonaggressive and aggressive gas-air environment.

When evaluating the diffusive permeability, the average value of neutralized concrete layer thickness was found for all developed compounds. It was found that the developed concrete has an effective diffusion coefficient of $D' = 1.34 \cdot 10^{-4} \text{ cm}^2/\text{s}$.

Thus, the clear link between the concrete properties and characteristics of the cement stone structure (the increase in the number of hydrosilicate neoplasms) at the complex reducing of gel and capillary porosity is revealed, which

TABLE 8: Physical and mechanical properties of fine-grained concrete depending on the binder composition [25].

Composition numbers	Material consumption per 1 m ³										
	Cement	Fly ash	Cementitious binder [kg]	Superplasticizer	Screenings of crushed granite [kg]	Sand [kg]	Water [l]	Slump [cm]	Compressive strength [MPa]	Prism strength [MPa]	Elastic modulus [MPa]
1*	550	—	—	—	—	—	220	—	107.5	86.3	61.2
2	288	235	27	—	—	—	240	—	83.7	59.5	43.8
3	275	246	29	—	—	—	241	—	84.2	60.3	44.5
4	257	257	36	1.2	1000	623	242	10-12	76.3	55.2	40.9
5	244	268	38	—	—	—	243	—	75.2	55.0	40.8
6	230	278	42	—	—	—	244	—	75.0	54.9	40.8
7**	550	—	—	—	—	—	215	—	63.1	42.3	36.2

*The binder of low water ratio with the specific surface of 550 m²/kg. **The binder based on Portland cement CEM I 42.5N.

TABLE 9: Dependence of the strength of fiber-reinforced concrete on the percentage of reinforcement.

Composition numbers	Material consumption per 1 m ³				Reinforcement [%]	R_{compr} [MPa]
	Binder [kg]	Water [l]	Aggregate [kg]	Fiber [kg]		
3-1*	550	240	1623	—	0	94.2
3-2	550	240	1623	23.97	1	96.1
3-3	550	240	1623	28.76	1.2	97.3
3-4	550	240	1623	33.56	1.4	99.8
3-5	550	240	1623	38.35	1.6	100.9
3-6	550	240	1623	43.15	1.8	99.5
3-7	550	240	1623	47.94	2	99.6

* Prototype composition corresponds to composition number 3 (according to Table 8).

TABLE 10: Compositions and strength characteristics of the fiber-reinforced concrete.

Number	Material consumption per 1 m ³				Slump [cm]	Prism strength [MPa]	Compressive strength [MPa]		
	Cementitious binder [kg]								
	Cement	Fly ash	Limestone	Superplasticizer					
1	550	—	—	—	1623	220	66.3	115.5	
2	288	235	27	—	1623	240	69.5	100.9	
3	275	246	29	1.2	1623	241	10–12	70.3	100.2
4	257	257	36	—	1623	242	—	65.2	96.3
5	244	268	38	—	1623	243	—	65.0	95.2
6	230	278	42	—	1623	244	—	64.9	95.0

TABLE 11: The concrete performance characteristics depending on the binder composition.

Number (according to Table 10)	Air permeability of concrete a_c [cm ³ /s]	Mark on water permeability, W	Effective diffusion coefficient [cm ² /s]	Water absorption by volume [%]	Vapor permeability [mg/(m·h·Pa)]	
					For dry climate	For wet climate
					1	0.0565
2	0.0253	W14	$1.34 \cdot 10^{-4}$	6.1	0.022	0.021
3	0.0289	W14	$1.39 \cdot 10^{-4}$	6.3	0.026	0.025
4	0.0402	W12	$1.64 \cdot 10^{-4}$	7.8	0.027	0.026
5	0.0465	W12	$1.79 \cdot 10^{-4}$	10.9	0.030	0.029
6	0.0423	W12	$1.82 \cdot 10^{-4}$	14.4	0.032	0.030

is especially observed at the molecular and submicroscopic levels determining the growth of strength and increase of concrete impermeability.

The approbation of theoretical and experimental studies is carried out on the example of monolithic fiber-reinforced concrete walls with permanent formwork developed by Fediuk et al. [18, 25, 56]. The thermal resistance of wall is $R_o = 4,223$ (m²·°C)/W; the vapor permeability coefficient is $\mu = 0,021$ mg/(m·h·Pa). The fiber-reinforced types of concrete developed on basis of the composite binder can be used in the construction of high-rise buildings [57].

The technological circuit production of the high-density fiber-reinforced concrete is developed. It comprises the following steps: cogrinding of Portland cement, fly ash, and limestone crushing waste; two-stage mixing with the filler and the fiber; filling of formwork; and mechanical compaction of the concrete mix. This production line can be implemented in cement plants in different regions.

Thus, the possibility of reducing permeability of fiber-reinforced concrete by varying the amount and type of additives and fineness and taking into account the conditions of curing is studied. It allows creating materials for multilayer load-bearing structures with a compressive strength of 100 MPa, with low permeability under actual operating conditions. Implementation of the research results will help to improve the environmental situation of regions, as fiber-reinforced concrete comprises 50–60% of industrial waste.

5. Conclusion

Positive dynamics of strength growth of the composite binder under the joint influence of the ash fine constituents, limestone crushing wastes, and superplasticizer with maximum increase in the activity of the binder at 62% were found. This is due to the fact that active mineral components of the composite binder contribute to the binding of Ca(OH)₂

produced during cement hydration, which results in formation of additional amount of hydrosilicate neoplasms. The overall reduction in porosity of compositions modified by the technogenic waste more than 2 times (from 16.3% to 8%) should be noted.

High strength is influenced by the complex actions:

- (i) Reduction of capillary porosity due to the intensification of the processes of growth of primary crystals of hydrosilicate phases
- (ii) Possible formation of secondary recrystallization and crystals creation
- (iii) Filling the space at the micro- and submicrolevels of structural organization composite with them and in conjunction with reduction technological porosity on 17%
- (iv) The formation of dense packing of the grain structure at the macrolevel, with the participation of spherical fine components of fly ash and limestone crushing wastes

The greatest effect is achieved through the synergistic impact of man-made pozzolanic additives (fly ash) and sedimentary-origin natural materials (limestone) at the content of OPC, 55 wt.%; LCW, 5 wt.%; and FA, 40 wt.%.

The fine-grained fiber-reinforced types of concrete on the developed composite binder, which achieve compressive strength of 100.2–100.9 MPa with the diffusion coefficient of $1.34 \cdot 10^{-4}$ – $1.39 \cdot 10^{-4}$ cm²/s, have the best physical and mechanical properties. As can be seen from the test results, composite binder of cement, fly ash from thermal power plants, and limestone at all dosages reduces the water permeability and air permeability of concrete.

Conflicts of Interest

The authors declare that they have no conflicts of interest.

References

- [1] S. Chithra, S. R. R. Senthil Kumar, and K. Chinnaraju, "The effect of Colloidal Nano-silica on workability, mechanical and durability properties of High Performance Concrete with Copper slag as partial fine aggregate," *Construction and Building Materials*, vol. 113, pp. 794–804, 2016.
- [2] K. S. Al-Jabri, M. Hisada, S. K. Al-Oraimi, and A. H. Al-Saidy, "Copper slag as sand replacement for high performance concrete," *Cement and Concrete Composites*, vol. 31, no. 7, pp. 483–488, 2009.
- [3] W. Wu, W. Zhang, and G. Ma, "Optimum content of copper slag as a fine aggregate in high strength concrete," *Materials and Corrosion*, vol. 31, no. 6, pp. 2878–2883, 2010.
- [4] H. Stang and C. Pedersen, "HPFRCC - extruded pipes," in *Proceedings of the 1996 4th Materials Engineering Conference. Part 1 (of 2)*, pp. 261–270, November 1996.
- [5] P. Tjiptobroto and W. Hansen, "Tensile strain hardening and multiple cracking in high-performance cement-based composites containing discontinuous fibers," *ACI Materials Journal*, vol. 90, no. 1, pp. 16–25, 1993.
- [6] V. C. Li, "From mechanics to structural engineering: the design of cementitious composites for civil engineering applications," *Structural Engineering/Earthquake Engineering*, vol. 10, pp. 37–48, 1993.
- [7] M. Li and V. C. Li, "Rheology, fiber dispersion, and robust properties of engineered cementitious composites," *Materials and Structures/Materiaux et Constructions*, vol. 46, no. 3, pp. 405–420, 2013.
- [8] J. Qiu and E.-H. Yang, "Micromechanics-based investigation of fatigue deterioration of engineered cementitious composite (ECC)," *Cement and Concrete Research*, vol. 95, pp. 65–74, 2017.
- [9] H. Luo, Y. Wu, A. Zhao et al., "Hydrothermally synthesized porous materials from municipal solid waste incineration bottom ash and their interfacial interactions with chloroaromatic compounds," *Journal of Cleaner Production*, vol. 162, pp. 411–419, 2017.
- [10] D.-Y. Yoo and N. Banthia, "Mechanical properties of ultra-high-performance fiber-reinforced concrete: A review," *Cement and Concrete Composites*, vol. 73, pp. 267–280, 2016.
- [11] D.-Y. Yoo, N. Banthia, and Y.-S. Yoon, "Predicting service deflection of ultra-high-performance fiber-reinforced concrete beams reinforced with GFRP bars," *Composites Part B: Engineering*, vol. 99, pp. 381–397, 2016.
- [12] J. Yang, H. Shin, and D. Yoo, "Benefits of using amorphous metallic fibers in concrete pavement for long-term performance," *Archives of Civil and Mechanical Engineering*, vol. 17, no. 4, pp. 750–760, 2017.
- [13] D. Yoo, I. You, and S. Lee, "Electrical properties of cement-based composites with carbon nanotubes, graphene, and graphite nanofibers," *Sensors*, vol. 17, no. 5, p. 1064, 2017.
- [14] M. Castellote, I. Llorente, C. Andrade, and C. Alonso, "Accelerated leaching of ultra high performance concretes by application of electrical fields to simulate their natural degradation," *Materiaux et Constructions*, vol. 36, no. 256, pp. 81–90, 2003.
- [15] M. Tabatabaeian, A. Khaloo, A. Joshaghani, and E. Hajibandeh, "Experimental investigation on effects of hybrid fibers on rheological, mechanical, and durability properties of high-strength SCC," *Construction and Building Materials*, vol. 147, pp. 497–509, 2017.
- [16] M. Sahmaran and I. O. Yaman, "Hybrid fiber reinforced self-compacting concrete with a high-volume coarse fly ash," *Construction and Building Materials*, vol. 21, no. 1, pp. 150–156, 2007.
- [17] R. S. Fediuk, "Mechanical Activation of Construction Binder Materials by Various Mills," in *Proceedings of the All-Russian Scientific and Practical Conference on Materials Treatment: Current Problems and Solutions*, vol. 125, November 2015.
- [18] R. Fediuk and A. Yushin, "Composite binders for concrete with reduced permeability," in *Proceedings of the International Conference on Advanced Materials and New Technologies in Modern Materials Science 2015, AMNT 2015*, November 2015.
- [19] R. S. Fediuk and A. M. Yushin, "The use of fly ash the thermal power plants in the construction," in *Proceedings of the 21st International Conference for Students and Young Scientists: Modern Technique and Technologies, MTT 2015*, vol. 93, October 2015.
- [20] M. Sánchez, M. C. Alonso, and R. González, "Preliminary attempt of hardened mortar sealing by colloidal nanosilica migration," *Construction and Building Materials*, vol. 66, pp. 306–312, 2014.
- [21] M. H. Mobini, A. Khaloo, P. Hosseini, and A. Esrafil, "Mechanical properties of fiber-reinforced high-performance concrete

- incorporating pyrogenic nanosilica with different surface areas," *Construction and Building Materials*, vol. 101, pp. 130–140, 2015.
- [22] N. Ranjbar, A. Behnia, B. Alsubari, P. Moradi Birgani, and M. Z. Jumaat, "Durability and mechanical properties of self-compacting concrete incorporating palm oil fuel ash," *Journal of Cleaner Production*, vol. 112, pp. 723–730, 2016.
- [23] A. Hendi, H. Rahmani, D. Mostofinejad, A. Tavakolinia, and M. Khosravi, "Simultaneous effects of microsilica and nanosilica on self-consolidating concrete in a sulfuric acid medium," *Construction and Building Materials*, vol. 152, pp. 192–205, 2017.
- [24] L. Xu, F. Deng, and Y. Chi, "Nano-mechanical behavior of the interfacial transition zone between steel-polypropylene fiber and cement paste," *Construction and Building Materials*, vol. 145, pp. 619–638, 2017.
- [25] R. Fediuk, "High-strength fibrous concrete of Russian Far East natural materials," in *Proceedings of the International Conference on Advanced Materials and New Technologies in Modern Materials Science 2015, AMNT 2015*, vol. 116, November 2015.
- [26] R. Ibragimov, "The influence of binder modification by means of the superplasticizer and mechanical activation on the mechanical properties of the high-density concrete," *ZKG International*, vol. 69, no. 6, pp. 34–39, 2016.
- [27] L. H. Zagorodnjuk, V. S. Lesovik, A. A. Volodchenko, and V. T. Yerofeyev, "Optimization of mixing process for heat-insulating mixtures in a spiral blade mixer," *International Journal of Pharmacy and Technology*, vol. 8, no. 3, pp. 15146–15155, 2016.
- [28] R. A. Ibragimov and S. I. Pimenov, "Influence of mechanochemical activation on the cement hydration features," *Magazine of Civil Engineering*, vol. 62, no. 2, pp. 3–12, 2016.
- [29] E. Glagolev, L. Suleimanova, and V. Lesovik, "High reaction activity of nano-size phase of silica composite binder," *Journal of Environmental and Science Education*, vol. 11, no. 18, pp. 12383–12389, 2016.
- [30] S. L. Buyantuyev, L. A. Urkhanova, S. A. Lkhasaranov, Y. Y. Stebenkova, A. B. Khmelev, and A. S. Kondratenko, "The methods of receiving coal water suspension and its use as the modifying additive in concrete," in *Proceedings of the 12th International Conference Radiation-Thermal Effects and Processes in Inorganic Materials*, vol. 168, September 2016.
- [31] S. L. Buyantuev, L. A. Urkhanova, A. S. Kondratenko, S. Y. Shishulkin, S. A. Lkhasaranov, and A. B. Khmelev, "Processing of ash and slag waste of heating plants by arc plasma to produce construction materials and nanomodifiers," in *Proceedings of the 12th International Conference Radiation-Thermal Effects and Processes in Inorganic Materials*, vol. 168, September 2016.
- [32] A. P. Semenov, N. N. Smirnyagina, L. A. Urkhanova et al., "Reception carbon nanomodifiers in arc discharge plasma and their application for modifying of building materials," in *Proceedings of the 12th International Conference Radiation-Thermal Effects and Processes in Inorganic Materials*, vol. 168, September 2016.
- [33] R. Chihaoui, H. Khelafi, Y. Senhadji, and M. Mouli, "Potential use of natural perlite powder as a pozzolanic mineral admixture in Portland cement," *Journal of Adhesion Science and Technology*, vol. 30, no. 17, pp. 1930–1944, 2016.
- [34] M. Koniorczyk, D. Gawin, and B. Schrefler, "Modeling evolution of frost damage in fully saturated porous materials exposed to variable hygro-thermal conditions," *Computer Methods Applied Mechanics and Engineering*, vol. 297, pp. 38–61, 2015.
- [35] K. Marcin, "Coupled heat and water transport in deformable porous materials considering phase change kinetics," *International Journal of Heat and Mass Transfer*, vol. 81, pp. 260–271, 2015.
- [36] A. Peschard, A. Govin, P. Grosseau, B. Guilhot, and R. Guyonnet, "Effect of polysaccharides on the hydration of cement paste at early ages," *Cement and Concrete Research*, vol. 34, no. 11, pp. 2153–2158, 2004.
- [37] R. S. Fediuk and D. A. Khramov, "Research on porosity of the cement stone of composite binders," *Int. Res. J.*, vol. 1, pp. 77–79, 2016.
- [38] Z. Liu, Y. Zhang, and Q. Jiang, "Continuous tracking of the relationship between resistivity and pore structure of cement pastes," *Construction and Building Materials*, vol. 53, pp. 26–31, 2014.
- [39] Z. Liu, Y. Zhang, G. Sun, Q. Jiang, and W. Zhang, "Resistivity method for monitoring the early age pore structure evolution of cement paste," *Journal of Civil, Architectural and Environmental Engineering*, vol. 34, no. 5, pp. 148–153, 2012.
- [40] M. Schmidt, H. Pöllmann, A. Egersdörfer, J. Göske, and S. Winter, "Investigations on the pozzolanic reactivity of a special glass meal in a cementitious system," in *Proceedings of the 32nd International Conference on Cement Microscopy 2010*, pp. 86–118, 2010.
- [41] M. Schmidt, H. Pöllmann, A. Egersdörfer, J. Göske, and S. Winter, "Investigations on the use of a foam glass containing metakaolin in a lime binder system," in *Proceedings of the 33rd International Conference on Cement Microscopy 2011*, pp. 319–354, 2011.
- [42] A. Sachdeva, M. J. Mccarthy, L. J. Csetenyi, and M. R. Jones, "Mechanisms of sulfate heave prevention in lime stabilized clays through pozzolanic additions," in *Proceedings of the International Symposium on Ground Improvement Technologies and Case Histories, ISGI'09*, pp. 555–560, December 2009.
- [43] A. J. Puppala, E. Wattanasatcharoen, V. S. Dronamraju, and L. R. Hoyos, *Ettringite induced heaving and shrinking in kaolinite clay*, vol. 162 of *Geotechnical Special Publication*, 2007.
- [44] S. Liu and P. Yan, "Hydration properties of limestone powder in complex binding material," *Journal of the Chinese Ceramic Society*, vol. 36, no. 10, pp. 1401–1405, 2008.
- [45] S. Liu and L. Zeng, "Influence of new admixtures on the properties of hydraulic concrete," *Journal of Hydroelectric Engineering*, vol. 30, no. 2, pp. 118–122, 2011.
- [46] K. Pushkarova, K. Kaverin, and D. Kalantaevskiy, "Research of high-strength cement compositions modified by complex organic-silica additives," *Eastern European Journal of Enterprise Technologies*, vol. 5, no. 5, pp. 42–51, 2015.
- [47] E. V. Fomina, V. V. Strokova, and N. I. Kozhukhova, "Application of natural aluminosilicates in autoclave cellular concrete," *World Applied Sciences Journal*, vol. 25, no. 1, pp. 48–54, 2013.
- [48] K. Ma, J. Feng, G. Long, and Y. Xie, "Effects of mineral admixtures on shear thickening of cement paste," *Construction and Building Materials*, vol. 126, pp. 609–616, 2016.
- [49] P. Shafiq, M. A. Nomeli, U. J. Alengaram, H. B. Mahmud, and M. Z. Jumaat, "Engineering properties of lightweight aggregate concrete containing limestone powder and high volume fly ash," *Journal of Cleaner Production*, vol. 135, pp. 148–157, 2016.
- [50] A. Balza, O. Corona, A. Alarcón, J. Echevarrieta, M. Goite, and G. González, "Microstructural study of Portland cement additivated with Nanomaterials," *Acta Microscopica*, vol. 25, no. 1, pp. 39–47, 2016.

- [51] F. Faleschini, M. A. Zanini, K. Brunelli, and C. Pellegrino, "Valorization of co-combustion fly ash in concrete production," *Materials and Corrosion*, vol. 85, pp. 687–694, 2015.
- [52] B. Boulekbache, M. Hamrat, M. Chemrouk, and S. Amziane, "Flexural behaviour of steel fibre-reinforced concrete under cyclic loading," *Construction and Building Materials*, vol. 126, pp. 253–262, 2016.
- [53] M. Rudzki, M. Bugdol, and T. Ponikiewski, "An image processing approach to determination of steel fibers orientation in reinforced concrete," *Lecture Notes in Computer Science*, vol. 7339, pp. 143–150, 2012.
- [54] T. Ponikiewski, J. Gołaszewski, M. Rudzki, and M. Bugdol, "Determination of steel fibres distribution in self-compacting concrete beams using X-ray computed tomography," *Archives of Civil and Mechanical Engineering*, vol. 15, no. 2, pp. 558–568, 2015.
- [55] R. S. Fediuk and D. A. Khramov, "Physical equipment spectroscopic study of coal ash," *Modern Construction and Architecture*, vol. 1, pp. 57–60, 2016.
- [56] R. S. Fediuk, A. K. Smoliakov, R. A. Timokhin, N. Y. Stoyushko, and N. A. Gladkova, *Fibrous Concrete with Reduced Permeability to Protect the Home Against the Fumes of Expanded Polystyrene*, vol. 66 of *Materials Science and Engineering*, 2017.
- [57] M. Quintard, "Transfers in porous media," *Special Topics and Reviews in Porous Media*, vol. 6, no. 2, pp. 91–108, 2015.

Research Article

Kinetic Hydration Heat Modeling for High-Performance Concrete Containing Limestone Powder

Xiao-Yong Wang

College of Engineering, Department of Architectural Engineering, Kangwon National University, Chuncheon-si 200701, Republic of Korea

Correspondence should be addressed to Xiao-Yong Wang; wxbrave@kangwon.ac.kr

Received 15 June 2017; Accepted 1 August 2017

Academic Editor: Doo-Yeol Yoo

Copyright © 2017 Xiao-Yong Wang. This is an open access article distributed under the Creative Commons Attribution License, which permits unrestricted use, distribution, and reproduction in any medium, provided the original work is properly cited.

Limestone powder is increasingly used in producing high-performance concrete in the modern concrete industry. Limestone powder blended concrete has many advantages, such as increasing the early-age strength, reducing the setting time, improving the workability, and reducing the heat of hydration. This study presents a kinetic model for modeling the hydration heat of limestone blended concrete. First, an improved hydration model is proposed which considers the dilution effect and nucleation effect due to limestone powder addition. A degree of hydration is calculated using this improved hydration model. Second, hydration heat is calculated using the degree of hydration. The effects of water to binder ratio and limestone replacement ratio on hydration heat are clarified. Third, the temperature history and temperature distribution of hardening limestone blended concrete are calculated by combining hydration model with finite element method. The analysis results generally agree with experimental results of high-performance concrete with various mixing proportions.

1. Introduction

The use of limestone powder blended cement is a common practice in the modern concrete industry. The benefits from technical, economic, and ecological aspects can be achieved by using limestone blended concrete [1]. Technical benefits mainly refer to limestone powder which can increase the early-age performance of concrete. Economic benefits mean obtaining cement with a compressive strength similar to control concrete at low production costs. The ecological aspects are the reduction of greenhouse gas emission by using limestone.

Many studies in experimental or theoretical aspects have been done about early-age properties and durability of limestone blended concrete. Bonavetti et al. [2] found that the addition of limestone can increase the early-age strength of concrete. However, the late-age strength is impaired due to the dilution effect of limestone addition. Mohammadi and South [3] reported that limestone addition can reduce the bleeding of fresh concrete and increase the viscosity and cohesiveness of fresh concrete. Mohammadi and South [4]

also reported that the concrete with various limestone contents up to 12% has a similar drying shrinkage and sulfate expansion resistance with control concrete. Chen and Kwan [5] measured heat generation of concrete with different limestone stone replacement ratios and binder contents. They found that the addition of limestone can significantly reduce the heat generation of concrete. Palm et al. [6] found that high-level limestone addition can increase the carbonation depth and chloride migration coefficient of concrete. Based on life cycle assessment, Palm et al. [6] also found high-level limestone additions can reduce the CO₂ emission about 25% in comparison with average cement with the same performance.

Compared with abundant experimental studies, the theoretical models for limestone blended concrete are relatively limited. Lothenbach et al. [7] proposed a thermodynamic model for limestone blended concrete. The formation of monocarboaluminate and bulk compositions of hydrating cement is calculated by thermodynamic models. Bentz [8] proposed a hydration model which analyzed the dilution effect, nucleation effect, and chemical effect of limestone

addition. Similarly, Mohamed et al. [9] also proposed a model to evaluate reaction degree of hydration for concrete with different limestone additions. However, Lothenbach et al. [7], Bentz [8], and Mohamed et al.'s [9] studies mainly focus on the degree of hydration in cement-limestone blends. The hydration heat is scarcely simulated in their studies. Poppe and Schutter [10] and Ye et al. [11] proposed models to analyze heat evolution of limestone blended self-compacting concrete. But their study mainly focuses on the isothermal condition or adiabatic temperature rise. For concrete structures in construction sites, the heat release from hydration and heat transfer to ambient environments occurs simultaneously. Poppe and Schutter [10] and Ye et al.'s [11] studies do not consider semiadiabatic temperature rise in real construction sites.

To overcome the shortcomings in current models [7–11], we proposed an integrated numerical procedure to analyze the temperature history and temperature distribution of hardening limestone blended concrete. The hydration model is combined with finite element method. The heat of hydration is calculated from the degree of hydration. The reduction of hydration heat due to limestone additions is clarified through analysis.

2. Hydration Heat Model of Limestone Powder Blended Concrete

2.1. Hydration Model of Portland Cement. Wang and Lee [12] proposed a kinetic hydration model for Portland cement which takes into account the effects of a water to binder ratio (W/B), compound compositions of cement, fineness of cement, and capillary water contents on the hydration of cement. The kinetic hydration model analyzes the involved kinetic processes of cement hydration, such as initial dormant process, phase boundary reaction-controlled process, and diffusion-controlled process. The kinetic hydration model is valid for concrete with various types of Portland cement, various mixing proportions, and various curing temperatures. The equation for the kinetic hydration model is shown as follows:

$$\frac{d\alpha}{dt} = \frac{3\rho_w C_{w-free} (S_w/S_0)}{r_0 \rho_c (\nu + w_g)} \cdot \frac{1}{(1/k_d - r_0/D_e) + (1/k_r)(1-\alpha)^{-2/3} + (r_0/D_e)(1-\alpha)^{-1/3}} \quad (1)$$

In (1), α is hydration degree of cement, k_d is the hydration rate coefficient in the initial dormant period, k_r is the hydration rate coefficient of phase boundary reaction-controlled process, D_e is the hydration rate coefficient in the diffusion-controlled stage, C_{w-free} denotes the amount of capillary water at the exterior of hydration products, S_w denotes the effective contacting surface area between the cement particles and capillary water, and S_0 denotes the total surface area if hydration products develop unconstrained [12]. Equation (1) also considers chemical and physical aspects of cement hydration. In (1), ν is the mass of chemically bound water

for one-gram hydrated cement ($=0.25$), w_g is the mass of physically bound water for one-gram hydrated cement ($=0.15$), ρ_w denotes the density of water, ρ_c denotes the density of the cement, r_0 denotes the radius of unhydrated cement particles.

The determinations of reaction coefficients k_d , D_e , and capillary water content C_{w-free} are shown in (2)–(4), respectively.

$$k_d = \frac{B}{\alpha^{1.5}} + C\alpha^3, \quad (2)$$

$$D_e = D_{e0} \ln\left(\frac{1}{\alpha}\right), \quad (3)$$

$$C_{w-free} = \left(\frac{W_0 - 0.4 * \alpha * C_0}{W_0}\right)^r. \quad (4)$$

Equation (2) can be used to determine reaction coefficient k_d . In (2), B is the rate of the initial impermeable layer formation, and C is the rate of the initial impermeable layer decay.

Equation (3) can be used to determine reaction coefficient D_e . In (3), D_{e0} is the initial diffusion coefficient, and D_e decreases as cement hydration proceeds.

Equation (4) can be used to determine capillary water content C_{w-free} . In (4), C_0 is the cement content in mixing proportion, W_0 is the water content in the mix proportion, and r ($r = 2.6 - 4(W_0/C_0)$) is an empirical parameter that considers the accessibility of water into an inner anhydrous part through an outer hard shell of cement particles. For high-strength concrete with low W/C ratio at late ages, C_{w-free} has a significant influence on the rate of hydration.

The influences of temperature on reaction coefficients can be described by using Arrhenius's law [12] as follows:

$$\begin{aligned} B &= B_{20} * \exp\left(-\beta_1 \left(\frac{1}{T} - \frac{1}{293}\right)\right), \\ C &= C_{20} * \exp\left(-\beta_2 \left(\frac{1}{T} - \frac{1}{293}\right)\right), \\ k_r &= k_{r20} * \exp\left(-\frac{E}{R} \left(\frac{1}{T} - \frac{1}{293}\right)\right), \\ D_{e0} &= D_{e20} * \exp\left(-\beta_3 \left(\frac{1}{T} - \frac{1}{293}\right)\right), \end{aligned} \quad (5)$$

where β_1 , β_2 , E/R , and β_3 denote the activation energies of B , C , k_r , and D_{e0} , respectively. B_{20} , C_{20} , k_{r20} , and D_{e20} denote the values of reaction coefficients B , C , k_r , and D_{e0} at 293 K, respectively.

Based on the degree of hydration of concrete with various types of Portland cement and various curing temperatures, Wang [13] proposed that the reaction coefficients of hydration model, such as B_{20} , C_{20} , k_{r20} , and D_{e20} , can be determined from compound compositions of cement. The temperature

sensitivity coefficients can be approximately regarded as constants for different types of cement [13]. These relationships are shown as follows:

$$\begin{aligned}
 B_{20} &= 6 * 10^{-12} (C_3S\% + C_3A\%) + 4 * 10^{-10}, \\
 C_{20} &= 0.0003C_3S\% + 0.0186, \\
 k_{r20} &= 8 * 10^{-8}C_3S\% + 1 * 10^{-6}, \\
 D_{e20} &= -8 * 10^{-12}C_2S\% + 7 * 10^{-10}, \\
 \beta_1 &= 1000, \\
 \beta_2 &= 1000, \\
 \frac{E}{R} &= 5400, \\
 \beta_3 &= 7500.
 \end{aligned} \tag{6}$$

Summarily, the kinetic hydration model is composed of four rate determining coefficients, that is, the rate of formation of the initial impermeable layer (B), the rate of destruction of initial impermeable layer (C), the rate of phase boundary reaction-controlled process (k_r), and the rate of diffusion-controlled process (D_e). By using compound compositions of cement, the reaction coefficients of kinetic hydration model can be determined. Furthermore, the degree of hydration can be calculated by using (1). The proposed hydration model is valid for Portland cement concrete with various materials properties and curing conditions.

2.2. Effect of Limestone Addition on Cement Hydration. Wang [13] reported that the addition of limestone presents dilution effect, nucleation effect, and chemical effect on cement hydration. Dilution effect is when cement is partially replaced by limestone, the content of cement is reduced and water to cement ratio increases correspondingly. Nucleation effect is that limestone can serve as nucleation sites of hydrating cement particles. Hydration of cement can accelerate due to nucleation effect. Chemical effect is the formation of monocarboaluminate due to limestone reaction in preference to a monosulfoaluminate.

On the other hand, because the reactivity of limestone is very weak compared with other supplementary cementitious materials, limestone can be approximately regarded as chemical inert filler [1, 11]. Hence in this study, the chemical effect of limestone is not considered.

The dilution effect of limestone powder can be considered by using (4). Wang [13] and Kishi and Saruul [14] proposed that the nucleation effect of limestone relates to the ratio of surface area of cement particles to that of limestone powder. The nucleation effect of limestone powder is significant in phase boundary reaction-controlled process and diffusion-controlled process. The nucleation effect of limestone powder can be considered as follows:

$$L_r = \frac{LS_0 * S_{LS}}{C_0 * S_C}, \tag{7}$$

$$k_{rLS} = k_r (1 + A_1 L_r), \tag{8}$$

$$D_{eLS} = D_e (1 + A_2 L_r). \tag{9}$$

In (7), L_r is the limestone nucleation effect indicator, LS_0 is the mass of limestone in concrete mixing proportions, and S_{LS} is the Blaine surface area of limestone powder.

In (8), k_{rLS} is the updated phase boundary reaction coefficient, and A_1 is enhanced coefficients of k_r . In (9), D_{eLS} is the updated diffusion coefficient D_e , and A_2 is enhanced coefficients of D_e . Based on analysis shown later (Section 3.1), the values of A_1 and A_2 are set as 0.6.

Summarily, for a cement-limestone blend, the dilution effect is considered through capillary water concentration. The nucleation effect is considered by nucleation effect indicator which considers binder proportions and surface area of binders. Furthermore, by using updated reaction coefficients, the reaction degree of cement in cement-limestone blends can be determined.

2.3. Temperature History Model of Hardening Concrete.

Hydrate heat of hydrating concrete is dependent on both cement content and degree of hydration. The relation heat from hydration of concrete can be determined as follows [15–17]:

$$\frac{dQ}{dt} = C_0 H_e \frac{d\alpha}{dt}, \tag{10}$$

where Q is hydration heat and H_e is released hydration heat from a unit mass of cement. H_e can be determined by using compound compositions and hydration heat of individual components of cement [15–17].

For hardening concrete, the temperature distribution is in a dynamic heat balance between the hydration heat generation inside the concrete and heat loss to the ambient. The heat generation comes from hydration reactions of the cement. The temperature distribution of hardening concrete is determined as follows [18]:

$$C_{hc} \frac{\partial T}{\partial t} = \text{div}(k\nabla T) + \frac{dQ}{dt}, \tag{11}$$

where C_{hc} is the heat capacity of hydrating concrete and can be calculated as the sum of the individual components of concrete, k is the thermal conductivity of concrete, T is the concrete temperature, t is time, and dQ/dt can be calculated based on the degrees of hydration of the cement (10).

For hardening concrete in construction sites, the boundary condition can be described as follows:

$$k\nabla T = \beta(T_s - T_a), \tag{12}$$

where β is the coefficient of heat convection between concrete surface and ambient; T_s is the temperature on the concrete surface; and T_a is ambient temperature.

Equation (11) is numerically solved by using finite element method. Three-dimensional (3D) eight-node isoparametric element is used to mesh the geometry model of hardening concrete. The iteration scheme of (11) is shown as follows [15–17]:

$$\begin{aligned}
 &\left(\frac{1}{\Delta t} [C] + \theta [B] \right) \{T\}_{n+1} \\
 &= \left(\frac{1}{\Delta t} [C] - (1 - \theta) [B] \right) \{T\}_n + \{P\}_n,
 \end{aligned} \tag{13}$$

TABLE 1: Mixing proportions of paste for isothermal heat evolution.

	Water (g)	Cement (g)	Limestone (g)	Blaine of limestone (cm^2/g)	Limestone/(cement + limestone)	Water/cement
M100	5	10	0	—	0	0.5
M90L10-35	5	10	1.11	3500	0.1	0.5
M70L30-35	5	10	4.29	3500	0.3	0.5
M70L30-89	5	10	4.29	8900	0.3	0.5

where $[C]$ is the global mass matrix, $[B]$ is global stiffness matrix, $\{P\}$ is the global vector of temperature, and θ is integration parameter. The global stiffness matrix $[B]$, global mass matrix $[C]$, and global temperature vector $\{P\}$ can be obtained by assembling of element mass matrix, element stiffness matrix, and element temperature vector, respectively. Generally, to guarantee the stability of the numerical integration in a time domain, the value of integration parameter θ should be higher than 0.5. In this paper, according to the Galerkin method, the value of the parameter θ is used as 2/3 [12].

2.4. Summary of the Proposed Numerical Procedure. The numerical procedure consists of a kinetic hydration model and a finite element model. The kinetic hydration model considers the dilution effect and nucleation effect from limestone additions. The heat of hydration of hydrating concrete is calculated by using the degree of hydration and cement content. The calculation results of the heat of hydration are used as a source term in finite element model. By using Galerkin method, the parabolic partial differential equation about temperature distribution of hardening concrete is solved. Temperature history of semiadiabatic temperature rise is calculated considering both concrete materials properties and ambient conditions. The proposed numerical procedure is valuable for thermal cracking analysis of hardening concrete and construction plan design and materials design of concrete structures.

3. Verification of Proposed Model

3.1. Heat of Hydration. Experimental results about isothermal heat evolution shown in [14] are used to verify the proposed limestone blended hydration model. Kishi and Saruul [14] measured isothermal hydration heat of limestone blended cement paste. The mixing proportions of paste specimens are shown in Table 1. In Kishi and Saruul's study [14], to demonstrate the nucleation effect of limestone, the water to cement is the same for all specimens. Limestone is added as an additional binder, not replacing partial cement, which is different from the general applications of limestone. The limestone ranges within 10% and 30% of total binder, and the Blaine surface area of limestone ranges from 3500 cm^2/g to 8900 cm^2/g . The curing temperature is 20°C. The used cement is moderate heat Portland cement. By using Portland cement hydration model shown in Section 2.1, the hydration rate of control cement paste without limestone is calculated and shown in Figure 1(a). The y -axis of Figure 1(a) represents

the heat release for cement portions in cement-limestone blends.

Furthermore, based on experimental results about hydration heat of limestone blended cement paste, the enhanced coefficients A_1 and A_2 (shown in (8) and (9)) are set as 0.6. As shown from Figures 1(b)–1(d), the analysis results generally agree with experimental results. Figure 1(e) shows calculation results of rate of hydration heat. When cement is partially replaced by limestone, the value of the second peak of hydration heat increases, and the time corresponding to the second peak becomes much earlier. This trend agrees with experimental results about the rate of heat evolution of limestone blended cement paste [11]. When the surface area of Blaine surface of limestone increases, the nucleation effect becomes more significant, and the value of the second peak of hydration heat also increases. Hence limestone with a high Blaine surface is more effective in improving the hydration of cement.

3.2. Parameter Analysis about Hydration Heat. Parameter studies are carried out to analyze the degree of hydration and hydration heat of hardening concrete with different limestone replacement ratios and water to binder ratios. The water to binder ratio ranges from 0.3 to 0.5, and limestone content ranges from 15% to 30%. The curing temperature is assumed as 20°C.

The calculated degree of hydration is shown in Figure 2. Due to dilution effect and nucleation effect, the degree of hydration in cement-limestone blends is higher than that in control concrete. Moreover, for concrete with a lower water to binder ratio 0.3, when cement is partially replaced by limestone, the change of water to cement ratio is significant; hence the improvement of the degree of hydration is also obvious.

The relative degree of hydration means the ratio of the degree of hydration of limestone blended concrete to that of control concrete. Figure 3 shows relative degree of hydration. Given a certain limestone content, concrete with a lower water to binder ratio has a higher relative degree of hydration. This agrees with Bonavetti et al. [19] and Bentz et al.'s [20] study. They stated that limestone filler used in low water to cement ratio concrete is a rational option for saving energy.

As shown in (10), hydration heat relates to both cement content and degree of hydration. For limestone blended concrete, the degree of hydration increases which increases hydration heat, while the cement content decreases due to limestone replacing partial cement which reduces hydration heat. The total hydration heat depends on the combined

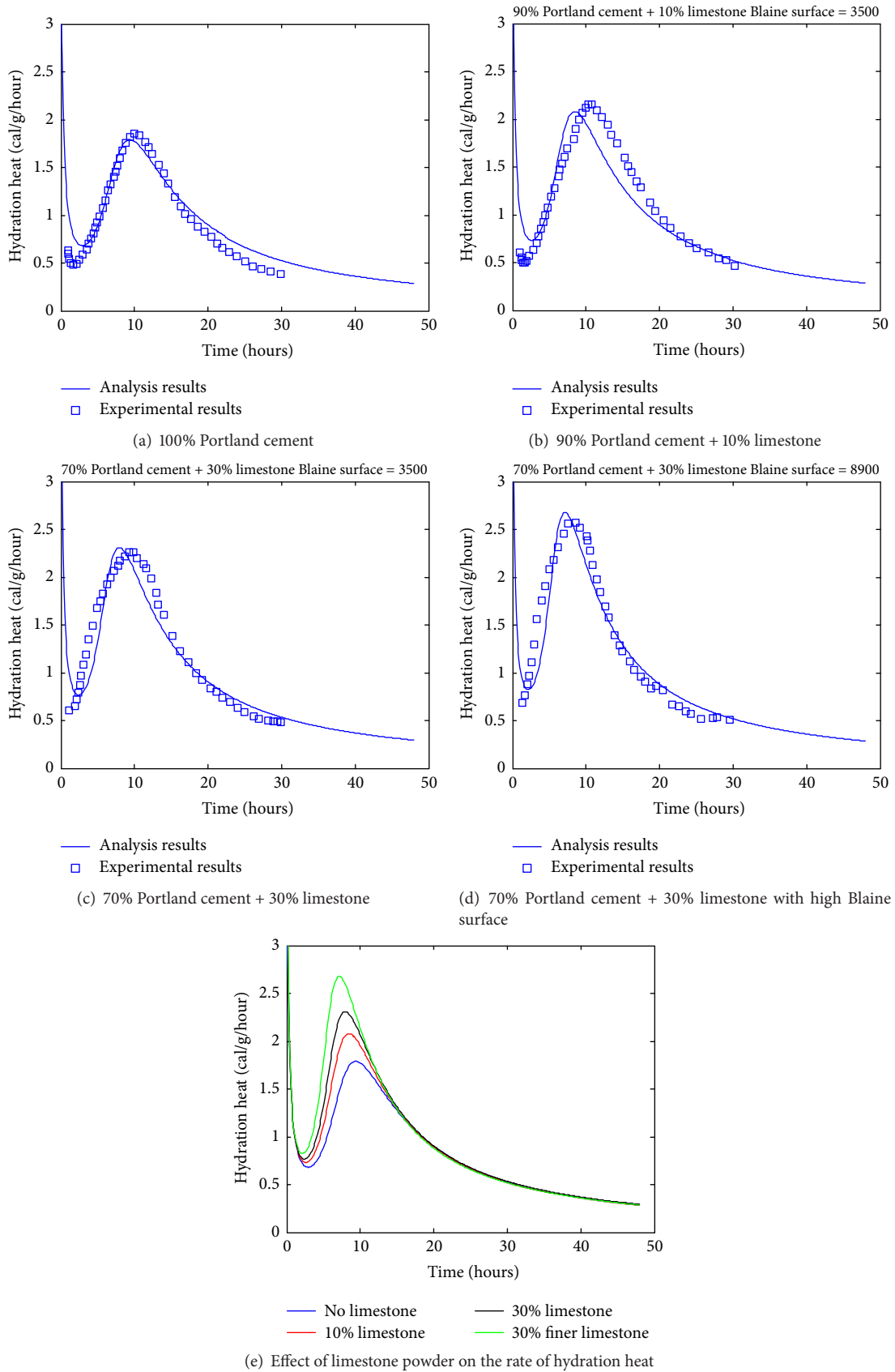


FIGURE 1: Rate of hydration heat.

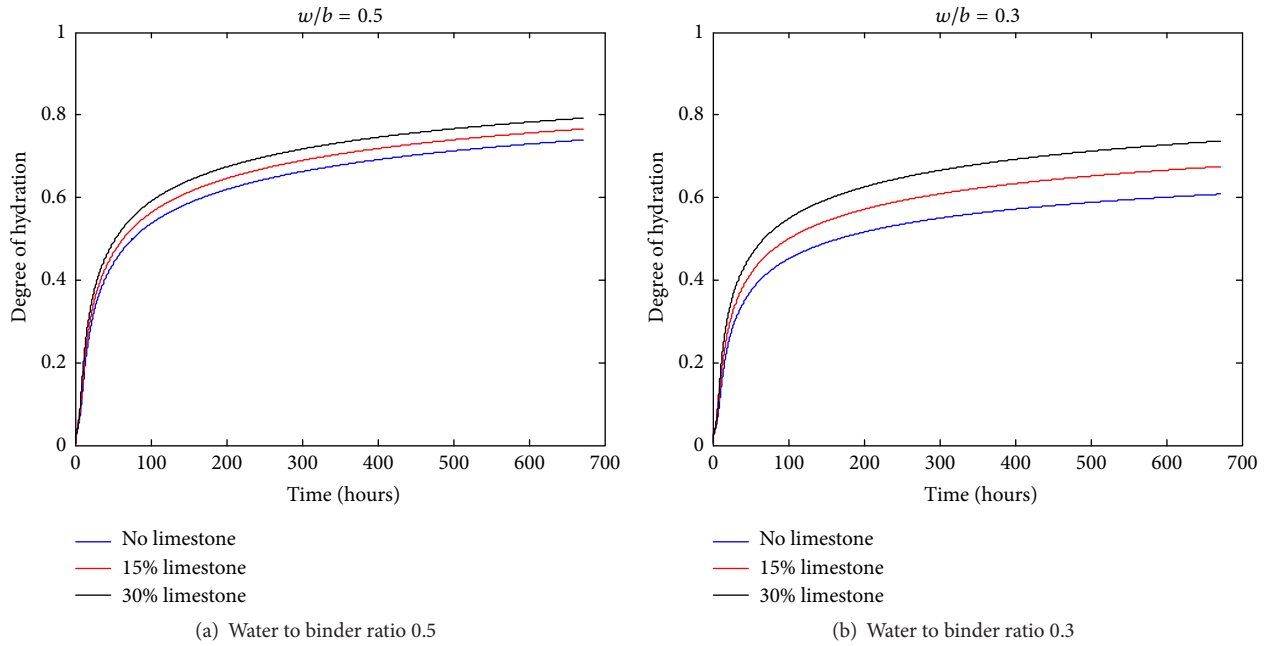


FIGURE 2: Degree of hydration.

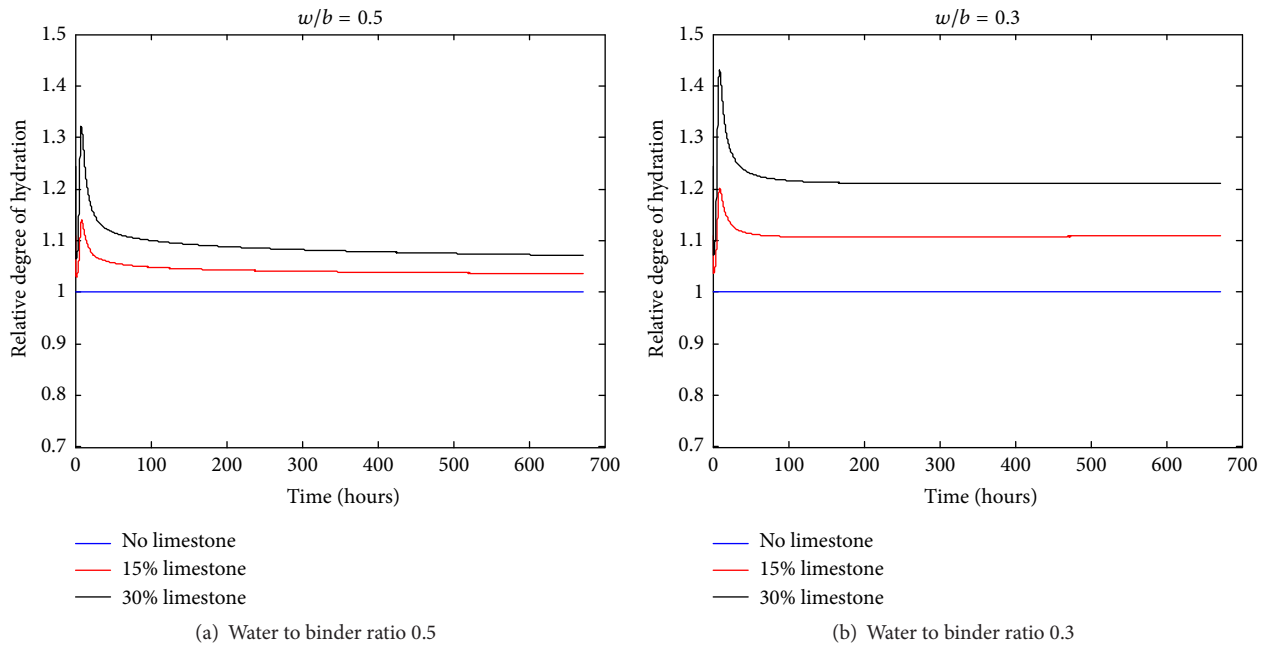


FIGURE 3: Relative degree of hydration.

action of increasing factor and decreasing factor, that is, degree of hydration and cement content. The relative heat of hydration means the ratio of heat of hydration of limestone blended concrete to that of control concrete. Figure 4 shows relative heat of hydration. Limestone blended concrete has a lower hydration heat than control concrete. Given a certain limestone content, concrete with a lower water to binder ratio has a higher relative heat of hydration. This agrees with Chen and Kwan's study [5]. Limestone addition can reduce

the hydration heat of concrete and decrease the tendency of thermal cracking of hardening concrete.

3.3. *Temperature History of Semiadiabatic Temperature Rise.* Experimental results about semiadiabatic temperature rise shown in [14] are used to verify the proposed semiadiabatic temperature rise model. Table 2 shows the mixing proportions of concrete. The initial temperature and ambient temperature for each specimen are also shown in Table 2.

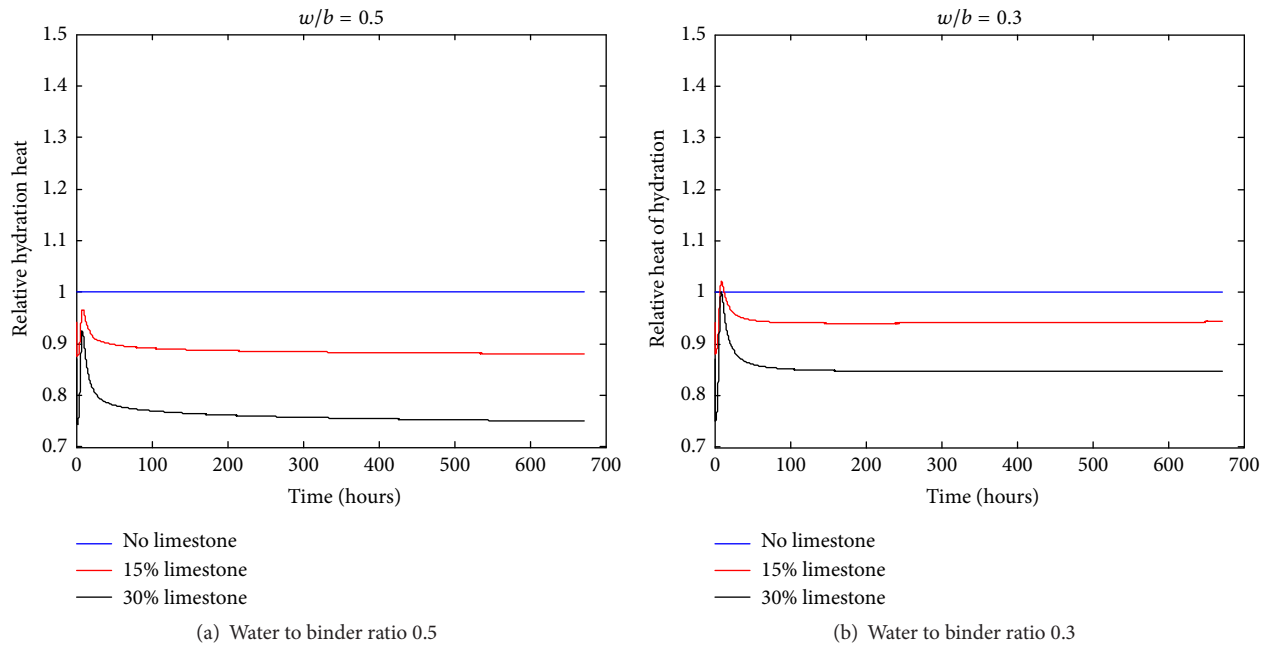


FIGURE 4: Relative heat of hydration.

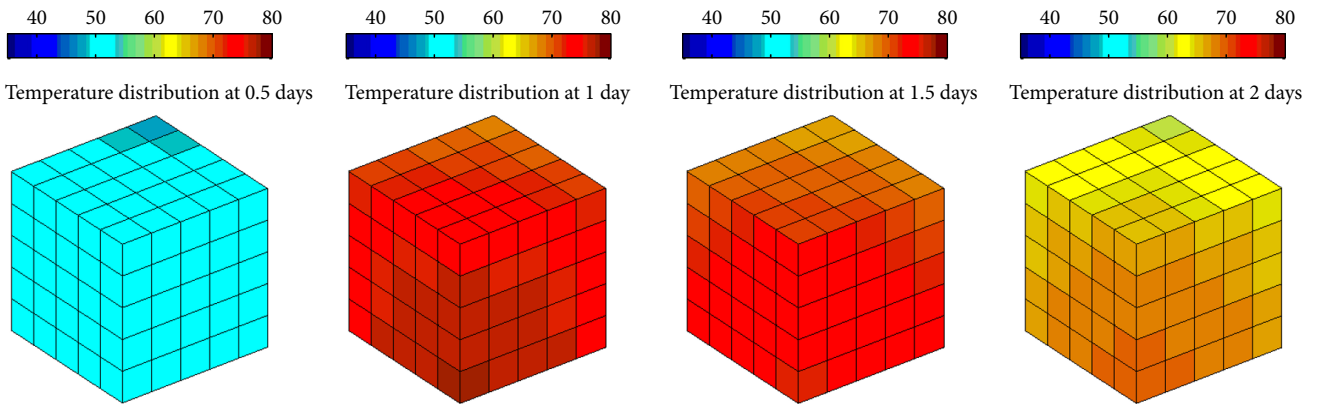
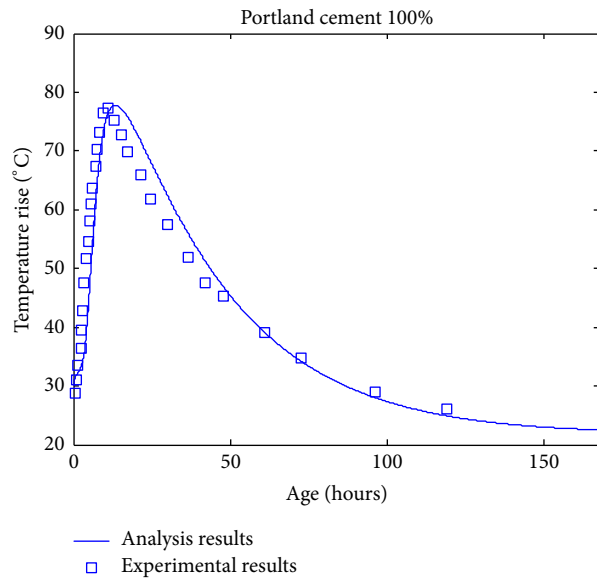
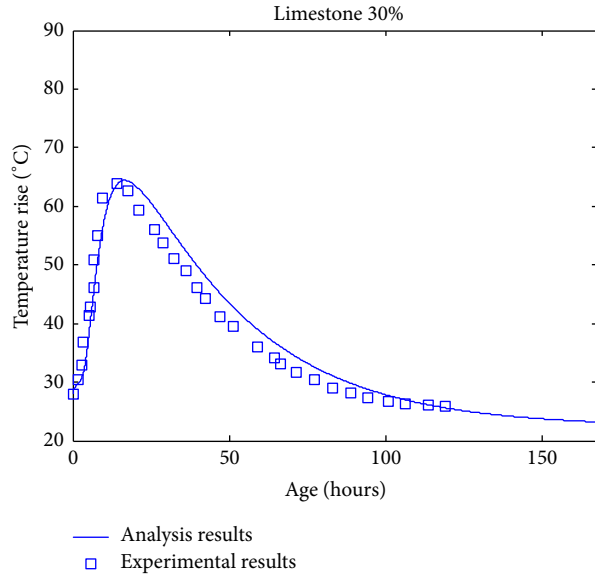
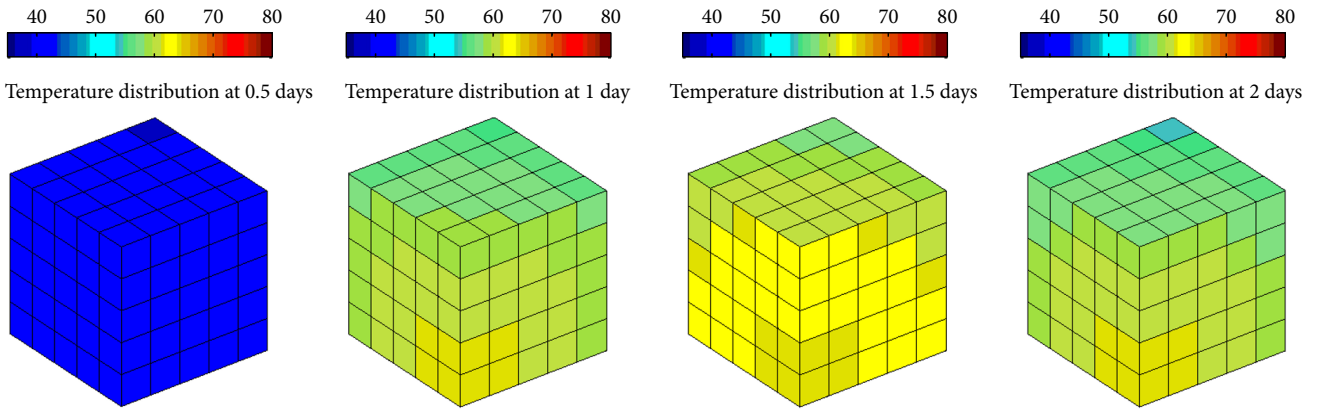


FIGURE 5: OPC concrete.



(a) Temperature history



(b) Temperature distribution

FIGURE 6: Limestone 30% concrete.

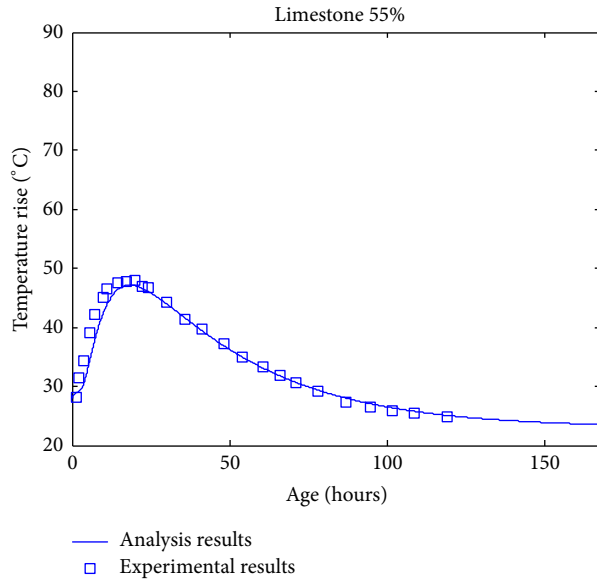
TABLE 2: Mixing proportions of concrete.

	Water/(cement + limestone)	Water (kg/m ³)	Cement (kg/m ³)	Limestone (kg/m ³)	Sand (kg/m ³)	Gravel (kg/m ³)	Superplasticizer (kg/m ³)	Initial temperature (°C)	Ambient temperature (°C)
OPC	30.3	171	565	—	820	915	1.0	30	23
Limestone 30%	32.7	177	396	146	820	915	0.7	28	23
Limestone 55%	32.6	168	226	291	820	916	0.7	28	23
Limestone 70%	32.0	165	155	362	820	915	0.7	28	28

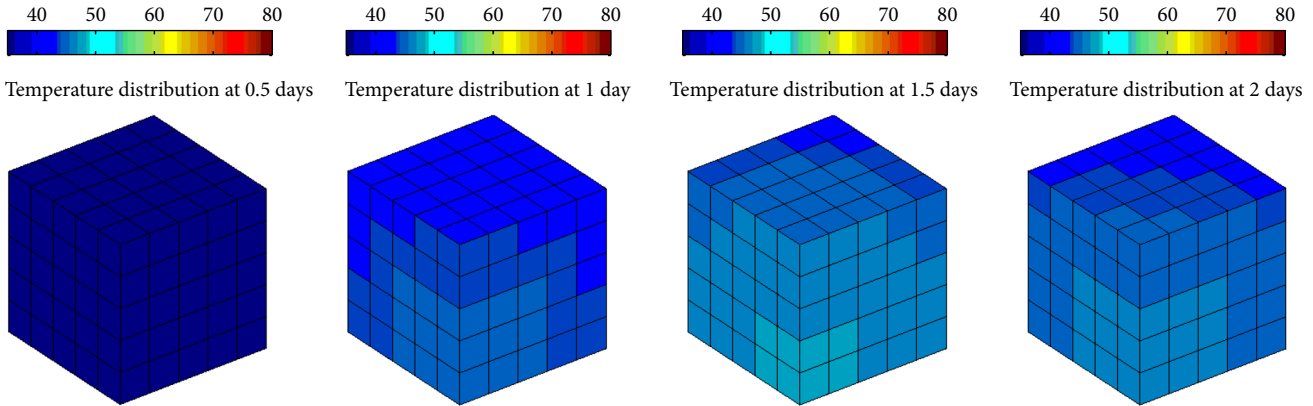
The water to binder ratio is about 0.3, and the limestone replacement ratio ranges from 30% to 70%. The compound compositions of cement are shown in Table 3. The used cement is ordinary Portland cement. The size of specimens is 445 mm * 445 mm * 445 mm. The temperature at center point is measured from mixing time to the age of five days.

Thermal conductivity and heat transfer coefficient of specimens are 41 kcal/m/day/k and 35 kcal/m²/day/k, respectively.

Because of symmetries of geometry condition and boundary condition of the specimen, a one-eighth specimen is adopted to represent the full specimen. The 8-node brick isoparametric element is used to mesh the specimen in



(a) Temperature history



(b) Temperature distribution

FIGURE 7: Limestone 55% concrete.

TABLE 3: Compound compositions of cement.

	C ₃ S %	C ₂ S %	C ₃ A %	C ₄ AF %	Gypsum %	Blaine (cm ² /g)
Cement	53.9	18.8	11.0	10.4	5.83	3350

three-dimensional spaces. Total 125 elements ($5 * 5 * 5 = 125$) are used. In each time step, the heat evolution rate of each element is determined from current temperature of the element. Figures 5–8 show the calculation results about temperature history and temperature distribution of hardening concrete. With the increasing of limestone content, the maximum temperature rise of concrete decreases. For control concrete, 30% limestone concrete, and 50% limestone concrete, the calculation results about temperature history generally agree with experimental results, while, for 70% limestone blended concrete, at early ages, the calculation result is slightly lower than experimental results. This may be due to heat release from the chemical reaction of limestone.

For concrete with very high content limestone, the chemical reaction of limestone becomes significant and can contribute to the temperature rise of hydrating concrete. The proposed model considers the acceleration of cement hydration due to temperature increasing. However, the reduction of solubility of concrete due to temperature increasing is not considered. The point should be taken into account in the future study.

4. Conclusions

This study proposes a numerical procedure for predicting temperature history of hardening limestone blended concrete. The numerical procedure combines a kinetic limestone blended cement hydration model with a finite element method.

First, the hydration model analyzes the dilution effect and nucleation effect due to limestone additions. For concrete with a lower water to binder ratio, the dilution effect due to limestone addition becomes obvious, and the degree of

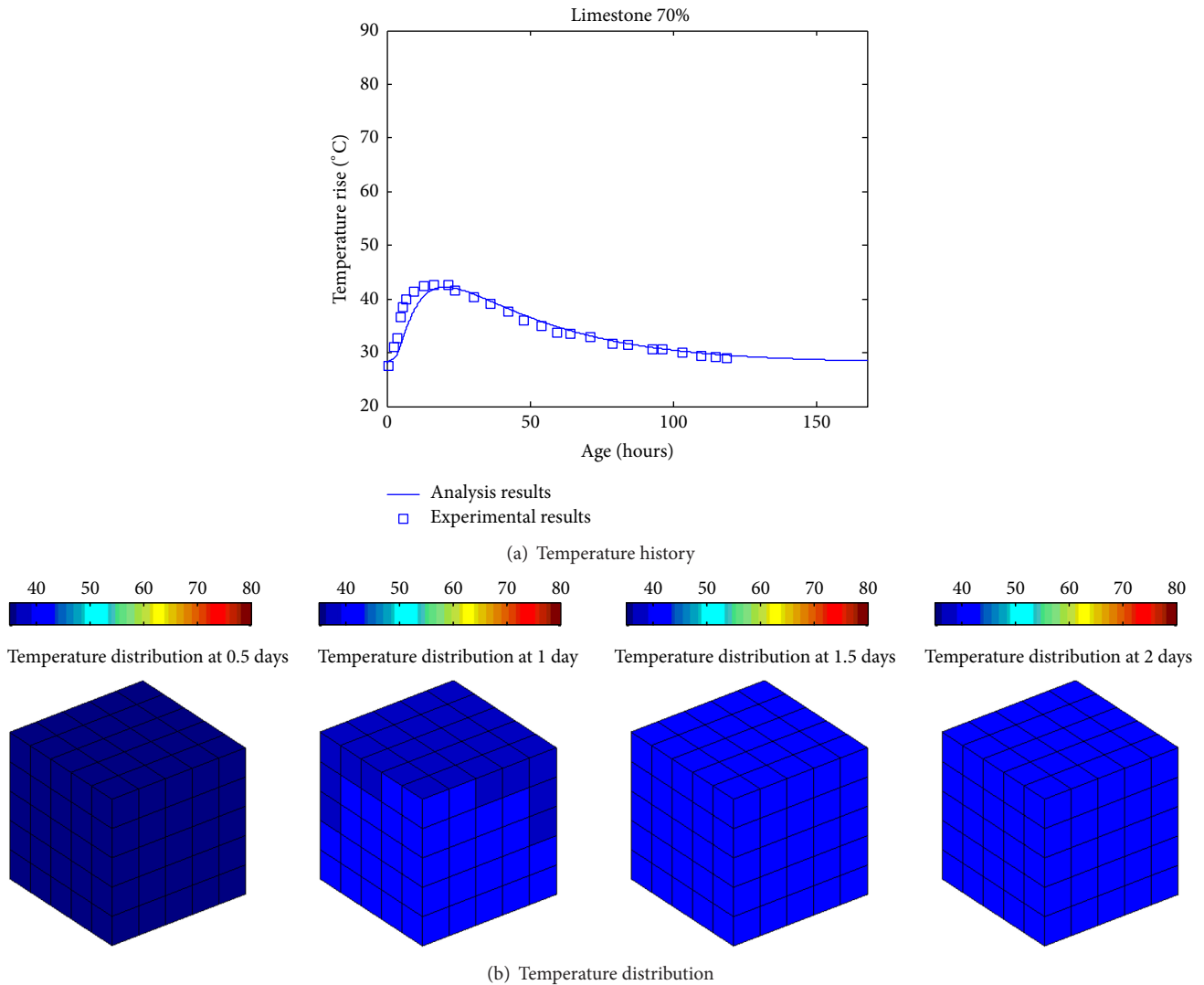


FIGURE 8: Limestone 70% concrete.

hydration is significantly improved compared with control concrete without limestone.

Second, the released heat of concrete relates to both cement content and degree of hydration. Limestone additions increase the degree of hydration but reduce cement content. The total hydration heat depends on the combined action of cement content and degree of hydration. The results of parameter analysis show that limestone additions can reduce the heat of hydration.

Third, the calculation results of hydration heat from hydration model are used as input parameters of finite element model. The combined hydration and finite element model can be used to evaluate temperature history and temperature distribution of semiadiabatic hardening concrete. The analysis results show that, with the increasing of limestone content, the maximum temperature rise of concrete decreases.

Conflicts of Interest

The author declares that they have no conflicts of interest.

Acknowledgments

This research was supported by a grant from Smart Civil Infrastructure Research Program (13SCIPA02) funded by Ministry of Land, Infrastructure and Transport (MOLIT) of Korean Government and Korea Agency for Infrastructure Technology Advancement (KAIA).

References

- [1] S. H. Liu and P. Y. Yan, "Effect of limestone powder on microstructure of concrete," *Journal Wuhan University of Technology, Materials Science Edition*, vol. 25, no. 2, pp. 328–331, 2010.

- [2] V. Bonavetti, H. Donza, V. Rahhal, and E. Irassar, "Influence of initial curing on the properties of concrete containing limestone blended cement," *Cement and Concrete Research*, vol. 30, no. 5, pp. 703–708, 2000.
- [3] I. Mohammadi and W. South, "Decision-making on increasing limestone content of general purpose cement," *Journal of Advanced Concrete Technology*, vol. 13, no. 11, pp. 528–537, 2015.
- [4] J. Mohammadi and W. South, "Effects of intergrinding 12% limestone with cement on properties of cement and mortar," *Journal of Advanced Concrete Technology*, vol. 14, no. 5, pp. 215–228, 2016.
- [5] J. J. Chen and A. K. H. Kwan, "Adding limestone fines to reduce heat generation of curing concrete," *Magazine of Concrete Research*, vol. 64, no. 12, pp. 1101–1111, 2012.
- [6] S. Palm, T. Proske, M. Rezvani, S. Hainer, C. Müller, and C.-A. Graubner, "Cements with a high limestone content - Mechanical properties, durability and ecological characteristics of the concrete," *Construction and Building Materials*, vol. 119, pp. 308–318, 2016.
- [7] B. Lothenbach, G. Le Saout, E. Gallucci, and K. Scrivener, "Influence of limestone on the hydration of Portland cements," *Cement and Concrete Research*, vol. 38, no. 6, pp. 848–860, 2008.
- [8] D. P. Bentz, "Modeling the influence of limestone filler on cement hydration using CEMHYD3D," *Cement and Concrete Composites*, vol. 28, no. 2, pp. 124–129, 2006.
- [9] A. R. Mohamed, M. Elsalamawy, and M. Ragab, "Modeling the influence of limestone addition on cement hydration," *Alexandria Engineering Journal*, vol. 54, no. 1, pp. 1–5, 2015.
- [10] A.-M. Poppe and G. De Schutter, "Analytical hydration model for filler rich binders in self-compacting concrete," *Journal of Advanced Concrete Technology*, vol. 4, no. 2, pp. 259–266, 2006.
- [11] G. Ye, X. Liu, A. M. Poppe, G. De Schutter, and K. Van Breugel, "Numerical simulation of the hydration process and the development of microstructure of self-compacting cement paste containing limestone as filler," *Materials and Structures/Materiaux et Constructions*, vol. 40, no. 9, pp. 865–875, 2007.
- [12] X. Wang and H. Lee, "Modeling the hydration of concrete incorporating fly ash or slag," *Cement and Concrete Research*, vol. 40, no. 7, pp. 984–996, 2010.
- [13] X.-Y. Wang, "Modeling of hydration, compressive strength, and carbonation of portland-limestone cement (PLC) concrete," *Materials*, vol. 10, no. 2, article 115, 2017.
- [14] T. Kishi and D. Saruul, "Hydration heat modeling for cement with limestone powder," *Iabse Colloquium Phuket*, vol. 81, pp. 133–138, 1999.
- [15] J. D. Logan, *A First Course in Differential Equations*, Undergraduate Texts in Mathematics, Springer, New York, 5th edition, 2011.
- [16] B. F. Zhu, *Thermal Stresses and Temperature Control of Mass Concrete*, Tsinghua University Press, Beijing, China, 2014.
- [17] K. Maekawa, T. Ishida, and T. Kishi, *Multi-Scale Modeling of Structural Concrete*, Taylor & Francis, New York, NY, USA, 2009.
- [18] W. Xiao-Yong, "Prediction of temperature distribution in hardening silica fume-blended concrete," *Computers and Concrete*, vol. 13, no. 1, pp. 97–115, 2014.
- [19] V. Bonavetti, H. Donza, G. Menéndez, O. Cabrera, and E. F. Irassar, "Limestone filler cement in low w/c concrete: A rational use of energy," *Cement and Concrete Research*, vol. 33, no. 6, pp. 865–871, 2003.
- [20] D. P. Bentz, E. F. Irassar, B. E. Bucher, and W. J. Weiss, "Limestone fillers conserve cement, part 2: durability issues and the effects of limestone fineness on mixtures," *Concrete International*, vol. 31, pp. 35–40, 2009.

Research Article

Flexural Strengthening of RC Slabs Using a Hybrid FRP-UHPC System Including Shear Connector

Jiho Moon,¹ Mahmoud M. Reda Taha,² and Jung J. Kim³

¹Department of Civil Engineering, Kangwon National University, Chuncheon-si, Gangwon-do 24341, Republic of Korea

²Department of Civil Engineering, University of New Mexico, MSC01 1070, Albuquerque, NM 87131-0001, USA

³Department of Civil Engineering, Kyungnam University, 7 Kyungnamdaehak-ro, Changwon-si 51767, Republic of Korea

Correspondence should be addressed to Jung J. Kim; jungkim@kyungnam.ac.kr

Received 11 April 2017; Accepted 7 May 2017; Published 5 June 2017

Academic Editor: Doo-Yeol Yoo

Copyright © 2017 Jiho Moon et al. This is an open access article distributed under the Creative Commons Attribution License, which permits unrestricted use, distribution, and reproduction in any medium, provided the original work is properly cited.

A polymeric hybrid composite system made of UHPC and CFRP was proposed as a retrofit system to enhance flexural strength and ductility of RC slabs. While the effectiveness of the proposed system was confirmed previously through testing three full-scale one-way slabs having two continuous spans, the slabs retrofitted with the hybrid system failed in shear. This sudden shear failure would stem from the excessive enhancement of the flexural strength over the shear strength. In this study, shear connectors were installed between the hybrid system and a RC slab. Using simple beam, only positive moment section was examined. Two full-scale RC slabs were cast and tested to failure: the first as a control and the second using this new strengthening technique. The proposed strengthening system increased the ultimate load carrying capacity of the slab by 70%, the stiffness by 60%, and toughness by 128%. The efficiency of shear connectors on ductile behavior of the retrofitted slab was also confirmed. After the UHPC top is separated from the slab, the shear connector transfer shear load and the slab system were in force equilibrium by compression in UHPC and tension in CFRP.

1. Introduction

Every year, more concrete is used in construction than any other material. In 2010, concrete produced in United States has been estimated to be worth \$35 billion [1]. The widespread use of concrete can be attributed to its attractive properties and accessibility. Because of its poor tensile strength, it is paired with reinforcing steel, which is cast away from the neutral axis, to form an effective composite. This composite, reinforced concrete (RC), is designed such that the compression forces are resisted by the concrete while the tension forces are resisted by the steel. This configuration of reinforcement provides acceptable flexural strength for RC.

RC is used in structures of all types, ranging from columns, beams, slabs, and foundations. Because of deterioration of the concrete due to aging, corrosion of the reinforcing steel, and increased loads that were previously unaccounted for, structural members may require strengthening after being constructed [2–5]. Moreover, due to the concern for blast-resistance of RC structures, strengthening

of existing RC structures has become an important topic in structural engineering [6, 7].

If strengthening existing infrastructures is feasible, it is much preferred over the demolition and construction of an entirely new system. This is due to the relatively low cost of strengthening compared to new construction in addition to the minimal impact that strengthening will have on the system. Two other major benefits include the short time of application and ability to maintain use of the structure during strengthening [4, 8].

In order to increase the flexural load carrying capacity of an existing RC beam, the amount of tensile capacity or compressive capacity must be increased. A relatively new method that has become accepted for strengthening existing structures is through the use of fiber reinforced polymer (FRP) composites. The high strength-to-weight ratio, resistance to corrosion, ease of application, the ability to install FRP without disrupting use of the structure, and relatively low maintenance of FRP make it an attractive composite to be used for strengthening.

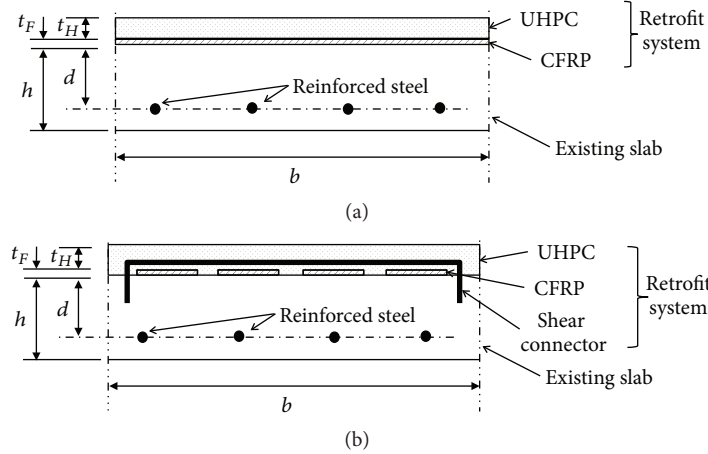


FIGURE 1: HPC-CFRP retrofit systems for flexural strengthening of the positive moment sections of RC slabs, (a) previously proposed system and (b) the modified system including shear connector.

Current methods of application recommend that the FRP be installed at the location of the extreme tensile fiber at the location of the maximum tension [9]. This application allows the normal concrete to act in compression while the reinforcing steel and FRP act in tension. The FRP is subjected to tensile forces during the entire loading. As the loading progresses, the neutral axis will move toward the compression side of the member and the member will fail, typically due to debonding of FRP prior to crushing of the concrete.

In this study, a hybrid system of high performance concrete (HPC) and carbon fiber reinforced polymer (CFRP) sheets including shear connectors for strengthening of RC slabs is proposed. Three main contributors, CFRP, HPC, and shear connectors, are responsible for the increased capacity of the strengthened RC slabs. To validate this novel strengthening technique at the positive moment section of RC slab, two one-way slabs were cast. The first slab was an unstrengthened concrete slab which was used as a control. The second slab was cast to mimic the first but featured an overlay of FRP and UHPC after installing shear connectors. Both slabs were treated as simple beams with a region that contained positive bending moment and theoretically no shear.

2. Proposed Retrofit System

Previously, a hybrid system composed of HPC and CFRP sheets was proposed to improve the strength and ductility of existing continuous RC slabs by installing the system only to the top of the slab [10] as shown in Figure 1(a) for the positive moment section. Experimental results of the previously proposed system showed that the ultimate load capacity and ductility of the strengthened RC slabs increased by 164% and 122%, respectively, as compared with the reference slab [10]. However, the slabs strengthened with the previously proposed system failed in shear. This sudden failure was initiated from CFRP debonding from the concrete slab. To ensure ductile failure of flexural members [11], flexural failure

design limits of a continuous RC slab according to its moment carrying and shear carrying capacities were proposed to develop a design method of the proposed hybrid FRP-HPC retrofitting system [12].

Here, another retrofit system to induce ductile failure of the strengthened slabs, a hybrid system of CFRP and HPC including shear connectors, is proposed as shown in Figure 1(b). Three main contributors, CFRP, HPC, and shear connectors, are responsible for the increased capacity of the strengthened RC system. The enhancing mechanism for this system was shown in Figure 2. The moment capacity for the strengthened RC slabs can be calculated as

$$M_n = T_s (j_1 d) + T_F (j_2 d), \quad (1)$$

where T_s and T_F are forces at failure in steel and CFRP, respectively. $j_1 d$ and $j_2 d$ are the corresponding moment arm length. It is important to note that the enhancing mechanism of the proposed system at the positive moment sections is valid only when CFRP takes tension at failure.

3. Experiments

A concrete having the 28-day characteristic compressive strength of 49 MPa is used for the slabs. Steel rebars having the yield strength of 400 MPa are used to reinforce the slabs. The typical flexural reinforcement bar chosen was number 13 deformed bar which had a cross sectional area of 126.5 mm². Transverse reinforcement was required to control shrinkage cracks and consisted of number 10 deformed bars with a cross sectional areas of 71 mm². The slab's size is 130 mm × 900 mm × 2440 mm. The minimum amount of reinforcement was calculated using ACI 318-08 [13]. Details for the RC slab are shown in Figure 3.

For the retrofitted RC slabs, three shear connectors were located as shown in Figure 4. Number 10 rebars having the area of 71 mm² were used for the shear connectors. 4-CFRP sheets were installed and concrete having the 28-day compressive strength of 79 MPa was overlaid. The strength

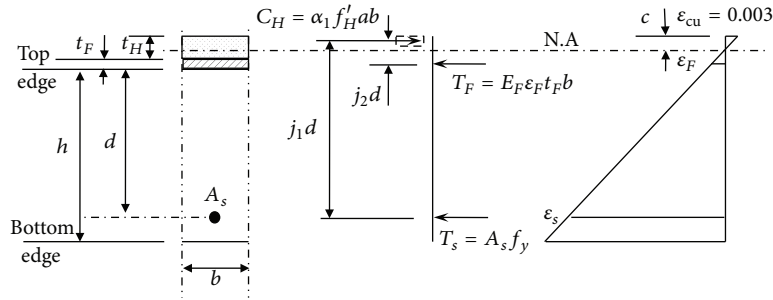


FIGURE 2: Enhancing mechanism of the proposed retrofit system for the positive moment sections of RC slabs.

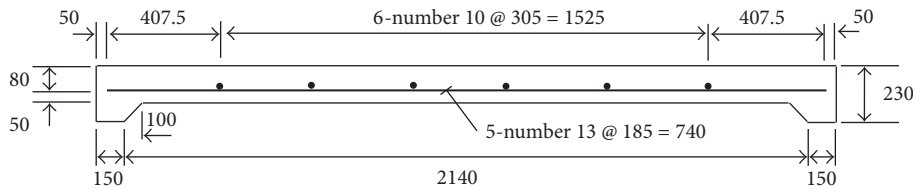


FIGURE 3: Reinforcement details for the control slab specimen having the width of 900 mm.

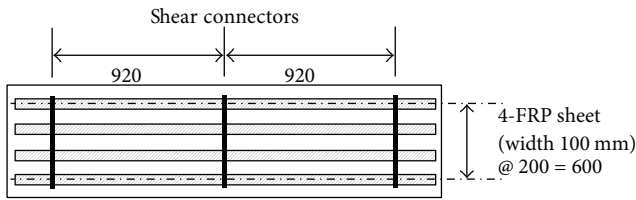


FIGURE 4: Locations of shear connector and CFRP sheets for the proposed retrofit system.

and elastic modulus of CFRP are 600 MPa and 40 GPa, respectively. The simply supported test setup for slabs was provided and loaded at two points as shown in Figure 5. The UTM used was capable of applying the maximum force of 5000 kN.

4. Results and Discussions

4.1. Observations. The full-scale structural test was performed in a successful manner. The slab developed cracks as the loading increased between the loading points. The cracks never developed into full-depth of slab. Some of these cracks can be seen in Figure 6. It shows slab cracking at approximately 20 kN of applied loads. The control slab showed higher failure load of 51.4 kN than was originally calculated with maximum load of 46.7 kN. The maximum load applied to the control slab is 34% higher than the predicted load. The reason for the higher strength of control slab is attributed to the assumption of linear elastic-perfectly plastic behavior of the steel. Testing of the reinforcing steel showed a higher strength in the slab due to strain hardening. The LVDTs had to be reset at different points during the test to continue to provide accurate readings. This maximum midspan deflection of 113 mm is shown in Figure 7 for the load-deflection ($P-\Delta$)

curve. It can be observed that the structure behaved in a linear elastic fashion until 23 mm of midspan deflection. The corresponding force at this displacement is 51.4 kN. The slope of the $P-\Delta$ curve represents the stiffness of the control slab. The stiffness of the control slab is found to be 10.8 kN/mm within its elastic limits. The toughness of the system can be calculated by integrating $P-\Delta$ curve. The resulting toughness of the control slab is 5322 kN·mm.

The $P-\Delta$ curve for the retrofitted slab is also shown in Figure 7 with that for control slab. The maximum load in the experiment was 2.7% higher than the predicted load of 84.8 kN. At the load of 40 kN, the slab lost capacity due to microbuckling of CFRP sheet as shown in Figure 8 for strain of CFRP. After that, the slab continued carrying higher load until it reached a load of 80 kN when the stress in CFRP was switched from compression into tension. Until the delamination of CFRP at the load of 87.1 kN, the slab continued carrying loads. Then, the slab experienced a decrease in capacity and dropped to 73.3 kN due to the delamination of CFRP. Shortly afterwards, the capacity increased to 95.9 kN and the CFRP takes compression until failure as observed in Figure 8. It shows that the shear connector takes loads after delamination of CFRP. The failure load and midspan deflection of the slab were 85 kN and 160 mm, respectively. At this time, it can be approximated as slab fails due to the yielding of the shear connectors.

Horizontal shear failure of the HPC overlay occurred at the midspan. The stiffness of the strengthened slab can be determined as 17.2 kN/mm. This is the stiffness of the retrofitted slab which is about 1.6 times that of the control slab. The toughness of the retrofitted slab was found to be 12114 kN·mm which is 2.3 times that of the control slab.

The main area of interest was the strain in the CFRP. The strain measurement on the CFRP was critical, as it would verify the system hypothesis that the CFRP sheets stayed in tension during the test and up to failure. As shown in (1), the

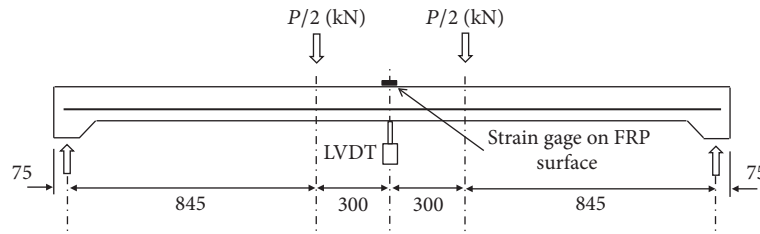


FIGURE 5: Slab loading test setup.

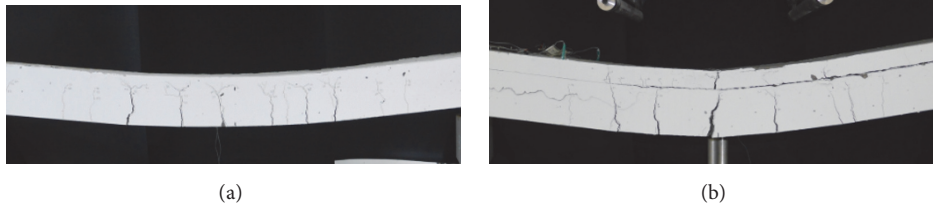


FIGURE 6: Midspan cracks of slabs at failure, (a) control slab and (b) retrofitted slab.

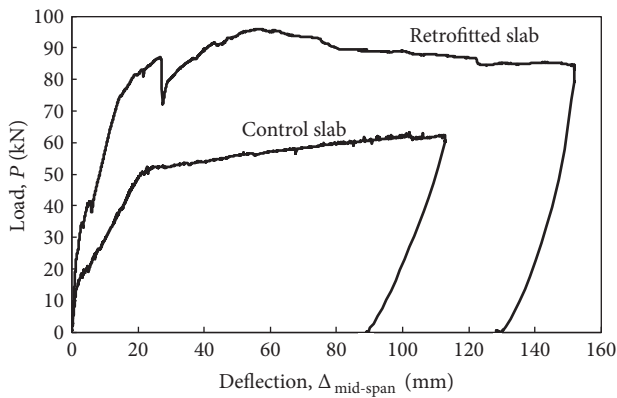


FIGURE 7: Load-deflection curves for the control and the retrofitted slab.

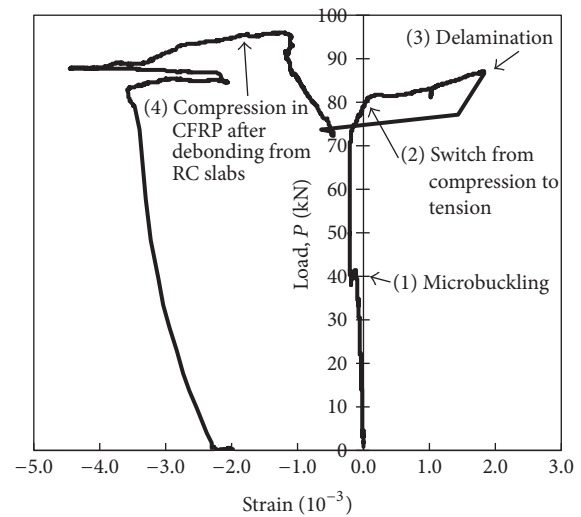


FIGURE 8: Strain evolution in CFRP.

flexural strength increases due to the moment generated by the tension forces in CFRP, T_F . After delamination of CFRP, shear connectors keep the bonding between the existing RC slab and overlay HPC and it provides ductility until the midspan deflection of 160 mm.

4.2. Finite Element Analysis. The main area of interest was the strain on the CFRP for the proposed retrofit system installed at the positive moment sections as it would verify the proposed system hypothesis that the CFRP sheet takes tension at failure. While CFRP takes tension until the strain of 0.0018, it did not reach at the debonding strain of 0.006 [9]. Therefore, the retrofitted slabs were analyzed by using nonlinear finite element (FE) analysis. CFRP behavior and the debonding mechanism were investigated. Figure 9 shows the typical analysis model for the retrofit model. For efficient modeling, only 1/4 of the system was modeled by taking advantage of the symmetry.

The general purpose structural analysis program ABAUQS was used [14]. The concrete and HPC were modeled using 8-node solid elements with reduced integration point. For CFRP sheet and rebar, 4-node shell and 2-node truss element were used for the analysis, respectively, as shown in Figure 9. The rebar and CFRP sheet were embedded into the concrete by using EMBEDDED option in ABAQUS [14]. Thus, rebar and CFRP sheet are perfectly bonded to the concrete. For CFRP sheet, this assumption is reasonable before the tensile strain of the CFRP is smaller than 0.006, where strain of 0.006 in CFRP sheet represents the debonding strain [9]. Analysis of concrete includes many nonlinear responses such as concrete cracking. Thus, to ensure the convergence of the solution, STABILIZE option in ABAQUS is used in this study [14]. STABILIZE option provides an automatic mechanism for stabilizing unstable quasi-static problems

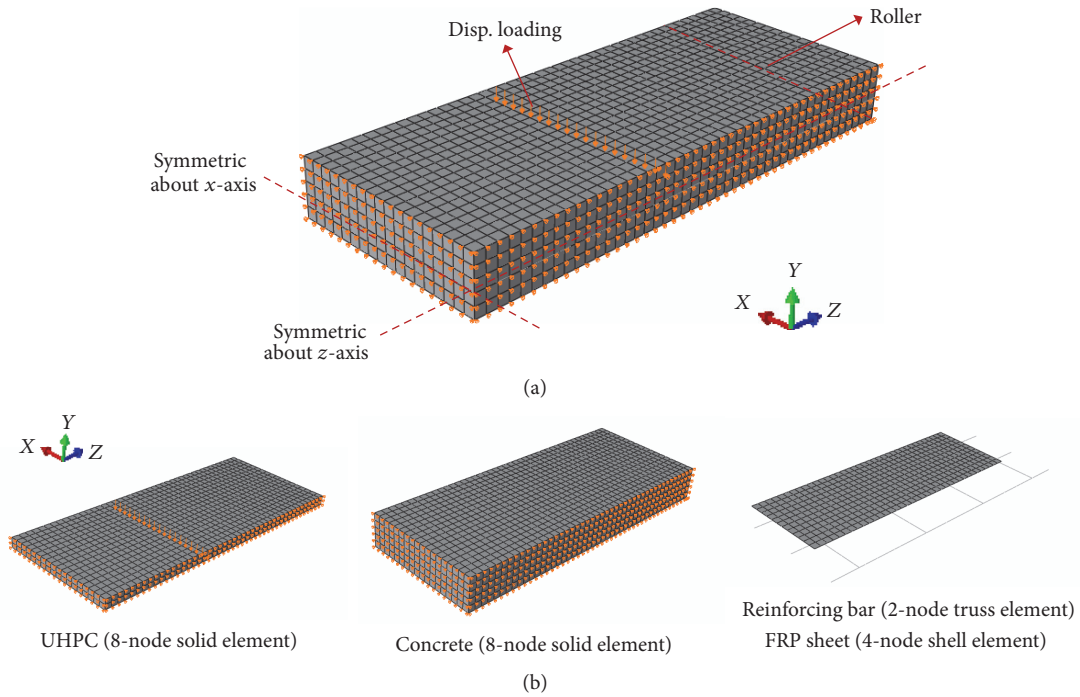


FIGURE 9: FE models: (a) FE model and boundary conditions and (b) elements for HPC-CFRP retrofit model.

through the automatic addition of volume-proportional damping to the model [14]. The translation in directions 1 and 3 were restrained to simulate the symmetric pane for x - and z -axis, as shown in Figure 9. The bottom line of the end of the analysis model was restrained in y direction to model the roller support. Then, a monotonic displacement loading was applied.

Figure 10 shows the comparisons of the load-displacement relationship for HPC retrofit model for verification of FE model with observation. For the retrofitted model, overall stiffness and ultimate strength of FE analysis model were matched well with the observation. Analysis was performed up to approximately 60 mm of deflection, and the model was yielded around 14.3 mm of deflection. For the yield point (deflection = 14.4 mm), the maximum tensile stress in the CFRP sheet was 56 MPa. Thus, the corresponding tensile strain of the CFRP is approximately 0.0014 (56 MPa/40 GPa), and it is similar to the observed strain of 0.0016. Figure 11 represents the Von-Mises stresses in the analysis model at the yield point. As shown in Figure 11, it can be found that the tensile stresses were developed in CFRP sheets. Thus, the neutral axis exists inside of the UHPC part when UHPC retrofit model is yielded. The delamination of CFRP with the substrate slab might be due to the cracks on the top of substrate slab as shown in Figure 11 for the stress distribution of substrate slab.

5. Conclusions

Considering the difficulty of the accessibility and installation of FRP laminates to the underside of RC slabs and bridge decks for flexural strengthening, a hybrid composite system,

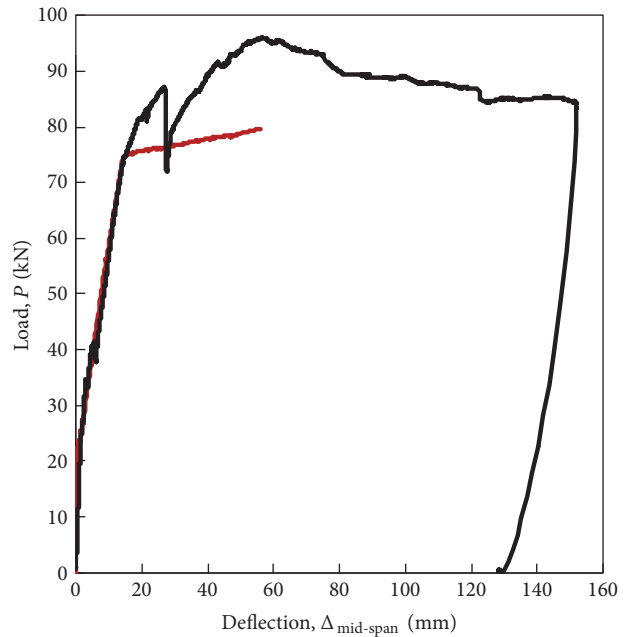


FIGURE 10: FE model verification.

which consists of UHPC, CFRP, and shear connectors, was proposed. The system is applied to the top surface of the floor slabs or bridge decks and it is introduced to improve the flexural carrying capacity of the existing RC floor slab and bridge decks. Using simply supported slab specimens, only positive moment section was examined to verify the effectiveness of the proposed system experimentally and

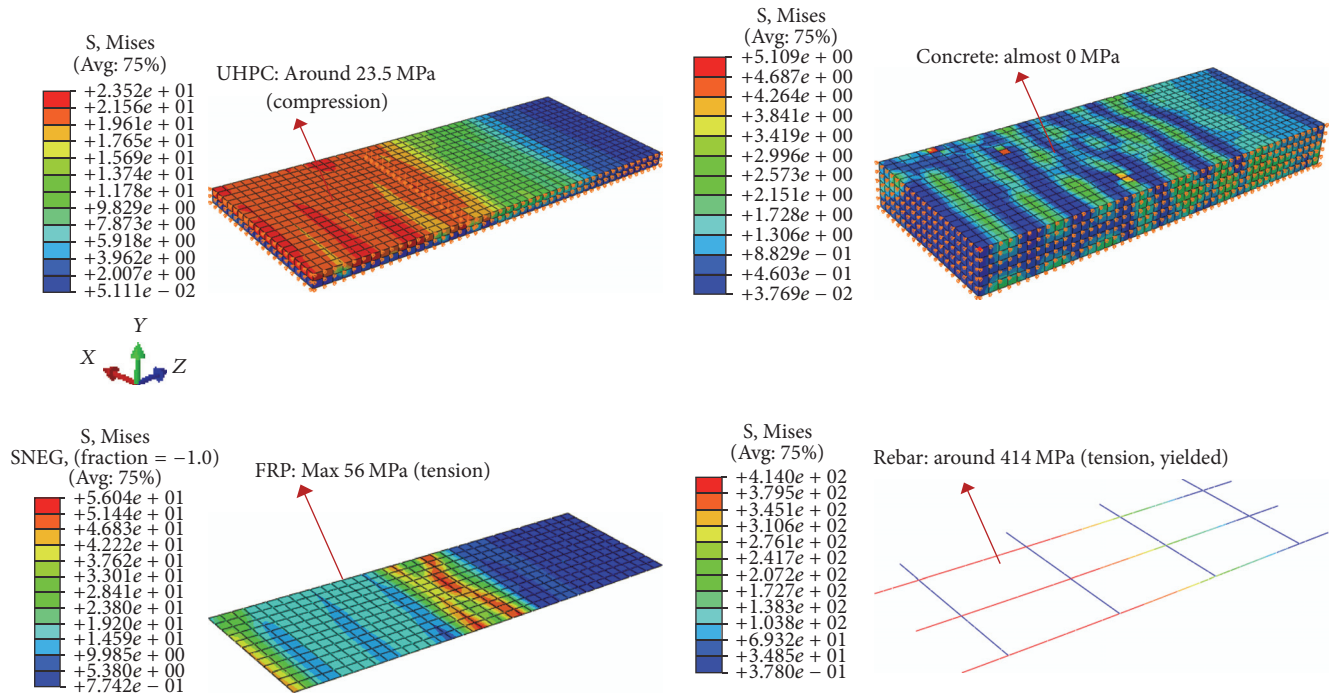


FIGURE 11: Stresses in HPC overlay at yield point.

numerically. The proposed strengthening system increased the ultimate load carrying capacity of the slab by 70%, the stiffness by 60%, and toughness by 128%. The efficiency of shear connectors on ductile behavior of the retrofitted slab was also confirmed.

Conflicts of Interest

The authors declare that there are no conflicts of interest regarding the publication of this paper.

Acknowledgments

This research was supported by Korea Agency for Infrastructure Technology Advancement (KAIA) (Grant no. 16CTAP-C097358-02) funded by Ministry of Land, Infrastructure and Transport (MOLIT) of Korea government.

References

- [1] K. M. Mosalam and A. S. Mosallam, "Nonlinear transient analysis of reinforced concrete slabs subjected to blast loading and retrofitted with CFRP composites," *Composites Part B*, vol. 32, no. 8, pp. 623–636, 2001.
- [2] A. S. Mosallam and K. M. Mosalam, "Strengthening of two-way concrete slabs with FRP composite laminates," *Construction and Building Materials*, vol. 17, no. 1, pp. 43–54, 2003.
- [3] M. I. Ary and T. H.-K. Kang, "Shear-strengthening of reinforced & prestressed concrete beams using FRP: part I—review of previous research," *International Journal of Concrete Structures and Materials*, vol. 6, no. 1, pp. 41–47, 2012.
- [4] C. J. Fleming and G. E. M. King, "The development of structural adhesives for three original uses in South Africa," in *Proceedings of the RILEM International Symposium, Synthetic Resins in Building Construction*, pp. 75–92, Paris, France, 1967.
- [5] P. H. Emmons, A. M. Vaysburd, and J. Thomas, "Strengthening concrete structures, Part II," *Concrete International*, vol. 20, no. 4, pp. 56–60, 1998.
- [6] J. Nam, H. Kim, S. Kim, N. Yi, and J. J. Kim, "Numerical evaluation of the retrofit effectiveness for GFRP retrofitted concrete slab subjected to blast pressure," *Composite Structures*, vol. 92, no. 5, pp. 1212–1222, 2010.
- [7] J. Li, C. Wu, H. Hao, Y. Su, and Z. Liu, "Blast resistance of concrete slab reinforced with high performance fibre material," *Journal of Structural Integrity and Maintenance*, vol. 1, no. 2, pp. 51–59, 2016.
- [8] S. Rizkalla, T. Hassan, and N. Hassan, "Design recommendations for the use of FRP for reinforcement and strengthening of concrete structures," *Progress in Structural Engineering and Materials*, vol. 5, no. 1, pp. 16–28, 2003.
- [9] ACI Committee 440, "Guide for the design and construction of externally bonded FRP systems for strengthening concrete structures," Tech. Rep. ACI 440.2R-08, Farmington Hills, Mich, USA, 2008.
- [10] A. Mosallam, M. M. Reda Taha, J. J. Kim, and A. Nasr, "Strength and ductility of RC slabs strengthened with hybrid high-performance composite retrofit system," *Engineering Structures*, vol. 36, pp. 70–80, 2012.
- [11] J. G. MacGregor and J. K. Wight, *Reinforced Concrete: Mechanics and Design 5th*, Prentice Hall, USA, 2005.
- [12] J. J. Kim, H.-C. Noh, M. M. Reda Taha, and A. Mosallam, "Design limits for RC slabs strengthened with hybrid FRP-HPC retrofit system," *Composites Part B*, vol. 51, pp. 19–27, 2013.

- [13] ACI Committee 318, "Building Code Requirements for Structural Concrete (ACI 318-05) and Commentary (318R-05)," International Journal of Cement Composites and Lightweight Concrete, American Concrete Institute, Farmington Hills, USA, 2005.
- [14] ABAQUS, "ABAQUS analysis user's manual version 6.9-2", Dassault Systemes Simulia Corp., Providence, RI, USA, 2009.